Clay Formation and Nutrient Cycling Across the Sturtian Snowball Earth Glaciation

Jalila Al Bahri

School of Earth and Environmental Sciences
Cardiff University

Submitted in partial fulfilment of the requirements for the degree of
Doctor of Philosophy
January 2025

Dedication

I wish to dedicate this thesis to my beloved parents.

Acknowledgements

First and foremost, I would like to extend my heartfelt thanks to my supervisors, Dr. Ernest Chi Fru and Dr. Morten Andersen. Their timely and invaluable advice, continuous support, and guidance over the past years have meant worth to me. Their patience, insightful ideas, motivation, and contributions throughout all phases of my PhD journey are truly appreciated.

I am sincerely grateful to the Ministry of Higher Education, Research and Innovation and the University of Technology and Applied Science, Sultanate of Oman, for their financial support during my PhD study.

Throughout my PhD journey, I have been privileged to receive exceptional technical and laboratory support, for which I am deeply grateful. Many thanks go to Dr. Duncan Muir for his invaluable mentorship and assistance in the SEM lab. I am grateful to Dr. Olabode Bankole and Prof. Abderrazzak El Albani at Université de Poitiers, France for their assistance with the 2-µm clay fraction analysis. I would also like to thank Dr. Anthony Oldroyd for assisting me with the preparation of thin sections and for his guidance with XRD work, as well as Dr. Alexandra Nederbragt for her expertise and help with stable isotope analysis of carbon.

To my beloved husband, Waleed, and my dear children, Khalid, Alaa, and Osama—thank you for standing by me every step of the way. Your unwavering belief in me, your prayers, and your understanding lightened the load. I am so grateful for all the sacrifices you have made for me, and words cannot express how much you mean to me. To my kids, thank you for the little letters slipped into my university bag to keep me motivated. Each one brought me joy and strength, and they mean more to me than words can express. Your thoughtfulness and love have been a true source of inspiration throughout this journey.

Finally, thank you to my dear parents, brothers, and sisters for your love, encouragement, and unwavering faith in me. Your emotional support and trust have been my strength throughout the entire PhD journey. I am forever grateful for having each of you in my life. Special thanks are extended to my niece, Adhraa Al Bahri, I am deeply grateful for everything you did for us, from your care and commitment to the countless ways you lightened my load.

Abstract

It has been proposed that the physical weathering of Earth's continents by thawing glaciers during the Neoproterozoic Sturtian Snowball Earth glaciation, ~ 720–660 million years ago, produced glacial till that fertilised post-Snowball oceans with nutrients, particularly phosphorus. This flux of nutrients into seawater is thought to have triggered a surge in primary production, contributing to ocean-atmosphere oxygenation and potentially driving a step change in biological evolution. However, the precise mechanism by which these nutrients were transported from land to the ocean and eventually released in a bioavailable form for primary production remains poorly understood. This thesis seeks to address this gap through detailed mineralogical and geochemical analysis of shallow marine sedimentary rocks deposited before, during and after the global Cryogenian Sturtian Snowball Earth glaciation. In addition to unravelling specific pathways by which nutrients were delivered to Cryogenian seawater following the glaciation, this study explores the interplay between redox dynamics and nutrient cycling during this transformative period in Earth's history.

Advanced mineralogical X-ray diffraction (XRD) and Scanning Electron Microscopy (SEM) analyses, alongside quantitative chemical extraction of Fe-bound P minerals, revealed a strong correlation between detrital clay mineral production by the melting Sturtian Snowball ice sheets and a short-lived increase in dissolved seawater phosphate content by at least 20-fold. These observations suggest that interactions between physical and chemical weathering of glacial till under the post-Snowball CO_2–rich atmosphere were critical in releasing nutrients from the continents to seawater. Clay minerals, acting as carriers, facilitated the transport of both detrital and dissolved nutrients. Upon entering the ocean, the changes in salinity and pH triggered the clays to release the bound elements, which fuelled biological productivity.

Seawater redox conditions explored using multiple redox proxies ($\delta^{238}U_{CAU}$, Fe_T/Al and iron speciation), reveal a transient oxygenation of the ocean margins immediately after the Sturtian Snowball glaciation. The results show that the rise and fall in seawater oxygenation matched nutrient maximum and minimum concentrations, respectively, supporting the proposition that Proterozoic seawater nutrient bioavailability, particularly dissolved phosphate content, regulated marine primary productivity and ocean-atmosphere oxygenation dynamics.

These findings underscore the pivotal role of clay mineral production and their involvement in nutrient delivery during post-Sturtian Snowball glacial runoff. Acting as nutrient vectors, clay

minerals facilitated the transport and release of key nutrients, highlighted by phosphate, from the continents into the ocean. It is therefore proposed that clay mineral formation played a central role in driving Neoproterozoic primary production and promoting ocean-atmosphere oxygenation in the aftermath of the Sturtian Snowball Earth glaciation and probably throughout Earth's history.

List of Publications

Part of the thesis outcomes were published in Peer-reviewed journal articles and presented as conference posters. A third manuscript is in preparation. The list of publications is as follows:

1- **Al Bahri, J**., Bankole, O., Muir, D., El Albani, A., Oldroyd, A., Contreras, D., Andersen, M. and Chi Fru, E, 2024. Clay mineral geochemistry and paleoenvironmental reconstruction across the Cryogenian Sturtian Snowball glaciation. *Precambrian Research*, *410*, p.107498.

2- Chi Fru, E, **Bahri, J.A**., Brosson, C., Bankole, O., Aubineau, J., El Albani, A., Nederbragt, A., Oldroyd, A., Skelton, A., Lowhagen, L. and Webster, D., 2023. Transient fertilization of a post-Sturtian Snowball ocean margin with dissolved phosphate by clay minerals. *Nature Communications*, *14*(1), p.8418.

Conference attend:

1- **Temporary Ocean oxygenation in the wake of the Sturtian glaciation** in Goldschmidt conference, 9-14 July 2023, Lyon, France. Poster.

2- **Clay mineralogy across Sturtian-snowball Earth, Islay Scotland** in Geochemistry Group Research in Progress (GGRiP) conference, 5th and 6th of May 2022, Cardiff University, UK. Poster

The manuscript is in preparation:
Al Bahri J., Chi Fru E., Andersen M. Uranium isotopes and ocean-atmosphere oxygenation dynamics across the Sturtian Snowball Earth glaciations. In preparation.

Table of Contents

List of Figures

List of Tables

List of Abbreviations

LLF	Lossit Limestone Formation
PATF	Port Askaig Tillites
BDF	Bonahaven Dolomite Formation.
XRD	X-Ray Diffraction
SEM	Scanning Electron Microscopy
EDS	Energy-dispersive system
BSED	BackScattered-Electron Detection
CIA	Chemical Index of Alternation
VPDB	Vienna Pee Dee Belemnite
$\delta^{13}C_{carbonate}$	Stable Carbon Isotope
$\delta^{13}C_{organic}$	Stable Organic Carbon Isotope
$\delta^{18}O_{carbonate}$	Stable Oxygen Isotope
$\delta^{238}U$	Uranium Isotope
GOE	Great Oxygenation Event
NOE	Neoproterozoic Oxygenation Event
PAL	Present Atmospheric Level
Ga	Giga-annum before present
kyr	Thousand years (duration)
LOI	Loss on Ignition
MIF-S	Mass-Independent Fractionation of Sulfur
BIF	Banded Iron Formation
Fe_{HR}	Highly Reactive Fe pool
Fe_{py}	pyritic iron
Fe_T	Total Iron
Th	Thorium
Fe	Iron
P	Phosphorus
PO_3^{-4}	Phosphate
Al	Aluminium
Ti	Titanium
V	Vanadium
Cr	Chromium
Co	Cobalt
SD	Standard Deviation

Chapter 1: Literature Review

1.1 Introduction

The Precambrian Era, spanning 4.0 to 0.54 giga-annum before the present (Ga), marks the earliest and most transformative period in Earth's geological history. This interval records the first and second appreciable rise of oxygen in Earth's atmosphere during the 2.45-2.2 Ga Paleoproterozoic Great Oxygenation Event (GOE) and the 0.85-0.54 Ga Neoproterozoic Oxygenation Event (NOE) (e.g., Farquhar et al., 2000; Bekker et al., 2004; Canfield, 2005; Holland, 2006; Shields-Zhou and Och, 2011; Och and Shields-Zhou, 2012; Lyons et al., 2014, 2024). During this time, life evolved from single-cell prokaryotes and eukaryotes to complex multicellular metazoans (Knoll et al., 2006, 2016; Parfrey et al., 2011; Lyons et al., 2018; Lyons et al., 2024). This period is further linked to the formation and break up of two major supercontinents, Columbia and Rodinia (Ernst et al., 2008; Gao et al., 2021), and to the deep ocean becoming progressively oxygenated (Holland, 2006; Scott et al., 2008; Frei et al., 2009; Och and Shields-Zhou, 2012; Wallace et al., 2017; Reinhard and Planavsky, 2021; Xu et al., 2022; Lyons et al., 2014, 2024). Within this interval, Earth experienced a series of dramatic climatic events known as Snowball Earth glaciations that covered the Earth from pole-to-pole with km-thick ice sheets for millions of years (Kirschvink, 1992; Hoffman et al., 1998; Hoffman and Schrag, 2002; Schrag et al., 2002; Warren et al., 2002; Hoffman et al., 2017). These events are thought to have irreversibly shaped the biogeochemical, geological and ecological trajectory of our planet's evolution to what it is today. Despite this advancement in our current understanding of the Precambrian ocean-atmosphere system, significant gaps still exist in our understanding of these events, especially with respect to the marine sedimentary, elemental, and mineralogical patterns that

drove these vital environmental changes. Further, there is a dearth of knowledge on the link between continental weathering dynamics, clay mineral formation, abundance, type and their role in enabling the progressive evolution of Earth's surface environments, the functioning of early biogeochemical cycles and the evolution of ocean-atmosphere redox state. The work described in this thesis examines clay mineral formation across the Neoproterozoic Cryogenian Sturtian Snowball Earth glaciation that occurred between 0.72-0.66 Ga, to unravel its implication on seawater nutrient cycling and redox evolution before, during and after the glaciations.

1.1.1 Precambrian Ocean-Atmosphere Oxygenation Dynamics

Despite oxygen being the third most abundant element in the universe, after H and He, and by weight in the Earth's crust (Anders and Grevesse, 1989), free molecular oxygen (O_2) was scarce or nearly absent in the atmosphere during most of Earth's history (Berner et al., 2003; Canfield, 2005; Berner, 2006). Estimates of atmospheric oxygen content suggest it was only about 0.001% of present atmospheric levels (PAL) during the Archean, before increasing abruptly to between 0.1% and 10% PAL during the Proterozoic, reaching modern levels in the Phanerozoic time (Farquhar et al., 2000; Laakso and Schrag, 2017; Krause et al., 2018). As a major oxidant, the eventual accumulation of oxygen in the atmosphere forever changed Earth's surface chemistry (e.g., Canfield, 2005) and inducing new oxidized chemical compounds or amplifying their quantity in seawater (Kah et al., 2004; Crowe et al., 2014; Stüeken et al., 2016; Fru et al., 2019; dos Santos et al., 2022; Robbins et al., 2023). Being the most energetic electron acceptor on the Earth's surface, oxygen participates in oxidative weathering of the crust (Catling and Claire, 2005), delivering nutrients to seawater for primary production and is critical for aerobic respiration, metabolism and growth of advanced life forms (Catling and Claire, 2005). Consequently, changes in the amount of

oxygen, in tandem with nutrient levels, present in the ocean-atmosphere system have played a vital role in shaping planetary surface evolution and the composition of early life to the present ecological dominance of animals (Lyons et al., 2014; Knoll et al., 2016; Chi Fru et al., 2024). Although, the role of oxygen in biological evolution, especially concerning the rise of animals, is a complex and debated topic (Erwin et al., 2011; Mills et al., 2014; Bozdag et al., 2021). Nonetheless, the processes responsible for the proposed fluctuations in early atmospheric oxygen content remain a puzzle and one of the most intensely debated topics in the Earth sciences.

These dynamic changes in atmospheric and oceanic oxygen content span many orders of magnitude in abundance and encompass a wide range of spatiotemporal scales, linked to a balance between the supply of O_2 to the ocean interior and consumption within the water column (Holland, 2006). In the modern ocean, dissolved oxygen concentration in the upper ocean commonly decreases from the well-mixed surface ocean layer (the top few tens of meters) into deeper subsurface waters (a few hundred meters), controlled by three key factors: 1) the partial pressure of atmospheric oxygen (pO_2) content; 2) the intensity of upper-ocean mixing; and 3) respiratory oxidation of organic matter in the water column, which consumes oxygen (Keeling et al., 2010). However, the early oceans were more reducing than today, thereby representing an additional sink for oxygen consumption which helped maintain widespread seawater anoxia and ocean redox stratification (Holland, 2006). Furthermore, seawater *p*O2 is thought to have been related to nutrient availability to oxygenic photosynthetic cyanobacteria and the pathways by which these nutrients, particularly phosphorus (P), were supplied to seawater, including transportation and delivery by clay minerals (Chi Fru et al., 2023).

Based on geochemical and sedimentological evidence, the major changes in the evolution of ocean and atmosphere oxygenation can be divided into five main stages

(Holland, 2006; Lyons et al., 2014, 2024) as summarised in Figure 1.1. In the first stage 4.0 – 2.45 Ga, the atmosphere and oceans remained largely anoxic, with atmospheric O_2 concentration being generally less than 10^{-5} present atmospheric level (PAL) (Farquhar et al., 2000; Bekker et al., 2004). Although photosynthetic production of oxygen may have emerged early in Earth's history at ~3.0 Ga, increases in atmospheric and marine reservoirs of oxygen were substantially delayed (Buick, 2008; Kump, 2008; Lee et al., 2016; Reinhard and Planavsky, 2020) or limited during the Archean, with some studies indicating transient "whiffs" of atmospheric oxygen at this period. For example, significant oxygen concentrations in the shallow oceans were estimated by Satkoski et al. (2015) using stable Fe and radiogenic U–Th–Pb isotope data at 3.2 Ga, by Crowe et al. (2013) using chromium isotopes at 2.98 Ga and by Ossa Ossa et al. (2018) using Fe and Mo isotope in banded iron formation (BIFs) before 2.46 Ga.

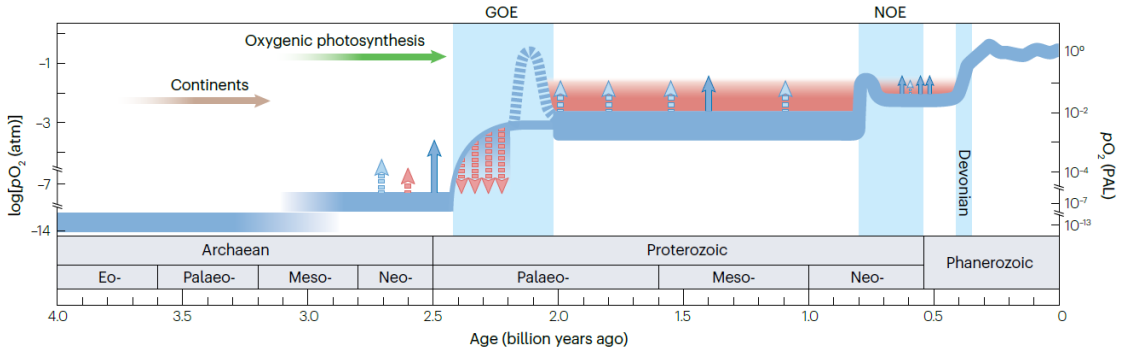

Figure 1. 1| A model of Earth's atmospheric O_2 evolution according to Lyons et al. (2024). See text for a summary and related references for surface and deep ocean redox state. The blue curve represents the Lyons et al. (2024) preferred model for O_2 long-term evolution. The red-shaded area shows the estimated level by numerical simulations that allow for O_2 stability only at higher pO_2.

The second stage, commonly referred to as the Great Oxygenation Event (GOE), began in the early Paleoproterozoic in association with global glaciations and continued until the end of the Lomagundi carbon isotope excursion between ca. 2.4 and 2.2 Ga (Bekker et al., 2004; Holland, 2006; Chi Fru et al., 2016a; Poulton et al., 2021). The GOE records the first stepwise permanent increase in atmospheric oxygen levels in Earth's history, from trace

levels to more than 10^{-5} PAL (Farquhar et al., 2000; Lyons et al., 2014, 2024). Accordingly, the GOE led to major changes in the biogeochemical cycling of most essential elements critical to Earth's surface chemistry, including phosphorus, carbon, sulfur and diversification of mineral types (Sverjensky and Lee, 2010; Pufahl and Hiatt, 2012). A variety of geochemical proxies capture this increase in O_2 levels at this time e.g., sulfur (S) isotope (Bekker et al., 2004; Ohmoto et al., 2006), chromium (Cr) isotope (Frei et al., 2009), molybdenum (Mo) isotopes (Asael et al., 2018; Hodgskiss et al., 2021), Fe speciation and trace metals concentrations and distribution (Canfield et al., 2013), copper (Cu) isotopes (Chi Fru et al., 2016), nitrogen (N) (Zerkle et al., 2017; Cheng et al., 2019), and carbon (C) isotope (Ossa Ossa et al., 2022). Although these proxies are diverse, each with a unique sensitivity range to environmental O_2 tension, they broadly converge on the redox state of the Earth's ocean-atmosphere system, permanently changing during the GOE towards more oxidizing conditions. Of particular significance, this transition in ocean-atmosphere redox state is tightly linked to the cessation of mass-independent fractionation of sulfur (MIF-S) isotopes in the marine sedimentary rock record as the smoking gun (Farquhar et al., 2000; Bekker et al., 2004; Holland, 2006; Philippot et al., 2018). Also, enrichment of redox-sensitive elements (e.g. Mo, U, V) (Scott et al., 2008; Partin et al., 2013b), apparent loss of detrital pyrite (FeS_2) and uraninite (Johnson et al., 2014; Zhou et al., 2017), easily oxidized by oxygen, from ancient sedimentary archives both point to the presence of oxygen. While the shallow surface seawater became globally oxygenated, the deep ocean, however, remained dominantly anoxic (Shen et al., 2002; Poulton and Canfield, 2011; Reinhard and Planavsky, 2021).

Following the GOE, the Earth experienced a long period of apparent environmental stability, the so-called 'Boring Billion' (Buick et al., 1995) which has been re- evaluated as 'Balance Billion' by Mitchell and Evans (2023), lasting from 1.80 – 0.80 Ga during the

Mesoproterozoic and Early Neoproterozoic, marked by considerable debated atmospheric O_2 concentrations reaching a nadir of ~ 0.01 and as high as ~ 10% PAL (Holland, 2006; Lyons et al., 2014, 2024). This redox shift from the GOE, is marked foremost by the reappearance of evidence for anoxic conditions in very shallow waters and the disappearance of sulfate evaporites (Canfield, 2005). After the 'Balance Billion', several lines of evidence point to a second major oxygenation event between 0.85 and 0.54 Ga—in what is now often referred to as the Neoproterozoic Oxygenation Event (NOE) (Shields-Zhou and Och, 2011; Och and Shields-Zhou, 2012; Lyons et al., 2014, 2024). The NOE was originally interpreted as an increase in atmospheric oxygen from Proterozoic to near-modern levels (~1–10% to ~100% PAL) (Lyons et al., 2014, 2024). This period is consistent with the negative $\delta^{13}C$ anomalies which reflect alternations in the sources and sinks of carbon, as well as shifts in ocean chemistry, biological activity, environmental and geological processes (Johnston et al., 2012; Shields et al., 2019). In contrast with GOE, the timing and magnitude of oxygenation in the Neoproterozoic are poorly constrained (Och and Shields-Zhou, 2012; Lyons et al., 2014, 2024). Most proxies indicate a complex dynamic oxygenation, instead of a single transition and stepwise increase in oxygen levels over this interval (Sahoo et al., 2012; Frei et al., 2013; Guilbaud et al., 2015; Pogge Von Strandmann et al., 2015; Wallace et al., 2017; Chi Fru et al., 2023; Lyons et al., 2024). As a consequence, marine redox evolution during this period is highly debated. However, surface ocean oxygenation persisted throughout this time, meanwhile, the deeper ocean likely remained predominantly anoxic (Dahl et al., 2011; Poulton and Canfield, 2011; Lenton et al., 2014). It remains unclear when precise deep ocean oxygenation occurred, while it has been suggested that this was sometime during the Late Neoproterozoic, recent evidence indicates that anoxic waters were common and that there was considerable variability in the temporal and spatial extent of deep ocean oxygenation, including the possibility of pulsed oceanic oxic events at this

time (Och and Shields-Zhou, 2012; Sahoo et al., 2016), with full ocean oxygenation coinciding with the Paleozoic oxygenation event (POE) (Krause et al., 2018). The latter stage is characterized by significantly varying but persistently high atmospheric oxygen levels, reaching near modern pO_2 levels and establishment of a predominantly oxygenated deep ocean during the Phanerozoic, sometime after ~0.541 Ga (Berner et al., 2003; Berner, 2006; Krause et al., 2018).

This thesis contributes towards unravelling oxygenation dynamics during Neoproterozoic time, by coupling nutrient cycling dynamics, to clay mineral production on land and supply to seawater, because of the impact of the dramatic Sturtian Snowball Icehouse.

1.2 Local and Global Ocean Redox Proxies

Our understanding of the above-described history of Earth's ocean-atmosphere oxygenation history comes from the use of diverse geochemical proxies that record changing ocean redox dynamics (e.g., Farquhar et al., 2000; Romaniello et al., 2013; Lyons et al., 2014; Chi Fru et al., 2016a, 2019; Tostevin et al., 2016; Algeo and Liu, 2020; Bennett and Canfield, 2020; Clarkson et al., 2021, Lyons et al., 2014, 2024). While some of these proxies indicate global oxygenation processes, others record local conditions. In this study, the widely used Fe speciation redox proxy, which is used to record local redox conditions (see Poulton and Canfield, 2011 and Raiswell et al., 2018 for reviews), trace element distribution and U isotope systematics, which records the global change in redox status (e.g., Romaniello et al., 2013; Algeo and Liu, 2020; Bennett and Canfield, 2020), are used to evaluate redox changes across the Neoproterozoic Cryogenian Sturtian Snowball Earth glaciation in ancient deposits preserved in Scotland (Tanner et al., 2013; Hoffman et al., 2017; Parnell and Boyce, 2017; Fairchild et al., 2018), with a major goal being to examine what links existed between clay

mineral formation during greenhouse and icehouse continental weathering, seawater nutrient enrichment and redox.

1.2.1 The Global Ocean Redox Uranium Tracer

1.2.1.1 Geochemical Behaviour and the Marine Uranium Budget

Uranium is a naturally occurring redox-sensitive element, which commonly exists in two stable redox states. Reduced and insoluble U(IV) is prevalent in the form of UO_2, U_3O_7 or U_3O_8 and the oxidized form as soluble U(VI), which forms uranyl bi-carbonate complexes in natural waters (Langmuir,1978, Klinkhammer and Palmers, 1991). Uranium behaves conservatively in the global ocean and is well mixed in the modern open ocean due to its long residence time of ~400 kyr (Ku et al., 1977), which is substantially longer than the average ocean mixing time of ~1-2 kyr (Broecker and Peng, 1982). Although the ocean mixing timescale fluctuated during Earth's history (Liu et al., 2024).

In this regard, uranium isotope ($\delta^{238}U$ ‰) systematics has emerged as a powerful tool for understanding marine redox conditions (Dunk et al., 2002; Andersen et al., 2014; Tissot and Dauphas, 2015; Holmden et al., 2015; Lau et al., 2017; Chen et al., 2022). The reduction of U(VI) to U(IV) is associated with a relatively large isotopic fractionation dominated by nuclear volume over mass-dependent effects (Bigeleisen, 1996). Under equilibrium conditions, the reduced U is enriched in the heavier ^{238}U isotope, and the remaining dissolved U(VI) becomes enriched in the lighter ^{235}U isotope. Consequently, $\delta^{238}U$ distribution has been leveraged as a useful proxy for reconstructing global marine redox states. Thus, if sedimentary $\delta^{238}U$ signatures can be linked to seawater composition, they have the potential to resolve past global changes in oceanic redox conditions.

However, it is crucial to understand the modern marine isotopic U cycle and ocean budget to reconstruct redox conditions in past environments. Modern open ocean seawater

has a uniform $\delta^{238}U$ value of −0.379 ± 0.023‰ (Kipp et al., 2022). The change in $\delta^{238}U$ of seawater ($\delta^{238}U_{sw}$) is controlled by the flux and isotopic composition of the ocean input/sources relative to its output/sinks. The major source of U to the ocean is from the weathering of continental crust and transport of dissolved U(VI) via riverine input, with a mean $\delta^{238}U$ of −0.34 to −0.26‰ (Andersen et al., 2016), which is close to the −0.29 ± 0.03‰ estimated $\delta^{238}U$ of the continental crust (Tissot and Dauphas, 2015). Other U sources, e.g., atmospheric dust and groundwater discharge are not well constrained, but minor compared to the riverine flux and likely negligible (Dunk et al., 2002). There are multiple U sedimentary sinks in the oceans, with U removal either as the oxidized U(VI) or reduced U(IV) species depending on local depositional redox conditions and associated with different U isotopic fractionations.

The most notable sinks are oxygen-deprived sediments and carbonates with minor sinks associated with Fe-Mn oxides and hydrothermal alteration of the oceanic crust (Figure 1.2) (Dunk et al., 2002). The different oceanic U sinks exhibit different $\delta^{238}U$ offsets from open ocean seawater. The euxinic (anoxic and sulfide-rich) sediments account for the largest average U isotope fractionation of ∼0.6 ‰ during U removal, driven by microbially mediated U(VI)−U(IV) reduction as observed in modern anoxic ocean basins (Stirling et al., 2007; Weyer et al., 2008; Andersen et al., 2014; Holmden et al., 2015; Noordmann et al., 2015; Rolison et al., 2017; Bura-Nakić et al., 2018; Brüske et al., 2020). The $\delta^{238}U$ of suboxic sediments is commonly ∼ +0.1– 0.3 ‰ heavier than the modern seawater, as observed in upwelling and coastal settings (Weyer et al., 2008; Andersen et al., 2016; He et al., 2021; Bruggmann et al., 2022).

Alternatively, oxic U removal via sorption onto metalliferous sediments (e.g., Fe and manganese (Mn) oxyhydroxides) preferentially take up isotopically light U with a mean $\delta^{238}U$– 0.24 ‰ lower than seawater, as observed in deep-sea Fe-Mn- nodules (Stirling et al.,

2007; Weyer et al., 2008; Brennecka et al., 2011; Goto et al., 2014; Tissot and Dauphas, 2015; Wang et al., 2016). The $\delta^{238}U$ offsets for the hydrothermal alteration of oceanic crust at high and low temperatures are approximately 0 ‰ and +0.25 ‰, respectively, as observed in Pacific altered oceanic crust (Andersen et al., 2015, 2016; Noordmann et al., 2015; Tissot and Dauphas, 2015). The modern global ocean U elemental and isotope mass balance (Figure 1.2) shows that the dominating removal of isotopically heavy U to anoxic sediments leaves the oceans enriched in the lighter ^{235}U isotopes, with a lower $\delta^{238}U$. The contrasting U isotopic behaviours among these sinks, particularly oxic vs. anoxic, give rise to the use of U isotopes as a paleo-redox proxy (Weyer et al., 2008) where shift towards lower $\delta^{238}U_{sw}$ in the past are commonly interpreted as expansions of marine anoxia. Yet reconstructing ocean redox in past environments faces challenges, e.g. the U isotopic fractionation in ferruginous settings (anoxic and iron-rich) is poorly constrained. Accordingly, ferruginous settings are often underestimated (poorly represented in models), especially during the Proterozoic when anoxic and iron-rich conditions were predominant (e.g., Gileadean et al., 2019). The most commonly used marine sedimentary archive of U is ancient carbonates (e.g., Elrick et al., 2017; Jost et al., 2017; Zhang et al., 2020; Clarkson et al., 2021). However, its ability to record seawater $\delta^{238}U_{sw}$ ($\delta^{238}U_{sw}$) is debated and may vary locally. This study examines U systematics associated with carbonates across the Neoproterozoic Sturtian Snowball Earth glacial and non-glacial shallow marine sediments in Scotland, in combination with Fe speciation to establish its ability to track global seawater and local sedimentary redox conditions before, during, and after the glaciation.

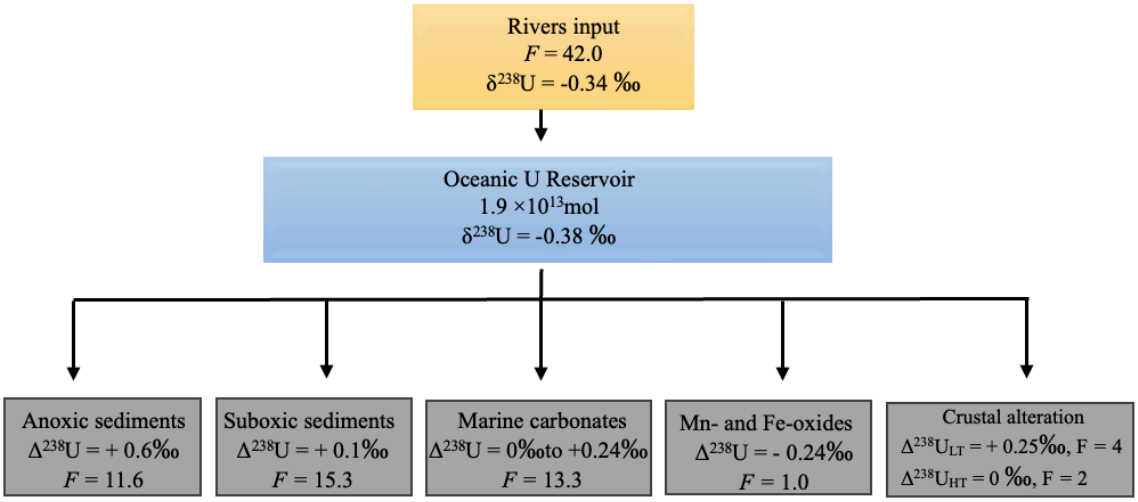

Figure 1.2 | Simplified schematic representation of the major source, sinks and fluxes of U in the modern ocean, along with their isotopic compositions (sources) or associated isotopic fractionations (sinks). Sinks include anoxic, suboxic sediment, marine marine carbonate, Mn- and Fe oxides, and ocean crust alternation. See the text for reference sources for isotope values. Fluxes (F) are in Mmol/yr, and isotopic compositions and fractionation factors are in permil (‰). $\Delta^{238}U = \delta^{238}Ux - \delta^{238}Usw$, x denotes different U sinks, LT= Low Temperature, HT= High Temperature. See text for related references for sources, sink and fluxes of U.

1.2.1.2 Uranium Isotopes in Marine Carbonates

Many existing paleo-redox proxies are essentially developed for black shales (e.g., Fe, Mo, and V isotopes) (e.g., Ye et al., 2021; Yang et al., 2022; Xu et al., 2024). However, the distribution of black shale in the geologic record is often confined to relatively rare marginal basins leading to a spatially- and temporally sporadic record compared to the carbonates, leaving significant gaps in our understanding of Earth's redox history (e.g., Chen et al., 2018). Additionally, the shale U isotope signatures are highly fractionated away from the seawater composition, and the magnitude of the fractionation factor relative to seawater has been shown to depend on environmental controls such as the depositional environments (Andersen et al., 2014), organic carbon, and sulfide burial rates (Cole et al., 2020) or the extent of oceanic anoxia (Chen et al., 2021).

Marine carbonates have attracted the study of $\delta^{238}U$ distribution as modern archives have shown a potential to record the primary seawater $\delta^{238}U$ signature (if is not affected by

diagenesis as mentioned below). Over a decade, more than 60 studies have used $\delta^{238}U$ systematics in different types of carbonates (e.g., dolomite, biogenic carbonates, limestone) to constrain oceanic anoxia (e.g., Romaniello et al., 2013; Andersen et al., 2014; Dahl et al., 2014; Noordmann et al., 2015; Tissot and Dauphas, 2015; Hood et al., 2016; Lau et al., 2016; Wang et al., 2016; Elrick et al., 2017; Lau et al., 2017; Bura-Nakić et al., 2018; Chen et al., 2018; Herrmann et al., 2018; Tissot et al., 2018; Zhang et al., 2018a, 2018b, 2018c; Brüske et al., 2020; He et al., 2021; Bruggmann et al., 2022; Chen et al., 2022; Brennecka et al., 2011). Carbonates exhibit a wide range of U concentrations, depending on the mineral composition and mechanism of carbonate precipitation. Aragonitic carbonates, including corals, typically contain high U concentrations due to their ability to directly incorporate $UO_2(CO_3)_3^{4-}$ from seawater in the crystal lattice, while calcitic carbonates generally have lower U concentrations (Reeder et al., 2000). There is a growing body of evidence showing that, under many oceanic conditions, modern marine carbonate sediments may preserve seawater $\delta^{238}U$ signatures without significant U isotope fractionations (Weyer et al., 2008; Romaniello et al., 2013; Andersen et al., 2014; Tissot and Dauphas, 2015; Chen et al., 2018; Kipp et al., 2022). The $\delta^{238}U$ in modern primary carbonates precipitate (e.g., corals, ooids, etc.) appear to faithfully record seawater value within ± 0.09 ‰ (Stirling et al., 2007; Weyer et al., 2008; Tissot and Dauphas, 2015; Chen et al., 2018). These results are supported by laboratory abiotic precipitation experiments, showing limited $\delta^{238}U$ fractionation during incorporation into major marine carbonate minerals under different aqueous media at pH 7.5 and 8.5 (Chen et al., 2016). Also, measurements of $\delta^{238}U$ composition of a variety of primary carbonate precipitates from modern Bahamian shallow-marine carbonates (such as calcareous green and red algae, Scleractinia coral, and ooids) show the $\delta^{238}U$ value of these materials close to seawater $\delta^{238}U$ value (within < 0.1 ‰) (Romaniello et al., 2013). Moreover, $\delta^{238}U$ from studies comparing the trends and absolute values of $\delta^{238}U$ for globally

distributed samples ranging from late Permian to early Triassic carbonate sediments with different diagenetic histories suggest that carbonate sediments can preserve $\delta^{238}U$ primary marine signals in ancient samples, supporting the usage of the carbonate $\delta^{238}U$ proxy for global-ocean redox analysis (Brennecka et al., 2011; Lau et al., 2016; Elrick et al., 2017; Zhang et al., 2018a, 2018b).

1.2.1.3 Uranium Isotopes and Diagenesis

As mentioned above, the $\delta^{238}U$ composition of primary marine carbonates may retain the $\delta^{238}U$ signatures of seawater (Andersen et al., 2017). However, marine carbonates are often influenced by both syn-depositional and post-depositional alterations (e.g. dissolution, recrystallization, and cementation), implying marine carbonates do not always record the $\delta^{238}U$ signature of seawater after diagenesis. The impact of diagenesis on marine carbonate U isotope compositions is a topic of ongoing research and is discussed below.

1.2.1.3.1 Dolomitization

Ancient dolomite [$CaMg(CO_3)_2$] is widespread in the geological record, yet the precise conditions under which it formed remain a subject of ongoing scientific discussion (Warren, 2000). The origin of dolomite in Precambrian marine sedimentary succession is still an ongoing debate, with some suggesting that dolomite formation was synsedimentary or formed during early diagenesis (Nutman et al., 2010; Hood et al., 2011, 2012; Chang et al., 2020). However, most geologists believe that the majority of ancient dolomites formed as a diagenetic transformation of calcium carbonate [$CaCO_3$] into dolomite ([$CaMg(CO_3)_2$], through the introduction of magnesium-rich fluids, a process known as dolomitization (Banerjee, 2016). While these geochemical models continue to provide valuable insights, they do not fully capture the diversity and complexity of dolomite formation mechanisms observed in modern and ancient settings (e.g., low-temperature environment).

Microbial mediation, particularly by sulfate-reducing bacteria and fermentative microbes, has emerged as a critical component of low-temperature dolomite formation (Bontognali et al., 2012; Krause et al., 2012; Zhang et al., 2015). These organisms produce metabolic byproducts and extracellular polymeric substances (EPS) that not only influence local geochemistry but also serve as nucleation sites for dolomite. For instance, anoxygenic photosynthesis, likely pervasive in Precambrian oceans, may have promoted dolomite precipitation by altering redox conditions and increasing alkalinity (Mather et al., 2023; Diloreto et al., 2021). In parallel, mineral surface interactions—particularly involving clay minerals such as illite and montmorillonite—have been shown to play a catalytic role in dolomite formation (Liu et al., 2019). These negatively charged mineral surfaces can adsorb and concentrate Mg^{2+} ions from solution. When combined with the high surface area and slow ion diffusion afforded by EPS, these conditions can help overcome kinetic barriers to dolomite nucleation. Experimental and natural examples suggest that disordered dolomite can initially form on clay or EPS substrates, providing a template that supports further crystallization and eventual ordering (Mather et al., 2023). Thus, clay minerals are not merely passive sedimentary components but may actively participate in dolomitization through both geochemical templating and microbial interactions.

Thus, dolomitization has a potential concern for the alteration of seawater $\delta^{238}U$ signals, depending on the stage of this process (i.e., early versus late dolomitization) (Hood et al., 2016; Herrmann et al., 2018; Zhang et al., 2018a, 2018c). Large variations in $\delta^{238}U$ compositions have been observed in dolomitized sediments. Romaniello et al. (2013), for instance, observed $\delta^{238}U$ changes associated with dolomitization in a modern Bahamian tidal pond that was suggested to have undergone dolomitization. The data demonstrated a shift to $\delta^{238}U$ values much lower than seawater (below −0.6‰) and a strong correlation of $\delta^{238}U$ vs. Mg/Ca. Furthermore, Stirling et al. (2007) reported a $\delta^{238}U$ of −0.83 ‰ for modern dolomite

chimney deposits. However, later studies by Chen et al. (2018) and Tissot et al. (2018), who revisited the dolomitization question with a larger sample set from multiple cores through the Bahamian carbonate platform, show no statistically significant variations between calcite and dolomite. In addition, Herrmann et al. (2018) have interpreted the lack of covariation between $\delta^{238}U$ and $\delta^{18}O_{carbonate}$ or $\delta^{13}C_{carbonate}$ in the Jurassic carbonate platform of the Franconian Alb to indicate that the dolomitization process did not affect the $\delta^{238}U$ signature, despite considerable changes in $\delta^{18}O_{carbonate}$ and $\delta^{13}C_{carbonate}$. Additionally, the congruent $\delta^{238}U$ records of dolomites in relation to non-dolomitized samples as seen in the modern Bahamas (Romaniello et al., 2013) and across the Permian-Triassic and Ediacaran units (Brennecka et al., 2011; Lau et al., 2016; Elrick et al., 2017; Zhang et al., 2018a, 2018b) suggest that early marine dolomitization does not have a strong effect on $\delta^{238}U$ systematics. Furthermore, a simple model of carbonate diagenesis predicts that $\delta^{238}U$ is more robust to diagenetic alteration than oxygen and carbon isotopes (Lau et al., 2017). Dolomitization significantly alters stable isotope compositions ($\delta^{18}O_{carbonate}$ or $\delta^{13}C_{carbonate}$), which are temperature-related fractionation and influenced by meteoric fluids. The $\delta^{18}O_{carbonate}$ is more susceptible to diagenetic alterations than $\delta^{13}C_{carbonate}$, typically resulting in more negative values (Swart, 2015; Swart and Oehlert, 2018). During dolomization, the $\delta^{13}C_{carbonate}$ can shift to a more negative $\delta^{13}C_{carbonate}$ signature particularly if the dolomitizing fluid contains carbon derived from processes like organic matter oxidation as organic matter is enriched in lighter carbon isotopes (^{12}C), resulting in a more negative $\delta^{13}C$ (Wang et al., 2023). In contrast, dolomization does not alter the primary U geochemistry from the original sedimentary components which is supported by the observation that dolomitized rocks did not show significant changes in the concentrations of redox-sensitive trace elements, which are often associated with uranium geochemistry (Swart, 1988; Reinhold, 1998).

1.2.1.3.2 Syndiagenetic Alteration

The $\delta^{238}U$ redox proxy relies on the essential assumption that U in carbonates originates from dissolved seawater U. Nonetheless, diagenetic processes within sedimentary pore-waters may induce the addition of isotopically heavy U(IV) into the carbonates, complicating the application of the U isotope proxy. This syn-depositional diagenesis of carbonates reflects the preferential incorporation of ^{238}U- enriched U(IV) into secondary carbonate phases during carbonate recrystallization and/or precipitation from pore-waters, changing the original isotopic signatures of carbonates toward higher values (Weyer et al., 2008; Romaniello et al., 2013; Andersen et al., 2014; Tissot et al., 2018). This process occurs via advective and diffusive transport of seawater into sediments with reducing pore-waters at depth (Weyer et al., 2008; Romaniello et al., 2013; Andersen et al., 2014; Tissot et al., 2018). The reducing conditions in pore-water are associated with the degradation of organic matter within marine sediments, resulting in the creation of U isotope fractionation during the reduction of U(VI) to U (IV) (Andersen et al., 2017). This semi-open system behaviour allows the change in $\delta^{238}U$ and can result in minor ^{238}U enrichment in bulk carbonates. This process has been shown to be active in shallow sediment depths for Bahamas carbonates due to severe restriction of U mobility in anoxic porewaters (Henderson et al., 1999). The higher U concentration and $\delta^{238}U$ values in these Bahamian sediments compared to seawater are consistent with authigenic U enrichment during pore-water circulation (Romaniello et al., 2013; Andersen et al., 2014). The accumulation of authigenic U enrichment is controlled through oxidization of organic matter by bacterial sulfate reduction in sulfidic porewaters below the sediment-water interface has been proposed as the explanation for the positive offset from ambient seawater as shown in Bahamian carbonate platform with an average value of +0.27 ± 0.14‰ (1 SD) (Romaniello et al., 2013; Chen et al., 2018; Tissot et al.,

2018). In some studies, this offset has been used as a correction factor in reconstructing seawater $\delta^{238}U$ from ancient carbonates (Chen et al., 2018).

1.2.1.3.3 Meteoric Diagenesis

Meteoric diagenesis refers to carbonate sediment alterations when exposed to meteoric waters (freshwater) due to sea-level changes (Swart, 2015; Higgins et al., 2018; Swart and Oehlert, 2018). The meteoric environment is typically divided into the vadose, phreatic, and mix zones depending on interactions with the water table (Swart, 2015; Higgins et al., 2018; Swart and Oehlert, 2018)**.** This interaction promotes the relatively rapid dissolution of carbonate grains and matrix, resulting in the formation of secondary porosity (Chang et al., 2020; Kim et al., 2023). The dissolved carbonate derived from this dissolution can eventually be re-precipitated nearby or elsewhere in the system. These dissolution/recrystallization reactions often led to mineralogy transformations, changes in pore-water chemistry (e.g., Mg^{2+}, Ca^{2+}, and CO_3^{2-} concentrations) and loss/absorption of U into the secondary carbonate precipitates (Swart, 2015). The transformation of aragonite into calcite is one of the most important early diagenetic transitions. Since calcite has significantly lower uranium partition coefficients compared to aragonite, this transformation leads to preferential loss of U from recrystallized sediments (Reeder et al., 2000; Swart, 2015; Chen et al., 2016).

Chen et al. (2018) observed that meteoritic diagenesis of Bahamian carbonates likely led to a ~0.2 ‰ enrichment of $\delta^{238}U$ in altered carbonates compared to samples that only experienced marine phreatic or marine burial diagenesis. The behaviour of U diagenesis in carbonate sediments is unlike the stable isotope proxies (e.g., $\delta^{13}C_{carbonate}$ and $\delta^{18}O_{carbonate}$), where the solubility and mobility of U is strongly controlled by porewater redox chemistry (Chen et al., 2018). The U(VI) is highly soluble and readily mobilized into and out of

sediments, which increases the potential for diagenetic alteration of U in carbonates. Thus, under oxic conditions, meteoritic alteration can potentially change the original $\delta^{238}U$ composition for vadose zone samples (Romaniello et al., 2013; Chen et al., 2018). While in the phreatic zone, under reducing pore-water conditions, authigenic U enrichment (IV), from the reduction of U(VI) diffusing into anoxic and sulfidic sediment porewater can occur, resulting in isotope fractionation (Chen et al., 2018).

Although no specific proxies are developed for determining whether carbonate $\delta^{238}U$ has been influenced by diagenesis, traditional diagenetic proxies (e.g., $\delta^{18}O_{carbonate}$, Mn/Sr, Mg/Ca ratios, Mn content, Sr content, and TOC) are often used to evaluate the post-depositional alteration of carbonates (Dahl et al., 2014; Lau et al., 2017; Zhang et al., 2018a; Chen et al., 2022). While these proxies have their limitations and may not be directly relevant for evaluating diagenetic effects on carbonate $\delta^{238}U$ fractionation, numerical modelling of diagenetic rock-fluid interactions suggests that $\delta^{238}U$ should be more robust against diagenetic fluid exchange than $\delta^{18}O$ (Lau et al., 2017; Chen et al., 2018). So the $\delta^{238}U$ proxy can be used with caution and may sometimes reflect local, not global, signatures. Thus, it is helpful to use other indices to interpret the local redox, such as Fe speciation, as shown in the next section.

1.2.2 Local Ocean Redox Proxy

Iron speciation is a widely utilized proxy for determining palaeo-redox conditions (e.g., Song et al., 2023; Maloney et al., 2024; Meng et al., 2024; Tu et al., 2024). Fe-speciation responds to regional bottom water column conditions, unlike some other redox proxies like U isotopes that provide a globally integrated signal. The distribution and systematics of Fe within ancient sedimentary rocks can provide crucial information about the local bottom water redox conditions of a depositional environment. Redox chemistry is determined using

a highly reactive Fe pool (Fe_{HR}) to total bulk Fe (Fe_T) ratio (Poulton and Canfield, 2005, 2011; Raiswell et al., 2018). Typically, anoxic water column settings promote Fe_{HR} enrichments in the underlying sediment, which according to the procedure described by Poulton and Canfield (2005), include iron phases considered to be highly reactive to biological/abiological reduction under anoxic conditions (Fe_{HR}) relative to total iron (Fe_T) and the proportion of this Fe_{HR} pool which is contributed by pyritic iron (Fe_{py}). This technique subdivides these Fe_{HR} minerals into operationally defined phases, including Fe(III) oxyhydroxides (e.g., hematite, goethite, lepidocrocite, and ferrihydrite), iron carbonates (e.g., siderite and ankerite), mixed-valence iron (magnetite), and sulfide-associated iron phases (e.g., mackinawite and pyrite).

Iron speciation is commonly used to distinguish three major redox conditions in ancient oceans, namely oxygenated, ferruginous (anoxic, iron-containing) and euxinic (anoxic, sulfidic). Samples deposited under anoxic water column conditions commonly have Fe_{HR}/Fe_T ratios > 0.38), with Fe_{HR}/Fe_T < 0.22 values generally considered to indicate oxic water column conditions due to the lack of highly reactive iron accumulation in the water column and Fe_{HR}/Fe_T ratios between 0.22-0.38 to be equivocal (Poulton and Canfield, 2005, 2011; Raiswell et al., 2018). In addition, the Fe speciation proxy can distinguish between euxinic sulfide-rich and ferruginous iron-rich conditions, where pyrite iron (Fe_{py})/Fe_{HR} < 0.6 ratios are considered indicative of ferruginous water column (Poulton and Canfield, 2005, 2011, 2018). On the other hand, under euxinic conditions the build-up of water column hydrogen sulfide (H_2S_{aq}) results in the sulfidation of iron oxides and enrichment of Fe_{py}, leading to elevated Fe_{py}/Fe_{HR} > 0.8 (Poulton et al., 2005). Fe_{py}/Fe_{HR} ratios <0.6 are associated with ferruginous conditions while those lying between 0.6 and 0.8 are considered equivocal (Poulton and Canfield, 2011; Poulton, 2021). The Fe speciation proxy has been used for organic-rich shales to constrain the ocean floor redox condition across most of Earth's

history. Later studies have focused on applying the proxy to carbonate-rich sediment, where Clarkson et al. (2014) showed that Fe speciation can provide reliable results when applied to carbonate-rich sediments when bulk Fe_T is >0.5 wt%. Recent research has argued that some Fe speciation data could be impacted or altered due to diagenetic processes (Pasquier et al., 2022). However, Fe speciation has been widely calibrated using ancient rocks, which have experienced the diagenetic changes which Pasquier et al. (2022) claimed compromised the use of the proxy as a paleo-redox proxy (Raiswell et al., 2001). These considerations are taken into account in the application of this proxy in this study, with a key goal to highlight the redox changes that accompanied greenhouse-icehouse transitions in a shallow Cryogenian-Sturtian seawater margin.

1.3 Climatic Shifts During the Precambrian Era

Earth's climate has alternated between warmer "Greenhouse" and cooler "Icehouse", periods primarily driven by orbital forcing, albedo (a measure of how much solar radiation is reflected back to space from the Earth's surface) and atmospheric greenhouse gas concentrations (Budyko, 1969). The term Snowball Earth, which referred to the glaciations that covered the Earth with ice from pole-to-pole, was coined by Kirschvink (1992), who first proposed a global glaciation model called the Global Snowball Model which was afterwards renamed as the 'Snowball Earth hypothesis, SEH' by (Hoffman et al., 1998; Hoffman and Schrag, 2002).

During the Precambrian time, geological evidence points to one major Snowball Earth episode in the early Paleoproterozoic era believed to have been coeval with the GOE (Kirschvink et al., 1999; Bindeman et al., 2010; Hoffman, 2013), succeeded by two consecutive events during the Neoproterozoic era, namely the Sturtian (717-659 Ma) and the Marinoan (~645-635 Ma) Snowball Earth glaciations (Hoffman and Li, 2009;

Macdonald et al., 2010; Evans and Raub, 2011; Hoffman et al., 2017). The 1000 - 541 Ma Neoproterozoic Era, the youngest and terminal Precambrian timeline, is one of the most significant intervals in Earth's geological history as it is marked by major transformations in the Earth system, including tectonics, climate and evolution of complex marine life (discussed in the next section). The Neoproterozoic was characterized by the formation and breakup of the supercontinent of Rodinia from about 1,000 to 800 Ma. The later breakup probably contributed to the onset of the Sturtian Snowball Earth glaciation (Hoffman et al., 2017), which primed the stage for the NOE and the eventual appearance of metazoans in the nutrient-rich Ediacaran Ocean.

The basic mechanism to initiate a Snowball Earth is thought to rely on positive ice-albedo feedback first theorized by Budyko (1969). This positive feedback is facilitated by accumulation of the continental landmasses within the middle to low palaeolatitudes, significantly increasing both the albedo and silicate weathering rates in the tropics (Kirschvink, 1992; Schrag et al., 2002). As a result, more reflected solar energy and greater drawdown of CO_2 is enhanced, initiating ice accumulation at high latitudes that promotes a runaway ice–albedo feedback and resultant ice build-up towards lower latitudes (Budyko, 1969; Hoffman and Schrag, 2002; Hoffman et al., 2017). It is widely believed that deglaciation was triggered by extremely high volcanic atmospheric CO_2 concentration (pCO_2) of ~350× PAL when ice cover prevented silicate weathering and photosynthetic CO_2 drawdown (Kirschvink, 1992; Hoffman and Schrag, 2002; Huang et al., 2016; Hoffman et al., 2017).

It however remains a matter of debate whether these would have featured a complete ice cover, the so-called hard snowball (HSB), or whether parts of the oceans remained ice-free to form a liquid water belt along the equator or refugia as indicated by the presence of eukaryotic life indicators in this period, discussed in the next section (Runnegar, 2000; Allen

and Etienne, 2008). Conversely, energy balance models, as well as simple and complex climate models, agree with HSB as it is one of the steady states of Earth's climate (Marotzke and Botzet, 2007; Voigt and Abbot, 2012; Walsh et al., 2019), whereas it is vastly more difficult to maintain an extreme icehouse state that retains open ocean surfaces (Lewis et al., 2007; Rose, 2015). However, in both scenarios, large parts of the continental surface and oceans would have been covered in ice (Warren et al., 2002; Lewis et al., 2003; Abbot et al., 2013).

The Snowball Earth hypothesis, supported by numerous biological, geological, and climate modelling studies (Hoffman et al., 2017), first arose when glacial deposits (sometimes referred to as tillites or diamictites) and sediments from that period that appeared to be glacial in origin, were found at low-latitude sites. These deposits were first discovered in South Australia and later in Africa (Hoffman, 1998). Glacial deposits are poorly sorted conglomerates and breccias that contain a wide range of clast sizes and shapes carved and carried by ice from the continents and deposited on the ocean seafloor. Similarly, cap carbonates, thin layers (~ 3-20 m) of limestone and/or dolostone carbonate that directly overlie some marine glacial deposits, show unusual texture, chemical, and isotopic patterns (Stern and Miller, 2021). These carbonates may have been a result of extreme chemical weathering triggered by the greenhouse condition that followed Snowball Earth glaciations (Kasemann et al., 2005; Bao et al., 2008; Abbot et al., 2012; Huang et al., 2016; Hoffman et al., 2017). Besides the glacial deposits and cap carbonates, isotopic analysis became more widely used as a potential chronostratigraphic tool. Several studies show a distinct positive carbon isotope, $\delta^{13}C_{carbonate}$ excursions prior to the onset of glaciations, followed by negative $\delta^{13}C$ signatures (Hoffman and Schrag, 2002; Halverson et al., 2005; Johnston et al., 2012). The positive $\delta^{13}C_{carbonate}$ has been interpreted to reflect the high fractionation of light ^{12}C isotopes by intense photosynthesis, leading to the enrichment of the remaining dissolved

carbon pool with heavy ^{13}C that was subsequently precipitated as ^{13}C-enriched carbonate minerals (Schrag et al., 2002). In response to the termination of the Neoproterozoic Snowball Earth glaciations, multiple lines of geochemical and geological evidence point to enhanced nutrient flux, from land to the oceans, with an increase in seawater phosphorous (P) supply suggested to have accelerated primary productivity and ocean oxygenation (Planavsky et al., 2010; Lyons et al., 2014; Reinhard et al., 2017; Chi Fru et al., 2023). However, the mechanisms by which these nutrients were delivered to seawater remain unclear and constitute the main aim of this thesis.

1.4 Biological Innovations During Precambrian Times

Information on biological and ecosystem evolution through Earth's history comes from available fossil, biomarker, geochemical, and genetic evidence (Simoneit, 2004; Newman et al., 2016; Betts et al., 2018; Javaux and Lepot, 2018; Walters et al., 2020; Cohen and Kodner, 2022; Summons et al., 2022), all thought to be intimately linked to the magnitude and expansion of Earth's surface oxygenation history (Lyons et al., 2014, 2024), which is in turned tied to the emergence of the continents, continental weathering rates and supply of nutrient to seawater (Cárdenas and Harries, 2010; Lenton et al., 2014; Shields, 2017; Zhang et al., 2021). Although the data do not definitively establish an exact oxygen threshold necessary for the emergence of animals on Earth, the existing data do suggest that the availability of oxygen was at least a significant factor that modulated biological diversification (Danovaro et al., 2010; Mills et al., 2014, 2018; Sperling et al., 2015). Importantly, this absolute oxygen requirement does not prevent certain animals from living anaerobically under anoxic conditions for extended periods of their life cycle (Müller et al., 2012).

All life forms on Earth are believed to have evolved from a single ancestral population of cells, referred to as LUCA—the Last Universal Common Ancestor (Kyrpides et al., 1999). These LUCAs eventually evolved into three different cell types, each representing a distinct phylogenetic domain: Eucarya (eucaryotes), Archaea and Bacteria (prokaryotes) (Pace, 2009). Recent progress in geological research has provided significant constraints on the origin of life which is believed to have originated around 3.7 to 3.5 billion years ago (Nutman et al., 2016; Betts et al., 2018). For billions of years, fossil evidence shows life was primarily composed of simple bacterial slime that lived in anoxic oceans (Knoll et al., 2006; Schopf, 2006; Sugitani et al., 2013). The tempo of the first appearance of oxygen-producing Cyanobacteria ranges over a billion years, from 2.3 Ga (Kopp et al., 2005), to 3.7 Ga (Rosing and Frei, 2004), but more recent estimates suggest an origin closer to 3 Ga (Planavsky et al., 2014a).

The Proterozoic Eon hosted the most important stages for the evolution of life: the transition from single-celled organisms to macroscopic multicellular in the Mesoproterozoic, to the global appearance of soft-bodied animals (metazoans) in the Ediacaran Period. At around ~1.9 Ga, the first organisms with complex, nucleated cells appear (Knoll et al., 2006; Parfrey et al., 2011). The literature consistently agrees on a notable surge in eukaryote diversification during the period 1.700 – 0.8 Ga (Beghin et al., 2017; Loron et al., 2019). Zhu et al. (2016), provided strong evidence for multicellular life by decimetre-scale macrofossils in the Gaoyuzhuang Formation in North China in the Mesoproterozoic Era at 1.56 Ga. This diversification contradicts previous beliefs that the Mesoproterozoic was an interval of biological stasis (Holland, 2006), requiring that the ‘Balance Billion’ Mesoproterozoic hypothesis may deserve a re-evaluation.

The interval that extends from the late Neoproterozoic through to the mid-Cambrian (~ 0.8 Ga - 0.501 Ga) observed the evolution of complex body plans, accompanied by an

increase in the diversity of acritarchs and protistan morphotypes in fossil assemblages (Knoll et al., 2006; Parfrey et al., 2011). Crown-group members of some algae (green, yellow-brown and red algae), heterokonts (today mostly consisting of diatom eukaryotes) and testate amoebae had all appeared by 750 Ma (Knoll et al., 2006). The most important revolution was seen in the Ediacaran–Cambrian period with the first global-scale appearance of definitive complex macroscopic life dated at ~575 Ma (Darroch et al., 2018; Wood et al., 2019; Bowyer et al., 2022). It was also marked by the widespread development of mineralized skeletons at ~550 Ma and the appearance of large, mobile animals that started to burrow into the sediment surface at around 560 Ma (Marshall, 2006; Buatois et al., 2014).

To what extent the Neoproterozoic 717-660 Ma Sturtian and 655-632 Ma Marinoan glaciations that preceded the global emergence of animals influenced biospheric evolution is an ongoing debate. It is however believed that the shutdown of the active hydrological cycle by Neoproterozoic icehouse conditions, acted as an evolutionary bottleneck (Hoffman, 1998) but that bacterial and eukaryotic life persisted throughout the glaciation period (Love et al., 2009; Erwin, 2015; Turner, 2021). Moreover, evidence shows undisturbed diverse eukaryotic life thriving during the glaciations (Corsetti et al., 2006; Parfrey et al., 2011). This is supported by geochemical data which show active marine biogeochemical cycling during the glaciation periods (Johnson et al., 2017; Ma et al., 2022; Shen et al., 2022). In addition, molecular clock, biomarker evidence, and fossil records, although sparse, have also verified that some extant eukaryotes, such as macroalgae and probable sponges survived the icehouse conditions (Erwin, 2015; Turner, 2021). For example, Love et al. (2009) propose the oldest indication for animals in the fossil record from the Huqf Group, Oman thought to be related to Demospongiae prior to the end of the Cryogenian glaciations (ca. 635 Ma). Some have suggested the presence of an open water belt in low-latitude regions during the

Snowball glaciations (Abbot et al., 2011; Rose, 2015; Johnson et al., 2017), thus providing refugia for aerobic eukaryotes in small meltwater ponds within glaciers (Song et al., 2023).

The evolution of oxygenic photosynthesis marked as a mile- stone in the history of life because it resulted in a significant increase of oxygen in the atmosphere, consequently, increase the diversity and complexity of living organisms (Bozdag et al., 2024). Importantly, these stepwise evolution from simple life to more complex life forms, as mentioned above, is linked to the changing nutrient budget of the oceans, required to support the high energy resource-rich ecosystems that enabled evolutionary gigantism and complexity (Ward et al., 2012; Brocks et al., 2017; Chi Fru et al., 2024).

1.5 Nutrient Cycling Precambrian Seawater

1.5.1 The Phosphorus Cycle

Phosphorus (P) is a bioessential macronutrient to all life. Being a structural and functional component of all organisms (Tyrrell, 1999), P forms the backbone of nucleic acids (DNA and RNA), is crucial in energy transfer systems through ATP molecules, and as (phospholipids), it is a key component of cell membranes (Kolodiazhnyi, 2021). Consequently, P availability plays a key role in controlling photosynthesis, where dissolved P is assimilated together with carbon (C) and nitrogen (N) by phytoplankton to form organic matter ($C_{106}H_{263}O_{110}N_{16}P$). Thus, P availability contributes to the regulation of the atmospheric composition of the greenhouse gas CO_2 and climate, where the photosynthetic link between P, C, and O_2 biogeochemical cycling can be summarised by Eq. 1 (Paytan and McLaughlin, 2007).

$$106CO_2 + 122H_2O + 16NHO_3 + H_3PO_4 \rightarrow C_{106}H_{263}O_{110}N_{16}P + 138O_2 \qquad \text{Eq. 1}$$

Phosphate is also considered the ultimate limiting nutrient for marine primary productivity over geological time scales (Tyrrell, 1999), and thus, P bioavailability exerts a fundamental control on the long-term rate of O_2 production through oxygenic photosynthesis and organic carbon (C_{org}) burial (Papineau et al., 2013; Reinhard et al., 2017; Guilbaud et al., 2020; Alcott et al., 2022; Dodd et al., 2023; Rasmussen et al., 2023).

P availability in the water column is dominantly controlled by a balance between continental weathering inputs and outputs to sediments (ultimately through sedimentary burial) (Ruttenberg and Berner, 1993; Benitez-Nelson, 2000), and recycling (Kipp and Stüeken, 2017). The main source of P to the ocean is generally considered limited compared to that of nitrogen (N), as it is mainly supplied by riverine input derived from continental weathering, whereas N is abundant in the atmosphere where it is transformed into biologically available forms through a process known as N_2 fixation (Benitez-Nelson, 2000). N-fixing microorganisms capture atmospheric N and convert it to ammonia (NH_3), which is subsequently transformed into nitrite and then to nitrate - an essential process in the global N cycle (Benitez-Nelson, 2000). Following the weathering of continental rocks, P is transported to the ocean primarily in the dissolved and particulate forms and enters estuarine or marine sediments without participating in biological reactions (Ruttenberg, 2003). When delivered to seawater, P is incorporated into biological molecules like DNA, RNA, cell membranes and some bound to organic matter (Paytan and McLaughlin, 2007).

The modern riverine flux of bioavailable P is very small (~2 Tg/yr) compared to the ~1200 Tg/yr utilized by the marine biosphere (Schlesinger, 1997). This large discrepancy between supply and demand is sustained by efficient recycling of P within the ocean (Kipp and Stüeken, 2017). In the marine system, there are four particularly important forms of P. These include authigenic Ca-P (P_{auth}), organic P (P_{org}), ferric iron bound P (P_{Fe}) and detrital apatite which does not participate in biological cycling (Ruttenberg and Berner, 1993; Wheat

et al., 1996; Ruttenberg, 2003). The first three phases are reactively recycled during early diagenesis in seafloor sediments by biogeochemical processes leading to what is commonly termed “sink switching”. Of initial importance are reactions that liberate P from the phases brought to sediments. The primary P removal mechanisms have been reviewed by Follmi (1996) and Delaney (1998). The most prevalent mechanism of P from the water column is organic matter remineralization, coupled mainly to microbial reduction of Fe-(oxyhydr)oxide, sulfate and nitrate in anoxic conditions using electrons from organic matter, resulting in the release of P into porewaters and into the overlying water column (Froelich et al., 1988; Van Cappellen and Ingall, 1994; Ingall and Jahnke, 1997; Slomp et al., 2004; Xiong et al., 2019). Conversely, P released to porewater can be sequestered by authigenic minerals such as apatite following porewater P saturation (Ruttenberg, 2003; Algeo and Ingall, 2007). Thus, because these processes are redox-sensitive, P cycling in the water column and sediments is strongly controlled by changing seawater and sediment porewater oxygen dynamics (Kipp and Stüeken, 2017; Reinhard et al., 2017; Guilbaud et al., 2020; Laakso et al., 2020; Alcott et al., 2022).

Because the Precambrian experienced major changes in oceanic oxygen concentrations as discussed in section 1.1.1, it is crucial to decipher how the P cycle functioned as a response to these redox changes in an ocean that was dominated by iron compared to the modern (Van Cappellen and Ingall, 1994; Ingall and Jahnke, 1994). The redox evolution of the water column through Earth’s history varied temporally and spatially which tended to be oxic, anoxic but euxinic (sulfidic) or anoxic but ferruginous (iron-rich) throughout Earth’s history (Poulton and Canfield, 2011) and thus, these will be the dominant redox states considered here.

Generally, under a well-oxygenated water column, P adsorbed to iron (oxyhydr)oxides, especially in the iron-rich Oceans (Bjerrum and Canfield, 2002; Planavsky et al., 2010;

Poulton and Canfield, 2011; Jones et al., 2015; Chi Fru et al., 2016b; Reinhard et al., 2017; Hemmingsson et al., 2018) and organic matter (Van Cappellen and Ingall, 1994; Ingall and Jahnke, 1994), were the dominant mechanisms by which P was enriched in seafloor sediments. The oxidation of organic matter during microbial respiration, and when coupled to the reduction of Fe (oxyhydr)oxides as mentioned earlier, releases dissolved P from organic matter and Fe (oxyhydr)oxides back into sea/porewaters. This released P is generally re-trap by Fe (oxyhydr)oxides phases and biological sequestration of polyphosphates or form new authigenic phases as carbonate fluorapatite (CFA) (Algeo and Ingall, 2007; Slomp and Van Cappellen, 2007; Schulz and Schulz, 2005; Hupfer et al., 2008; Brock and Schulz-Vogt, 2011). In anoxic bottom waters, the released P can be captured, as in sediment porewaters, to form Fe(II)-phosphate vivianite or CFA minerals (Ruttenberg et al., 1993; Egger et al., 2015). Brady et al. (2022) show phosphate-rich oceans may have persisted under ferruginous conditions as Fe^{2+} can significantly increase the solubility of all phosphate minerals (Reinhard et al., 2017; Bowyer et al., 2020; Guilbaud et al., 2020). However, sulfidic environments would have strongly limited drawdown and fixation of P in association with reactive Fe minerals, because reduced Fe(II) forms iron sulphide minerals such as pyrite which do not significantly sequester P from seawater (e.g., Guilbaud et al., 2020; Alcott et al., 2022).

In sum, an understanding of P recycling thus requires a detailed analysis of both the phase partitioning of P and the redox context in which P was transported to, and preserved in ancient sediments. These processes are particularly important in evaluating the processes that enriched P in post-Cryogenian seawater (Bjerrum and Canfield, 2002; Planavsky et al., 2010; Poulton and Canfield, 2011; Jones et al., 2015; Chi Fru et al., 2016b; Reinhard et al., 2017; Hemmingsson et al., 2018; Chi Fru et al., 2023), which constitute an integral part of this study. For example, it is considered that the melting of ice sheets during the terminal

phase of the Neoproterozoic Snowball Earth glaciations supplied mechanically eroded P from land to seawater, but it is not known how this P became bioavailable to life to trigger photosynthetic activity and ocean-atmosphere oxygenation. This link is also examined in this study, with a particular focus on the role of clay minerals as P vectors to seawater.

1.5.2 Phosphorus Cycling and Marine Primary Production in the Precambrian

As mentioned in the previous section, understanding the oceanic phosphate concentration is critical for reconstructing marine primary productivity and oxygen evolution throughout Earth's history. A critical constraint in quantifying the ancient marine P budget is a lack of inherent isotopic tracers, since P has only one stable isotope (^{31}P), it cannot be used to monitor P systematics in a similar manner to other essential elements. Therefore, reconstructions of dissolved P concentrations in Precambrian oceans are highly debated and rely on geological records, including banded iron formation (BIFs), shales and phosphorites, which are interpreted to reflect seawater conditions at their time of formation (Bjerrum and Canfield, 2002; Planavsky et al., 2010; Jones et al., 2015; Chi Fru et al., 2016a; Hemmingson et al., 2018; Reinhard et al., 2017).

Banded iron formations, marine chemical sediments deposited extensively during the Precambrian, provide a temporally well-resolved archive of seawater phosphorus between 3.5 Ga and 1.5 Ga because of the strong positive correlation between dissolved P and incorporation into solid phase Fe (oxyhydr)oxides abundant in BIFs (Bjerrum and Canfield, 2002; Jones et al., 2015). Thus, dissolved seawater phosphorus concentrations in ancient marine waters can be estimated using the phosphorus-to-iron ratio (P/Fe), expressed as $(P/Fe)_{100}$, in well-preserved Fe-rich chemical sedimentary rocks (Bjerrum and Canfield, 2002; Planavsky et al., 2010). Based on what is known about the adsorption of P on the Fe

(oxyhydr)oxides in the modern ocean, the overall positive charge acquired by iron (oxyhydr)oxides following the oxidation of ferrous Fe (Fe^{2+}), induces a stronger affinity for negatively charged anions such as phosphate (PO_4^{3-}). Using P/Fe ratios in the modern ocean (Feely et al., 1998), Bjerrum and Canfield (2002) suggested phosphorus (in the form of orthophosphate) would have been around 10-25% of present-day levels in the Proterozoic ocean, with Konhauser et al. (2007) and Jones et al. (2015) further indicating that it is important to take into account the role of Si^{2+} that was abundant in Precambrian seawater in the absence of biological Si precipitation, together with Mg^{2+}, and Ca^{2+} in the sorption of phosphorus on Fe (oxyhydr)oxides. Moreover, the rise of arsenate enrichment, a strong phosphate analogue, in seawater after the GOE, may also have competitively constrained the incorporation of phosphate into Fe (oxyhydr)oxides (Chi Fru et al., 2019) and biological availability (Planas et al., 1978; Takashi et al., 1980; Thiel 1988; Elias et al.,2012; Wang et al., 2015).

In contrast to BIFs, which are discontinuous temporal records, shales offer a significant advantage of a continuous ubiquitous record through the entire geologic timescale. Using this advantage, Reinhard et al. (2017) investigated 7,970 shale samples from marginal marine environments as archives of seawater P history throughout Earth's history. Their approach was to use bulk P content to track broad changes in authigenic P burial and identified consistent lower [P] throughout the Precambrian time with a significant increase, approximately fourfold on average, in the P content in shales deposited about 800 million years ago, which might support inferences of extremely low atmospheric pO_2 (<0.001 PAL) until the Neoproterozoic rise in atmospheric oxygen (Planavsky et al., 2014b). A recent examination of P concentrations in similar marine sedimentary shales in the 2.1 Ga Francevillian sub-basin in Gabon, however, shows a localised rise in seawater P levels similar to those recorded around 800 Ma (Chi Fru et al., 2024). Intriguingly, this event is

linked to seawater oxygenation and the emergence of debated large body-size fossils in the Francevillian basin similar to observations made in the Neoproterozoic (El Albani et al., 2010, 2014, 2023; Ossa Ossa et al., 2023; Chi Fru et al., 2024). However, bulk shale P contents are limited in that they do not specifically track bioavailable P. Furthermore, bulk shale P contents cannot provide a detailed understanding of the extent of P recycling from the sediment back to the water column, which is highly dependent on the redox state of both the water column and sediment pore waters, as mentioned in the previous section (Poulton, 2017).

The third P record is phosphorite which are phosphate-rich sedimentary rocks that contain more than 15% P_2O_5 (Papineau, 2010). Sedimentary records show the dearth of phosphorites in the Precambrian (Holland, 2006) and begin to sporadically occur after the GOE at ~2.3 Ga (Lyons et al., 2014). In addition, Reinhard et al. (2017) showed a large P enrichment which is consistent with observations from the phosphorite record during the Ediacaran Period (635–541 Ma). It is suggested that the low P concentration in Precambrian seawater was due to low continental weathering input (Laakso and Schrag, 2014) with an exception being the 2.1 Ga basin where elevated shale P content is linked to an increase in intense weathering (Chi Fru et al., 2024). A peak in phosphate levels uncovered after the Cryogenian Snowball Earth glaciations has been explained as a high weathering influx produced by melting ice sheets, which enriched the ocean with nutrients (Planavsky et al., 2010; Reinhard et al., 2017). Some contend that the low P concentrations in Precambrian marine waters were due to strong scavenging of P from the water column by Fe minerals in a Fe-rich Ocean as discussed in the previous section (Bjerrum and Canfield, 2002; Jones et al., 2015; Reinhard et al., 2017). Kipp and Stüeken (2017) further suggested that P scarcity limited biomass cycling in the oxidant-poor Precambrian oceans, thus proposing that recycling of biomass P is critical for maintaining a high seawater P content for primary production. Furthermore,

the rise of sulfate in the GOE ocean, linked to increasing continental weathering is thought to have facilitated the recycling of P in the deep anoxic ocean (Alcott et al., 2022), while low primary productivity at the start of the Neoproterozoic was coupled to low marine P content forced by iron oxyhydr (oxide) sequestration (Guilbaud et al., 2020).

In sum, marine geological records and biogeochemical models suggest that phosphate was scarce during Precambrian times compared to the modern (Kipp and Stüeken, 2017; Reinhard et al., 2017; Guilbaud et al., 2020; Alcott et al., 2021, 2022; Walton et al., 2023). This work further interrogates how the Cryogenian phosphorus cycle operated, considering the role of clay mineral composition in sediments deposited before, during and after the Sturtian Snowball glaciations and correlations to iron cycling and formation of authigenic P phases, particularly apatite.

1.6 Clay Minerals, Nutrients, and Oxygenation

Generally, rock minerals represent a vast reservoir of nutrients and elements to the oceans; many (e.g., Mn, Mo, Fe, Co, Ni, Cu, Zn) are essential to all life, including the macronutrient P considered to control primary productivity in the oceans through Earth's history (Tyrell, 1999; Planavsky et al., 2010; Reinhard et al., 2017; Guilbaud et al., 2020; Alcott et al., 2022). The availability of these nutrients in the ocean exerts a significant impact on bio-productivity and thereby photosynthetic activity and the release and concentration of oxygen in the ocean-atmosphere system over geological timescales (Kennedy et al., 2006; Tosca et al., 2010; Large et al., 2015).

Clay minerals, which are highly enriched in sedimentary environments (Chamley, 1989), due to their large surface area and charge, have been historically considered native sorbents of bioessential trace elements, including P (Zhao et al., 2018; Hao et al., 2021a, 2021b). The production, transportation and supply of nutrients like P and various micronutrients to the

ocean derive mostly from chemical and physical weathering of the continents (Paytan and McLaughlin, 2007; Jaisi and Blake, 2010). Most of these nutrients are transported in the particulate phase, including P adsorbed onto Fe(III)-Al(III) oxyhydroxides, including clay minerals and as organic complexes (Gérard, 2016). Consequently, detrital clay minerals play a key in the supply of nutrients to seawater, while diagenetic clays serve as archives of post-depositional sedimentary processes. In addition to the fact the non-uniform adsorption behaviour of individual clay minerals towards trace elements, <2-micron clay particles, provide a buoyant freeboard for long-distance riverine transportation of nutrients. Moreover, their high surface sorption capacity and area contribute to suspended sediments possessing high concentrations of cations, including transition metal ions such as Cu, V and Cd (Manning and Goldberg, 1997; Bhattacharyya and Sen Gupta, 2006; Ozdes et al., 2011). For instance, Hao, et al. (2021a) suggest that kaolinite readily adsorbs P under more acidic freshwater conditions, but quantitatively releases P under seawater conditions, where it becomes bioavailable to phytoplankton. In addition, Hao et al. (2020) show that clay minerals play a crucial role in the transportation and supply of a considerable fraction of trace elements, including Cd, to the oceans. However, not much is known about the connection between clays and nutrient cycling, transportation and liberation from land to the oceans, seawater and marine sediments throughout the Precambrian. This is made particularly difficult because studies on clay minerals in the Precambrian are rare. Especially, the link between primary productivity, ocean-atmosphere oxygenation and nutrient cycling connected to clay formation at this time and their association with the extreme climate events such as the Snowball Earth glaciations that characterised this time, remain elusive. An understanding of the link between clay mineral formation, Snowball climates and post-depositional enrichment of P in seawater, resulting in ocean-atmosphere may help improve our understanding of how these dramatic climate events shaped the

marine P reservoir. It is even more crucial as continental weathering patterns and clay formation would be expected to respond to these dramatic climate fluctuations, as a function of the rate and type of dominant weathering processes in action.

Here, 'clay minerals' are defined as hydrated phyllosilicates of any size often formed by silicate mineral weathering (Berner and Berner, 2004; Warr, 2022). Once formed, clay minerals modulate aqueous bioessential ion concentrations due to their varying cation exchange capacity and pH-dependent surface charge area affinity for trace elements (Garrels and Mackenzie, 1971; Froelich, 1988; Berner and Berner, 2004; Gerard, 2016; Hao et al., 2019, 2021a; Baldermann et al., 2022; Warr, 2022). For example, clay minerals have been shown to regulate the seawater content of bioessential phosphorus (P) and the concentration of various redox-sensitive trace metals and metalloids (e.g., Violante and Pigna, 2002; Hao et al., 2020; Hao et al., 2021a, 2021b; Chi Fru et al., 2023). In addition, clay composition and abundance influence the burial efficiency of organic carbon in continental margin platforms (Tosca et al., 2010; Kennedy and Wagner, 2011; Keil and Mayer, 2014), again pointing to their importance as archives of past seawater biogeochemical elemental cycles and ocean-atmosphere redox history (e.g., Frei et al., 2009; Jeandel and Oelkers, 2015; Chi Fru et al., 2016a, 2019; Ramos et al., 2018; Abbott et al., 2019; Hao et al., 2021a; Baldermann et al., 2022; Wei et al., 2024) and climate (Warr, 2022; Krause et al., 2023). This thesis hypothesizes that detrital clay mineral formation, composition, transport and deposition, modulated seawater nutrient concentrations, with particular focus on marine P supply, across the Cryogenian Snowball climatic interval.

1.6.1 Origin of Clay Minerals, Climate, and Weathering

Clay minerals are an abundant component of fine-grained sediments and rock material present in various geological environments (e.g., mudrocks, shales and siltstone) (Chamley,

1989), making up about one-third of sedimentary rocks (Moore and Reynolds, 1989) and constituting the most abundant minerals in marine sediments. Moreover, clay formation archives distinctive events associated with the geological and historical evolution of various sedimentary basins. The genesis of such clay minerals can be attributed to three distinct mechanisms: (1) inheritance, where clay derived from pre-existing parent rock or weathered rocks, is transported and accumulated in marine sedimentary environments that are stable enough to maintain its composition; (2) solid-state transformation, where the clay undergoes chemical reaction but keeps some of its inherited structure (Wilson, 1999; Dias et al., 2020); and (3) neoformation where the clay precipitates directly from solution onto the sediment pile. The second and third types are called authigenic clay minerals. Authigenic clays can be formed *in situ* by 'reverse silicate weathering'' within the sedimentary basin, often present as sediment pore-lining filling material (Isson and Planavsky, 2018) or through mineral transformation during and after burial diagenesis in sediments, for example the authigenic formation and/or transformation of clay minerals in alkaline-saline environments (diagenetic clay minerals) (Furquim et al., 2008). In contrast, detrital clay minerals are derived from erosion and mechanical weathering of parent rock which are then transported by river and other media, and subsequently deposited in another place. From modern evidence, sedimentary clay minerals inherited from weathered parent rocks and soils constitute up to 8.6% of the total clay mineral inventory on modern Earth, where they are deposited primarily through detrital inheritance (Warr, 2022). Nonetheless, the large reservoir of clay minerals, making up to 12.9 wt.% of the upper continental crust, UCC (Warr, 2022), suggests that marine sediments represent a significant sink when this material is eroded on land and delivered by riverine detritus to continental margin seawater.

Generally, clay minerals occur in different geological environments under varying climates, geological and chemical conditions. Clay minerals formed during weathering are generally

the most stable phases under ambient conditions. They can however be broken down, dissolved or converted to new minerals by a range of processes which are defined as physical, chemical (Velde and Meunier, 2008) and biological (microbial) weathering processes (Konhauser et al., 2007). Clay diagenesis (also known as post-depositional alteration) is a fundamental process in the geological cycle of clay formation, which encompasses the sum of the physical, chemical, and biological (microbial) processes and changes those sediments undergo to attain equilibrium with the surrounding environment after deposition. Changes in clay mineralogy during diagenesis are principally correlated with rising temperatures associated with burial depth (Weaver, 1989).

1.6.1.1 Mechanical or Physical Weathering and Clay Formation

Mechanical weathering of rocks results in the disintegration of rock minerals, producing smaller particles without a resultant geochemical and mineralogical change in the bulk rock composition of the particles relative to the parent rock (Bahlburg and Dobrzinski, 2011). For example, as a glacier advances across an area, it mechanically pulls rock material off the rock surface, mixes it with the ice and then transports and deposits the material essentially undamaged in a sedimentary basin, unless it undergoes chemical weathering, as shown below.

1.6.1.2 Chemical Weathering and Clay Formation

The processes involved in chemical weathering include dissolution, oxidation, hydration, carbonation and hydrolysis, which change the rock's mineral composition following instability when exposed to for example oxygen-rich surface conditions and acidic solutions (White and Brantley, 1995; Bahlburg and Dobrzinski, 2011). During chemical weathering, the minerals in rocks react with their new environment to produce new minerals that are

stable under conditions near the surface and the addition of ions released from the rocks to the weathering solution (Burley and Worden, 2009).

1.6.1.2.1 Oxidation (Redox Reactions) or Oxidative Weathering and Clay Formation

The formation of clays through oxidative weathering occurs when free oxygen reacts with minerals on the exposed rock surface due to an exchange of electrons from the mineral or element to the oxygen atom which acts as an electron acceptor (Burley and Worden, 2009). For example, the oxidation of ferrous iron (Fe^{2+}) by oxygen dissolves and converts Fe^{2+} rock content to highly insoluble Fe^{3+} minerals or iron oxyhydr(oxides), typically enriching the weathering solution with dissolved silica in the process (Krauskopf and Bird, 1995).

1.6.1.2.2 Hydrolysis and Clay Formation

This is a primary silicate weathering process that involves a water–mineral interaction during which water dissolves and leach ions from rock minerals and carries them away. Through hydrolysis, a mineral such as k-feldspar is leached and changed into the important clay mineral kaolinite according to Eq. 2 (White and Brantley, 1995; Essington, 2015).

$$2KAlSi_3O_8 + 2H+ + 9H_2O \rightarrow H_4Al_2Si_2O_9 + 4H_4SiO^4 + 2K^+ \quad \text{Eq. 2}$$

k-feldspar kaolinite

$$CO_2 + H_2O \rightarrow H_2CO_3 \quad \text{Eq. 3}$$

1.6.1.2.3 Carbonation and Clay Mineral Formation

During carbonation, water reacts with CO_2 to produce carbonic acid according to Eq. 3. This reaction promotes the release of rock-forming elements like Na, Ca and Mg and the

formation of carbonate and clay minerals (Liu et al., 2011; Renforth et al., 2011; Saldi et al., 2015).

The Chemical Index of Alteration (CIA) is widely utilized as a geochemical indicator of chemical weathering intensity, given by the formula: CIA = [Al_2O_3/ (Al_2O_3 + CaO* + Na_2O + K_2O)] × 100, where CaO* denotes the CaO associated with the silicate fraction of the sample (Nesbitt and Young, 1982). Chemical weathering plays a major role in controlling the mineralogical composition of fine-grained siliciclastic rocks and is therefore a key metric in understanding compositional changes in their major element distribution, particularly in relation to the regional supply of nutrients from the continent and the maturity of terrigenous clay (Singer, 1980). During chemical weathering, labile elements are preferentially removed, by a combination of the chemical weathering processes outlined above, resulting in elevated ratios of immobile elements (Al, Ti) to mobile alkalis (Na, Ca, K) in the weathered residue (Nesbitt and Young, 1982).

The CIA value increases with higher weathering intensity. In arid and cold climates, physical weathering dominates, leading to rock fragmentation and relatively low weathering intensity. Conversely, in humid and warm climates, the intensity of weathering increases, resulting in the dissolution of primary rock forming minerals and the subsequent formation of new clay minerals. The relationship between clay mineral composition and CIA highlights the predominant influence of climate on the formation of clay minerals in the sediments. Consequently, the predominance of illite and chlorite suggests weak chemical weathering and significant rock erosion, while abundant kaolinite indicates high chemical weathering (Darby, 1975; Hallam et al., 1991; Ehmann et al., 1992; Wahsner et al., 1999; Worden et al., 2020).

The question regarding whether a particular clay mineral is essentially authigenic or detrital is particularly important when it comes to paleo-studies. Depending on the origin

(authigenic or detrital) of the clay mineral assemblages present in sedimentary basins, various interpretations can be made. The detrital clay mineral assemblages are important archives for reconstructing paleo-environmental, paleo-climate, and paleo-tectonic as well as provenance analysis of sediments (Baldermann et al., 2020). The paleoclimatic interpretation of clays is based on the assumptions that they are detrital and have not been significantly altered by diagenesis, that their source areas can be identified, and that they represent secondary products of continental weathering. Authigenic clay minerals play an important role in global marine element cycles throughout Earth's history, resulting in them being excellent indicators of past and present biogeochemical cycling in marine sediments (Baldermann et al., 2022).

In this context, to achieve an adequate characterization of the paleoenvironmental variations in the different sedimentary records as well as paleo-climate associated with post-sedimentary evolution, it is essential to carry out a detailed analysis to discriminate detrital from authigenic phases with their different genetic contexts. Detrital from authigenic phase discrimination can be made based on textural, structural, and chemical characteristics that allow the distinction between various clay minerals (e.g., Rafiei et al., 2020). Scanning electron microscopy (SEM) with secondary electron (SE) and backscattered electron (BSE) images are useful tools used to differentiate distinctive morphologies and chemistries associated with these different clay mineral types (e.g., Rafiei et al., 2020; Han et al., 2024; Yu et al., 2024). A set of petrographic identification criteria is required for detrital and authigenic clay minerals during SEM examination. Petrographic identification criteria of detrital and authigenic clay minerals under SEM are summarized in Table 1.1.

Table 1.1| Petrographic identification criteria of detrital origin, solid-state transformation and neoformation

Type	Criteria
Detrital	1. Discrete grain boundaries, which show evidence of physical transport. 2. Long axes (sub)parallel to primary sedimentary structures such as lamination, compacted or across cut by secondary phases.
Solid-State transformation	1. Inherited mica with obvious cleavage or the appearance of feldspar remnants. 2. Inherited crystal profile. 3. Orientation surrounding the profile resulting from the original compaction
neoformation	1. Generally smaller in size and usually in the form of clay aggregates. 2. Fibrous morphology (e.g., illite and chlorite) or blocky to vermiform appearance (e.g., dickite and kaolinite). 3. Random orientation and sometimes form over pores (pore-filling distribution).

1.6.2 Clay Minerals and Their Structures

In a broader sense, clay minerals are a diverse group of hydrous layer aluminosilicates consisting of four main sub-groups: illite, kaolin, smectite, and chlorite (Elert and Rodriguez-Navarro, 2022). Clay is a naturally occurring substance that exhibit the property of plasticity at a suitable water content but become permanently hard when fired (Moreno-maroto and Alonso-azcárate, 2018). The basic components of the phyllosilicate layer are tetrahedral (T) and octahedral (O) sheets (Chamley, 1989; Brigatti et al., 2006). In clay mineral terminology, a single tetrahedron contains Si^{4+}, which is often substituted by Al^{3+} and in some cases Fe^{3+}, surrounded by four apical oxygen ions (O_2^-) in a tetrahedral configuration, making up the fundamental unit of the tetrahedral sheet. In the octahedral

sheet, the fundamental structural unit is an octahedron consisting of a central cation (O), with the most common being Al^{3+}, Fe^{2+}, Ca^{2+}or Mg^{2+}, and coordinated by a packing of six oxygens ions (O_2^-) or hydroxyl groups (OH^-) give rise to eight-sided building block known as a octahedron. Octahedral sheets are present in two forms: di-octahedral or tri-octahedral sheet. In the di-octahedral sheet, each O_2^- or OH^- is surrounded by two trivalent cations, like Al^{+3}. In contrast, in the tri-octahedral sheet, each O_2^- or OH^- is surrounded by three divalent cations, like Mg^{+2} or Fe^{+2}. When tetrahedral and octahedral sheets are joined to form a layer, the resulting structure can be either electrically neutral or negatively charged (Moore and Reynolds, 1989).

The bonding of octahedral and tetrahedral sheets forms the structure of various clay minerals, giving clay minerals different structural combinations and chemical and physical properties. Interstratification of clay mineral layers leads to the development of mixed clay minerals (Velde and Meunier, 2008). Clay minerals are classified based on the structure of layer type (1:1 (T:O) vs 2:1 (T:O: T); if the silicate layers are composed of one tetrahedral and one octahedral sheet, the structure is denoted as a 1:1 layer silicate structure (e.g., kaolinite). If the structure is composed of one octahedral sheet sandwiched between two tetrahedral sheets, it is called a 2:1 layer type (e.g., illite, smectites). Clays are also classified according to the charge per formula unit (pfu) on the layers and the type of material occurring between the layers (Brown, 1984). The dominant clay minerals in marine sediments are illite (I), smectite (S)–often occurring as mix-layer I/S clays, chlorite (C) and kaolinite (K) (Chamley 1989b).

1.6.2.1 Illite

Illite is a dioctahedral (2:1) phyllosilicate, comprising an octahedral sheet centred on aluminium surrounded by two tetrahedral sheets centred on silicon. It is poor in magnesium, but rich in iron and calcium (Środoń et al., 1984). Illite is a non-expandable clay mineral in

which ionic substitution occurs in both the octahedral and tetrahedral layers (Brigatti et al., 2006). Illite clays also have a high negative layer charge which encourages the interlayer space to be occupied by anhydrous alkaline and alkaline earth cations, such as K^+. Illite occurs in various sedimentary and hydrothermally altered volcano-sedimentary deposits (Meunier et al., 2004). Also, it can be a chemically weathered product of muscovite and mica in general and/or K-feldspars from parent rocks. Illite can also form from the illitization of smectite, muscovite and kaolinite (Mantovani and Becerro, 2010). Illitization occurs in the presence of potassium in sediment porewater, assumed to be derived from the dissolution or alteration of K-feldspar or muscovite (Weaver, 1967). Illite is characterized by a series of peaks located mainly at 10 Å in the XRD (X-Ray Diffraction) diffractogram.

1.6.2.2 Chlorite

Chlorite can be described as a 2:1 non-expanding clay mineral. It is sometimes referred to as 2:1:1 in some literature and 2:2 in others (Moore and Reynolds, 1989). Chlorite contains abundant iron and magnesium (Worden et al., 2020) and is stable in modern marine sediments formed in cold regions marked by strong physical and weak chemical weathering (Worden et al., 2020). While it is unstable under the physicochemical conditions of the Earth's surface, it can form over a wide range of temperatures in the subsurface of geological systems. Low-temperature chlorite is a common mineral in rocks that have experienced hydrothermal or diagenetic processes. The common morphologies of authigenic chlorites are as follows: (1) grain-coating chlorites occur in intergranular pores of sandstones and conglomerates with good textural maturity; (2) replacement and alteration products of amphibole, pyroxene, and biotite; (3) precipitated within feldspar cleavage, (4) pore and fracture fillings (Shifa et al., 2016).

1.6.2.3 Kaolinite

Kaolinite is a 1:1 clay mineral with the chemical formula $Al_2Si_2O_5(OH)_4$, composed of one tetrahedral layer linked to one octahedral layer and lacks a cation interlayer. Kaolinite is the main Al-bearing phase in highly weathered sediments. It is a common authigenic clay mineral associated with the diagenetic transformation of detrital minerals in low and high-temperature environments as kaolinite forms through chemical weathering of feldspar or muscovite mica (kaolinization of muscovite) or hydrothermal alteration of aluminosilicate minerals (Zhang et al., 2017; Aubineau et al., 2021). XRD can discriminate kaolinite at peaks of 7.15A^o (001) and 3.58A^o (002) (Moore and Reynolds, 1989).

1.6.2.4 Smectite

Smectite is a 2:1 expandable clay mineral that includes montmorillonite. During burial diagenesis, most smectite is transformed into the more stable illite clay mineral through illitization in the presence of sufficient dissolved K concentrations (Rafiei et al., 2020). Two mechanisms describe the chemical transformation of smectite to illite: (1) layer collapse, which is solid-state transformation (Bethke and Altaner, 1986) and (2) partial smectite lattice dissolution and reprecipitation of illite, termed neoformation (Kingdom, 1986). Tosca et al. (2010) suggest the broad absence of smectite in Precambrian rocks is due to quantitative diagenetic conversion to illite during burial diagenesis. Kennedy et al. (2006) linked the absence of smectite in Proterozoic shales and its appearance near the Proterozoic–Cambrian boundary to fundamental changes in continental weathering processes resulting from the early evolution of metazoans. However, recently the presence of smectite-rich layers was confirmed in Paleoproterozoic rocks from the Francevillian basin (Ngombi-Pemba et al., 2014).

1.6.2.5 Mixed Layer Illite/Smectites, I/S MLM

Mixed-layer illite/smectites are expandable layer minerals that are more common than either discrete illite or smectite (Moore and Reynolds Jr, 1989). They are products of a multi-step process that takes place during diagenesis and is controlled mainly by temperature, time, and K^+ availability (Velde et al., 1986; Lanson et al., 2009; Aubineau et al., 2019). They also form during hydrothermal alteration or contact metamorphism or form at surface temperatures because of wetting and drying processes. However, most of the mixed layer illite/smectite found in sedimentary environments conditions are due to burial diagenesis.

1.7 Thesis Outlines

The availability of nutrients, particularly phosphorus, played a central role in shaping early Earth's biogeochemical cycles (Reinhard et al., 2017; Guilbaud et al., 2020; Alcott et al., 2022; Dodd et al., 2023; Rasmussen et al., 2023). It has been proposed that physical weathering of continental landmasses by thawing glaciers generated glacial flour, which fertilized post-Snowball oceans and stimulated primary productivity (Reinhard et al., 2017). However, the specific mechanisms by which these nutrients were transported to the oceans remain poorly understood for this period.

Observations from modern glaciated environments indicate that the physical weathering associated with melting ice sheets contributes substantially to the enrichment of seawater and primary sediments in phosphorus (P), iron (Fe), and a range of trace metals (e.g., Bhatia et al., 2013; Hawkings et al., 2014, 2016, 2020; Hopwood et al., 2014; Hodson et al., 2005, 2017). These processes enhance the delivery of bioavailable nutrients and trace elements to marine systems, consistent with the elevated fluxes documented along present-day glaciated continental margins. This has led to growing recognition that glaciers are not merely physical erosive agents, but active geochemical reactors that influence downstream

productivity in fjords and polar oceans. In contemporary settings, Hao et al. (2021a) show that the strong weathering intensities and associated high kaolinite content in post-GOE suggest enhanced phosphorus shuttling from the continents into marine environments.

Two primary challenges underlie the gap in understanding the mechanisms of nutrients delivery to oceans after Sturtian glaciation. First, few studies have integrated detailed mineralogical analyses of glacial and post-glacial sediments with nutrient cycling and redox geochemical proxies across Cryogenian successions. Second, the coupled roles of physical and chemical weathering in mobilizing nutrients under CO_2-rich post-glacial atmospheric conditions remain inadequately quantified regarding sedimentary clay mineral assemblages and phosphorus geochemistry. This highlights the need for integrated studies of clay mineralogy, nutrient geochemistry, and redox-sensitive proxies to resolve how early deglaciations influenced nutrient dynamics during critical transitions in Earth's surface environments and biosphere. Thus, this study aims to test the hypothesis that the supply of nutrients to post-Snowball oceans stimulated primary production and initiated dramatic ocean-atmosphere oxygenation. Specifically, high-resolution targeting of clay minerals as proxies of bioavailable nutrient delivery to seawater and how this relationship varies in Pre-Snowball greenhouse, Snowball icehouse and post-Snowball greenhouse conditions, is motivated and investigated for the first time. This thesis unravels the link between the supply of nutrients by clay minerals from the continents and the impact on ocean-atmosphere oxygenation before, during and after glaciations. Specifically, this study provides a detailed exploration of clay mineral formation processes and biogeochemistry associated with the Cryogenian Sturtian shallow continental margin siliciclastic platform deposits in Islay, Scotland. The thesis is divided into three research chapters and methods and conclusion chapters, together comprising five chapters plus the literature.

The first research chapter focuses on mineralogical investigations of the ca. 350 m thick Pre-Snowball Lossit Limestone deposit formed in a tropical seawater setting, the deglaciating 1-km thick Port Askaig Tillites and the overlying post-Snowball deposits, beginning with the Bonahaven dolomite Formation extending upwards for over 350 m. These rocks were analysed for their clay mineral abundances, types and high-resolution chemical compositions compared to the unweathered source-rock fragments trapped in the samples using XRD, SEM, and SEM-EDS. The second chapter provides a detailed geochemical analysis of the bulk trace elemental compositions of the sections studied in the first research chapter, coupled with Fe and P speciation of the studied rocks to decipher the role of clay minerals in nutrient delivery to seawater before, during and after the Sturtian Snowball Earth glaciation. The third research chapter investigates the marine redox condition in which the sedimentary units studied in the first and second research chapters were deposited, using multiple proxy approaches of uranium isotope systematics and iron speciation. These data are then summarised in the concluding chapter to draw global and regional conclusions on the coupling between the evolution of the Cryogenian clay mineral factory, phosphate biogeochemistry and ocean-atmosphere oxygenation dynamics.

Chapter 2: Material and Methods

2.1 Geologic Setting and Sample Collection

This chapter covers the details of the samples used in this thesis and the methods employed to analyse them. The studied samples are composed of shallow marine sedimentary rocks deposited before, during and after the global Cryogenian Sturtian Snowball Earth glaciation 720-660 million years ago (Ma) (e.g., Parnell and Boyce, 2017; Fairchild et al., 2018; Shuster et al., 2018) that outcrop on the Isles of Islay and Garvellachs, Scotland (Figure 2.1 & Figure 2.2).

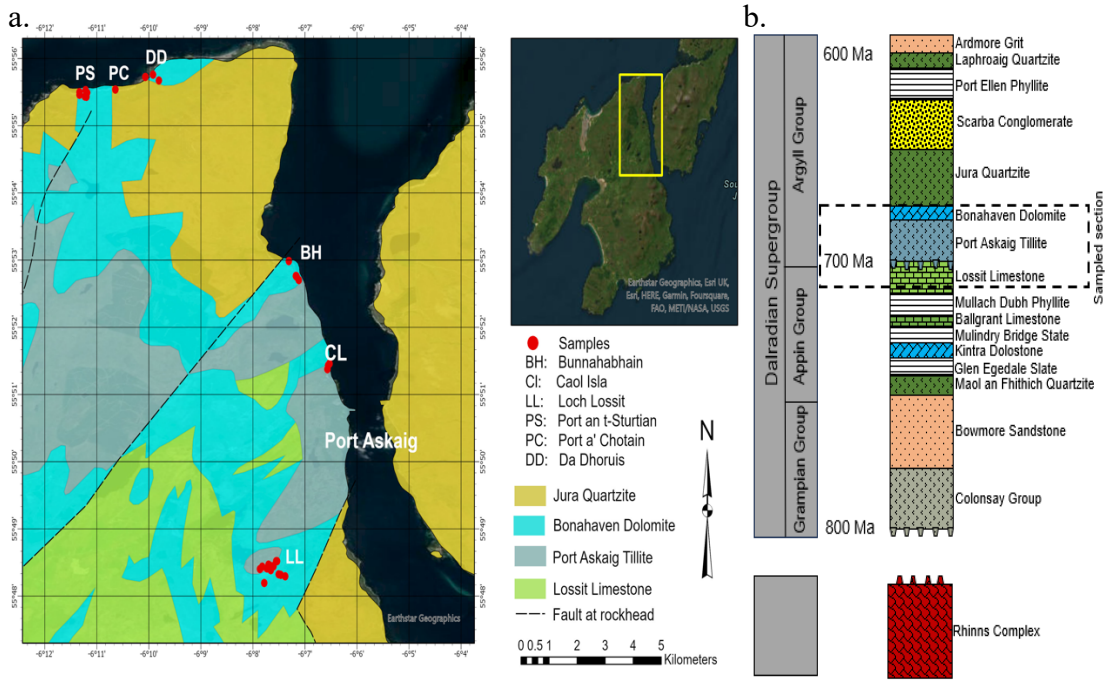

Figure 2.1| a. Simplified geological map of Islay and b. Location of the studied section in the stratigraphic profile.

Sampling locations, coordinates and field characterisation of sedimentary features are shown in Table 2.1. The samples were obtained from well-described outcrops (Tanner et al., 2013; Parnell and Boyce, 2017; Fairchild et al., 2018; Shuster et al., 2018), with care taken in the field to exempt lithologies exhibiting visible signs of weathering resulting from

exhumation on the Earth's surface. As part of the mid-Neoproterozoic Cryogenian Period to the Early Palaeozoic, the Dalradian Supergroup to which the sampled formations belong, is subdivided into the Grampian, Appin and Argyll groups.

Figure 2.2| Examples of field photographs showing sampled outcrops in Islay taken by Alasdair Skelton. a. Base of Port Askaig Tillite Formation (PATF) – cliff height is 3 m high. b. Port Askaig Tillite shows clasts that are typically 10 cm across. c. Fossilised stromatolites in the Bonahaven Dolomite Formation (BDF) overlying the Port Askaig Tillites – each stromatolite is ca. 1 m across d. Stromatolitic facies seen from the side – each stromatolite is ca. 10 cm across.

The Appin and Argyll groups deposited on the palaeo-ocean continental shelf margin and later in the open ocean, with the shift in depositional style linked to the initial rifting of the Rodinia Supercontinent around 840 Ma and the opening of the Iapetus Ocean shortly after 600 Ma (Tanner et al., 2013; Parnell and Boyce, 2017; Fairchild et al., 2018; Shuster et al., 2018). The sustenance and intensification of the extensional tectonic activity through the Argyll Group is evidenced by the increasing deposition of rocks associated with volcanic activity. The studied interval includes the late Tonian Lossit Limestone Formation (LLF) belonging to the 4 km thick Appin Group, precipitated from warm tropical shallow marine waters (Fairchild et al., 2018). The LLF contains organic-rich mudstones, sandstones, and a variety of carbonate lithologies, some hosting stromatolites. The upper layer is composed of tillites believed to transition conformably into the overlaying 1.1 km-thick Port Askaig Tillite Formation (PATF), associated with the melting stages of the Sturtian Snowball glaciations. The PATF comprises a sequence of alternating layers consisting of coarse-grained and poorly sorted diamictite interbedded with sandstone, mudstone, conglomerate and megaclast. The PATF is succeeded by the post-glacial Bonahaven Dolomite Formation (BDF) consisting of an estimated 300 m-thick fine-grained clastic succession made up predominantly of dolostones and evaporite minerals (Tanner et al., 2013; Parnell and Boyce, 2017; Fairchild et al., 2018; Shuster et al., 2018).

Table 2.1| Studied sample description.

Locality	Coordinates	Formation and Stratigraphy
Port an t-Struthain		
PS-16-01	N55°55.499' W006°11.332'	Bonahaven Dolomite, Member 4 metapelite
PS-16-02	N55°55.500' W006°11.331'	Bonahaven Dolomite, Member 4 Semi metapelite
PS-16-03	N55°55.460' W006°11.331'	Bonahaven Dolomite, Member 4, Middle of the sandwich cream dolostone
PS-16-04	N55°55.528' W006°11.216'	Bonahaven Dolomite, Member 4, cream dolostone

PS-16-05	N55°55.434' W006°11.230'	Bonahaven Dolomite, Member 3, iron rich dolostone
PS-16-06	N55°55.432' W006°11.199'	Bonahaven Dolomite, Member 2, quartzite
PS-16-10	N55°55.489' W006°11.184'	Bonahaven Dolomite, Low member 4 or high member 3
PS-16-11	N55°55.542' W006°10.769'	Bonahaven Dolomite, Member 3 Muddy dolostone
PS-16-12	N55°55.539' W006°10.644'	Bonahaven Dolomite, Member 3 Dolomitic mudstone
Port a'Chotain		
PC-16-01a	N55°55.726' W006°10.069'	Bonahaven Dolomite, Member 4, Foliated
PC-16-01b	N55°55.726' W006°10.069'	Bonahaven Dolomite, Member 4, Massive
PC-16-02	N55°55.672' W006°09.806'	Bonahaven Dolomite, Member 4, Dolostone
PC-16-03	N55°55.760' W006'09.918'	Bonahaven Dolomite, Member 3 (just under member 4), Dolostone
Bagh an da Dhoruis		
DD-16-04	N55°56.005' W006°09.425'	Bonahaven Dolomite, Member 3 Muddy dolostone under stromatolite
DD-16-06	N55°56.002' W006°09.072'	Bonahaven Dolomite, Member 3 Muddy dolostone
DD-16-07	N55°55.973' W006°08.664'	Bonahaven Dolomite, Member 4
Caol Isla		
Ci-16-01	N55°51.375' W006°06.570'	Bonahaven Dolomite, Member 1 unit 1 Metapelite mudstone biotite
Ci-16-02	N55°51.431' W006°06.555'	Bonahaven Dolomite, Member 1 unit 4 (very base)
Ci-16-23	N55°51.460' W006°06.531'	Bonahaven Dolomite, Top member 4 mudstone
Ci-16-03b	N55°51.460' W006°06.531'	Bonahaven Dolomite, Base member 5 dolostone
Bonahaven		
BH-16-01	N55°52.704' W006°07.118'	Bonahaven Dolomite, Member 1 unit 1 Metapelite with carbonate pebbles
BH-16-02	N55°52.750' W006°07.156'	Bonahaven Dolomite, Member 1 unit 4 Mud and siltstone. Unmetamorphosed
BH-16-03	N55°52.763' W006°07.168'	Bonahaven Dolomite, Member 1 unit 5 Mud layer growing over mica cement. Unmetamorphosed
BH-16-03b	N55°52.762' W006°07.177'	Bonahaven Dolomite, Member 1 unit 5 Mud layer
BH-16-04	N55°52.987' W006°07.309'	Bonahaven Dolomite, Member 3 Stromatolitic dolostone
Lossit Limestone Formation		
LL-16-k	N55°48.293' W006°07.379'	Lossit Limestone

LL-16-01	N55°48.194' W006°07.781'	Lossit Limestone
LL-16-j	N55°48.317' W006°07.464'	Lossit Limestone, Grey limestone
LL-16-j(b)	N55°48.323' W006°07.505'	Lossit Limestone, Oolitic dolostone
LL-16-i	N55°48.374' W006°07.525	Lossit Limestone, Stromatolitic
LL-16-h	N55°48.383' W006°07.655'	Lossit Limestone, Slate
LL-16-g	N55°48.412' W006°07.732'	Lossit Limestone, Muddy limestone
LL-16-c	N55°48.451' W006°07.670'	Lossit Limestone, Limestone
LL-16-d	N55°48.467' W006°07.698'	Lossit Limestone, Muddy layer in metacarbonate (mudstone)
LL-16-e	N55°48.435' W006°07.823'	Port Askaig tillite, Muddy layer in diamictite
LL-16-f	N55°48.401' W006°07.863'	Port Askaig tillite, Magnetic sandstone interlayered by dolostone diamictite
LL-16-b2	N55°48.445' W006°07.609'	Port Askaig tillite, Dolostone diamictite
LL-16-b1	N55°48.442' W006°07.605'	Port Askaig tillite, Mudstone diamictite. Contain a carbonate clast
LL-16-a	N55°48.520' W006°07.553'	Port Askaig tillite, Muddy tillite
LL-16-a2	N55°48.519' W006°07.535'	Port Askaig tillite, Clast of dolostone in tillite
Creagan Loisgte		
CL-16-01	N55°49.262' W006°06.787'	Port Askaig tillite, Member 3, Dolostone
CL-16-02	N55°49.353' W006°06.695'	Port Askaig tillite, Member 3, dolostone, the second diamictite
CL-16-03	N55°49.370' W006°06.747'	Port Askig tillite, Top member 3, Metapelite

2.2 Methods

Rock samples were cut using a saw. Any weathered and exposed surfaces were carefully removed, and only the fresh unweathered areas were used for further analysis. These were then crushed using a jaw crusher and powdered with a Tungsten Caribide Tema Mill. To avoid contamination, the grinding barrel and all its parts (lid, ring, cylinder, rubber seal and barrel) were thoroughly cleaned with deionized water using a brush. The components were

then rinsed with acetone or isopropanol to remove any remaining residues and dried between sample.

2.2.1 Mineralogical Analysis

In the Earth Sciences, mineralogical analysis is used to show the mineral composition of materials and to distinguish authigenic from detrital phases. Such approaches have been used to link for example weathering dynamics associated with changing patterns (Singer, 1980; Velde and Meunier, 2008; Warr, 2022). Mineralogical analysis can also provide information about the mechanisms of nutrient cycling in marine basins and the means by which they are removed, buried and recycled into porewater spaces (Zegeye et al., 2012; Large et al., 2015; Hao et al., 2020; Baldermann et al., 2022; Chi Fru et al., 2023; Krause et al., 2023). This thesis used a number of methods to study mineralogical changes before, during and after the Neoproterozoic Sturtian Snowball Earth glaciations to reconstruct both climate patterns and potential nutrient cycling mechanisms as indicated in the aims and goals given in Chapter 1.

2.2.1.1 X-Ray Diffraction (XRD) Analysis

X-Ray Diffraction (XRD) is a non-destructive technique used to determine the phase of crystalline materials through investigation of atomic and molecular structure. Over the past century, XRD has gained wide application in quantitative and qualitative studies to identify clay minerals present in sediments and rocks (Brindley, 1980; Bish and Howard, 1988; Środoń, 2002; Chipera and Bish, 2013). However, according to Moore and Reynolds (1989), an accurate identification of the amount of different clay minerals present in clay is more difficult and may not reflect the exact quantity of each clay mineral phase present in the sample. Consequently, it is widely accepted that the amount of clay minerals determined from XRD is often semi-quantitative.

Prior to XRD analysis, samples were cut to remove the exposed surfaces, pulverised and homogenized into a fine powder. A finely ground powdered sample was exposed to a beam of monochromatic X-rays that interact with the atoms in the sample's crystal lattice. This interaction causes X-rays to scatter in different directions, producing a diffraction pattern specific to the mineralogical composition of the sample. The diffracted rays were collected by a detector, and the information was relayed to a computer where, using the Bragg equation ($n\lambda = 2d\sin\theta$, where n is an integer order of the diffracted beam, λ the wavelength of the incident X-ray beam, and d is the distance between adjacent planes of atoms). The mineralogical phases were identified by comparing and matching the X-ray diffraction patterns of the sample of interest to those in a reference database.

XRD analysis was conducted on bulk and the <2 μm separated clay fraction to characterise and investigate representative samples spanning the pre-Snowball LLF, the Snowball PATF and the post-Snowball BDF as outlined below. Mineralogical analysis using the XRD method was carried out semi-quantitatively at Cardiff University and for qualitative bulk mineralogy and clay fraction at the University of Poitiers, France.

2.2.1.1.1 Whole Rock (bulk) XRD Analysis

This analysis was used to identify and quantify the mineral composition of our rock samples (Al-Jaroudi et al., 2007; Sandaruwan et al., 2022; Combaudon et al., 2024; Tostevin and Ahmed, 2023; Hillier, 1999). Whole rock semi-quantitative XRD analysis was carried out in the X-ray diffraction Laboratory in the School of Earth and Environmental Sciences, Cardiff University. The analysis was performed using a Philips PW1710 Automated Powder Diffractometer with automatic divergence slit, Cu-Ka Radiation at 35 kV and 40 mA between 2 and 70 °2θ at a scan speed of 0.04 °2θ/s. The powdered samples were packed into aluminium holders, placed in the sample holder of the Goniometer and bombarded with

X-rays generated from the Copper tube. The whole rock mineralogical composition was determined by processing the measured diffractograms with software PW1877 APD version 3.6 Identification Software: PW1876 PC-Identify version 1.0b (Analytical, 2001).

Whole rock qualitative analyses at the Institute de Chimie des Milieux et Matériaux de Poitiers (IC2MP), University of Poitiers, France was performed on a Bruker D8 ADVANCE diffractometer (CuKα radiation) with operating conditions of 40 kV, 40mA, and 0.025/s step size at 2°-65° 2θ angular range.

2.2.1.1.2 Clay Size Fraction XRD Analysis

Before XRD analysis, the clay-mineral fractions in powdered samples were first ultrasonically dispersed in distilled water to liberate the fine fraction. Then, the clay-size fraction was separated by sedimentation and program-timed centrifugation at 20 ℃ with a Sorvall LEGEND XRF centrifuge at a rotating speed of 1000 rpm for 2 minutes 30 seconds at the University of Poitiers. Oriented mounts of the <2 μm fractions were prepared by sedimentation on glass slides and analyzed after air-drying (AD) at room temperature overnight and after saturation with ethylene-glycol (EG) treatment. The oriented AD and EG mounts were scanned from 2° to 35° 2θ angular range at a scan speed of 0.02 °2θ/3s by XRD analysis as described above. The minerals were identified based on the mineral principal peak positions and comparison with International Centre for Diffraction Data (ICDD) files (Moore and Reynolds, 1989) using an X'pert Highscore software (Analytical, 2001).

2.2.1.2 Scanning Electron Microscope (SEM) Mineralogical Analysis

The scanning electron microscope is an extremely useful tool for studying mineralogical composition (e.g., Bish and Howard, 1988; Rafiei et al., 2020; Won et al., 2020; Liivamägi et al., 2021; Ikouanga et al., 2023; Han et al., 2024; Yuan et al., 2024). The SEM

petrographic observations of polished thin sections were performed to study the textural relationships, morphology, mineral assemblages, and chemical composition of the studied samples. It can provide high-resolution images of the sizes and surface texture of sediment particles and the orientation of materials making up the sample by scanning with a beam of high-energy electrons. An SEM, in general, is composed of an electron gun source, electron lenses, sample stage, detectors for signals of interest, display, and data output sources. Different types of electrons are produced from the beam, which are secondary and backscattered electrons. An energy-dispersive spectroscopy (EDS) system coupled with backscattered-electron detection (BSED) was used to aid in identifying mineral phases by the interpretation of element spectra as well as for elemental mapping of samples.

Mineral identification was achieved by a combination of morphology, shape, elemental composition, comparison of EDS spectra against references for known mineral standards and by independent XRD-based mineral identification following the approach of Reed (2005). In general, coarse (sub)angular particles such as mica, quartz and feldspar with discrete grain boundaries characteristic of physical transportation were classified as primary minerals. Secondary, diagenetic and neoformed minerals were identified by their hairy, fibrous morphology in the case of illite and chlorite, blocky kaolinite, and as randomly oriented intergranular and intragranular pore space fillings (Rafiei et al., 2020).

The analysis was done on polished carbon-coated thin sections using the Zeiss Sigma HD Field Emission Gun SEM in the School of Earth and Environmental Sciences at Cardiff University equipped with two Oxford Instruments energy-dispersive spectroscopy (EDS) detectors. BSED patterns were acquired with a Nordlys Oxford Instruments detector and 15 kV accelerating voltage and 8.9 mm working distance. Samples tested for this research were carbon coated to a thickness of about 14 nm using BIO-RAD SC5.

2.2.2 Phosphorous Minerals Analysis

As mentioned earlier, Phosphorus is considered a limiting factor for marine productivity and a key element for the functioning of Earth's biogeochemical cycles through geologic time scales (Tyrrell, 1999). One of the most important factors controlling seawater phosphorus content is the release of phosphorus from sediments back into pore space water and the ocean water column (Defforey and Paytan, 2018). For example, phosphorus tends to be abundant in sedimentary environments bound to calcium (P–Ca; apatite), iron (P–Fe, e.g., magnetite) and aluminium (P–Al; e.g., clay minerals) (Ruttenberg and Berner, 1993; Egger et al., 2015; Chi Fru et al., 2023). These observations suggest that various minerals, including clays, represent likely mechanisms for the delivery and preservation of phosphorus in marine sediments, P can potentially be recycled back into seawater at the sediment-water interface during early diagenesis. Hence, mineralogical analysis was conducted to investigate the different clay mineral phases likely associated with P preservation in the shallow marine sedimentary records formed before, during and after the Sturtian Snowball Earth glaciations, using chemical extraction, SEM and XRD approaches.

2.2.2.1 Phase Composition

SEM-EDS element mapping and BSED imaging were performed as described in section 2.2.1.2.

2.2.2.2 Chemically Extractable Fe- Bound P analysis

Association of phosphorus (P) with various reactive iron minerals phases, except for pyrite, which does not bind P, together with sheet silicate associated P, was chemically extracted using the sequential Fe extraction method of Poulton and Canfield (2005), adopted for the quantification of acid-extractable P phases by Thompson et al. (2019) on powdered samples. The extracted dissolved P in solution was analysed by ICP-AES. These included potential

Fe carbonate bound-P (Fe-P_{carb}), Fe oxyhydr(oxides) associated-P (Fe-ox_{HR}-P), magnetite bound-P (P_{Mag}) and sheet silicate Fe associated P (P_{SS}). The remaining P was assumed to be tied up mainly with unreactive silicates (P_{URS}), first verified by a lack of correlation between total organic carbon and total P (P_T) obtained from analysis of acid-dissolved bulk powdered samples. Further, multiple lines of geochemical evidence, combined with Loss on Ignition (LOI), were used to deduce whether P trapped in the sediments was predominantly bound to inorganic or organic mineral phases. Where LOI values are elevated, they presumably predict higher combustible sedimentary organic and/or carbonate content, while lower values indicate the contrary, due to the higher susceptibility of carbonates and organic matter to complete combustion to CO_2 under elevated temperatures (Heiri et al., 2001). From this analysis, the potential P_{URS} fraction was estimated as $P_{URS} = (P_T) – (Fe\text{-}P_{carb} + Fe\text{-}ox_{HR}\text{-}P + P_{mag} + P_{ss})$. Because of the strong linear correlation between dissolved P and particulate Fe-P_{carb} + Fe-ox_{HR}-P + P_{mag} in marine sediments (Wheat et al., 1996; Feely et al., 1998; Bjerrum and Canfield, 2002), this analysis assumed that P bound to various reactive iron minerals, except for pyrite), proportionately reflect the volume of P dissolved in the aqueous solution from which the reactive iron minerals formed. By comparing temporal changes across the sampled section, temporal changes in dissolved seawater P content were approximated.

2.2.3 Bulk Rock Geochemical Analysis

The bulk major, trace and rare earth element compositions of samples were performed at the Pôle Spectrométrie Océan, Institut Universitaire Européen de la Mer (PSO/IUEM) Brest, France, following the analytical procedure of Cotten et al. (1995). About 250 mg of rock powder was dissolved with concentrated 3 ml of 40% HF, 3 ml of 32% HCl and 1 ml of 65% HNO_3 in closed screw-top Teflon Savillex vessels at 90°C for one day. Excess HF in the dissolved samples was neutralised with 93 ml 20 g/L H_3BO_3 aqueous solution. All

elements were measured by inductively coupled plasma atomic emission spectroscopy (ICP-AES) and trace elements by inductively coupled plasma mass spectroscopy (ICP-MS) using a Horiba Jobin Yvon® Ultima 2 spectrometer with a boron solution as internal standard. Calibrations were made using international standards, ACE, JB2 and WSE. The relative standard deviation was estimated to be ≤1% for SiO_2, ≤2% for the remaining major elements and ≤5% for trace elements.

2.2.4 Carbon and Oxygen Stable Isotope Analysis

Carbon, organic carbon, and oxygen isotopes of carbonate rocks have been widely used for global stratigraphic division and correlation, paleoclimate and paleoenvironment reconstructions, and to assess diagenetic processes (e.g., diagenetic fluids) (e.g., Kump and Arthur, 1999; Tiwari et al., 2015; Godfrey et al., 2018; Xiaofeng et al., 2023; Edmonsond et al., 2024). The carbon isotope ratio is generally expressed in the $\delta^{13}C$ notation as $\delta^{13}C = [(^{13}C/^{12}C)_{Sample}/(^{13}C/^{12}C)_{standard} - 1] \times 1.000$, and the oxygen isotope ratio in the $\delta^{18}O$ notation as $\delta^{18}O = [(^{18}O/^{16}O)_{Sample}/(^{18}O/^{16}O)_{standard} - 1] \times 1.000$. All measured $\delta^{13}C$ and $\delta^{18}O$ are reported in the standard delta notation as per mil (‰) deviation from the Vienna-Pee Dee Belemnite (V-PDB) scale. In this study, stable isotope analyses were done to check whether the stratigraphic correlation was within the range reported during, before and after the Cryogenian glaciations and to investigate post-depositional influence (metamorphic fluids) on the studied samples.

2.2.4.1 Carbonate Analysis

Carbon and oxygen stable isotopes were analyzed at the Stable Isotope Mass Spectrometry Lab, Cardiff University, under the supervision of an appointed full-time laboratory technician. Powdered samples were weighed into septum vials, which were flushed with helium and then acidified manually with 99% orthophosphoric acid. All samples were left

to react for 24 hours at 60°C to ensure a complete reaction of dolomite. Isotopic analysis of the $\delta^{13}C_{carbonate}$ and $\delta^{18}O_{carbonate}$ composition of samples was measured on a Thermo Delta V Advantage mass spectrometer, coupled to a Thermo gasbench II for head-space sampling of carbonate samples. The precision of an in-house Carrara marble standard, which is calibrated against NBS19, was used to determine the standard deviation of repeated analyses to be 0.05‰ for both $\delta^{18}O_{carbonate}$ and $\delta^{13}C_{carbonate}$. Samples were analysed in combination with three in-house standards, composed of lab-grade caffeine and two commercial collagen food supplements (MarCol and MCF) with $\delta^{13}C$ = -16.20‰, -33.30‰ and -22.36‰, respectively. The in-house standards were calibrated against the IAEA-CH6 and IAEA-600 international standards and the $\delta^{13}C_{carbonate}$ and $\delta^{18}O_{carbonate}$ values of samples reported in the δ-notation on the Vienna-Pee Dee Belemnite (VPDB) scale.

2.2.4.2 Organic Carbon Analysis

Prior to organic carbon isotope analysis, samples were acidified in 10% HCl, left to react for two days to remove inorganic carbon (carbonates), the residues rinsed three times to eliminate residual acid, dried and weighed into tin capsules. Samples were then measured on a Thermo Delta V Advantage mass spectrometer with Thermo Flash EA and Conflo II and $\delta^{13}C_{org}$ results reported in the δ-notation on the Vienna-Pee Dee Belemnite (VPDB) scale. The maximum amount of sample that could be analysed for C_{org} was determined to be 60-80 mg based on the aperture of the autosampler. Considering that most samples contained C_{org} content as low as 10 µg, to allow for efficient calibration of such small amounts, three standards; IAEA-CH6, IAEA-600 and an in-house caffeine standard with $\delta^{13}C$ compositions of −10.449‰, −27.771‰, and −33.30‰, respectively, were dissolved in de-ionised water to improve homogeneity and to allow for accurate dosing of small aliquots using a micro-pipette. Results for the IAEA-CH6 and the in-house caffeine standards were used to estimate a correction function for sample size and size-dependent 2-point normalization and applied

to IAEA-600 as an independent standard. The resultant precision was determined to be dependent on sample size, while the long-term $\delta^{13}C_{org}$ precision was estimated to be 0.09‰ (±1 sd) for routine samples containing ≥100 µg C. However, upon decreasing the sample size to 10–30 µg C, the standard deviation increased to ±0.38‰ (IAEA-600, n = 15).

2.2.5 Redox Reconstruction

A multi-proxy approach using uranium isotope and iron speciation was used to infer the redox depositional conditions of the sampled lithologies—before, during and after the Neoproterozoic Sturtian Snowball Earth intervals.

2.2.5.1 Uranium Isotope Analysis

Uranium was used as a redox proxy because of its redox-dependent behaviour, abundance as redox-sensitive carbonate associated U (CAU), (Dunk et al., 2002; Andersen et al., 2014; Holmden et al., 2015; Tissot and Dauphas, 2015; Lau et al., 2017; Chen et al., 2022) and because of the prevalence of authigenic carbonate minerals across the sampled sections (e.g., Tanner et al., 2013; Parnell and Boyce, 2017; Fairchild et al., 2018). A total of 19 rock samples spanning the pre-Snowball, tillite and post-Snowball intervals were analysed for U systematics. Only samples with more than 5% carbonate content were selected following baseline requirements. Sample dissolution and separation of U carbonates were carried out in the CELTIC Trace Element and Isotope Analysis clean laboratory, at Cardiff University. Preceding analysis, matrix carbonate was prepared using the protocol outlined in Clarkson et al. (2020) and associated U isotopes measured according to the protocols described in Chen et al. (2022). Briefly, the carbonate-associated U (CAU) $^{238}U/^{235}U$ ratios ($\delta^{238}U_{CAU}$) were extracted from ~2 g powdered samples leached with 40 ml 1 N acidic acid at room temperature for several hours, until no further effervescence was observed. This was followed by centrifugation at 3000 rpm for 15 minutes to separate the detrital fraction from

the leachate by decanting the supernatant into 60 ml Teflon beakers using the pipette. The solution was then acidified with 5 ml concentrated HNO_3, dried down on a hotplate, and redissolved in 10 ml 1.5 N HNO_3. A small aliquot of the leachates (~1%) was taken and the U, Mg, Ca, Mn, Sr and Th concentrations were measured on an ICAP ICPMS at CELTIC. The concentrations were measured according to previously described analytical techniques (Andersen et al., 2013). Interspersed measurements of the standard BCR-2 reproduced results within ±10‰ standard deviation (1sd). After the U concentration of the leachate was determined, samples were doubled spiked with the IRMM3636 ^{236}U-^{233}U aiming to achieve $^{238}U/^{236}U$ ratios of ~30. A double-stage U purification column chemistry (TRU and U-Teva) procedure was then carried out following published protocols by Andersen et al. (2015). The samples were dried overnight and then redissolved in 2% HNO_3 + trace HF. Uranium isotope composition analyses were carried on a Nu Instruments *Nu Plasma II* MC-ICP-MS (Wrexham, Wales, UK) through a Teledyne Cetac Technologies *Aridus II* desolvating nebulizer system (Omaha, Nebraska, USA) and data collected in static mode for ^{234}U, ^{235}U and ^{238}U in Faraday cups fitted with 11^{11} Ω resistors, following the set-up in Stirling et al. (2007). General U transmission efficiencies were ~1% and measurements were conducted using typical ^{238}U ion beams of $\sim 4\times10^{-10}$ amps and data integrated over 60×5 s periods. The resulting $^{238}U/^{235}U$ ratios were reported as $\delta^{238}U = [(^{238}U/^{235}U)_{Sample}/(^{238}U/^{235}U)_{CRM145} - 1] \times 1.000$, relative to the CRM145 U standard. The internal precision on measured $\delta^{238}U$ values was better than ±0.10‰ (2 standard error) for all samples. Four measurements of in-house CZ-1, duplicate HU-1, and four carbonate SRM-1D standard splits, processed through the full carbonate leaching procedure, gave $\delta^{238}U$ values of −0.04 ± 0.10‰ (2 sd), −0.55 ± 0.06‰ (2 sd) and -0.10±0.06‰ (2 sd), respectively, in good agreement with other published values on these samples (Stirling et al., 2007; Hiess et al., 2012; Andersen et al., 2014).

2.2.5.2 The Iron Redox Proxy Analysis

Iron speciation analysis was conducted at Cardiff University using the procedure developed by Poulton and Canfield (2005) and reviewed by Poulton and Canfield (2011) and (Raiswell et al., 2018). Low carbonate-containing samples containing sufficient Fe were selected for analysis as reviewed in Raiswell et al. (2018). The sequential extraction scheme allowed for the chemical quantification of the following operationally defined and sequentially leached Fe phases: (1) Carbonate-bound Fe (siderite and ankerite) leached with sodium acetate for 48 hrs. (2) Oxide-bound Fe (goethite, hematite and akageneite) leached with sodium dithionite for 2 hrs; (3) magnetite Fe leached with ammonium oxalate for 6 hrs; (4) followed by boiling for 2 min in 12 M HCl to extract poorly reactive sheet silicates Fe or sheet silicates (e.g., chlorite, glauconite, biotite). (5) Pyrite Fe (Fe_{Py}) was obtained by chromium extraction; and (6) total bulk rock Fe (Fe_T) was measured together with minor, major and rare earth elements from solutions of bulk whole-rock powder dissolution with hydrofluoric acid (HF) as described in section 2.2.3. The composition of Fe in extracted solutions, except for Fe_T which was measured by ICP-OES as described previously, was quantified by the ferrozine method (Gibbs, 1976; Viollier et al., 2000; Husler et al., 2011). Redox trends were further constrained using the distribution of Fe/Al ratios across the studied section, where average ratios of ~0.55 ±0.11 are common for oxic waters, with much greater values for anoxic settings (Clarkson et al., 2014; Raiswell et al., 2018). Sediment Al/(Al+Fe+Mn) content was used to demonstrate that hydrothermal contribution (Boström et al., 1969; Boström, 1970; Boström et al., 1972; Boström et al., 1973; Pecoits et al., 2009; Chi Fru et al., 2024) of Fe to the sediments was negligible and that observed high Fe/Al ratios cannot be associated with hydrothermal activity. The Al/(Al+Fe+Mn) ratios have been shown to correlate geographically with submarine volcanic ridge activity and the distribution of pelagic seawater Al/(Al+Fe+Mn) ratios (Boström et al., 1969; Boström, 1970; Bender et al., 1971).

Chapter 3: Clay Mineral Geochemistry and Paleoenvironmental Reconstruction Across the Cryogenian Sturtian Snowball Glaciation

3.1 Introduction

Clay mineral assemblages preserved in ancient and modern sedimentary rocks are commonly used as proxies for paleo-environmental reconstructions due to their ability to record sediment and fluid histories during geological processes, including transport, deposition and post-depositional modification by diagenesis and metamorphism (Bristow et al., 2009; Ngombi-Pemba et al., 2014). While primary detrital clays are important tracers of provenance and pre-depositional sedimentary drivers (Baldermann et al., 2020), secondary diagenetic clays are excellent for tracking post-depositional changes associated with chemical, physical and fluid modification of the primary sediments (Baldermann et al., 2015; Isson and Planavsky, 2018; Isson & Rauzi, 2024). Further, detrital clays have been proposed as key vectors of bioessential nutrients to seawater (e.g., Hao et al., 2020; Hao et al., 2021a; Chi Fru et al., 2023), suggesting that marine sedimentary clay minerals may represent critical archives of past seawater nutrient budgets, with direct implications for reconstructing marine primary productivity, ocean-atmosphere oxygenation and climate perturbations (Hao et al., 2021a; Chi Fru et al., 2023; Krause et al., 2023).

Physical erosion of continental land mass by melting glaciers (Bland and Rolls, 2016) forms glacial till or tillites composed of grains of various sizes of the same mineralogical and chemical composition as the parent rocks. Chemical weathering on the other hand, which often correlates with the amount of CO_2 in the atmosphere and temperature (Isson et al., 2020; Kump et al., 2000; Krause et al., 2023), dissolves and transforms rock silicates

into more stable minerals like clays under surface conditions (Fedo et al., 1995), with the resulting chemical leaching producing Al-rich clays like kaolinite and gibbsite (Tosca et al., 2010). During this process, mobile alkali and alkaline earth metals such as Na, K, Ca and Mg as well as bioessential and redox-sensitive elements like P, Ni, Co, Cu, Mo, V, As and Cr are dissolved from the parent rock matrix to form soluble aqueous ions, while immobile elements like Al, Ti, Sc, Zr, Hf, Th, Y, and various REEs are retained in the solid parent residue (e.g., Tosca et al., 2010; Fedo et al.,1995).

Of particular relevance, the Neoproterozoic Earth witnessed major global glaciations that may have covered the Earth with kilometre-thick ice sheets from pole to pole (Hoffman et al., 1998, 2017). As the landmass is protected by a thick ice sheet cover from atmospheric agents of chemical weathering, such icy conditions that lasted millions of years are thought to severely curtail chemical weathering rates. Consequently, marine sediments deposited at this time are expected to contain weak CIA (chemical index of alternation) values relative to greenhouse intervals. This would also have affected the type of clay formation, nutrient supply to seawater and by extension redox variation and ocean-atmosphere oxygen content (Planavsky et al., 2010; Brocks et al., 2017; Fru et al., 2023). Gaining insights into Cryogenian clay mineralogy and geochemistry is therefore crucial for high-resolution reconstruction of a broad range of environmental processes in which the Cryogenian world operated, including deciphering proposed connections to post-glacial nutrient enrichment dynamics and relevance to the Neoproterozoic rise of atmospheric oxygen content and the emergence of metazoan life.

This chapter couples high–resolution clay mineralogy and geochemistry to interpret paleoenvironmental conditions across the Cryogenian Sturtian Snowball Earth. A detailed understanding of clay composition, mineralogy and abundance, coupled with geochemistry and formation mechanism, is investigated to explore principal pathways for nutrient supply

to seawater before, during, and after the Sturtian Snowball glaciation ~717 to 660 million years ago (Ma) (Hoffman et al., 1998, 2017).

3.2 Materials and Methods

The location, stratigraphy and lithologies of the studied samples in this chapter are listed in Figure 2.1 and Table 2.1. The mineralogical analysis was determined by XRD and SEM as outlined in section 2.2.1 and the bulk rock geochemical analysis described in section 2.2.3.

3.3 Results

3.3.1 Bulk- Rock Mineralogy

The bulk XRD mineralogical and SEM-EDS mineral data indicate that non-clay minerals across the sample set (i.e., pre-Snowball, Tillites, and post-Snowball lithologies) are mainly composed of different proportions of quartz, feldspar (K-feldspar and albite), muscovite, carbonate dolomite and calcite, while illite, kaolinite and chlorite constitute the main clay minerals identified in this study (Figures 3.1- 3.4 and Tables 3.1- 3.2). The framework detrital grains in the pre-Sturtian Snowball facies are composed primarily of poorly to moderately sorted subangular to subrounded >10 μm quartz and feldspar grains dispersed in a dominantly dolomite cement (Figure 3.1a and Figure 3.2a). The overlying tillites are dominated by poorly sorted fine-grained quartz, albite, and platy micaceous muscovite and biotite within the illicit matrix and Fe/Mg-rich dolomite cement, with occasional pore-filling framboidal to subhedral/euhedral pyrite crystals, together with Fe-rich clay minerals (Figure 3.1b, Figure 3.2b and Figure 3.3a-b). Disseminated magnetite grains are observed in a few of the mudstones up the section of the immediate post-Sturtian Snowball interval (Figure 3.1c, Figure 3.2c and Figure 3.3c-d).

Table 3.1| Qualitative mineralogical composition determined by XRD for representative samples. - = Not detected. + = Detected. BH and PS samples = Bonahaven Dolomite Formation. LL samples = Lossit Limestone Formation. PAT = Port Askaig Tillite Formation.

Locality	Quartz	Albite	Microcline	Hematite	Chlorite	Dolomite	Anorthite	Kaolinite	Muscovite	Magnetite	Calcite	Pyrite	Orthoclase
PS-16-00	+	-	-	-	-	-	-	-	+	-	-	-	-
PS-16-03	+	+	-	-	-	+	-	-	-	-	+	-	-
PS-16-05	+	-	+	-	-	+	-	-	+	-	-	+	-
PS-16-06	+	+	+	-	-	+	-	-	+	-	+	-	-
PS-16-09	+	+	-	-	-	+	-	-	+	-	+	-	+
PS-16-12	+		+	-	-	+	-	+	-	-	+	+	
BH-16-02	+	+	+	+	+	+	-	+	-	-	-	-	-
BH-16-03	+	+	+	+	-	+	-	-	+	-	-	-	-
PAT1	+	+	+	-	-	-	-	-	+	-	-	-	-
PAT2	+	+	-	-	+	+	-	-	+	-	-	+	-
PAT3	+	+	+	+	+	+	-	-	+	-	-	-	-
PAT4	+	+	+	-	+	+	-	-	+	-	-	-	-
LL-16-E1	+	-	+	+	+	+	-	-	+	+	-	-	-
LL-16-E2	+	-	-	-	-	+	-	+	-	-	-	-	-
LL-16-F	+	-	-	+	-	+	-	+	+	+	-	-	-
LL-16-D1	+	+	+	-	-	+	-	+	+	-	-	-	-
LL-16-D2	+	-	-	-	-	+	-	-	+	-	-	-	-
LL-16-G	+	+	+	-	-	-	+	-	+	-	+	-	-
LL-16-H	+	+	-	-	-	-	-	-	+	-	-	-	-
LL-16-I	+	+	-	-	-	+	-	-	+	-	-	-	-
LL-16-J1	+	-	-	-	-	+	-	-	-	-	+	-	-
LL-16-J2	+	-	-	-	-	+	-	-	-	-	-	-	-

Table 3.2| The bulk XRD quantitative mineralogical analysis (%) for the studied samples.

Location	Quartz	Dolomite	Albite	Microcline	Muscovite	Calcite	Magnetite	Hematite	Illite	Kaolinite
PS-16-00	87	0	2	0	11	0	0	0	0	0
PS-16-03	4	90	2	0	0	2	0	0	2	0
PS-16-05	70	27	0	0	3	0	0	0	0	0
PS-16-06	93	6	1	0	0	0	0	0	0	0
PS-16-09	6	87	4	0	0	3	0	0	0	0
PS-16-12	77	8	0	1	0	13	0	0	0	1
BH-16-02	85	0	4	0	8	0	0	1	0	1
BH-16-03	62	19	12	0	0	0	0	4	3	0
PAT1	71	0	15	13	1	0	0	0	0	0
PAT2	70	2	19	0	0	4	0	0	4	1
PAT3	71	23	2	0	3	0	0	0	0	1
PAT4	48	31	17	0	0	0	0	0	3	1
LL-16-d1	6	94	0	0	0	0	0	0	0	0
LL-16-d2	24	67	7	0	1	0	0	0	0	1
LL-16-e1	57	25	3	0	8	0	0	0	3	4
LL-16-e2	12	86	1	0	0	0	0	0	0	1
LL-16-f	75	9	5	0	0	0	0	5	5	1
LL-16-g	64	0	13	0	0	18	0	0	5	0
LL-16-h	81	0	13	0	0	0	0	0	6	0
LL-16-i	5	90	2	0	0	1	0	0	1	0
LL-16-j1	3	1	0	0	0	96	0	0	0	0
LL-16-j2	2	96	0	0	0	0	1	0	1	0

The upper part of the post-Sturtian Snowball (late post-Snowball) mudstones consists mainly of fine-grained quartz dispersed in illite and carbonate (calcite and dolomite) dominated matrix (Figures 3.1c-d and 3.2c- d). Hematite occurs in a few pre-/post-Snowball samples as well as trace amounts of magnetite (Figure 3.2c and Table 3.1). The bulk XRD data show that quartz is the dominant mineral in most of the samples. It is present across the whole section with concentrations varying from 2.0 to 93.0 wt.%, whereas feldspars (Na-/Ca-rich plagioclases and alkali feldspar minerals) and K-rich muscovite, although prevalent, are absent in some samples (Figure 3.4, Tables 3.1- 3.2).

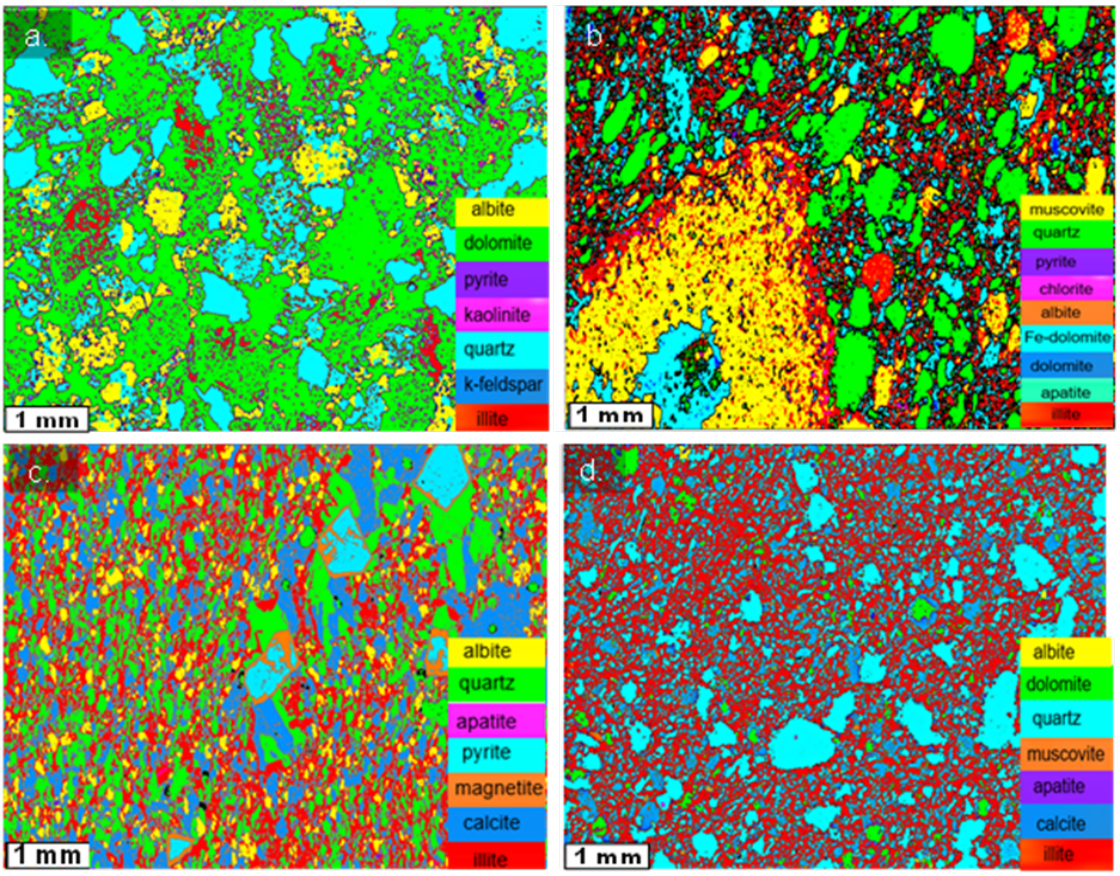

Figure 3.1| SEM-EDS mineral maps. a. pre-Snowball (LL-16-g). b. Tillite (LL-16-A2). c. Immediate post-Snowball (Bh-16-03). d. Late post-snowball (PS-16-05).

Sodium (Na) rich plagioclase (albite) is common across all three climatic intervals compared to Ca-rich plagioclase (anorthite) detected in only one pre-Snowball sample (Figure 3.1 and Table 3.1). A trace amount of microcline is the main alkali K-feldspar in most of the samples, while orthoclase was identified in one post-Snowball sample (Table 3.1). Muscovite, the

dominant platy micaceous mineral, is present across the studied section, with averages of 2.8 wt.%, 1.0 wt.% and 0.9 wt.% in the studied post-Snowball, tillite and pre-Snowball samples, respectively (Figs. 3.1-3.3a & Table 3.2), while biotite is common only in the tillite facies (Figure 3.2b).

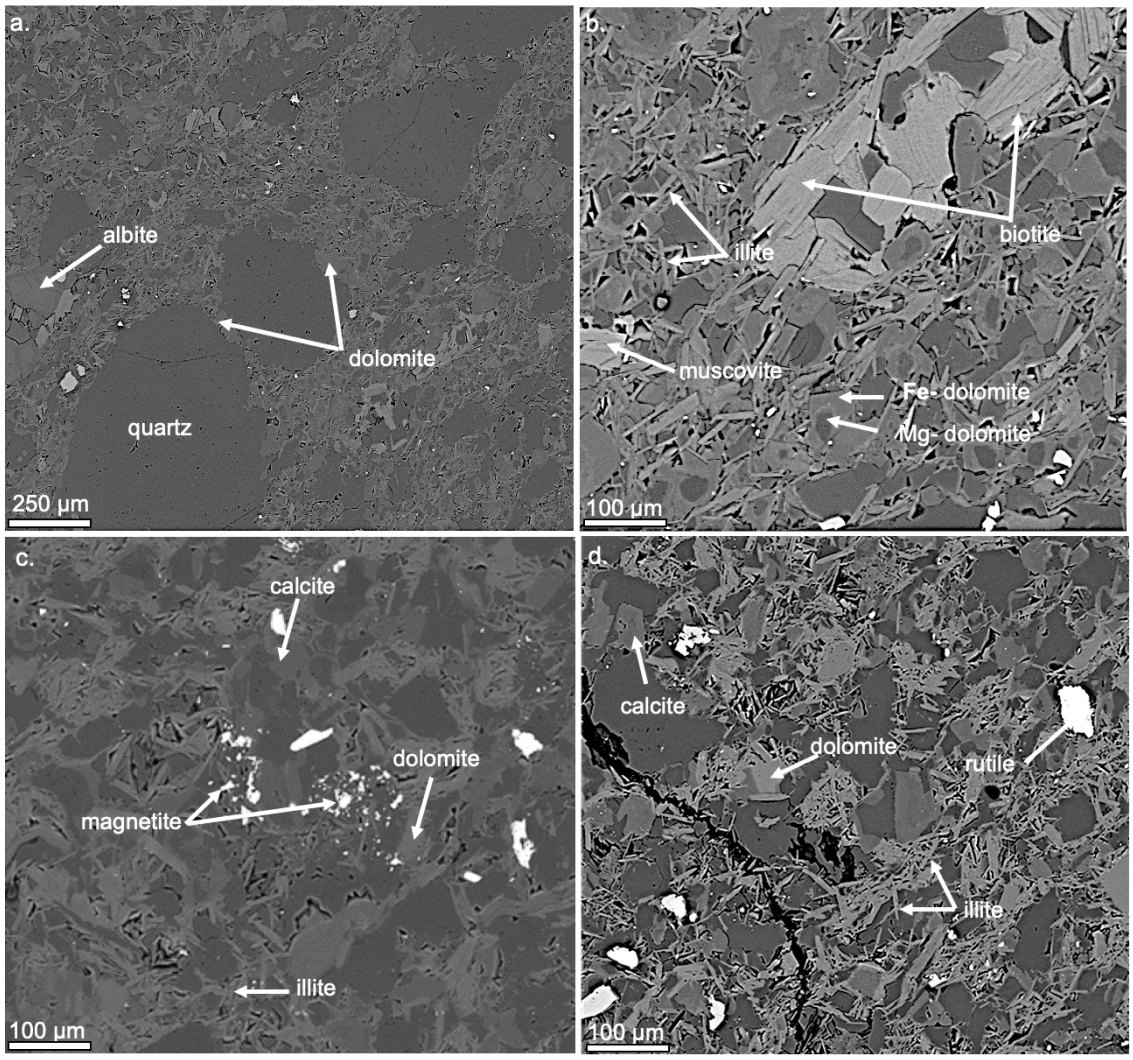

Figure 3.2| Representative BSE images. a. pre-Snowball (LL-16-g). b. Tillite (PAT3). c. Immediate post-Snowball (Bh-16-02). d. Late post-snowball (PS-16-05).

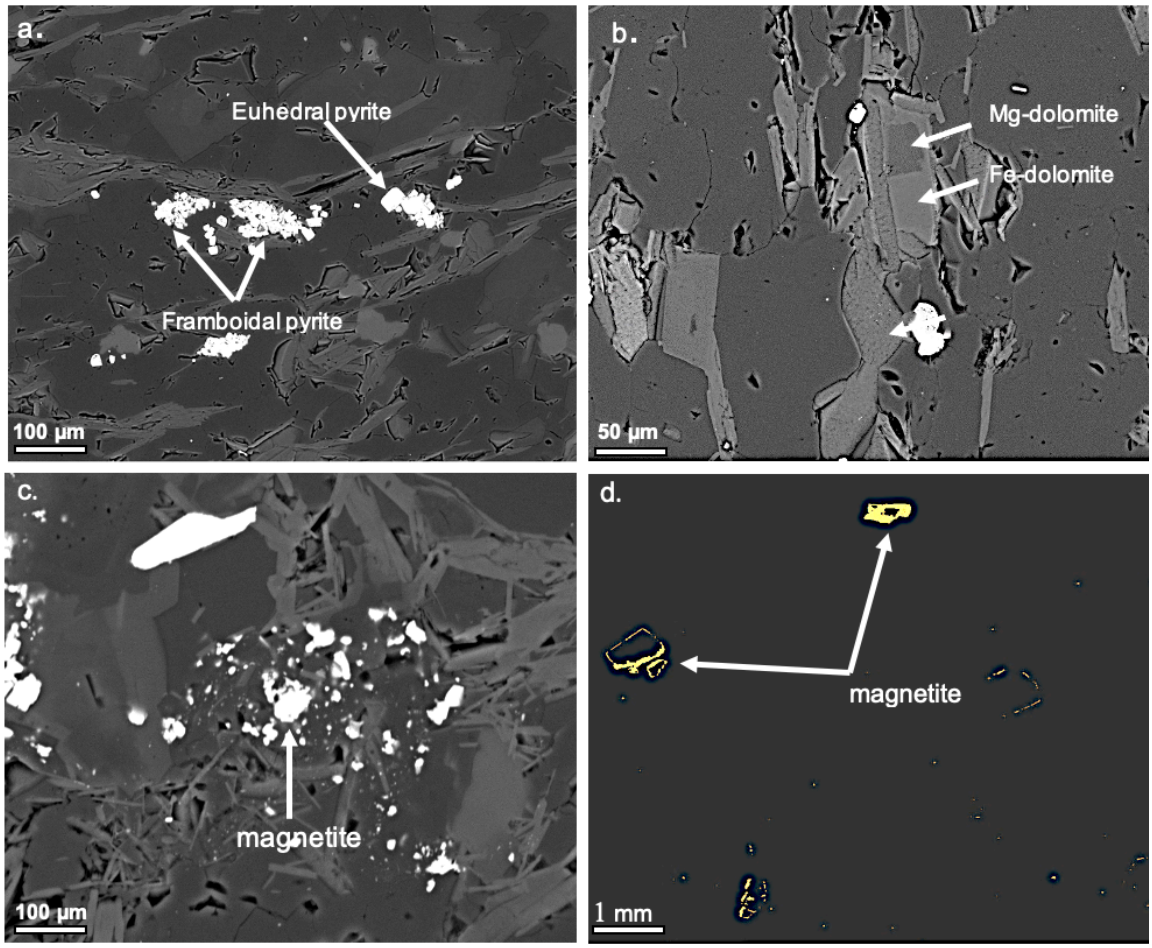

Figure 3.3| Backscatter (BSE) photomicrographs for representative samples. a. Pyrite grains in PAT1. b. Fe/Mg dolomite in PAT1. c. Magnetite grains in the immediate post-Sturtian Snowball sample Bh-16-03. d. SEM map shows magnetite (yellow colour) thin coatings around pyrite in the immediate post-Sturtian sample Bh-16-02.

Carbonate minerals, mostly present as dolomite and as calcite in a few instances (Figures 3.1 - 3.4), predominate the pre-Snowball and late post-Snowball successions compared to the immediate post-Snowball lithologies. The amount of carbonate minerals is significantly lower in the tillites compared to the overlying and underlying post-Snowball and pre-Snowball samples, respectively (Figures 3.1 and 3.4). Dolomite in the tillites is Fe/Mg-rich, with the Fe-rich variety being the most common, while EDS analysis shows that dolomite in the pre-Snowball and late post-Snowball successions is mainly non-ferroan (Figure 3.1b). Illite was observed in varying amounts across all three distinct climatic intervals with an

average of 0.63 wt.% (n = 8), 1.75 wt.% (n = 4), and 2.1 wt.% (n = 10) in the post-Snowball, tillite and pre-Snowball samples, respectively (Figure 3.4). Kaolinite makes up 0.25 wt.%, 0.75 wt.% and 0.7 wt.% of analysed post-Snowball, tillite and pre-Snowball samples, respectively (Figure 3.4 and Table 3.2). Combined, clay minerals constitute up to 3.7 wt.%, 3.5 wt.% and 3.7 wt.% in the post-Snowball, tillite, and pre-Snowball facies, respectively, which are significantly lower than the estimated global 8.6 wt.% inventory for the modern oceanic crust and sediments (Warr, 2022).

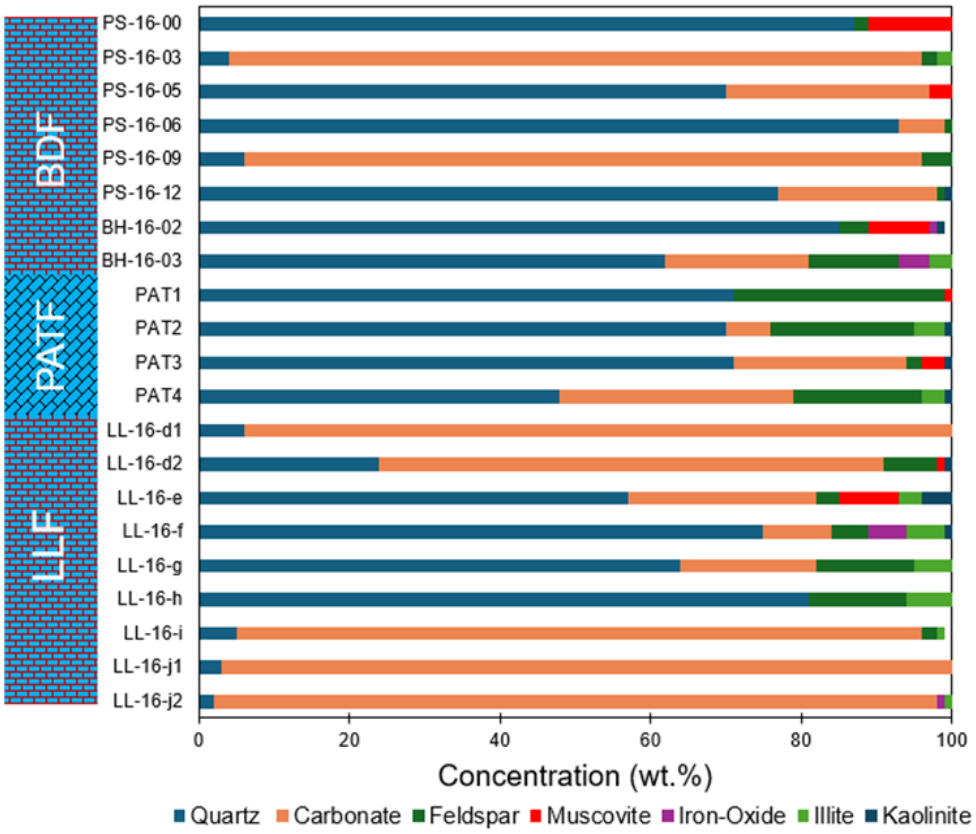

Figure 3.4| Semi-quantitative XRD bulk mineralogy of the analysed samples grouped into quartz, carbonates (dolomite and calcite), feldspars (K-feldspars and plagioclase), Fe-oxides, muscovite, and clay minerals (kaolinite, chlorite, illite).

3.3.2 Bulk Rock Geochemistry

Bulk SiO_2, Fe_2O_3, K_2O, MgO, CaO, P_2O_5 and MnO concentrations (Figure 3.5a-d and Tables 3.3 - 3.4), major elements considered essential to clay mineral formation and distribution, generally track average upper continental crust (UCC) trends (Figure A3.1).

Sustained enrichment of SiO_2, Fe_2O_3, K_2O and P_2O_5 in the tillite and immediate post-Snowball samples, is counterbalanced. By a persistent MgO and CaO decline across this interval (Figure 3.5c).

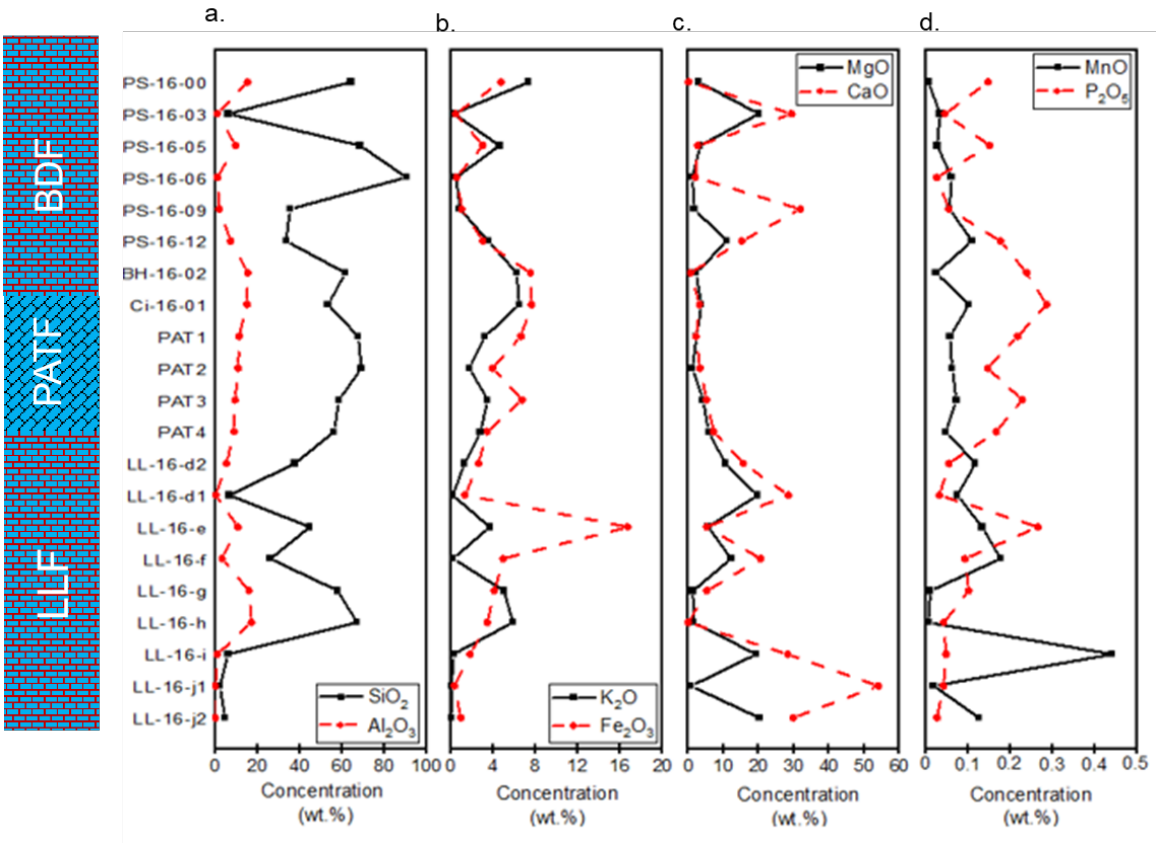

Figure 3.5| Variation of key major elements with sequence stratigraphy. a. SiO_2 and Al_2O_3. b. K_2O and Fe_2O_3. c. MgO and CaO. d. MnO and P_2O_5. See Tables 3.2 – 3.4 for detailed mineral and elemental evolution/distribution with stratigraphy.

The corresponding Ni, V, Cr and Co trace element concentrations display multiple peaks along the studied succession, recording sustained enrichment across the tillite-immediate post-Snowball interval (Figure 3.6a-b).

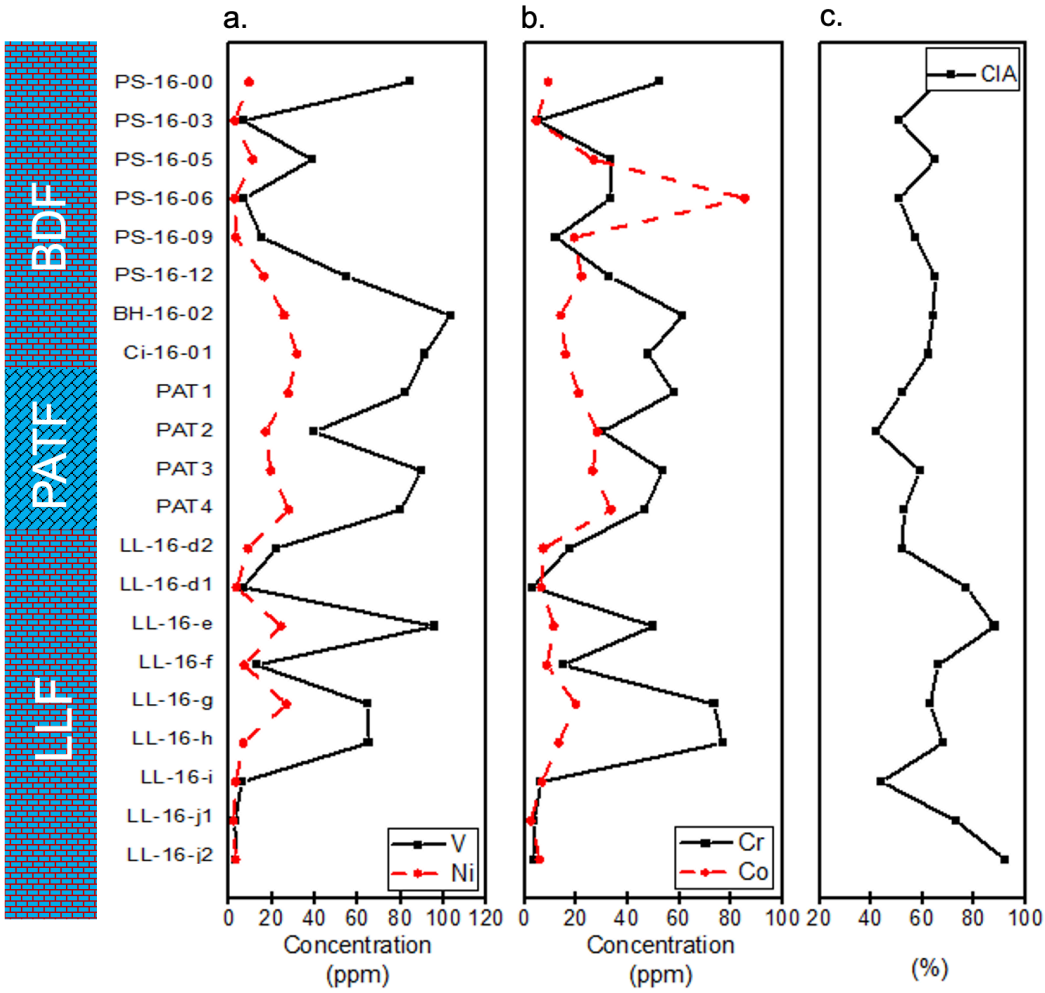

Figure 3.6| Variation of key trace with sequence stratigraphy. a.V and Ni. b. Cr and Co. c. CIA – chemical index of alteration. See Tables 3.2 – 3.4 for detailed mineral and elemental evolution/distribution with stratigraphy.

Comparative bivariate plots and Pearson correlation analysis indicate that Al_2O_3 correlates positively with SiO_2, Fe_2O_3, TiO_2, K_2O, Na_2O, P_2O_5, V, Ni and Cr and K_2O with V, Ni and Cr concentrations, suggesting the dominant control and supply of these elements by associated detrital silicate minerals (Figures 3.7-3.8 and Table A3.1), including clays, micas, and feldspars into the basin. However, MgO, CaO and MnO display negative correlations with Al_2O_3, indicating likely enrichment by the non-silicate carbonate minerals that are of a chemical rather than detrital origin. Bioessential V, Cr, Ni and Co display strong positive correlations with the detrital indicators TiO_2 and Al_2O_3, including Fe_2O_3 and negative correlations with MgO, CaO and MnO, especially for the pre-/late post-Snowball samples (Table A3.1).

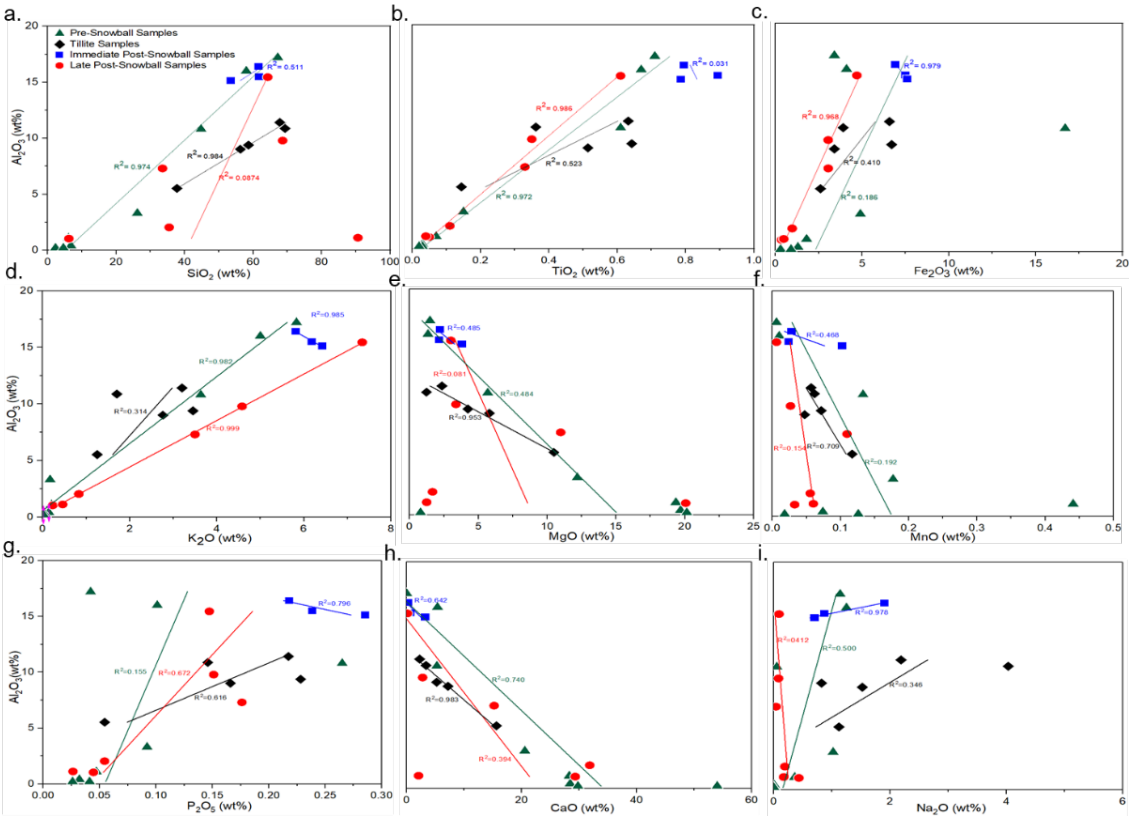

Figure 3.7| Major elements cross plots with Al_2O_3 content.

These bioessential and/or redox-sensitive trace metals also correlate positively with P_2O_5 in the pre-/late post-Snowball samples, except for Co in the late post-Snowball interval. Vanadium is positively correlated with TiO_2 and Fe_2O_3, Cr with Al_2O_3 and TiO_2 and Co with Al_2O_3 in the immediate post-Snowball samples. A weak positive correlation is observed for V and Ni, together with a strong negative correlation for Cr and Co with P_2O_5 in the immediate post-Snowball interval. In the tillites V and Ni, together with redox-sensitive Cr, are positively correlated with TiO_2 and Fe_2O_3. While Co is not correlated to these major elements in the tillites and with Al_2O_3, a stronger positive association is instead suggested with MgO and CaO (Table A3.1) and mainly V and Cr show a strong positive correlation with P_2O_5 in the tillites. Further, the strong Pearson linear correlation of these trace elements with K_2O in the pre-/late post-Snowball interval suggests a potential association with K-rich illitic phases as shown in Figure 3.8.

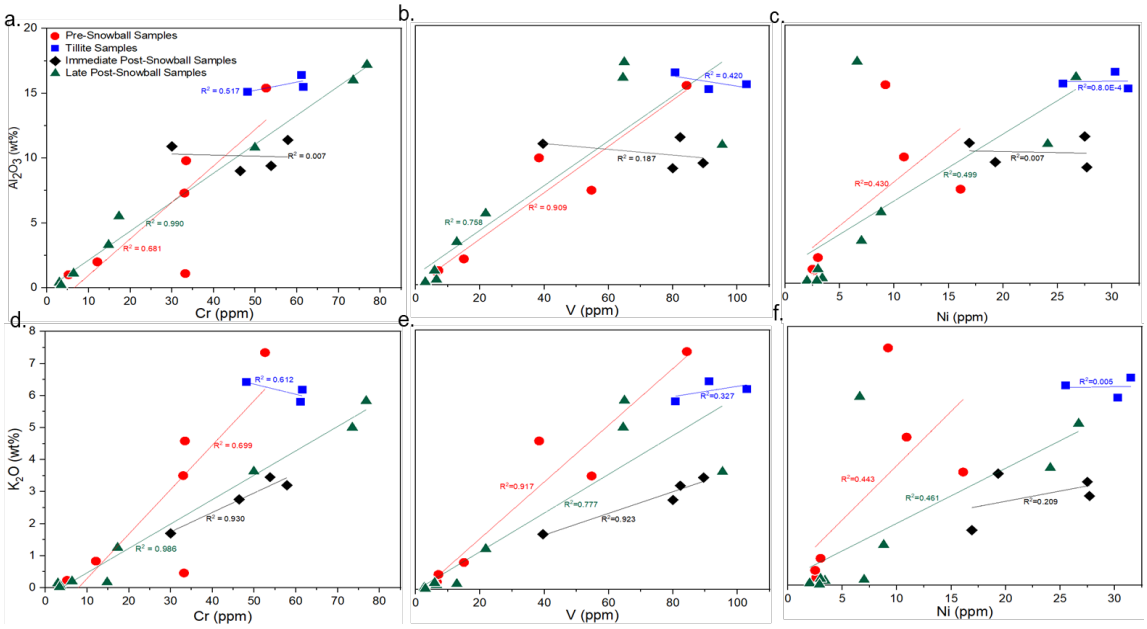

Figure 3.8| Trace elements (Cr, V and Ni) cross plots with Al_2O_3 and K_2O content.

The calculated CIA values for the studied samples range from 44-92, 42- 59, 62-64 and 51-66 for pre-Snowball, tillite, immediate post-Snowball and late post-Snowball intervals, respectively (Figures 3.6c &3.9 and Table 3.3).

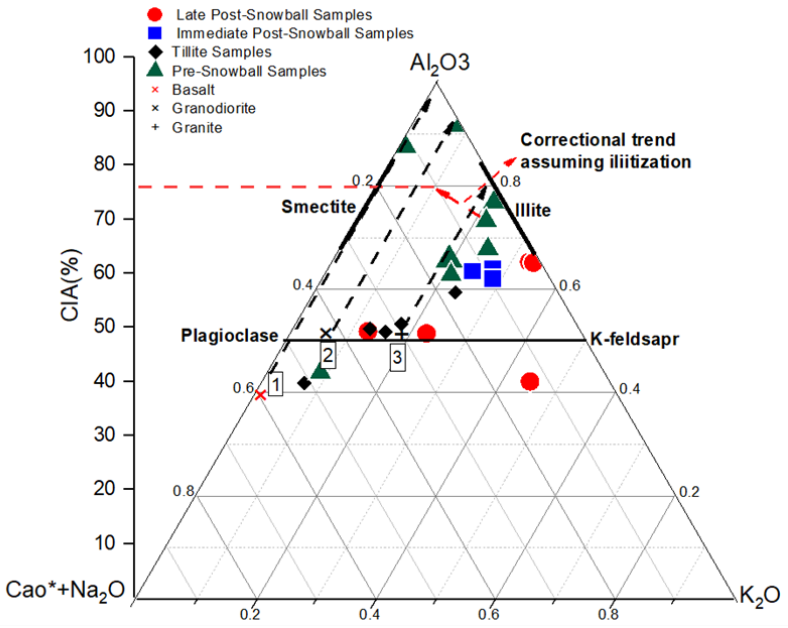

Figure 3.9| Ternary A-CN-K (Al_2O_3-CaO* + Na_2O-K_2O) diagram in molar proportions according to Nesbitt & Young (1984) for the studied samples. Data for basalt, granite, and granodiorite are from Condie (1993). The arrows 1, 2, and 3 indicate possible weathering trends for un-metasomatized basalt, granodiorite, and granite, respectively.

Table 3.3| The concentrations of major elements (wt.%) for the studied samples.

Samples	SiO_2	TiO_2	Al_2O_3	Fe_2O_3	MnO	MgO	CaO	Na_2O	K_2O	P_2O_5	LOI	CIA	Al_2O_3/TiO_2
PS-16-00	64.27	0.61	15.45	4.70	0.01	3.00	0.14	0.09	7.34	0.15	3.12	66.00	25.28
PS-16-03	6.21	0.05	1.03	0.35	0.03	20.07	29.33	0.43	0.23	0.05	43.10	51.00	20.62
PS-16-05	68.63	0.35	9.79	3.02	0.03	3.37	2.78	0.08	4.58	0.15	6.04	65.00	27.61
PS-16-06	90.60	0.04	1.14	0.48	0.06	1.24	2.06	0.17	0.46	0.03	3.12	51.00	25.53
PS-16-09	9.73	0.08	1.58	0.16	0.07	17.16	27.43	0.19	0.83	0.05	25.03	57.00	19.10
PS-16-12	33.55	0.33	7.30	3.05	0.11	10.98	15.22	0.04	3.50	0.18	24.32	65.00	22.36
BH-16-02	61.68	0.89	15.49	7.46	0.02	2.14	0.66	0.87	6.18	0.24	3.6	64.00	17.41
BH-16-03	53.48	0.79	15.13	7.64	0.10	3.80	3.21	0.70	6.42	0.29	7.37	62.00	19.23
Ci-16-01	61.62	0.79	16.41	6.95	0.03	2.20	0.25	1.90	5.81	0.22	2.84	63.00	20.64
PAT1	67.75	0.63	11.42	6.57	0.06	2.34	2.23	2.19	3.35	0.22	3.53	52.00	18.10
PAT2	69.28	0.36	10.87	3.85	0.06	1.23	3.35	4.03	1.70	0.15	3.87	42.00	30.03
PAT3	58.66	0.64	9.38	6.74	0.07	4.23	5.20	0.82	3.45	0.23	9.35	59.00	14.60
PAT4	56.27	0.51	9.01	3.41	0.05	5.80	7.20	1.52	2.76	0.17	12.5	53.00	17.52
LL-16-D2	37.85	0.14	5.52	2.56	0.12	10.49	15.59	1.12	1.25	0.05	24.76	52.00	39.30
LL-16-D1	6.85	0.03	0.42	1.30	0.07	19.69	28.43	0.01	0.14	0.03	43.33	77.00	13.33
LL-16-E	44.77	0.61	10.8	16.7	0.13	5.68	5.25	0.05	3.63	0.27	10.85	88.00	17.64
LL-16-F	26.23	0.15	3.33	4.90	0.18	12.19	20.54	1.02	0.17	0.09	31.29	66.00	21.84
LL-16-G	57.18	0.67	16.04	4.11	0.01	1.34	5.36	1.25	5.00	0.10	7.23	63.00	24.01
LL-16-H	67.18	0.71	17.20	3.42	0.01	1.48	0.01	1.14	5.83	0.04	2.87	68.00	24.20
LL-16-I	6.11	0.07	1.08	1.79	0.44	19.35	28.29	0.36	0.20	0.05	42.68	44.00	14.71
LL-16-J1	2.29	0.03	0.24	0.25	0.02	0.80	54.01	0	0.06	0.04	42.53	73.00	8.23
LL-16-J2	4.57	0.02	0.24	0.93	0.13	20.14	29.79	0	0.02	0.03	44.59	92.00	10.05

Table 3.4| The concentrations of trace and rare earth elements (ppm) for the studied samples across Sturtian Snowball.

Samples	Sr	Ba	Sc	V	Cr	Co	Ni	Y	Zr	Nb	La	Ce	Nd	Sm	Eu	Gd	Dy	Er	Yb	Th	Th/Sc	Zr/Sc
PS-16-00	6.19	423.60	12.48	84.30	52.59	52.59	9.17	21.42	173.28	21.87	39.16	79.71	36.61	6.43	1.19	5.10	3.77	1.86	2.46	10.03	0.80	13.90
PS-16-03	255.01	54.29	0.82	6.64	5.16	5.16	2.62	4.87	11.97	0.33	3.58	7.44	3.72	0.99	0.20	0.49	0.84	0.68	0.39	1.06	1.45	15.49
PS-16-05	31.27	505.17	5.55	38.38	33.37	33.37	10.90	15.47	163.13	7.90	17.67	38.08	17.68	3.40	0.62	2.98	2.39	1.58	1.56	5.68	1.09	29.37
PS-16-06	27.36	538.72	0.73	7.08	33.21	33.21	2.48	3.63	18.82	1.03	5.15	10.52	4.76	0.80	0.28	0.70	0.61	0.15	0.27	0.79	1.09	25.83
PS-16-09	314.52	219.80	1.21	15.51	8.68	8.68	3.62	10.15	34.68	2.40	5.29	12.65	5.12	1.25	0.37	1.49	1.68	1.31	0.77	1.57	1.30	28.73
PS-16-12	116.32	249.41	5.81	54.66	33.04	33.04	16.08	21.30	94.08	7.29	12.23	25.11	13.18	3.06	0.63	3.25	3.44	2.10	1.85	5.14	0.88	16.22
BH-16-02	71.65	449.30	14.41	102.89	61.52	61.52	25.53	36.93	255.69	28.76	54.49	114.91	54.75	10.70	1.66	7.66	6.40	3.50	3.90	17.81	1.24	17.74
BH-16-02	79.66	383.35	16.27	91.22	48.12	48.12	31.49	34.36	205.19	25.72	27.14	57.25	26.73	5.27	1.01	5.71	5.65	3.08	3.54	13.98	0.88	12.60
Ci-16-01	38.76	669.53	14.69	80.78	61.09	61.09	30.30	18.96	181.46	22.64	18.51	76.84	19.45	4.25	0.70	4.23	3.78	1.60	2.23	21.91	1.49	12.35
PAT1	113.75	512.43	11.08	82.33	57.80	57.80	27.51	19.42	153.64	15.19	21.19	44.32	18.82	3.71	0.69	2.82	2.33	1.10	1.35	7.01	0.63	13.87
PAT2	176.49	292.61	6.68	39.58	30.04	30.04	16.86	24.21	132.85	10.62	21.39	45.21	20.29	4.36	0.81	4.24	3.93	2.20	2.80	24.18	3.62	19.98
PAT3	112.97	511.24	11.04	89.52	53.84	53.84	19.33	14.92	120.69	13.03	12.96	28.34	14.26	2.58	0.70	2.81	2.60	1.73	1.65	3.48	0.31	10.93
PAT4	157.25	458.69	9.12	80.03	46.45	46.45	27.75	15.49	129.98	9.14	17.56	37.13	16.46	3.58	0.65	3.09	2.41	1.67	1.75	5.38	0.58	14.24
LL-16-D2	436.27	192.77	3.48	21.76	17.34	17.34	8.79	9.77	37.24	1.82	6.11	11.54	7.18	1.55	0.33	1.47	1.36	1.19	0.99	1.94	0.59	10.70
LL-16-D1	308.26	14.73	0.29	6.50	3.03	3.03	3.37	2.53	7.77	0.44	2.09	4.13	2.70	1.00	0.07	0.44	0.34	0.36	0.17	0.21	0.72	26.87
LL-16-E	249.41	478.54	13.46	95.37	49.85	49.85	24.07	17.48	110.37	10.97	19.43	38.87	20.19	3.91	0.83	3.61	3.12	1.95	1.96	5.31	0.39	8.20
LL-16-F	924.18	67.39	5.19	12.75	14.76	14.76	6.98	16.97	32.36	3.22	7.52	19.77	10.88	2.24	0.56	2.67	2.72	1.52	1.52	2.29	0.44	6.23
LL-16-G	66.86	404.95	11.41	64.49	73.52	73.52	26.69	10.47	171.12	13.37	17.27	33.43	16.23	2.80	0.29	2.25	1.86	1.23	1.54	9.83	0.86	15.99
LL-16-H	37.19	768.19	13.14	64.89	76.81	76.81	6.59	14.88	195.23	18.58	48.72	99.04	49.01	9.12	1.65	6.48	3.14	1.35	1.77	12.73	0.97	14.85
LL-16-I	277.07	50.23	0.96	5.89	6.45	6.45	3.01	7.92	33.70	1.08	5.92	13.17	6.23	1.37	0.11	1.09	1.17	0.30	0.64	2.16	2.25	35.21
LL-16-J1	2387.20	7.32	0.40	2.70	3.57	3.57	1.97	2.58	2.40	0.09	2.08	6.32	1.55	0.23	0.02	0.39	0.30	0.31	0.15	0.32	0.75	6.00
LL-16-J2	330.25	0.00	0.13	3.05	3.44	3.44	2.88	9.79	2.41	0.31	3.55	9.09	4.67	0.88	0.10	1.32	1.51	0.56	0.84	1.41	10.97	18.70

3.3.3 Clay Mineralogy and Chemistry

SEM-EDS and XRD analysis of the < 2 μm clay-sized fractions corroborate the bulk XRD analysis, showing illite, chlorite and kaolinite as the main clay minerals in the studied samples (Figures 3.10-3.11 & Table 3.5). Our SEM results demonstrate a persistent occurrence of detrital and authigenic clay minerals formed mainly by a diagenetic transformation of detrital minerals in the studied samples (Figures 3.11). Minor neoformed authigenic clays precipitated either directly from seawater or porewater, were detected for some clay minerals such as kaolinite (Figures 3.11g). Illite, identified by its characteristic basal 9.97 Å (001) and 4.99 Å (002) peaks is unaffected by ethylene glycol treatment (Figure 3.10). The symmetrical and Gaussian shape of the peaks in both the air-dried and ethylene glycol treatment indicate the dominance of well-crystallised illite and the absence of smectite and illite-smectite mixed layers in the samples (Figure 3.10).

The characterized detrital and diagenetic clay minerals, together with their EDS spectra are shown in Figures 3.11 - 3.12. These observations show that illite is present either as pore filling or diagenetic replacement of detrital muscovite and K-feldspar grains (Figure 3.11). Particularly, the occurrence of flaky and well-crystallised tiny micaceous materials points to the presence of detrital illite in the samples (Figure 3.11). These well-crystallised illitic minerals have well-defined boundaries and elongated crystal shapes with no preferred direction or orientation (Figure 3.11e). The detrital illite phase is marked by a distinct higher enrichment of Al compared to the authigenic illite phase (Table 3.6) and they all fall in the illite field on the 4Si-M^{+}-R^{2+} chemographic projection (Figure 3.13a).

Chlorite is identified by its characteristic 14.2Å (001), 7.10Å (002), 4.74Å (003), and 3.55Å (004) peaks, which are equally unaffected by ethylene glycol treatment (Figure 3.10). Chlorite is observed mainly in both the glaciogenic tillites at the top of the LLF and the

overlying PATF in the tillite succession (Figure 3.10b). The higher intensities of the even 002 and 004 peaks compared to the odd 001 and 003 peaks (Figure 3.10b) suggest the dominance of Fe(II)-rich chlorites (Moore and Reynolds, 1989) in the tillites. Chlorites are present mainly in the tillite samples filling the pore spaces and along the cleavages of biotite as a pseudomorphic replacement mineral as well as well-crystallised discrete detrital particles with well-defined boundaries dispersed within the matrix (Figure 3.11f).

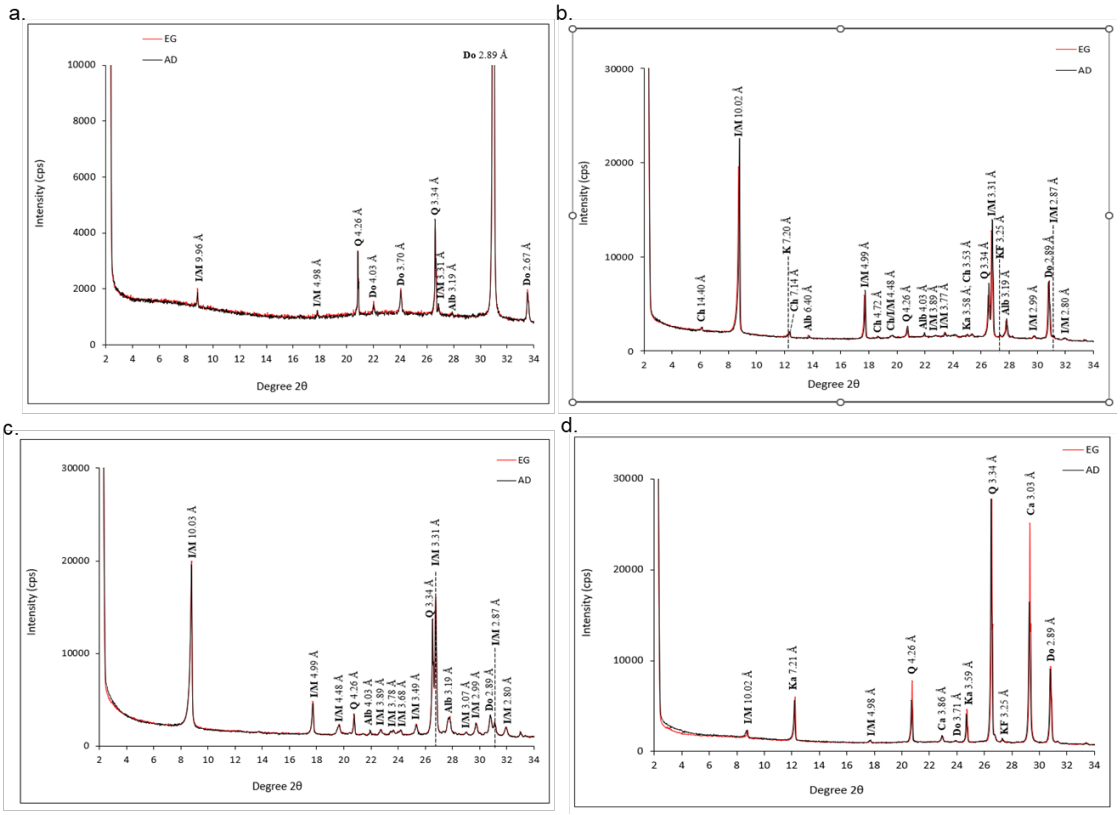

Figure 3.10| XRD patterns of the air-dried (black) and glycolated (red) for the studied samples. a. Pre-Snowball (LL-16-d). b. Tillite sample (PAT3). c. Immediate post-Snowball (BH-16-03). d. post-Snowball sample (PS-16-12). Q, Quartz; M, Muscovite; Alb, Albite; Do, Dolomite; KF, K-felspar; Ch, Chlorite; K, Kaolinite; Py, Pyrite; I/M, Illite/Muscovite; Ch/I/M, Chlorite/Illite/Muscovite.

EDS point chemical analyses show that the pore filling, grain replacement, and detrital chlorites are Fe-rich and have a similar composition with Fe/(Fe+Mg) ratios >0.3 (Figure 3.13b) and they all plot in the chlorite field on the $4Si\text{-}M^{+}\text{-}R^{2+}$ chemographic projection (Figure 3.13a; Meunier and Velde, 2004). Kaolinite was identified by its 7.16Å (001) and 3.58Å (002) peaks that were also unaffected by ethylene glycol treatment (Figure 3.10).

Kaolinite sparsely occurs in some of the PATF tillites overlying the LLF; however, it is more common in the pre-Snowball and post-Snowball lithologies (Figure 3.4), defined by its booklet morphologies and EDS spectra, filling both primary and secondary pores of dissolving detrital grains (Figures 3.11g).

Table 3.5| XRD result of extracted clay mineral fraction. I/M= illite/ muscovite, Ch/I/M = chlorite/illite/muscovite, Ka/I/M= Kaolinite/illite/muscovite, - = not detected and + = detected.

Locality	Chlorite	kaolinite	I/M	Ch/I/M	Ka/I/M
PS-16-00	-	-	+	-	-
PS-16-03	-	-	+	-	-
PS-16-05	-	+	+	-	+
PS-16-06	-	-	+	-	-
PS-16-09	-	-	+	-	-
PS-16-12	-	+	+	-	-
BH-16-02	-	+	+	-	-
BH-16-03	-	-	+	-	-
PAT1	-	-	+	-	-
PAT2	+	-	+	-	-
PAT3	+	+	+	+	-
PAT4	+	+	+	+	-
LL-16-e1	+	-	+	+	-
LL-16-e2	-	+	-	-	-
LL-16-f	-	+	+	+	-
LL-16-d1	-	+	+	-	-
LL-16-d2	-	-	+	-	-
LL-16-g	-	-	+	-	-
LL-16-h	-	-	+	-	-
LL-16-i	-	-	+	-	-
LL-16-j1	-	-	+	-	-
LL-16-j2	-	-	-	-	-

Table 3.6| EDS spot chemical composition for some SEM illite and chlorite spectra.

Spectra							
Illite							
SiO_2	24.42	27.42	24.70	23.66	26.60	24.66	24.38
Al_2O_3	13.57	12.26	13.43	14.68	12.04	13.81	14.41
FeO	4.56	4.18	5.31	5.01	5.16	5.17	4.82
MgO	2.16	1.41	1.90	1.66	1.86	1.90	1.87
K_2O	9.29	8.04	9.25	9.75	8.34	8.83	8.78
Na_2O	0.06	0.02	0	0.02	0	0	0
CaO	0.08	0	0	0	0	0	0
Structural formulae on the basis of 11 oxygens							
Si	3.72	3.72	3.44	3.31	3.65	3.42	3.37
Al(IV)	0.28	0.28	0.56	0.69	0.35	0.58	0.63
Al(VI)	1.45	1.45	1.38	1.45	1.37	1.41	1.45
Fe	0.29	0.29	0.37	0.35	0.36	0.36	0.34
Mg	0.22	0.22	0.31	0.27	0.29	0.30	0.30
Ti	0.03	0.03	0.03	0.03	0.03	0.03	0.04
K	0.78	0.78	0.93	0.93	0.82	0.88	0.87
Interlayer	0.96	0.81	0.93	1.00	0.82	0.88	0.87
Chlorite							
SiO_2	14.50	14.11	14.37	16.09	14.28	16.27	15.19
Al_2O_3	11.95	12.26	12.22	11.43	12.06	11.95	11.84
FeO	20.69	21.38	19.92	20.33	20.03	18.85	19.64
MgO	11.83	11.55	11.05	10.01	11.97	10.33	10.67
K_2O	0.12	0	0.41	1.04	0.08	0.42	0.77
Structural formulae on the basis of 14 oxygens							
Si	2.83	2.76	2.81	3.12	2.97	3.11	2.96
Al(IV)	1.17	1.24	1.19	0.88	1.21	0.89	1.04
Al(VI)	1.25	1.27	1.30	1.43	1.23	1.49	1.35
Fe	2.03	2.11	1.96	1.98	1.97	1.81	1.92
Mg	2.67	2.61	2.50	2.24	2.70	2.28	2.40
Ti	0.00	0.00	0.01	0	0	0.01	0.01
K	0.02	0.00	0.06	0.14	0.01	0.06	0.11
Interlayer	0.02	0.00	0.09	0.14	0.03	0.10	0.13
Fe/Fe+Mg	0.43	0.44	0.44	0.42	0.42	0.44	0.44

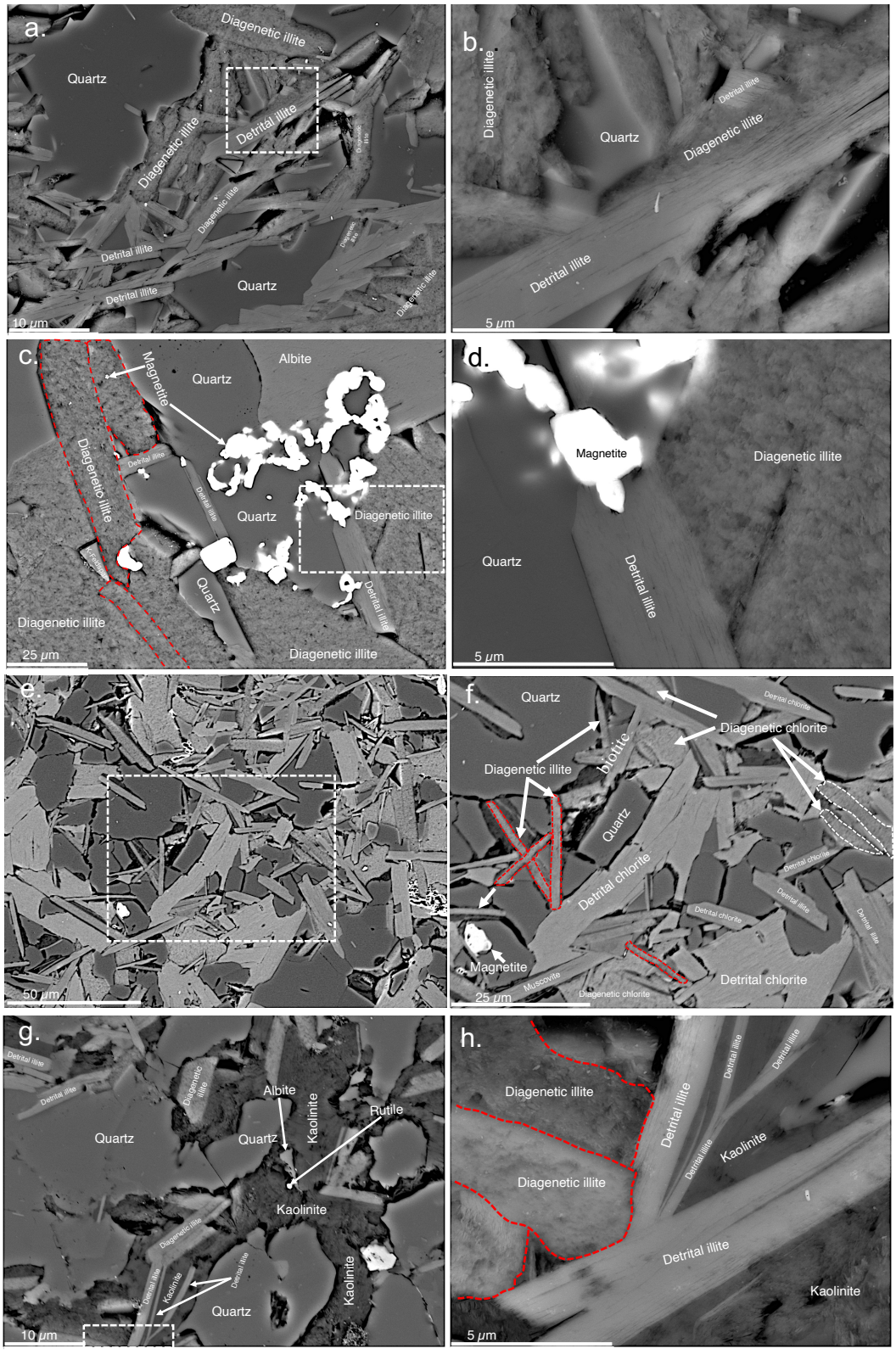

Figure 3.11| Backscatter (BSE) photomicrographs showing exemplary mineral phases across the studied sequence. a-b. Late post-Snowball (PS-16-00). c-d. Early post-Snowball. e-f. Tillites (PAT3); g-h. pre-Snowball (LL-16-d). White dotted lines in panels a, c, e and g show selected areas amplified in panels b, c, f and h to show specific details of key clay mineral phases. Red dotted lines show distinct boundaries of primary mineral phases that have been diagenetically transformed into secondary clay minerals.

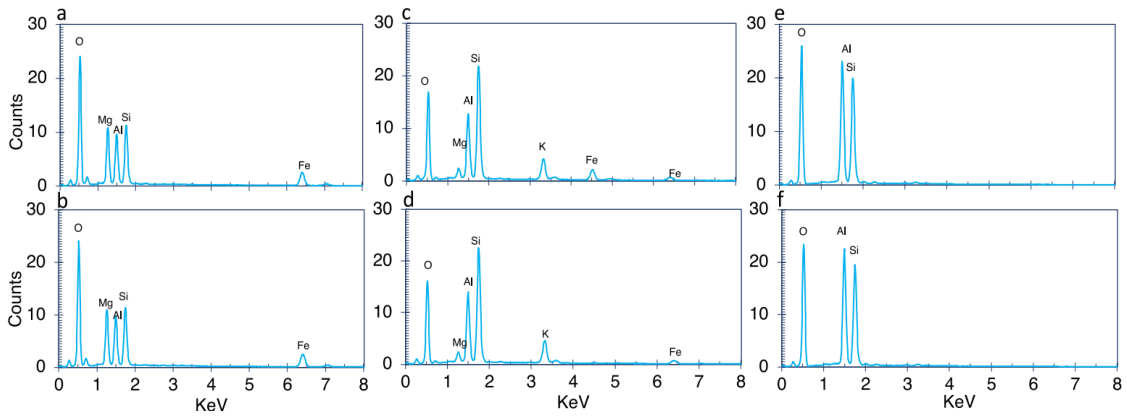

Figure 3.12| Examples of SEM-EDS spectra of chlorite, illite and kaolinite clay minerals. a. Detrital chlorite. b. Diagenetic chlorite. c, Detrital illite. d. Diagenetic illite. e. Detrital kaolinite. f. Diagenetic Kaolinite. Chlorite and illite spectra – sample PAT3. Kaolinite spectra -sample LL-16-d.

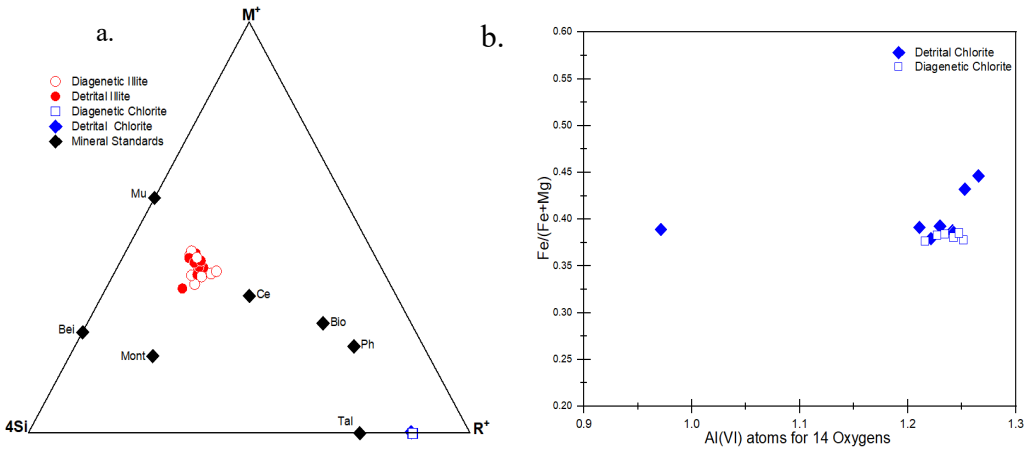

Figure 3.13| a. Chemographic projection of illite and chlorite chemistry on the 4Si-M+-R2 ternary diagram (Meunier and Velde, 2004). b. Co-variation of octahedral Fe/(Fe+Mg) index and Al(VI) cations of chlorites (Velde, 1985). Mu- muscovite, Bei – beidellite, Mont – montmorillonite, Ce-celadonite, Ch-chlorite, Ph-phengite, Bio-biotite.

3.4 Discussion

3.4.1 Post-Depositional Mineral Alteration and Preservation of Primary Signatures

Geological marine records are usually more or less altered during post-burial diagenesis and metamorphism, requiring an assessment of these effects on primary sedimentary signals

before any information about paleoenvironment or paleoclimate conditions can be deduced from such data, especially in the clay-fraction assemblage (Thiry, 2000). The use of clay minerals as paleoclimatic and provenance proxies is based on the assumption that they are conservatively delivered into the basin without undergoing any significant modifications after deposition. However, the change in the physico-chemical conditions, temperature, pressure, and other kinetically controlled processes immediately after sediment deposition may trigger chemical, structural, and physical changes in detrital clay minerals and pseudomorphic or direct recrystallization of new ones during sediment burial. The abundance of detrital framework grains and micaceous minerals indicates the samples analysed in this study are largely composed of continental detritus (Figures 3.1-3.4 and Figure 3.11). However, the presence of dissolving detrital minerals (e.g., feldspars), filling of primary and secondary pores by authigenic carbonates and diagenetic clay minerals (Figures 3.1 & 3.11), and pseudomorphic replacements of muscovite and biotite along their cleavages by illite and chlorite, respectively (Figure 3.11), demonstrate that the sediments have undergone some degree of post-depositional diagenetic modifications.

The occurrence of pyrite in the tillite and post-Sturtian samples is associated with high continental silicate weathering, which drives up the concentration of (Fe^{2+}) ferrous Fe (Parnell and Boyce, 2017). When combined with sulphide produced by the metabolic respiration of sulphate by the sulphate-reducing microorganisms, dissolved ferrous Fe is transformed to pyrite in anoxic bottom waters/sediment pore water settings (Hoffman et al., 2017; Parnell and Boyce, 2017; Wei et al., 2020). Therefore, the observed framboidal pyrite grains in the tillite samples are probably an early diagenetic mineral phase. Pyrite framboids (Figure 3.3a) precipitate when both dissolved Fe^{2+} and Fe mono-sulphides are supersaturated in pore waters, while euhedral pyrite (Figure 3.3a) is formed in pyrite oversaturated and Fe monosulphide undersaturated pore waters, during early diagenesis (Rickard 1997; Roberts

and Turner 1993). The overgrowth of magnetite grains in some instances on pyrite grains suggests that in some cases, diagenetic magnetite formed from the oxidative weathering of pre-existing pyrite grains (Figure 3.2c). Iron-rich and Fe-poor (non-ferroan) dolomite cement, a common feature in Neoproterozoic sedimentary deposits (Hood et al., 2011), occurs locally as rhombic crystals (Figure 3.3b) in primary pore spaces, indicating that they precipitated directly from seawater and/or pore water fluids. Contact with meteoric water may lead to the dissolution and re-precipitation of secondary Fe-rich dolomite carbonate phases (Stern and Miller, 2021).

However, the bulk composition of dolomite in our samples is Fe-poor with subordinate Fe-rich dolomite observed in a few cases. The non-ferroan dolomite is thus suggested to pre-date the Fe-rich equivalent. During deglaciation, intense weathering of lithogenic silicates, by up to ~350 times more carbon dioxide present in the atmosphere at the end of Snowball Earth glaciations (Fabre and Berger, 2012; Huang et al., 2016), would have promoted the rapid precipitation of carbonate minerals in the post-Sturtian Snowball ocean (Fairchild and Spiro, 1990; Hoffman et al., 2017). This is depicted in the sedimentary record as cap carbonates (Hood et al., 2021) that usually overly the tillites formed during the deglaciating phase. In Scotland, although present, the carbonate content in the immediate post-Sturtian Snowball is sparse before intensifying up section. Recently, it was revealed, that siliciclastic deposits overly Sturtian Snowball tillites, are indicative of post-Snowball intense chemical weathering of continental rocks resulting in marine precipitation of quartz (Zhu et al., 2024). Similarly, the immediate post-Snowball samples investigated in this study are dominated by quartz, with a distinct subordinate carbonate content (Figure 3.4). The low carbonate versus high quartz concentration in the immediate post-Snowball interval is therefore likely coupled to increased continental silicate weathering leading first in preferential quartz

precipitation (Zhu et al., 2023), before switching to enhanced marine carbonate deposition up sequence.

There are multiple interpretations regarding the origin of these dolomite, reflecting the complex interplay of depositional and early diagenetic processes. Although precise timing of dolomitization remains difficult to constrain, the widespread pore-filling nature of dolomite and its occurrence between detrital grains strongly suggest early diagenetic precipitation directly from seawater**,** as supported by Tucker (1982). This interpretation aligns with broader models proposing that dolomite in Precambrian sedimentary successions predominantly formed through primary marine dolomitization (e.g., Hood and Wallace, 2014; Shuster et al., 2018). Fairchild (1980) further proposed that dolomite in the Bonahaven Formation formed under conditions of fluctuating salinity and seasonal variations in algal productivity**,** with microbial mediation particularly evident in stromatolitic horizons**,** suggesting a biologically influenced early diagenetic origin. Supporting this, the co-occurrence of dolomite with clay minerals and the preservation of fine-scale sedimentary textures could indicate that dolomitization was likely abiotic**,** rather than the result of deep burial alteration (Fairchild, 1998; Liu et al., 2019). Additionally, the presence of Fe-rich dolomite in glacially influenced units such as the Port Askaig Formation has been interpreted as authigenic**,** possibly forming during deglaciation from Fe^{2+} remobilized from minerals like biotite or introduced by glacial erosion of Fe-bearing bedrock (Spence, Le Heron, and Fairchild, 2016; Bhatia et al., 2013; Hawkings et al., 2014, 2016, 2020). This model is consistent with modern analogues from glaciated polar regions, where melting ice sheets deliver Fe- and phosphate-rich detritus to coastal marine systems, influencing mineral precipitation and nutrient dynamics (Hopwood et al., 2014; Hodson et al., 2017; Chi Fru et al., 2023). Taken together, these lines of evidence support an interpretation of the Bonahaven Formation dolomite as forming through early, potentially microbially influenced or abiotic

precipitation**,** driven by local geochemical conditions within a shallow, semi-restricted marine setting, rather than through late-stage diagenetic processes.

Clay minerals are the products of weathering and soil formation processes, and are strongly associated with biological activity, but with less contribution from soil and biological activity during Precambrian times because of limited land colonisation by life. It is therefore thought that in modern soils, life is central to clay mineral production through promoting weathering, the elevation of ionic pore water fluid chemistry, enhancement of soil water retention capacity and the production of organic acids and chelating ligands (Rafiei and Kennedy, 2019; Singer, 1980). Consequently, the main composition of Neoproterozoic clay minerals is believed to have derived primarily from the physical and chemical weathering of primary rock minerals, as opposed to a significant contribution by soils (Kennedy et al., 2006; Wei et al., 2024). For example, even in the absence of strong biological processes involved in clay mineral production on land, variable quantities of detrital and diagenetic clay minerals dominated mostly by illite, illite/smectite [I/S] and chlorite, have been reported for Paleoproterozoic marine shales (Baruch et al., 2015).

Clay mineral texture and relationships with detrital grains, crystal shapes, primary and secondary pore space-filling and replacement of detrital grains, reflect a mixture of abundant detrital and subordinate authigenic clay minerals (Figure 3.11). It is possible that marine clay mineral authigenesis resulting from continental silicate weathering could have initiated direct clay mineral precipitation from seawater and sediment porewater (Yin et al., 2023; Li et al., 2021a). However, XRD mineralogical analysis, together with high-resolution SEM petrology, point to a dominant detrital composition of identified clay minerals, with most authigenic clays formed mainly by the diagenetic transformation of detrital grains. It is also possible that the lower carbonate content in the immediate post-Snowball interval could have been generated by acidity produced during reserve weathering, enabling authigenic clay

mineral formation at the expense of carbonate deposition (Isson and Planavsky, 2018; Li et al., 2021b). However, quartz is abundant in this interval, and Al_2O_3 exhibits a generally positive correlation with SiO_2 (Figures 3.4 & 3.7a) while the negative correlation with CaO and MgO (Figures 3.5c, 3.7e & 3.7h), hints on dominant detrital supply of SiO_2 and chemical precipitation of sparse carbonate.

Kaolinite is typically formed under warm climatic conditions characterised by intense chemical weathering (Nesbitt and Young, 1984; Fedo et al., 1995). However, the presence of kaolinite within the secondary pores of albite and its absence between grain boundaries, suggest an authigenic origin (Figure 3.11g), with the conspicuous lack of well-crystallised blocky stable authigenic dickite kaolin polytype morphologies indicating association with low-temperature alteration and absence of deep burial diagenetic and hydrothermal influence (Lanson et al. 2002; Aubineau et al. 2021). Therefore, the authigenic kaolinites were likely derived from the alteration of detrital feldspar in a warm climate.

However, kaolinite is also found in XRD spectra in the tillite succession formed during the deglaciating Snowball phase (Table 3.5), which can be attributed to increased weathering of silicate minerals by carbonic acid produced in the CO_2-rich atmosphere that characterised Snowball Earth deglaciating intervals. The presence of kaolinite in the post-Snowball greenhouse conditions could be due to increased continental aluminosilicate weathering by carbonic acid, with resulting detrital supply to the basin. For example, kaolinite content in the post-Snowball deposit is consistent with increasing CIA values, which reflects enhanced chemical weathering, although much limited compared to the modern. Additionally, the degradation of organic matter through sulphate reduction produces organic acids within pore waters, conditions that favour the precipitation of kaolinite (Hao et al., 2021a). However, previous studies do not indicate the widespread distribution of kaolinite in Precambrian

sedimentary rocks (Tosca et al., 2010), possibly because of the transformation of primary kaolinite to illite during diagenetic illitization (Meunier and Velde, 2004).

Chlorite is stable in modern marine sediments formed in cold regions marked by strong physical and weak chemical weathering (Darby, 1975; Hallam et al., 1991; Ehrmann et al., 1992; Wahsner et al., 1999; Worden et al., 2020). In these glaciated environments associated with dominant physical weathering, chlorite can be preserved after glacial erosion of country rocks (Shi et al., 2018; Föllmi et al., 2009), including detrital kaolinite supplied by continental shales and soils (Darby, 1975). Further, the early Oligocene transition to illite-/chlorite-rich marine sediments has been interpreted to indicate a change from warm-humid chemical weathering conditions to a cool greater physical weathering state (e.g., Ehrmann et al., 1992; Wahsner et al., 1999).

My observations show a dominance of chlorite in the glaciogenic tillites. As depicted in Figure 3.11f, the alteration and replacement of ferromagnesian biotite is also suggested as a potential source of diagenetically formed authigenic chlorite (Weaver, 1989; Jinag and Peacor, 1994; Worden et al., 2020). An examination of the Fe/(Fe+Mg) content of putative chlorite grains prevalent in the tillites by SEM-EDS, indicates a mainly chamosite composition characterised by Fe/(Fe+Mg) > 0.3 as shown in Figure 3.13b &Table 3.6 (Bozkaya et al., 2017). Direct precipitation of chlorite cements is commonly observed in the sediment pore spaces, implying, as discussed above, Fe enrichment within the basin during the deglaciation phase. Taken together, the abundance of detrital chlorite in the tillites (Figure 3.11f) is consistent with the expected strong physical weathering associated with the grinding of continental landmass by the end-Snowball melting ice sheets (Paige-Green, 1980; Chamley,1989).

Chlorite is a common rock-forming mineral typically found in very low-grade metamorphic facies (Árkai and Ghabrial, 1997; Zane et al., 1998). Its formation can result from aggradation (positive transformation) following the evolution of neomineralization of trioctahedral smectite → interlayered smectite-chlorite (C-S) → chlorite, which implies prograde metamorphism due to burial and subsequent diagenesis (Nieto et al., 1994; Tetiker et al., 2015). It may also form during diagenesis from volcanic glass or detrital feldspars in tuffaceous sediments. At this stage, it is typically Fe-rich, poorly crystalline and often associated with smectite or mixed-layer clays. Although Fe-rich chlorite is detected, it is not associated with smectite or mixed-layer clays. I note that smectite and mixed-layer clays are minor or completely absent in the samples analysed. The absence of mineral assemblages typical of low-grade metamorphism, along with the presence of chlorite group minerals (such as chamosite), albite, calcite, Fe-dolomite, clay minerals (including illite), and quartz, suggests diagenetic alteration without progressing to metamorphic conditions (Nejbert et al., 2025). In addition, the sedimentary rocks analysed here are rich in Cr, showing mostly a uniform distribution across the pre-Snowball, Snowball and post-Snowball facies (Chi Fru et al., 2023). These conditions should enable increasing incorporation of Cr in chlorite with increasing metamorphic grade (e.g., Randive et al., 2015), within or across the different climatic intervals. However, no such effects were observed in our samples.

The stratigraphic and facies distribution of chlorite provides compelling evidence against a metamorphic origin. Chlorite is most abundant in the Snowball glacial facies, coinciding with periods of intense physical erosion and detrital flux associated with cold climate glacial encroachment. Similarly, its lower enrichment in the greenhouse facies suggests the contrary, conclusions which are critical to establish the hypothesis of the present study. That is, the experimental design was produced to answer the specific question of the link between climate and the accumulation of phyllosilicates in the sedimentary pile across the three-

climate successions. Further, because there is no evidence that the three facies sections experienced different levels of metamorphic alteration, the increase or decrease of chlorite composition across the sections cannot be pinned on metamorphism. The same principle applies for muscovite and all the other clay minerals distributed across the facies

On the other hand, illite forms under a variety of conditions and tends to crystallise in different forms (Środoń et al., 1984). In this study, illite is detected in all three distinct lithologies, including cold climate deposits (Darby 1975; Ehmann et al., 1992; Wahsner et al., 1999). Petrographic observation and the SEM- EDS chemical composition show the presence of detrital illite derived from the physical weathering of mica (e.g., muscovite). Besides detrital illite, authigenic or diagenetic illite was observed as pore-filling and pore-lining material (Figure 3.11).

The studied samples are completely devoid of smectite and mixed-layer clay mineral assemblages. Smectite is considered to be inherited from continental weathering (Tosca et al., 2010). Thus, its absence across the sampled lithologies is most likely due to burial diagenesis, leading to the formation of illite. For instance, while detrital illite grains are apparent in the samples, additional illite formation is suggested to have formed via the transformation of micaceous minerals like K-rich muscovite, as indicated by their association with illite. Overall, the above observations hint that the studied samples have not undergone significant metamorphic alteration, consistent with previous studies (Thomas et al., 2004; Arnaud and Fairchild, 2011; Skelton et al., 2015).

3.4.1.1 Clay Mineral Illitization

During burial diagenesis, potassium metasomatism (K-metasomatism) may strongly change sediment bulk composition and, consequently, the CIA index (Fedo et al., 1995). K-metasomatism leads to the conversion of plagioclase to K-feldspar and/or Al-rich clay minerals (e.g., kaolinite) to illite (Fedo et al., 1995; Tosca et al., 2010). This illitization

process has been widely reported in many Precambrian sediments (Fedo et al., 1995; Rieu et al., 2007; Tosca et al., 2010; Rafiei and Kennedy, 2019).

The influence of K-metasomatism is visualised by the Al_2O_3– (CaO* + Na_2O)–K_2O (A-CN- K) ternary diagram (Figure 3.9), according to Fedo et al. (1995). Theoretically, the chemical weathering trend without K-metasomatism should be distributed along an ideal line that runs parallel to the A–CN boundary axis, which reflects the concurrent loss of Na, Ca, and K, while deviations towards the K- apex indicate significant K addition by K-metasomatism (Fedo et al., 1995; Tosca et al., 2010). However, most samples deviate from the ideal weathering curve (Figure 3.9). Particularly, the pre-/post-glacial samples are suggested by the A-CN-K plot to have experienced K addition, which is common for aluminous clays through the growth of authigenic illite (Nesbitt and Young, 1984; Fedo et al., 1995). The corrected CIA value (CIA_{corr}), which minimizes the interference of K-metasomatism on the CIA, has been corrected through backward projection to the predicted weathering trend (Fedo et al., 1995; Tosca et al., 2010), leading to the corrected CIA values (CIA_{corr}) exhibiting a linear trend similar to the predicted ideal weathering line of granodiorite, with no shift towards the K endpoint (Figure 3.9). To allow for a maximum possible effect of K-metasomatism on CIA values, we applied a correction assuming that the ideal weathering trend originated from granite and a granodioritic source rock composition (Figure 3.9). Whereas the absence of a similar observation for the tillite succession implies insignificant K enrichment (Figure 3.9).

3.4.2 Weathering Conditions, Sediment Maturity and Sediment Recycling

Climate change has been linked to variations in siliciclastic rock compositions, related to the vulnerability of rock silicates to chemical weathering induced by atmospheric CO_2 in the

form of acidic rain (e.g., Gaillardet et al., 1999; Zhai et al., 2018). In this regard, CIA indices have been widely used to determine the degree of chemical weathering of glacial sediments (Nesbitt and Young, 1984; McLennan and Taylor, 1991; Rieu et al., 2007; Scheffler et al., 2003, 2006). Particularly, the effects of chemical weathering on sedimentary rock composition are dependent on climatic conditions and the residence time of material exposed to chemical weathering while stored in continental basins (Rieu et al., 2007). Hence, to determine climate change patterns from calculated weathering indices, it is necessary to address the effects of sedimentary processes such as sediment sorting, recycling and diagenesis, from those due to the character of the protolith (McLennan et al., 1993).

Sedimentary recycling is likely to be accompanied by the enrichment of poorly mobile heavy minerals, notably zircon because the elemental composition of zircon is dominated by trace elements that track sedimentary cycling processes (e.g., Zr). Therefore, to uncouple potential variations in the CIA values caused by transport sorting and possible recycling during deposition, Zr/Sc vs. Th/Sc cross plots were adopted (McLennan et al., 1993). Th and Sc are immobile and therefore do not undergo significant fractionation during transport and deposition (McLennan et al., 1993). In addition, Zr is highly stable throughout the sedimentary cycle, so the Zr/Sc ratio increases with the enrichment of zircon during the process of transportation and sedimentation, while Th/Sc ratios remain relatively unchanged during the sedimentary cycle (McLennan et al., 1993). The plot of Th/Sc versus Zr/Sc suggests that the studied samples were derived mainly from intermediate igneous rocks and that they experienced insignificant sediment recycling. Most of the analysed samples cluster close to the UCC values, and the provenance-dependent compositional variation trend on the Th/Sc vs Zr/Sc binary diagram (Figure 3.14) shows that Zr/Sc ratios are positively correlated with Th/Sc ratios. This correlation does not support Zr enrichment by sediment recycling processes. Therefore, the studied samples are considered the result of first-order

cycling of eroded continental rocks, exempting polycyclic reworking (Rieu et al., 2007). The low Zr/Sc ratios of <35 across the successions further indicate that sediment deposition was primarily controlled by the composition of the source rocks and that sediment recycling did not significantly influence the chemical composition of the samples (Figure 3.14). Moreover, Th/Sc (provenance indicator) vs. CIA had no discernible covariance (Figure 3.16), implying that the first-order change in CIA reflects weathering processes and that the CIA values are not influenced by changes in the source rock composition (Taylor and McLennan, 1985; McLennan et al., 1993; Rieu et al., 2007).

Based on mineralogical mapping (Figure 3.1), the tillites are compositionally dominated by less mature sheet silicate mineral components like muscovite and biotite compared to the pre-/post-Snowball successions.

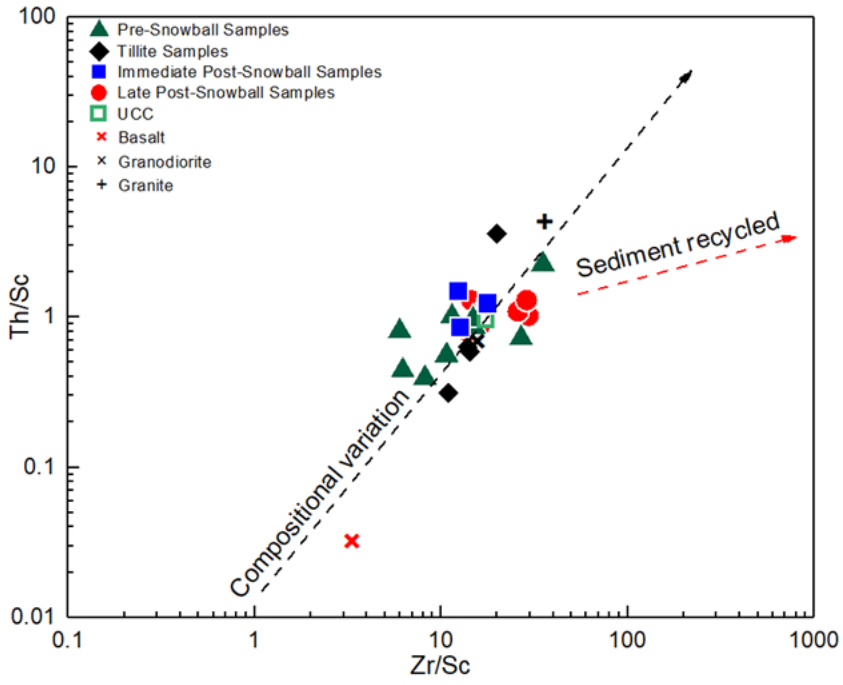

Figure 3.14| Th/Sc versus Zr/Sc ratio plots for the studied samples according to (McLennan et al. (1993).

3.4.3 Provenance Interpretation

Provenance analysis is important for determining the origin and evolution of sediments. Source rock identification and provenance were therefore investigated based on assessing

facies' chemical composition using major and trace elements to retain source rock compositions (Cullers, 2000). The analysis relied on elements that have low immobility, are resistant to alteration during weathering and sedimentary processes, and are believed to be transported specifically on the terrigenous component of sediments. These elements which are thought to reflect the chemistry of the source rocks, include Al, Fe, Ti, Th, Sc, Co, Zr and rare earth elements (Taylor and McLennan, 1985; Cullers, 2000).

In weathered igneous rocks, Al is hosted primarily in mica, clays and residual feldspars, whereas Ti is hosted chiefly by mafic minerals like pyroxene, biotite and ilmenite. Therefore, the Al_2O_3/TiO_2 ratio was used to broadly predict the source rock composition, since these two oxides do not experience strong fractionation during weathering and diagenesis, where Al_2O_3/TiO_2 ratios <8, 8-21 and >21, approximate a mafic, intermediate and felsic igneous source rock composition, respectively (e.g., Hayashi et al., 1997). The Al_2O_3/TiO_2 ratios (Table 3.3) of the studied samples are broadly homogeneous, indicating a relatively uniform source provenance. The Al_2O_3/TiO_2 ratios of the studied samples range from 16.7-24 across the section — averaging 16.7±2.3 for the pre-Snowball, 24.0±4.7 for the tillites, 19.1±0.9 for the immediate post-Snowball and 23±1.6 for the late post-Snowball facies. These values suggest that the source area was potentially dominated by intermediate igneous and felsic rock.

In addition, the composition of high field-strength elements (HFSE) Th, La and Sc was used to further assess the source provenance (McLennan et al., 1993). Moreover, incompatible trace elements are more enriched in UCC felsic rocks compared to compatible elements which are more abundant in mafic and ultramafic rocks (McLennan et al., 1993). Consequently, the compositional ratios of the incompatible element (Th) and the compatible element (Sc) were also used to discriminate primary sediment provenance (Condie, 1993). The La–Th–Sc ternary diagram (Figure 3.15) places all samples close to the La apex, far

away from Sc, which implies a predominant felsic source composition, since Sc is enriched in mafic igneous rocks (Taylor and McLennan, 1985; McLennan et al., 1993). Most of them fall into the area between granite and granodiorite indicating the potential mixture of these rocks in the source area and a mainly felsic parent rock composition. This further agrees with the dominance of albite, muscovite and quartz-rich content of the studied facies and, to a lesser extent, the presence of orthoclase in some samples.

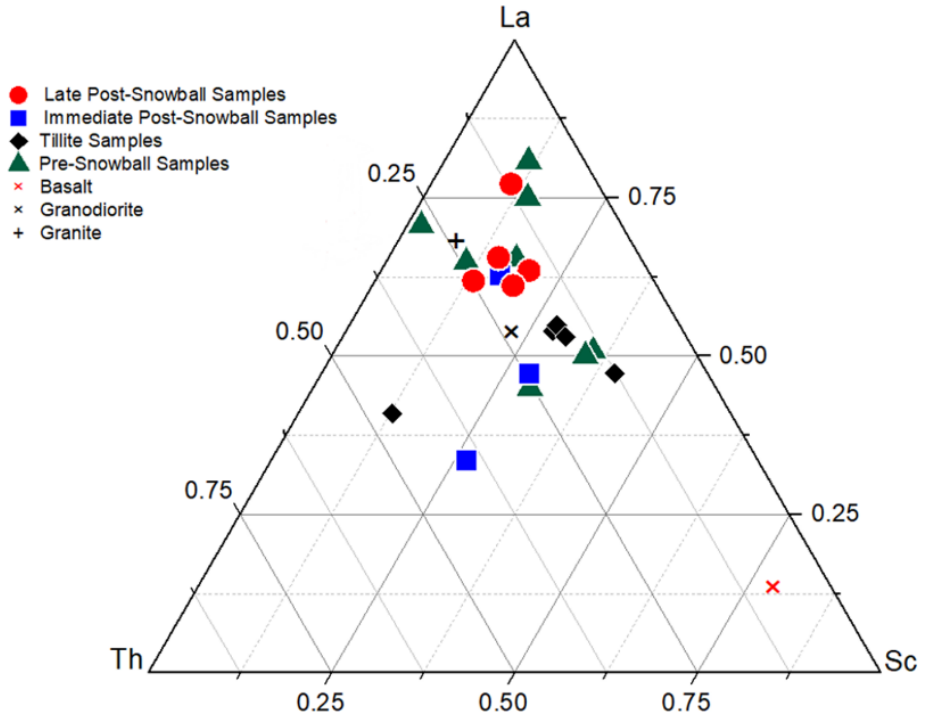

Figure 3.15| La–Th–Sc ternary diagram for the studies samples. Note that most samples plot in the area between granite and granodiorite. Data for basalt, granite, granodiorite, and UCC (Upper Continental Crust) are from Condie (1993).

The inferred granodiorite source for most samples is also supported by the relatively high Th/Sc ratios (Table 3.4). The Th/Sc ratio was applied to distinguish between felsic and mafic contribution to facies composition when Th/Sc ratios are >0.4 for felsic and <0.2 for mafic lithologies because Th tends to be enriched in felsic rocks and Sc in mafic rocks. The variable enrichments and depletions in incompatible and compatible elements in the studied samples (Figure 3.14 and Figure 3.15) point to a predominantly felsic source for the post-Snowball lithology. In contrast, the tillite and pre-Snowball facies are more associated with a dominant intermediate igneous rock source as they are mostly enriched in incompatible

elements and depleted incompatible elements with respect to UCC (Figure 3.14). Taken together, the major elements and incompatible trace elements' geochemical data suggest that the source rocks were mainly felsic and/or intermediate igneous.

A low Th/Sc ratio across the succession, together with ternary A-CN-K versus corrected CIA variations indicate a felsic source for the sedimentary rocks (Figure 3.16), consistent with their strong UCC-like profile (Figure A3.1). Moreover, Th/Sc versus Zr/Sc ratios plot along the expected compositional array of primary sediments that have experienced insignificant recycling and sorting effects (Figure 3.14). This together with the La, Th and Sc ternary diagram associates the primary sediments with a felsic provenance (Figure 3.15).

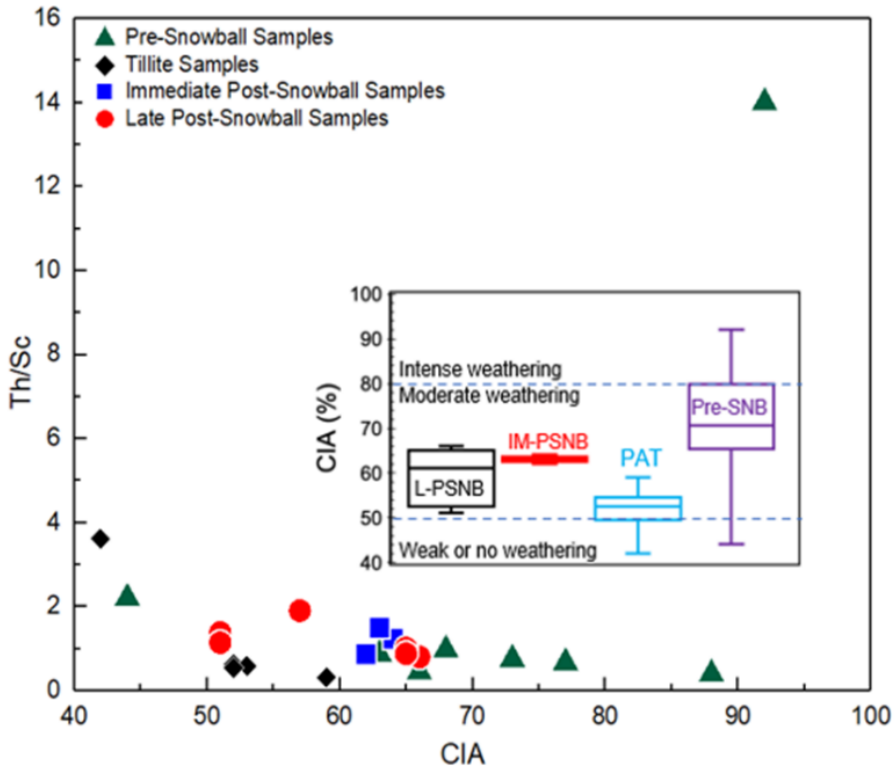

Figure 3.16| Th/Sc versus CIA indices with inset showing a box and whisker plot of CIA values for the pre-Snowball (Pre-SNB), Port Askaig Tillites (PAT), immediate post-Snowball (IM-PSNB) and late post-Snowball (IM-PSNB) intervals.

3.4.4 Weathering and Paleoclimate Variations

By excluding the potential effects of post-depositional diagenesis, sedimentary recycling, and provenance, the corrected CIA values and sediment composition can therefore be used to evaluate climate fluctuations and chemical weathering intensities in the source area. Climate exerts a strong influence on bulk sediment chemistry, with greater leaching of cations under warm and humid climates. Significant changes in chemical weathering intensity, as recorded by the CIA values pre-Snowball, during deglaciation and post-Snowball phases, are believed to have occurred over the studied interval. First, the association of the A-CN-K data for the glaciogenic tillite deposits with feldspar indicate that their primary composition experienced negligible chemical alternation, as reflected by low CIA values in the range of 42-59. Further, clay mineralogy is sensitive to variations in weathering, sediment source area, transport processes and regime over time, and thus careful study of the clay mineralogy provides some insights into paleoclimate variability across the section.

In this regard, mica and chlorite are considered common by-products of physical weathering reactions linked with the low hydrolysis typical of cool to temperate and/or dry climates. This agrees with the cold/dry climatic conditions expected to have been prevalent during the glaciating interval (Chamley, 1989). These values hint that physical weathering was dominant over chemical weathering at this time, consistent with the expected physical weathering of country rocks by the thawing ice sheets (Rieu et al., 2007; Ding et al., 2016; Wang et al., 2020). Moreover, evidence for this conclusion is provided by the SEM data (Figure 3.1), which shows the dominant deposition of sheet silicates. Whereas the CIA values of pre-/post-Snowball facies (Figure 3.6c and Figure 3.9), point to intensification of chemical weathering as would be expected for interglacial periods with warmer and more humid conditions (Rieu et al., 2007; Ding et al., 2016; Wang et al., 2020).

The variations in CIA recorded in the studied facies correspond well with major climatic changes (glacial versus non-glacial) inferred from independent paleoenvironmental interpretations (Rieu et al., 2007). My results are, thus, in agreement with a number of studies that report paleo-CIA values for siliciclastic sediments of a similar age (Fedo et al., 1995; Rieu et al., 2007; Tosca et al., 2010; Ding et al., 2016; Zhu et al., 2020; Du et al., 2021). In addition, my CIA data is consistent with the detrital composition as shown by SEM-EDS mineral mapping and strong correlation of various major and trace elements with detrital indicators like TiO_2 and Al_2O_3. Below, the observed changes in the degree of chemical weathering of source rocks before, during and after the Sturtian Snowball are explored to gain insights into nutrient supply from land to the seawater and the potential impact on marine primary productivity.

3.4.5 Implications for Marine Nutrient Concentrations

Clay minerals, through their physical and chemical properties, have been identified as potentially important bioessential trace element transporters, including phosphorus (P), from land to the ocean (Uncles et al., 2006; Zhao et al., 2018; Hao et al., 2021a, 2021b; Chi Fru et al., 2023). Their pH and ionic strength-dependent high affinity for ions, due to their large surface area and charge, results in a high capacity for adsorptive accumulation of a variety of bioessential elements (Landry et al., 2009; Hao et al., 2019; Hao et al., 2021a, 2021b). Particularly, the surface charge of clay minerals like illite and kaolinite identified in this study varies with solution pH and ionic strength (Bradbury and Baeyens, 2009; Gu and Evans 2007; Hao et al. 2019). Accordingly, as clay minerals are transported from land to the oceans by rivers, the change from freshwater and slightly acidic to saline-alkaline pH conditions, impact clay mineral surface properties, which in turn affects their ability to effectively bind and adsorb trace metals and P (e.g., Hao et al. 2021a and 2021b).

Because different clay minerals have different P and trace element binding capacities (Hao et al., 2019, 2020, 2021a, 2021b), it is therefore expected that changes in detrital clay supply and composition across the sequence would have influenced seawater P and trace element content accordingly. Although the present study did not quantify the amount of P and trace elements associated with specific clay mineral phases, the next chapter shows that P is preferentially enriched in the chlorite-rich tillites, as are the representative trace elements Co, Ni, V and Cr (Figures 3.5-3.6). This observation points to a likely association between detrital chlorite enrichment, P and trace element supply to seawater at this time. Moreover, the predominance of illite across the sampled succession further represents a likely constant pathway for nutrient delivery to seawater.

Bioessential trace element nutrients and P are integral to the functioning of biogeochemical processes at the Earth's surface and play an important role in supporting marine biological productivity and seawater-atmosphere oxygenation (e.g., Hopwood et al., 2014; Partin et al., 2013a; Twinning et al., 2013; Reinhard et al., 2017; Lohan, 2018). Particularly, the fertilisation of seawater with particulate and dissolved Fe and P by glacial till in modern glaciated environments has been recognised (e.g., Bhatia et al., 2013; Hawkings et al., 2014, 2016, 2020; Hopwood et al., 2014; Hodson et al., 2005, 2017). This process affects seawater chemistry through a combination of inputs and outputs where adsorption/desorption and dissolution/precipitation reactions linked to the exchange of ions on clay minerals and Fe oxyhydr(oxides) surfaces for example, are the main mechanisms involved in the transfer of nutrients from land to oceans (Jeandel and Oelkers, 2015; Large et al., 2015; Hao et al., 2020, 2021b). In this regard, the moderate to strong co-variation of most of the whole-rock elements, including bioessential V, Ni, Co and P, with the Al_2O_5 detrital tracer and K_2O (Figure 3.6 and Figure 3.7), indicate that the detrital fluxes, including the clay minerals and their precursors, were predominantly responsible for the bulk supply

of nutritious elements to the basin. The behaviour of key bioessential and redox-sensitive trace elements, based on correlation coefficients, reveals the crucial role played by Al and clay minerals in the fixation and regulation of seawater elemental composition.

Interestingly, the positive correlation between Al_2O_3 and Fe_2O_3 as well as with P_2O_5 and representative trace elements, with persisting elevated records encountered in the immediate post-Snowball samples (Figure 3.5b-e and Figure 3.7), indicate that the physical weathering processes that accompanied the melting ice sheets were a likely contributor to seawater and primary sediment P, Fe and trace metal enrichment, similar to reports for modern glaciated seawater margins (e.g., Bhatia et al., 2013; Hawkings et al., 2014, 2016, 2020; Hopwood et al., 2014; Hodson et al., 2005, 2017), as well as trace element supply. The well-described release of Fe(II) by glacial weathering in these cold climate environments to seawater, is consistent with the Fe-chlorite and Fe-dolomite enrichment in the tillites and potential formation of magnetite/hematite in the immediate aftermath of the Snowball (Chi Fru et al., 2023). Moreover, given that kaolinite forms under extremely humid greenhouse chemical weathering conditions, the lack of strong chemical weathering in the tillites, suggests that if not produced diagenetically, kaolinite could have been eroded from land, where it formed during the high chemical weathering conditions of the pre-Snowball Earth greenhouse state, into the sedimentary basin. In such conditions, kaolinite may have played a crucial role in the delivery of P to seawater from land during the melting of the Snowball ice sheets, together with detrital illite to a lesser extent (Hao et al., 2021b).

3.5 Conclusion

The clay minerals reported in this study carry valuable paleoenvironmental and paleoclimatic information, including the potential to unlock their role in nutrient delivery to seawater and sediments, recycling in sediment pore waters and back to seawater. Their

diversity, the presence of significant compositional variations and the bulk sediment CIA values across the studied successions, reasonably track changing climatic cycles before, during and after the Sturtian Snowball. This is interpreted to imply that the switch in clay mineralogy from pre-Sturtian Snowball times to the deglaciation phase, reflects a change in paleoenvironmental conditions rather than post-depositional primary sediment alteration. Collectively, the data agree with the independent study by Tosca et al. (2010), suggesting that clay minerals are a consistent weathering product associated with changing Neoproterozoic Cryogenian climates. Based on modern evidence and experimental data linking clay mineralogy and seawater nutrient content, I propose that abundant clay mineral production by the Cryogenian Snowball glaciations, coupled with end-Snowball intensification of chemical weathering, likely played a fundamental role in the fertilisation of post-Snowball seawater with key bioessential nutrients, contributing eventually to the Neoproterozoic Oxygenation Event as shown in next chapters.

Chapter 4: Transient Fertilization of a post-Sturtian Snowball Ocean Margin with Dissolved Phosphate by Clay Minerals

4.1 Introduction

The secular increase of phosphorus (P) in Cryogenian marine sediments has been linked to post-Snowball Earth deglaciation resulting in enhanced phosphate (PO_4^{3-}) supply to seawater, greater marine primary production, ocean-atmosphere oxygenation, and ultimately the evolution of metazoans (Lyons et al., 2014; Planavsky et al., 2010; Reinhard et al., 2017). The inference of higher dissolved seawater PO_4^{3-} concentrations across the Neoproterozoic glaciations comes from Fe-rich deposits and shales containing significantly higher P concentrations relative to older sediments of similar depositional settings (Planavsky et al., 2010; Reinhard et al., 2017). However, except for a broad association with mechanical weathering caused by the erosional action of end-Snowball melting ice sheets, it remains unclear how PO_4^{3-} was sourced from the continents and transported in quantitatively dissolvable forms to seawater to enable pervasive global ocean-atmosphere oxygenation.

In the modern world, most PO_4^{3-} is transferred from land to the oceans by riverine in various forms, i.e., dissolved organic P, dissolved inorganic P, or particulate P associated with river-suspended sediments (clay and metal oxide particles) rather than in solution (Froelich, 1988; Gérard, 2016; Hao et al., 2021a). The concentration of dissolved free P in rivers is generally low; however, the particulate P fractions from suspended sediments can easily be released into seawater once aqueous environmental conditions change (Hao et al., 2021a). This view is consistent with the suggestion that detrital clay minerals associated with more acidic rivers during the Great Oxygenation Event (GOE) played a significant role

in conveying PO_4^{3-} from land to Paleoproterozoic seawater (Hao et al., 2021a). During the GOE, the proliferation of aerobic oxidation of sulfide minerals such as pyrite and other iron-bearing minerals generates acidic water, leading to an extended episode of acid rock drainage, and solubilization of nutrient-bearing minerals (e.g., clay minerals) (Migaszewski et al., 2007; Konhauser et al., 2011). This is indicated by chromium (Cr) isotope fractionations; the degree of acidity needed to dissolve Cr(III) from an ultramafic source has been produced by aerobic respiration of the pyrite oxidation reservoir during GOE (Konhauser et al., 2011).

At times of less acid generation on land, highly reactive iron oxyhydroxides (Fe-ox_{HR}) instead served as efficient particulate sorbents for dissolved phosphate (Hao et al., 2021a). As a corollary, this study hypothesizes that extensive weathering of continental landmasses by melting ice sheets at the end of the Cryogenian Snowball Earth glaciations (Hoffman et al., 2017) drove up the production, transport, and supply of fine-grained detrital clays and Fe-ox_{HR} to the oceans, which served as vectors of marginal seawater enrichment with PO_4^{3-}. Indeed, melting of the modern Greenland ice sheet shows that up to 97% of PO_4^{3-} exported by glacial meltwater is associated with suspended sediment particles (Hawkings et al., 2016). This relationship is predictable, given that clay minerals, which tend to form rapidly upon the retreat of glaciers with climate warming (Mavris et al., 2011), together with Fe-ox_{HR}, possess large surface-to-volume ratios. Together, they contain positively charged surfaces at the pH range of rivers that make them efficient adsorbents of dissolved PO_4^{3-} anions (Froelich, 1988; Violante and Pigna, 2002; Daou et al., 2007; Némery and Garnier, 2007; Kim et al., 2011; Gérard, 2016; Ajmal et al., 2018; Hao et al., 2021a; Liang et al., 2021; Liu et al., 2021; Warr, 2022).

In this chapter, I test the potential of clay minerals and Fe-ox_{HR} minerals to act as vectors of dissolved PO_4^{3-} to post-Snowball seawater by using a combination of geochemical

techniques to demonstrate a causal relationship between continental erosion and the supply of dissolved PO_4^{3-}, thereby demonstrating that the unique Sturtian Snowball conditions overproduced clay size P-bound silicate minerals that fertilised seawater with P.

4.2 Methods

The methods used in this chapter are described in Chapter 2. The bulk rock geochemical analysis was conducted as outlined in section 2.2.3 mineralogical analysis determined by XRD and SEM as laid out in section 2.2.1 and stable isotopes in section 2.2.4. The P and Fe extraction protocol is outlined in section 2.2.2.2.

4.3 Results

4.3.1 Bulk Facies Chemostratigraphy and Mineralogy

4.3.1.1 Sample Quality, Stratigraphy and Carbon Systematics

Carbon systematics was conducted to confirm the equality of samples and to ascertain their position within the sequence based on comparison with previous lithostratigraphy analyses using similar analysis (Brasier and Shields, 2000; Prave et al. 2009; Sawaki et al., 2010; Arnaud and Fairchild, 2011; Fairchild et al., 2018). The pre-/late post-Snowball samples are marked by higher $\delta^{13}C_{org}$, C_{org}, $\delta^{13}C_{carbonate}$, and carbonate (wt.%) excursions, compared to persistently lower tillite and immediate post-Snowball values (Figure 4.1a-d and Table 4.1). $\delta^{13}C_{org}$ values ranging from -28.57‰ to -11.87‰, with an average of -24.51±4.36‰ (1σ) (Figure 4.1a and Table 4.1). Organic carbon concentrations are generally low across sequence stratigraphy. They range from 0.02 - 0.08 wt.%, averaging 0.038 wt.% (Figure 4.1b and Table 4.1). The $\delta^{13}C_{carbonates}$ values range from as low as -7.02‰ and up to +5.64‰ with average $\delta^{13}C_{carbonates}$ values of -2.04±4.1‰ (1σ).

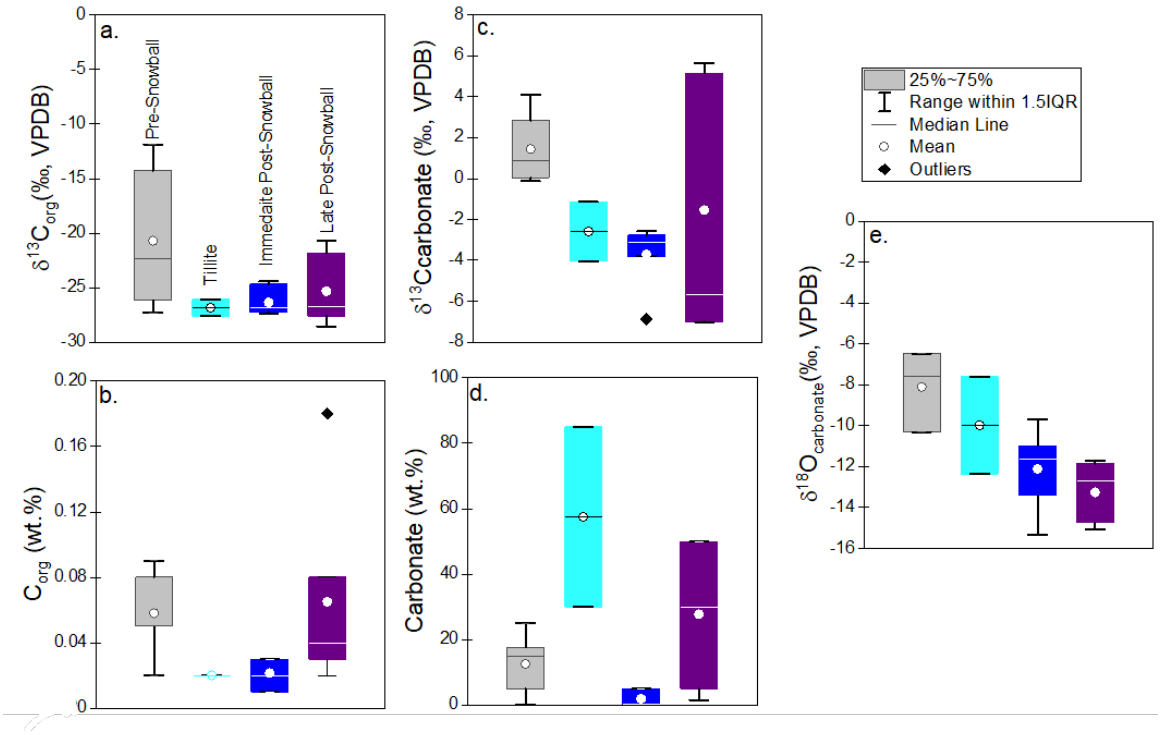

Figure 4.1| Box and whisker plots showing lithostratigraphic carbon systematics for representative samples. a. $\delta^{13}C_{org}$ distribution. b. Organic carbon (C_{org}) concentration. c. $\delta^{13}C_{carbonate}$ distribution. d. Carbonate concentration. e. $\delta^{18}O_{carbonates}$ distribution. (n= 22 samples).

The data show that the highest carbonate concentrations are recorded in dolomite-rich samples further up from the interval immediately following the deglaciation in the Bonahaven Dolomite Formation and in the underlying pre-glacial Lossit Limestone Formation. The lowest carbonate concentrations are encountered in the immediate post-glacial deposits (Figure 4.1c-d and Table 4.1). $\delta^{18}O_{carbonates}$ values are spread between -15.09‰ up to -6.48‰, with an average of -11.66±2.26‰ (Figure 4.1e & Table 4.1) with trends generally decline up sequence. No correlations were found between $\delta^{18}O_{carbonates}$ and $\delta^{13}C_{carbonates}$ (Figure 4.2a), $\delta^{13}C_{org}$ and $\delta^{13}C_{carbonates}$ (Figure 4.2b), $\delta^{18}O_{carbonates}$ and $\delta^{13}C_{org}$ (Figure4.2c), C_{org} (wt.%) and $C_{carbonates}$ (wt.%) (Figure 4.2d).

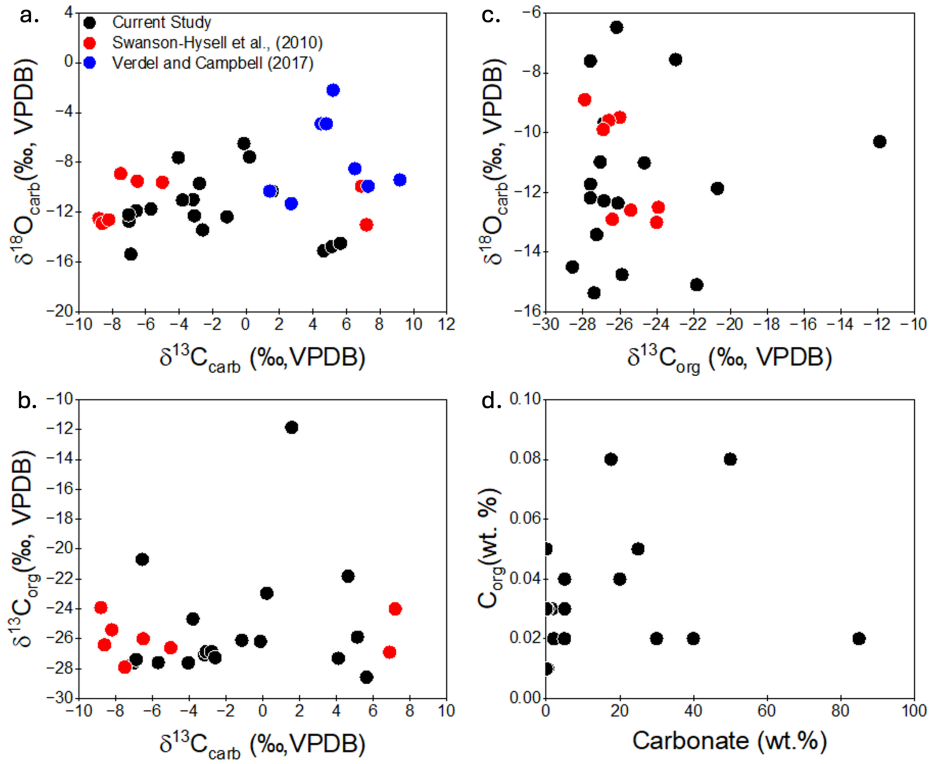

Figure 4. 2| a. $\delta^{18}O_{carbonate}$ versus $\delta^{13}C_{carbonate}$ cross plot. (b) $\delta^{13}C_{org}$ versus $\delta^{18}O_{carbonate}$ cross plots. c. $\delta^{18}O_{carbonate}$ versus $\delta^{13}C_{org}$ cross plot. d. C_{org} versus carbonate content cross plot.

4.3.1.2 Hydrothermal Influence

The potential influence of hydrothermal activity was investigated using Fe/Ti versus Al/(Al+Fe+Mn) ratio plots as shown in Figure 4.3. The studied samples contain Fe/Ti ratios <100 and Al/(Al +Fe +Mn) ratios between 0.2 - 1.0.

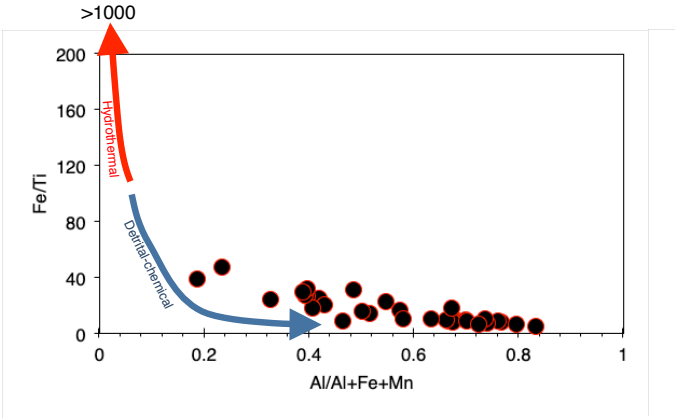

Figure 4.3| Fe/Ti and Al/(Al+Fe+Mn) cross plots showing a mainly detrital origin for the sampled sequence. Red arrow=hydrothermal origin (cut off minimum threshold at 100≥Fe/Ti>1000). The blue arrow shows continuous gradation towards mixed chemical+detrital to pure chemical sediments at increasing Al/(Al+Fe+Mn) (Pecoits et al., 2009).

Table 4.1| Stable isotope ($\delta^{18}O_{carbonate}$, $\delta^{13}c_{carbonate}$ and $\delta^{13}O_{org}$), carbonate and organic carbon (wt.%) concentrations.

Sample	Mass (mg)	Carbonate (wt.%)	$\delta^{13}C_{Carbonate}$ (‰, VPDB)	S.D	Organic carbon (wt.%)	$\delta^{13}C_{Org}$ (‰, VPDB)	$\delta^{18}O_{Carbonate}$ (‰, VPDB)	S.D
PS-16-01	1.20	50.00	4.63	0.08	0.08	-21.82	-15.09	0.04
PS-16-02	0.30	5.00	5.14	0.07	0.04	-25.88	-14.75	0.05
PS-16-10	2.20	40.00	5.64	0.06	0.02	-28.57	-14.49	0.05
PS-16-11	0.40	20.00	-5.68	0.04	0.04	-27.59	-11.73	0.06
PS-16-12	0.70	50.00	-7.00	0.04	-	-	-12.72	0.07
DD-16-04	0.20	ND	-6.56	0.09	0.18	-20.69	-11.87	0.08
DD-16-06	0.60	1.49	-7.02	0.07	0.03	-27.00	-12.19	0.05
BH-16-03b	4.10	0.35	-3.17	0.22	0.03	-27.06	-10.99	0.13
BH-16-03	2.30	5.00	-3.09	0.08	0.03	-26.86	-12.28	0.07
BH-16-02	23.30	5.00	-2.78	0.16	0.02	-26.86	-9.69	0.10
Ci-16-01	38.00	2.04	-2.59	0.06	0.02	-27.26	-13.41	0.04
Ci-16-02	87.10	0.39	-3.80	0.05	0.01	-24.67	-11.01	0.08
BH-16-01	3.70	0.01	-6.89	0.12	0.03	-27.39	-15.36	0.15
Ci-16-23	3.70	0.04	-	-	0.01	-24.43	-	-
PAT1	154.10	85.00	-4.05	0.08	0.02	-27.61	-7.61	0.10
PAT2	1.10	30.00	-1.14	0.05	0.02	-26.12	-12.36	0.07
LL-16-01	0.20	15.00	1.57	0.08	-	-11.87	-10.31	0.10
LL-16-b1	0.50	25.00	0.21	0.07	0.05	-22.96	-7.56	0.06
LL-16-c	0.70	5.00	-0.13	0.04	0.02	-26.17	-6.48	0.04
LL-16-d	61.70	0.01	4.10	0.07	0.05	-27.32	-	-
LL-16-g	79.10	-	-	-	0.09	-14.27	-	-
LL-16-h	166.50	17.60	-	-	0.08	-21.82	-	-

4.3.1.3 Mineralogical Distribution

XRD and SEM-EDS data from thin sections are consistent with reported higher and more homogenous carbonate enrichment in the pre-/late-Snowball facies (Figure 4.4& Table 3.2). The SEM-EDS mineral maps, together with the XRD mineralogical profile, show a variable prevalence of siliciclastic detrital material in all lithologies, as stated in Chapter 3. The tillites are noted for hosting abundant detrital grains likely associated with illite, muscovite, albite, and, to a lesser extent, kaolinite as already discussed in the preceding chapter (Figure 4.4 & Table 3.2). Again, although detected in the pre-Snowball rocks, illite is not always present in readily quantifiable amounts. The SEM-EDS maps are consistent with XRD mineralogical analysis and suggest an absence of goethite in all samples. Instead, putative crystalline magnetite grains were observed in the immediate post-Snowball section, but rarely in the tillites and the pre-and post-Snowball intervals, interpreted as either absent, sparsely distributed or present below detection levels (Figure. 4.4).

Apatite particles were found in all the samples as shown by SEM-EDS mineral maps (Figures 4.5-4.8). However, these maps reveal apatite scarcity relative to other dominant minerals like sheet silicate, quartz, calcite and dolomite across the successions, especially in the immediate post-Snowball samples. Elemental maps for the distribution of P, Fe and P, Ca and P and Al and P for representative pre-Snowball, tillite, immediate post-Snowball and post-Snowball samples are shown in Figures 4.5a-d- 4.8a-d. EDS analysis indicates that the apatite grains are composed of Ca, P and O atoms, with minor fluorapatite indicated by a low F concentration in all samples (Figures 4.5f- 4.8f). BSE photomicrographs suggest mostly subhedral-euhedral apatite grains, while SEM photomicrographs associate apatite particles with putative magnetite minerals in the immediate post-Snowball succession (Bh-16-02) (Figure 4.7e), and mainly with clay minerals in the tillites and late post-Snowball samples (LL-16-A1 and PS-16-00) (Figures 4.6e & 4.8e).

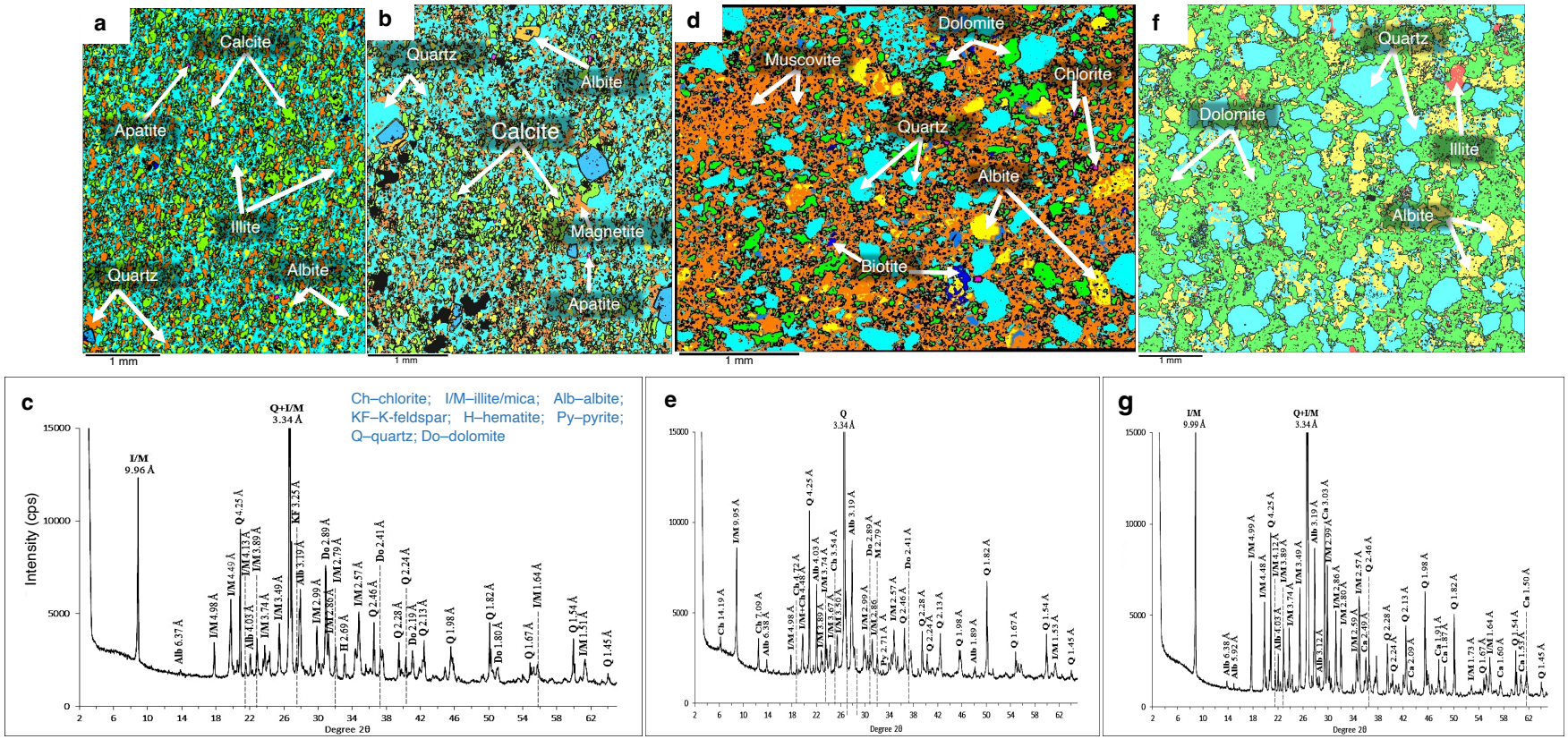

Figure 4.4| SEM-EDS maps and bulk XRD mineralogical patterns for representative samples. a-b. SEM mineral maps for immediate post-Snowball, composed of fine-grain siliciclastic sediments. c. Corresponding immediate post-Snowball whole rock XRD mineral diffractogram. d. Representative SEM mineral map for Post Askaig tillite showing coarse siliciclastic grains dominated by fine orange muscovite phyllosilicate (sheet silicate) grains. e. Corresponding XRD mineral diffractogram for the Port Askaig Tillites. f. An example of an SEM-EDS mineral map for a pre-Snowball sample from the LLF, showing coarse siliciclastic grains, but with much lower phyllosilicate silicate content compared to the tillites. g. Corresponding immediate post-Snowball whole rock XRD mineral diffractogram.

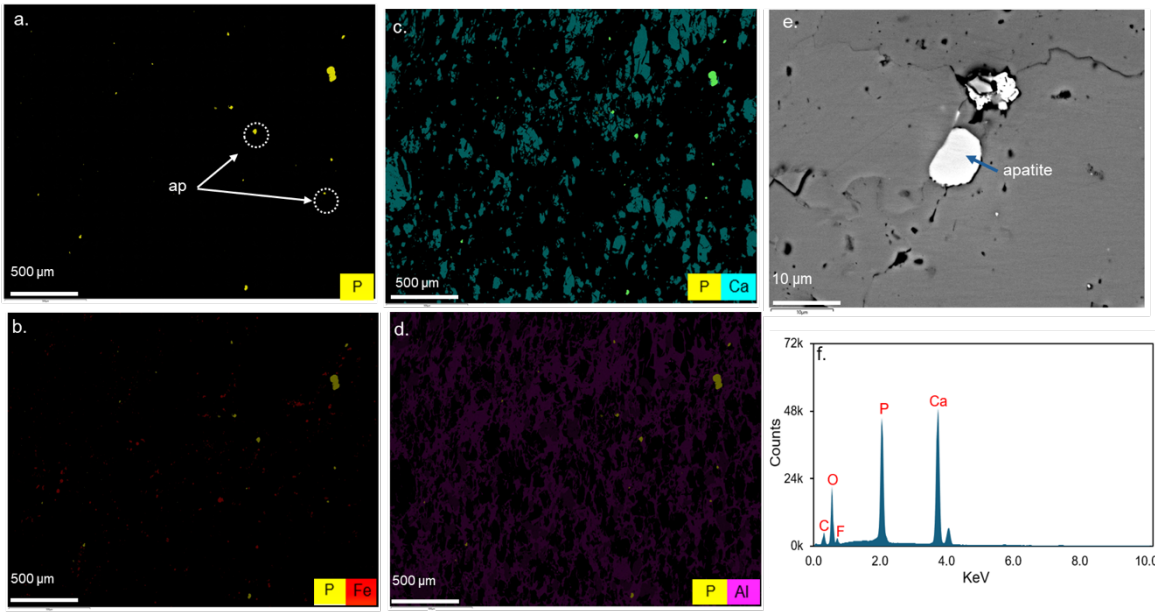

Figure 4.5| Distribution of P and its different phases observed by SEM in pre-Snowball sample LL-16-J1 from the Lossit Limestone Formation. a. Electron map of P distribution, showing the location of apatite (ap) nanoparticles. b. Electron map of P-Fe. c. Electron map of P-Ca. d. Electron map of P-Al. e. BSE photomicrograph of CFA grains. f. SEM-EDS spectra of fluorapatite. SEM-EDS Detection limit of P is 0.3 wt. %.

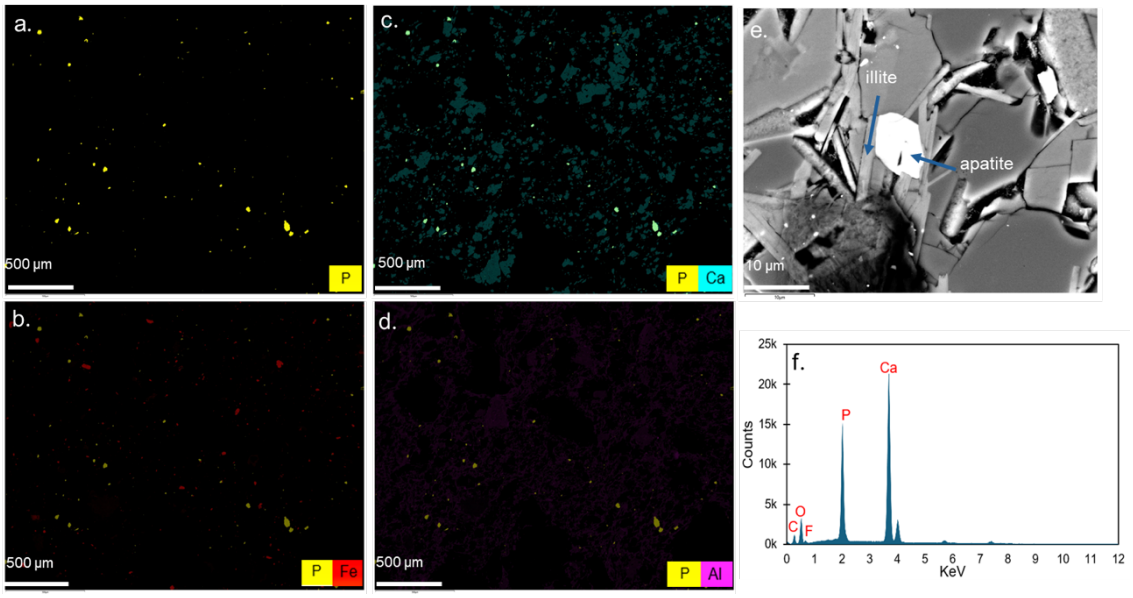

Figure 4.6| Distribution of P and its different phases observed by SEM in Snowball sample PAT3 from the Port Askaig Tillite Formation a. Electron map of P distribution showing the location of apatite (ap) nanoparticles. b. Electron map of P-Fe. c. Electron map of P-Ca. d. Electron map of P-Al. e-f. BSE photomicrograph of CFA grains. f. SEM-EDS spectra of fluorapatite.

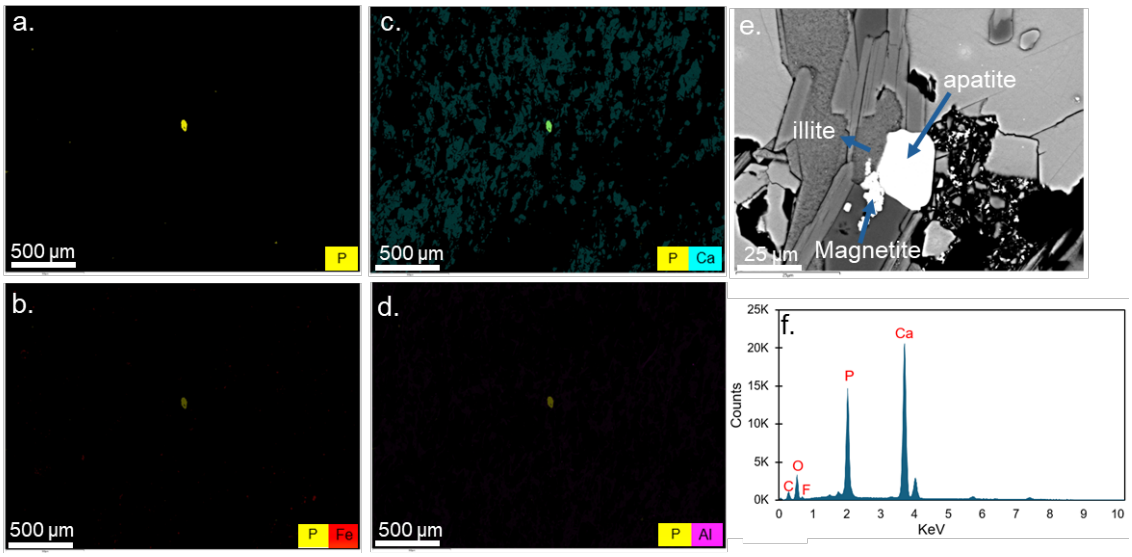

Figure 4.7| Distribution of P and its different phases observed by SEM in immediate post-Snowball sample Bh-16-02 from the Bonahaven Dolomite Formation. a. Electron map of P distribution showing the location of apatite (ap) nanoparticles. b. Electron map of P-Fe. c. Electron map of P-Ca. d. Electron map of P-Al. e. BSE photomicrograph of CFA grains. f. SEM-EDS spectra of fluorapatite.

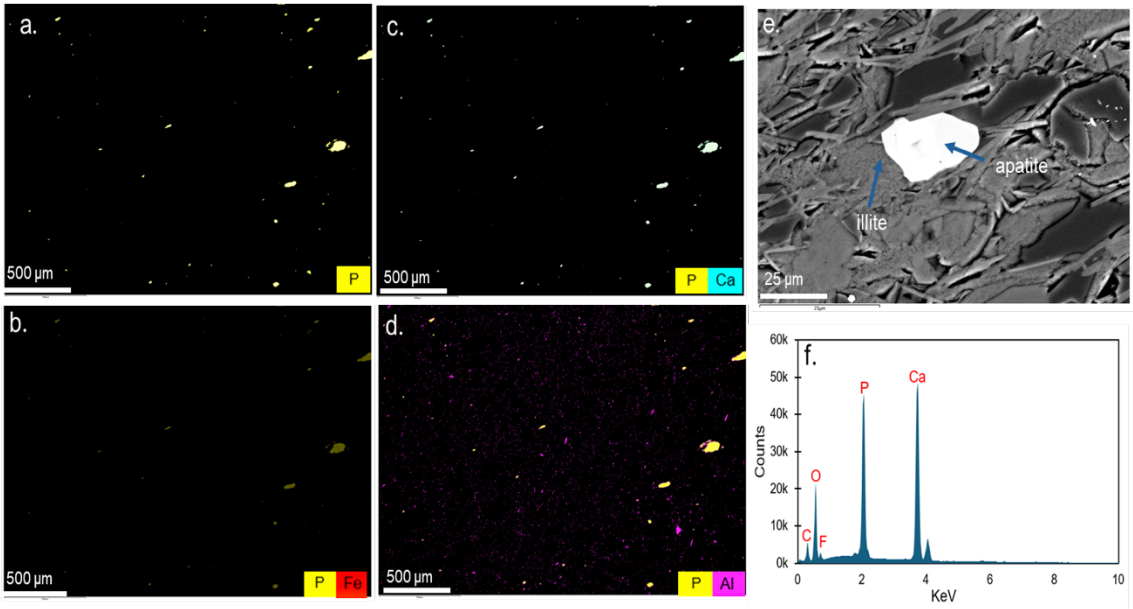

Figure 4.8| Distribution of P and its different phases observed by SEM in late post-Snowball sample PS-16-00 from the Bonahaven Dolomite Formation. a. Electron map of P distribution showing the location of apatite (ap) nanoparticles. b. Electron map of P-Fe. c. Electron map of P-Ca. d. Electron map of P-Al. e. BSE photomicrograph of CFA grains. f. SEM-EDS spectra of fluorapatite.

4.3.2 Bulk Sediment Geochemistry

Bulk concentrations of TiO_2, Al_2O_5, Fe_2O_3, MnO, and P_2O_5 (Figure 4.9a-e and Tables 3.3 – A2), are marked by persistently elevated P_2O_5, TiO_2, Al_2O_5, and Fe_2O_3 concentrations in the tillite and immediate post-Snowball samples, with much lower and more variable concentrations recorded in the PS-16 section of the Port an t-Struthain rocks in the upper BDF (Figures 4.9a-e). Notable Al_2O_5 and TiO_2 peaks are encountered especially in the tillite and immediate post-Snowball samples. When major elemental concentrations are normalized against Ti, the relatively constant Al to Ti ratios (Figure 4.9f), confirm a near-steady contribution of detrital Al and Ti to the basin. Normalization of P_2O_5 and Fe_2O_3 to Ti point to similar enrichment patterns across the successions (Figure 4.9g-i). Measured major metals are generally enriched across the sequence relative to UCC values (Figure 4.14a-c and Figure A1). Notably, Fe_2O_3 to TiO_2 and P_2O_5 to TiO_2 ratios, together with Loss on Ignition (LOI), are inversely correlated with P_2O_5 and Fe_2O_3 content throughout the sampled section (Figure 4.9j & Figure 4.10).

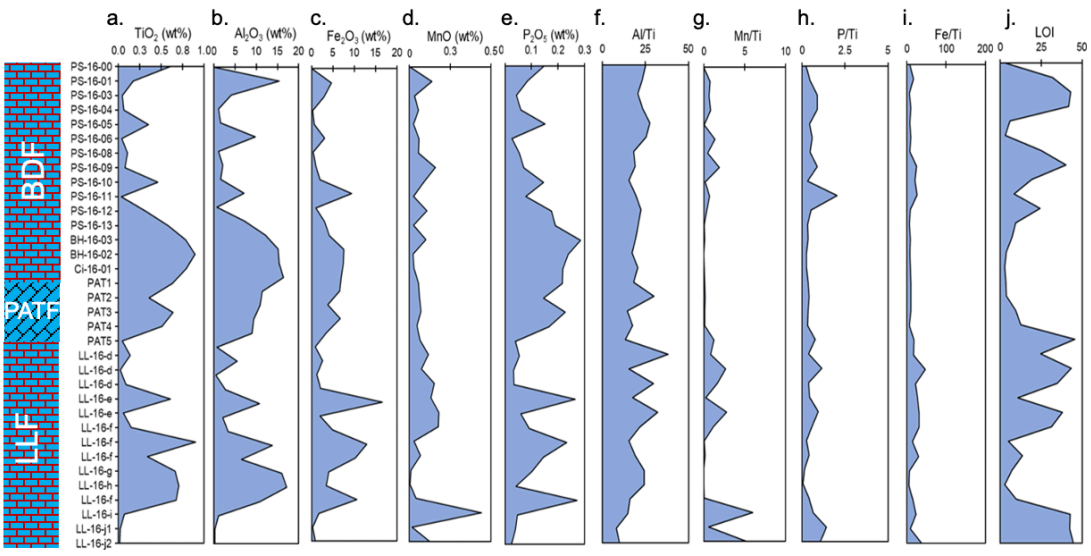

Figure 4.9| Major element distribution and loss on ignition (LOI) trends across the sampled sequence. a-e. Major element distribution. f-i. Major metal composition normalized to TiO_2. j. LOI trend.

The bulk P content, in terms of P_2O_5 data for the studied samples relative to fine-grain marine siliciclastic sedimentary rock content through time is shown in Figure 4.11.

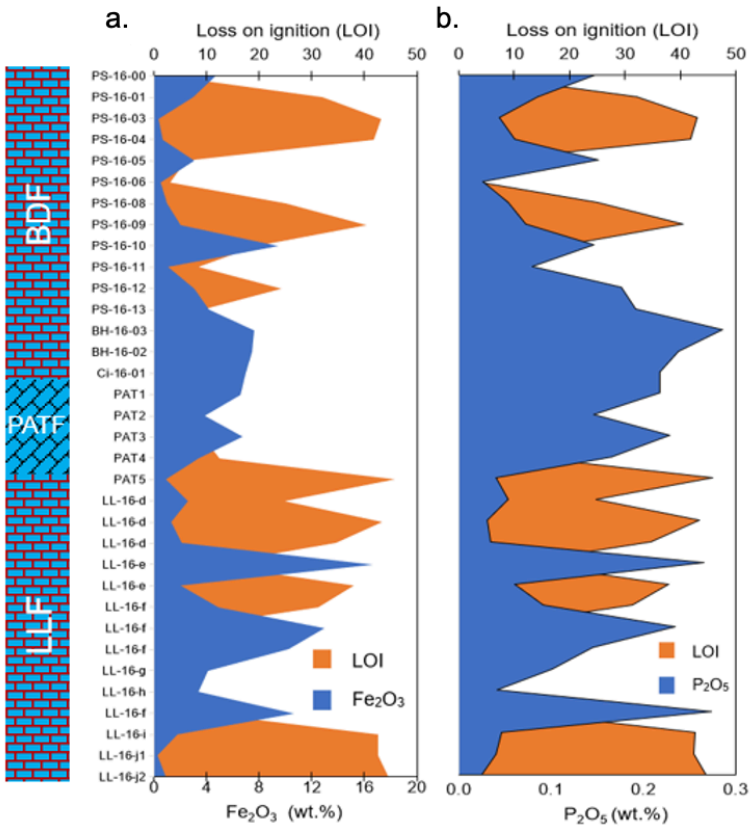

Figure 4.10| Graphs showing an inverse oscillatory behaviour between a. LOI versus Fe_2O_3 (wt. %) and b. LOI versus P_2O_5 (wt. %) distribution across the sampled succession.

Bivariate plots and Pearson correlations show positive correlations of P_2O_5 with poorly mobile TiO_2 and Al_2O_3 across lithostratigraphy. However, they are much weaker for Al_2O_3 in the pre-Snowball Earth LLF samples (Figure 4.12b-c). A similar relation appears for Fe_2O_3 versus TiO_2 and Al_2O_3 plots, but like P_2O_5 the correlation is unsupported for Al_2O_3 in the LLF section (Figure 4.12d-e). Al_2O_3 and TiO_2 (Figure 4.12f) and Fe_2O_3 and P_2O_5 (Figure 4.12a) in all three lithological sections also show a strong positive correlation. These observations suggest some level of decoupling of pre-Snowball P_2O_5 and Fe_2O_3 enrichment pathways to Al_2O_3 sources (Figure 4.12d-f). The bulk P concentration is inversely correlated with CaO, except for some immediate post-Snowball samples as shown in Figure 4.13a-b.

The tillite and immediate post-Snowball samples show low $\delta^{13}C_{org}$ and C_{org} (Figure 4.13c-d).

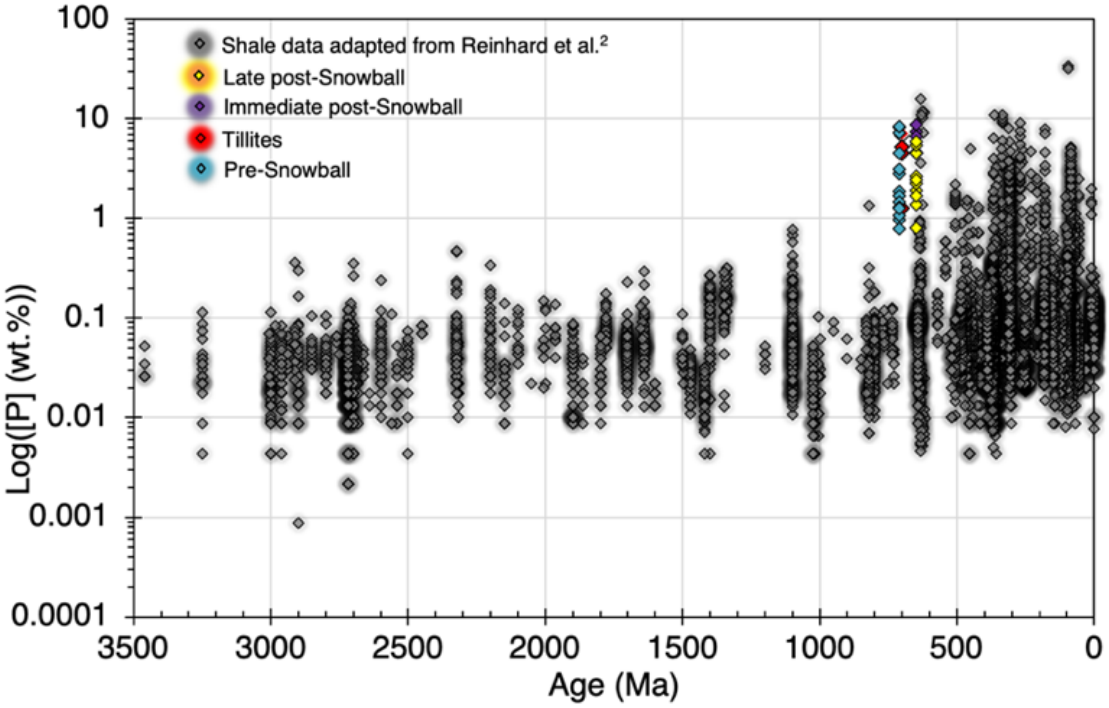

Figure 4.11| Distribution of sample P concentration across the sampled section relative to near continental margin marine siliciclastic sedimentary rock content through time (Reinhard et al., 2017).

The bulk Cr, V, Ni, and Co distribution across the succession (Figure 4.14a-d) exhibits enrichment across the tillite-immediate and post-Snowball intervals. Their corresponding V/Ti, Cr/Ti, Ni/Ti, and Co/Ti ratios however suggest minimal correlation (Figure 4.14e-h), suggesting that their accumulation was co-regulated by the same sedimentary processes. The enrichment of Ni, Co, Cr, and V is shown in Figure 4.15d-g. Chromium displays two anomalous enrichment peaks relative to UCC, one in the LLF that is also seen for V and Fe and a second corresponding to samples shown above to have high Cr/Ti ratios in the upper BDF (Figure 4.14f).

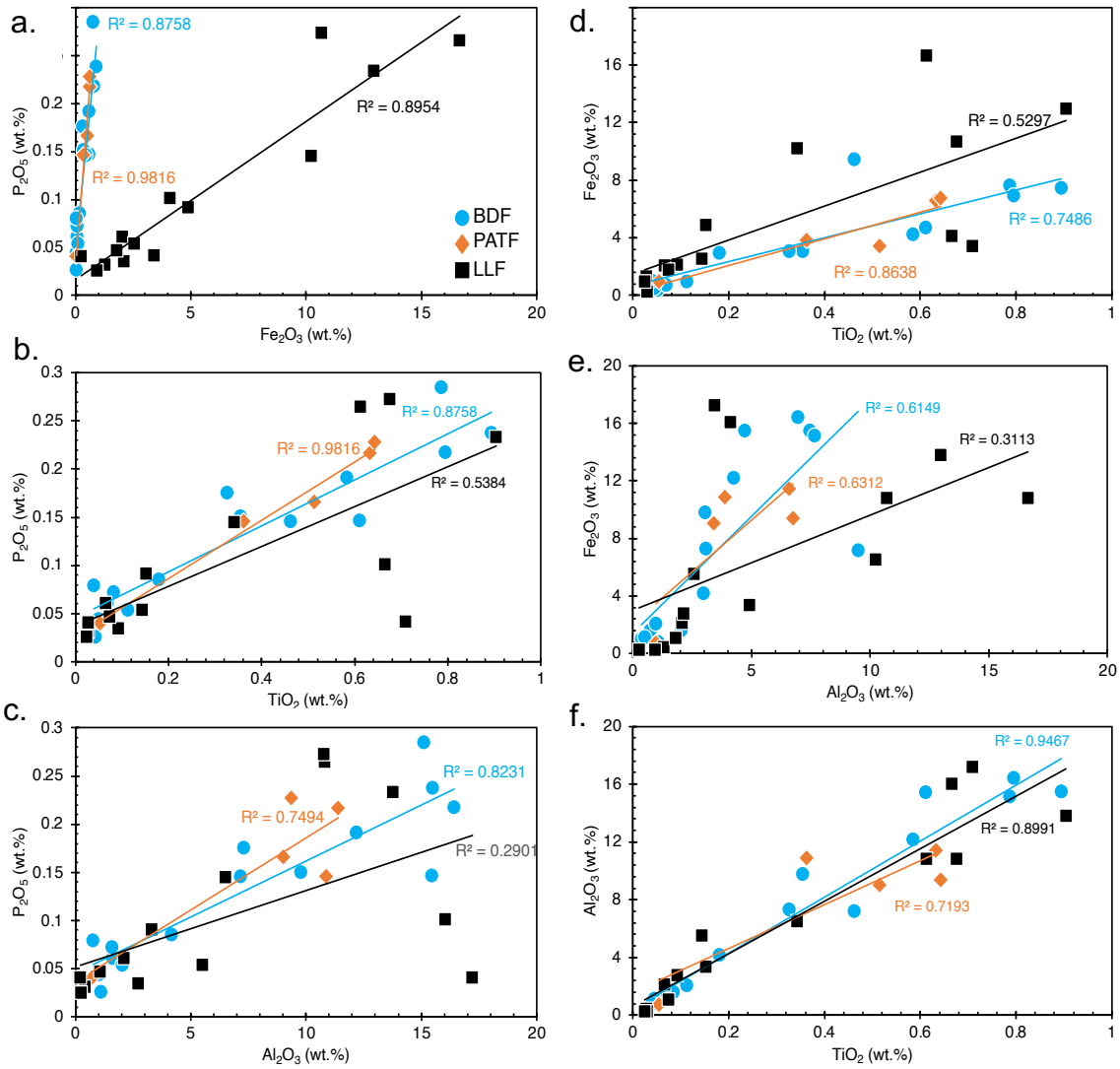

Figure 4.12| Major elements cross plots for pre-Snowball (LLF), Tillites (PATF) and post-Snowball (BDF). a. P_2O_3 versus Fe_2O_3. b. P_2O_3 versus TiO_2. c. P_2O_3 versus Al_2O_3. d. Fe_2O_3 versus TiO_2. e. Fe_2O_3 versus Al_2O_3. f. Al_2O_3 versus TiO_2.

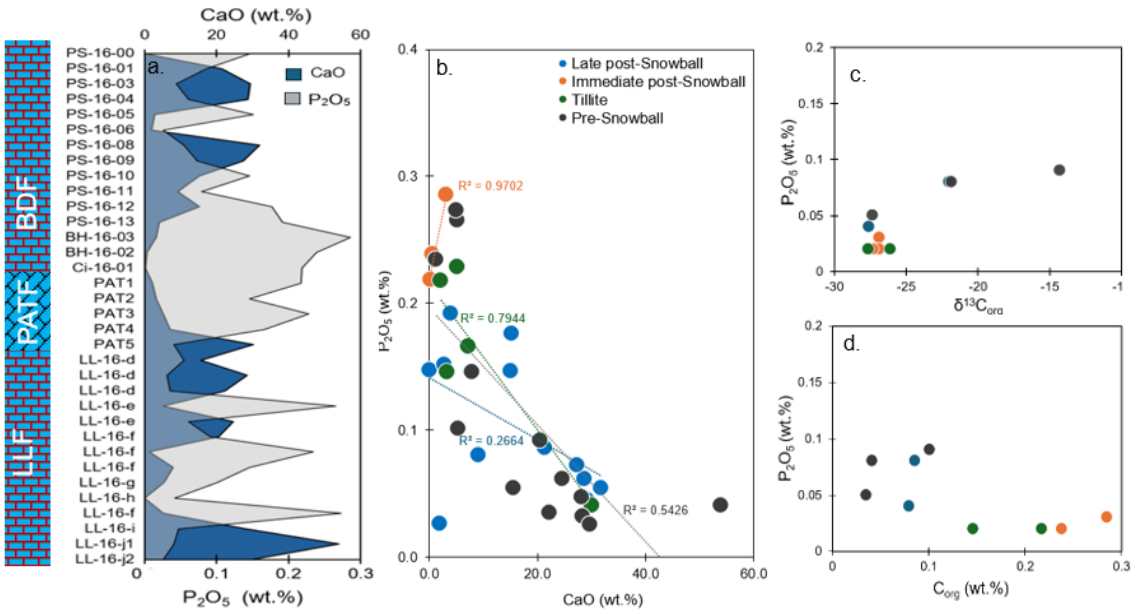

Figure 4.13| Relationship between facies Ca, P, $C_{org,}$ and $\delta^{13}C_{org}$ content. a. CaO versus P_2O_5 distribution along sequence stratigraphy. b. CaO versus P_2O_5 scatter plot. c. Scatter plot for representative data available for P_2O_5 and $\delta^{13}C_{org}$. d. Scatter plot for representative data available for P_2O_5 and C_{org}.

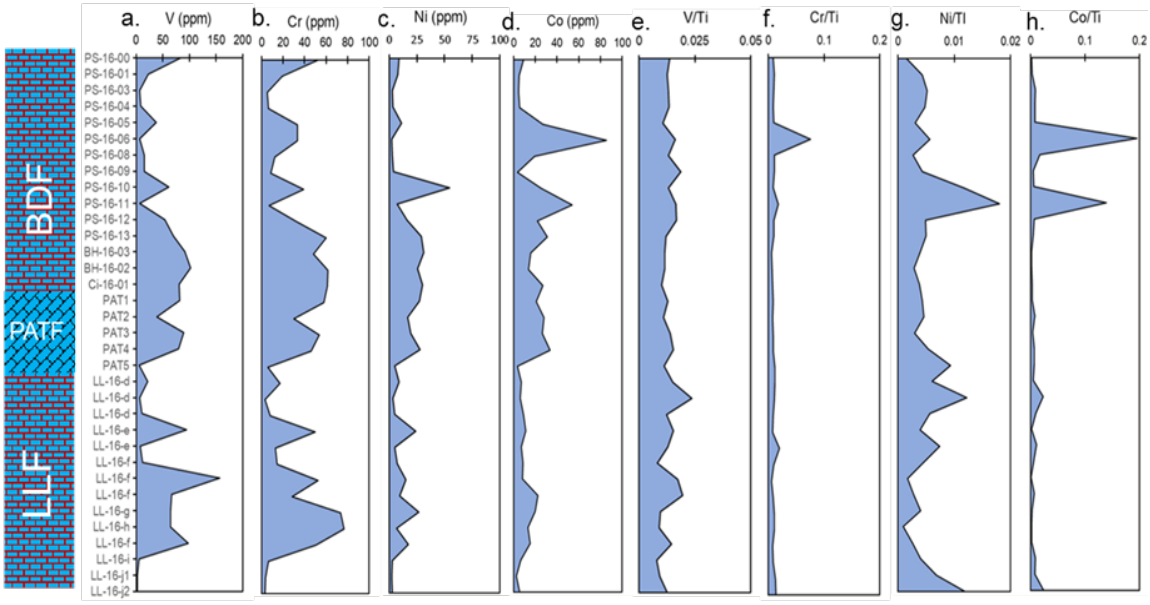

Figure 4.14| Trace element distribution trends across the sampled sequence. a-d. Trace element distribution. f-h. Trace metal composition normalized to TiO_2.

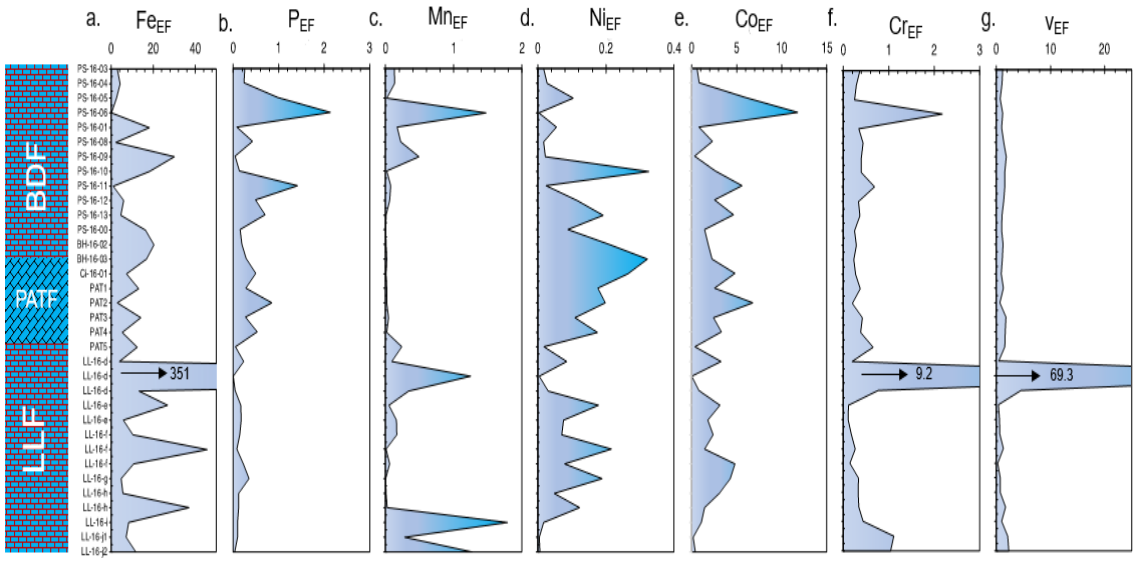

Figure 4.15| Major and trace element enrichment factors (EF), calculated as EFX = [(X/Al)sample/(X/Al)UCC], where X = concentration of element of interest according to Tribovillard et al. (2006). UCC, upper continental crust reference values according to Rudnick and Gao (2003).

4.3.3 Highly Reactive Fe and Seawater Dissolved P Content

The mineralogy data show that P is present in the samples and that its concentration varies predictably up the sequence. To estimate the amount of P that would have been accessible to life, sequential extraction analyses of the proportions of P and Fe associated with iron mineral phases were conducted. This analysis assumes that highly reactive Fe oxides (Fe-ox$_{HR}$) are a strong P sink and that the direct precipitation of Fe-ox$_{HR}$ from seawater would chemically remove dissolved P, thereby preserving the seawater history of dissolved P (e.g., Bjerrum and Canfield, 2002; Planavsky et al., 2010).

The distribution of chemically extracted Fe mineral phases in representative samples is shown in Figure 4.16a and Table 4.2. The Fe-ox$_{HR}$ phases (Fe$_{magnetite}$ +Fe$_{hematite}$ +Fe$_{carbonate}$ +Fe $_{oxyhydroxides +hematite}$) decline by a factor of two when emerging from the Snowball ice sheet melting stage and transitioning into the post-Snowball greenhouse state (Figure 4.16b). The ratio of Fe-ox$_{HR}$ over total Fe content displays distinct fluctuation patterns across the successions, marked by high ratios in pre-Snowball and late post-Snowball samples (Figure

4.16c). A similar pattern is noted when Fe-ox$_{HR}$ concentrations are compared to unreactive sheet silicate Fe content (Figure 4.16c).

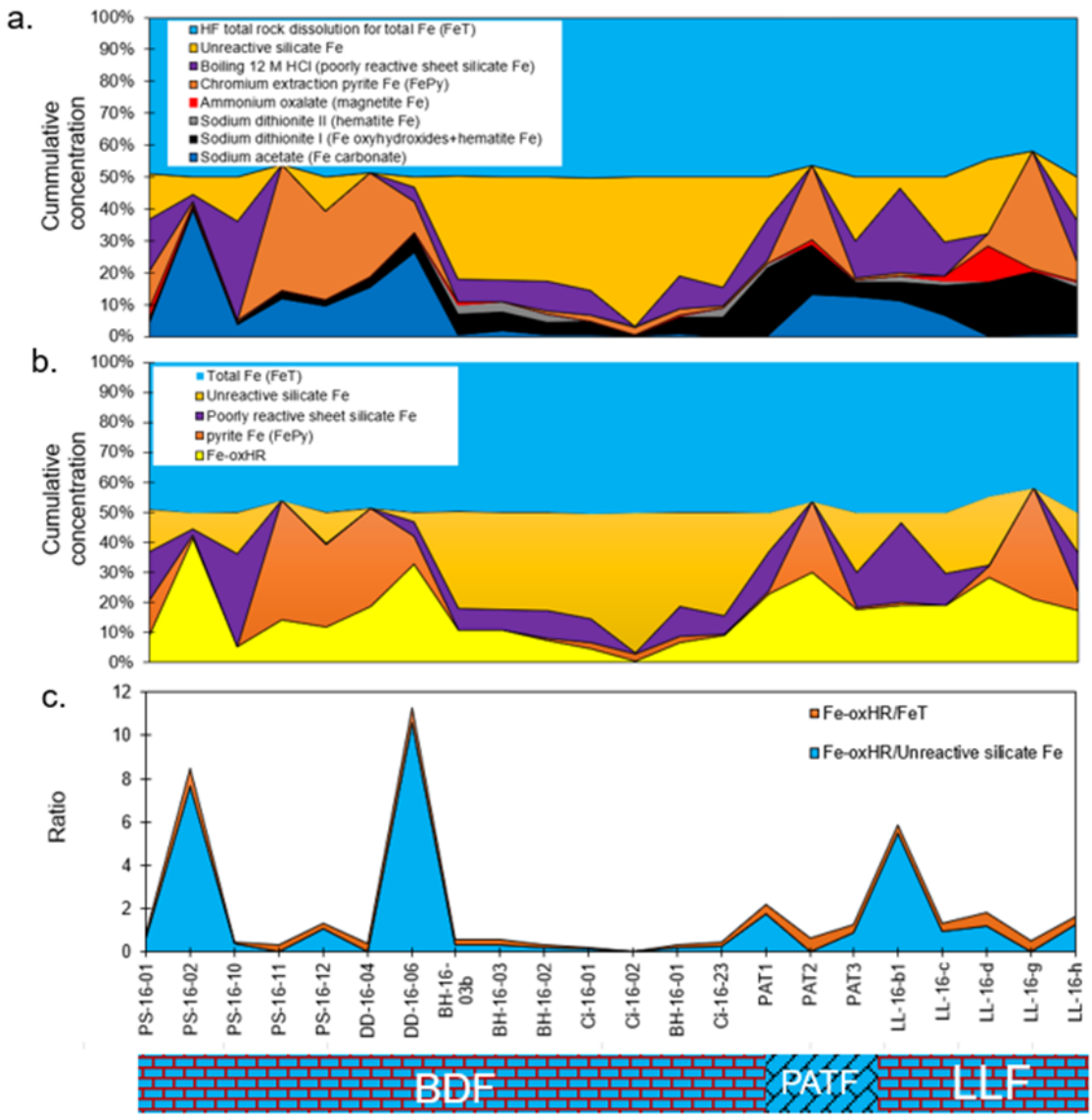

Figure 4.16| The distribution of reactive, poorly reactive, and unreactive Fe mineral phases. a. Contribution of defined Fe mineral phases expressed as a percentage of total Fe content across sequence stratigraphy. b. Contribution of highly reactive Fe oxyhydr(oxide) (Fe-ox$_{HR}$), poorly reactive sheet silicate Fe, unreactive sheet silicate Fe and pyrite Fe, expressed as a fraction of total Fe content across sequence stratigraphy. c. Fe-ox$_{HR}$ to total Fe ratio (Fe$_T$) (Fe-ox$_{HR}$/FeT) and Fe-ox$_{HR}$/unreactive Fe ratio.

The distribution of P associated with the sheet silicates and the iron oxide reservoirs is presented in Figure 4.17 and Table 4.3. The results reveal that 39.4% of measurable leached P is associated with the tillites and post-Snowball sheet silicates (Figure 4.17a), ~45.5% with

magnetite (42.5% post-Snowball and 3.0% pre-Snowball) (Figure 4.17b); ~6.1% with hematite (all pre-Snowball) (Figure 4.17c); ~9.1% of measurable leached P associated with the combined goethite, akageneite and hematite phases (all post-Snowball) (Figure 4.17d), compared to ~0% with Fe carbonates (Figure 4.17e). The data show that sedimentary P is fractionated mainly between the sheet silicates and magnetite in the PATF and post-Snowball BDF sequences (Figure 4.17 and Figure 4.18a). The sheet silicate bound P peaks in the tillites, ~361-403 times greater than during the pre-Snowball times. It is also noticed that magnetite-associated P/Fe ratios remained low and invariable through the pre-Snowball, the tillites and the immediate post-Snowball lithologies (Figure 4.18b) with elevated ratios appearing in the late post-Snowball samples.

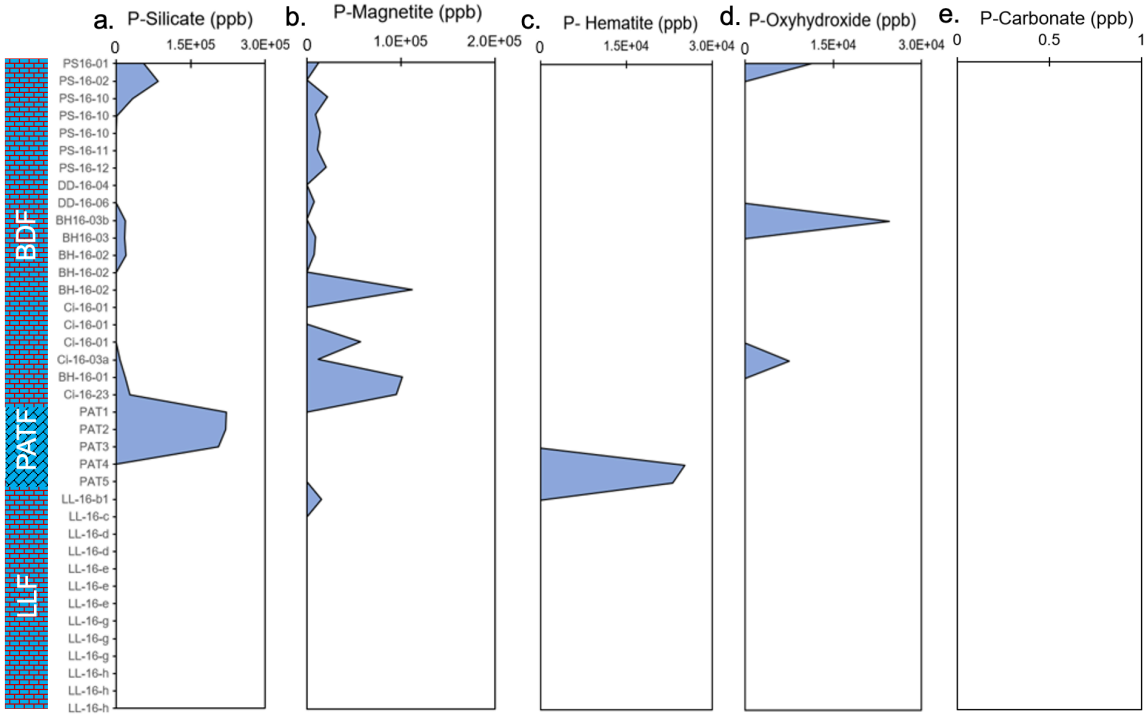

Figure 4.17| Chemically extractable P associated with iron oxides and phyllosilicates (sheet silicates) phases. a. Sheet silicate associated P. b. Magnetite associated P. c. Hematite associated P. d. Fe oxyhydr(oxide) associated P. e. Carbonate-associated P. Points where there are no data imply values were below the analytical detection limit of ~5 ppb and must therefore not be interpreted to imply absence. The trends are considered representative of true P distribution, considering that all samples were normalized to the same procedural treatment and analysis. P-oxyhydr(oxides) represent extractions that include goethite, akageneite and some hematite.

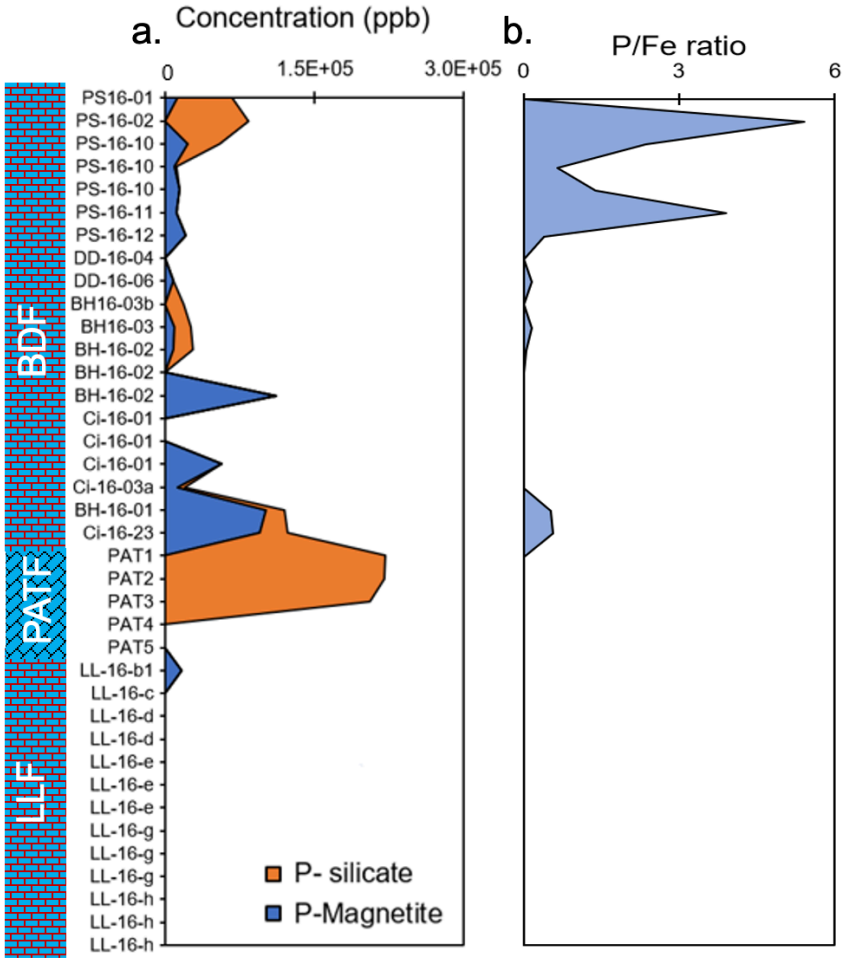

Figure 4.18| a. Representative putative magnetite- and sheet silicate-bound P distribution across sequence stratigraphy. b. Representative putative magnetite-bound P/Fe ratios across sequence stratigraphy.

Table 4.2| Iron extraction concentration (wt. %) for studied samples according to Poulton and Canfield (2005). PRSS= Poorly Reactive Sheet Silicate, URSS= UnReactive Sheet Silicate, and HR = Highly Reactive.

Samples	$Fe_{Carbonate}$	$Fe_{Oxyhydroxide}$	$Fe_{Hematite}$	$Fe_{Magnetite}$	Fe_{Pyrite}	Fe_{PRSS}	Fe_{URSS}	Fe_{T}	Fe_{HR}
PS-16-01	0.17052	0.07088	0.01042	0.08937	0.43247	0.59829	0.53149	1.81407	0.68429
PS-16-02	0.96685	0.03351	0.00697	-	0.02590	0.05568	0.13147	1.22039	1.03324
PS-16-10	0.07695	0.01031	0.01395	0.00095	-	0.61568	0.27290	0.98979	0.10121
PS-16-11	0.58670	0.12480	0.00269	0.00029	1.96694	0.00364	-	2.28318	2.68113
PS-16-12	0.69332	0.13010	0.00783	0.00526	1.97568	0.01364	0.74855	3.56912	2.80693
DD-16-04	1.02355	0.21784	0.00290	0.00357	2.13997	0.01682	-	3.20939	3.38426
DD-16-06	1.06205	0.24003	0.00890	0.00520	0.37839	0.19392	0.12406	2.00735	1.68937
BH-16-03b	0.06735	0.56146	0.26423	0.08698	-	0.64688	2.88931	4.42924	0.89304
BH-16-03	0.21388	0.69916	0.38288	0.00577	-	0.81505	3.82285	5.93381	1.29592
BH-16-02	0.05111	0.45775	0.26601	0.02487	0.09023	1.03799	3.60839	5.51148	0.86510
Ci-16-01	0.07807	0.39645	0.07921	0.00604	0.21489	0.77156	3.57724	5.12347	0.77466
Ci-16-02	0.01872	0.01497	0.00290	-	0.15534	0.01293	2.96024	3.16509	0.19192
BH-16-01	0.07593	0.36972	0.03901	0.01947	0.14060	0.76070	2.32411	3.71006	0.62526
Ci-16-23	0.01556	0.81858	0.40330	0.01716	0.06505	0.82090	4.74942	6.87281	1.30248
PAT1	0.04627	2.21897	0.12014	0.00755	0.10827	1.35487	1.36547	5.22153	2.50119
PAT2	0.18133	0.22100	0.00214	0.01400	0.32677	-	-	0.63943	0.73123
PAT3	1.06019	0.36554	0.05027	-	0.06598	0.97642	1.65521	4.17361	1.54198
LL-16-b1	1.61126	0.81952	0.29754	-	0.11132	3.78705	0.49480	7.12149	2.83965
LL-16-c	1.57704	2.12276	0.31494	0.35629	-	2.44125	4.68382	11.49609	4.37103
LL-16-d	0.00723	0.44654	0.00213	0.29000	0.10565	0.00099	0.61131	1.17385	0.56155
LL-16-g	0.03628	1.25208	0.00461	0.03400	2.32218	0.00323		2.62237	3.61516
LL-16-h	0.03828	0.57134	0.06391	0.00356	0.24565	0.50581	0.52585	1.95442	0.92275

Table 4.3| Co-extraction of Iron and Phosphorus according to Thompson et al. (2019). Measurements were conducted in ppb with instrument detection limits for P and Fe of 5.47 and 1.01 ppb, respectively.

Samples	$P_{Fe\ carboate}$	$P_{Fe\ oxyhydroxide\ +\ hematite}$	$P_{Magnetite}$	$P_{Hematite}$	$P_{Sheet\ silicate}$	$Fe_{Carbonate}$	$Fe_{Oxyhydroxide\ +\ hematite}$	$Fe_{Magnetite}$	$Fe_{Hematite}$
PS16-01	<5.47	11377.50	12439.50	<5.47	55037.30	576962.40	2019060.30	893670.10	104200.00
PS-16-02	<5.47	<5.47	<5.47	<5.47	83908.92	9668548.00	349100.80	<1.01	69696.50
PS-16-10	<5.47	<5.47	22211.90	<5.47	32707.10	3548.10	393526.00	9458.20	139450.40
PS-16-10	<5.47	<5.47	9129.81	<5.47	1583.20	503.00	385614.40	14084.50	345236.30
PS-16-10	<5.47	<5.47	13870.50	<5.47	<5.47	5870.10	1031272.31	10023.10	186665.11
PS-16-11	<5.47	<5.47	11212.70	<5.47	<5.47	6968.50	178972.92	2875.11	454608.50
PS-16-12	<5.47	<5.47	20239.20	<5.47	<5.47	6036.55	196343.34	52567.23	78283.20
DD-16-04	<5.47	<5.47	<5.47	<5.47	<5.47	10235520.00	204658.70	35655.91	28981.90
DD-16-06	<5.47	<5.47	8159.60	<5.47	<5.47	10620480.00	205571.50	51993.20	89049.30
BH16-03b	<5.47	24510.51	<5.47	<5.47	18182.48	731020.70	1304151.60	869752.80	2642321.00
BH16-03	<5.47	<5.47	8961.60	<5.47	16874.80	6624.50	52804.54	57744.13	36105.31.00
BH-16-02	<5.47	<5.47	7626.80	<5.47	19677.40	511091.90	1051874.70	182623.90	2660078.00
BH-16-02	<5.47	<5.47	<5.47	<5.47	<5.47	<1.01	31138.70	403486.20	89302.90
BH-16-02	<5.47	<5.47	111793.70	<5.47	<5.47	<1.01	45401.22	159990.40	81899.60
Ci-16-01	<5.47	<5.47	<5.47	<5.47	<5.47	780693.80	345062.81	24037.40	792078.20
Ci-16-01	<5.47	<5.47	<5.47	<5.47	<5.47	11961.30	353819.90	78.80	<1.01
Ci-16-01	<5.47	<5.47	57087.90	<5.47	<5.47	<1.01	<1.01	3163741.70	<1.01
Ci-16-03a	<5.47	7483.83	11908.20	<5.47	7197.10	596868.30	1823723.70	8074443.00	<1.01
BH-16-01	<5.47	<5.47	101228.30	<5.47	18241.10	759257.40	11220.30	194721.40	<1.01
Ci-16-23	<5.47	<5.47	95326.40	<5.47	28157.50	155604.00	66283.70	171608.80	4032970.00
PAT1	<5.47	<5.47	<5.47	<5.47	221195.90	44070.90	61077.90	57401.80	1201361.00
PAT2	<5.47	<5.47	<5.47	<5.47	220540.30	43053.30	69472.70	139987.60	21360.20
PAT3	<5.47	<5.47	<5.47	<5.47	205709.40	10601900.00	272647.60	<1.01	308746.70
PAT4	<5.47	<5.47	<5.47	25275.70	<5.47	7203.80	<1.01	<1.01	<1.01
PAT5	<5.47	<5.47	<5.47	23075.80	<5.47	89174.00	<1.01	<1.01	30658.41
LL-16-b1	<5.47	<5.47	15906.00	<5.47	<5.47	16112650.00	8195195.00	107204.00	2975413.00
LL-16-c	<5.47	<5.47	<5.47	<5.47	<5.47	72326.10	4465405.00	2760849.40	72326.10
LL-16-d	<5.47	<5.47	<5.47	<5.47	<5.47	<1.01	<1.01	2991426.20	<1.01
LL-16-d	<5.47	<5.47	<5.47	<5.47	<5.47	<1.01	502674.50	1018189.90	<1.01
LL-16-e	<5.47	<5.47	<5.47	<5.47	<5.47	<1.01	<1.01	<1.01	<1.01
LL-16-e	<5.47	<5.47	<5.47	<5.47	<5.47	<1.01	<1.01	<1.01	<1.01
LL-16-e	<5.47	<5.47	<5.47	<5.47	<5.47	<1.01	<1.01	<1.01	24073.10
LL-16-g	<5.47	<5.47	<5.47	<5.47	<5.47	362838.50	12520750.00	332936.65	46149.02
LL-16-g	<5.47	<5.47	<5.47	<5.47	<5.47	<1.01	<1.01	339640.57	<1.01
LL-16-g	<5.47	<5.47	<5.47	<5.47	<5.47	<1.01	<1.01	344212.29	<1.01
LL-16-h	<5.47	<5.47	<5.47	<5.47	<5.47	<1.01	<1.01	<1.01	1514491.44
LL-16-h	<5.47	<5.47	<5.47	<5.47	<5.47	<1.01	<1.01	<1.01	<1.01

4.4 Discussion

4.4.1 Evaluation of Sample Quality

4.4.1.1 Stratigraphic Associations

Comparative chemostratigraphic correlation of bulk facies geochemistry and $\delta^{13}C_{carbonate}$ and $\delta^{18}O_{carbonate}$ compositions (Figures 4.1-4.2 and Table 4.1) with previous studies of the same section (Arnaud & Fairchild, 2011; Brasier & Shields, 2000; Fairchild et al., 2018; Prave et al., 2009; Sawaki et al., 2010; Thomas et al., 2004) and from other Cryogenian sections (e.g. Amadeus Basin, central Australia And Mongolia (Swanson-Hysell et al., 2010; Verdel and Campbell, 2017)), was used to evaluate data quality and to account for potential post-depositional alteration of primary geochemical composition. The $\delta^{13}C_{carbonate}$ and $\delta^{18}O_{carbonate}$ values fall within the range reported in previous studies for the pre-glacial, glacial and post-glacial lithologies (Brasier and Shields, 2000; Prave et al. 2009; Sawaki et al., 2010; Arnaud and Fairchild, 2011; Fairchild et al., 2018), which have been correlated by geochronology and chemo/lithostratigraphy to the Cryogenian-Sturtian interval in Australia, Mongolia, Siberia, China, Oman, Namibia and Canada (Brasier and Shields, 2000; Arnaud and Fairchild, 2011; Hoffman et al., 2017). The pre-/late-Snowball samples were characterized by higher $\delta^{13}C_{org}$, C_{org} and $\delta^{13}C_{carbonate}$ excursions (Figure 4.1a-c) and lower carbonate content relative to concentrations in tillite samples analyzed for C isotope distribution (Figure 4.1d). However, XRD and SEM-EDS data are consistent with reported higher and more homogenous carbonate enrichment in the pre-/late-Snowball facies (Arnaud & Fairchild, 2011; Brasier & Shields, 2000; Fairchild et al., 2018; Prave et al., 2009; Thomas et al., 2004) (Figure 4.4 & Table 3.2). Associated $\delta^{18}O_{carbonate}$ trends generally decline up

sequence (Figure 4.1e), while the absence of $\delta^{13}C$ and $\delta^{18}O$ correlation suggests negligible diagenetic alteration of the primary $\delta^{13}C_{carbonate}$ signal (Figure 4.2).

4.4.1.2 Depositional Mechanisms, Primary and Secondary Mineral Phase

The enrichment of iron (Fe) and manganese (Mn) in sedimentary rocks is often associated with hydrothermal processes, while aluminium (Al) and titanium (Ti) are commonly linked to terrestrial sources (Pecoits et al., 2009). In marine sediments, identification of the hydrothermal influence can be estimated using various elemental discrimination diagrams such as the cross plots of Fe/Ti vs. Al/(Al+Fe+Mn) (Boström et al., 1969; Boström, 1970; Boström et al., 1972; Boström et al., 1973; Pecoits et al., 2009; Chi Fru et al., 2024). This plot is based on the calibration of average continental and oceanic crust, active hydrothermal ridge sediments and a mixture of these sources, with Fe/Ti >100 and low Al/(Al +Fe+ Mn) ratios indicating hydrothermal fluid influence The binary diagram supports the predominantly detrital origin components of studied samples. The < 100 Fe/ Ti (Figure 4.3) pointed to negligible hydrothermal influence on the composition of studied samples, and a dominant detrital origin (Pecoits et al., 2009).

Lithologies affected by greenschist metamorphism, confined to the margins of metabasaltic sills (Skelton et al., 2000), were excluded. Consistent with this sampling strategy, XRD and thin-sectioned SEM-EDS mineralogical analyses, revealed a major dominance of no to low-grade metamorphic clay minerals (as discussed in Chapter 3). Typical clay minerals like kaolinite, often associated with strong terrestrial weathering by chemical processes, are rare in the samples, while muscovite and illite clay minerals abundant in the modern upper continental crust (UCC) (Warr, 2022), occur more commonly across the lithofacies (Chapter 3). Chlorite, which also tends to be enriched in the UCC, was detected mainly in the deglaciating tillites. At the same time, the presence of albite (a

tectosilicate mineral) in all samples regardless of lithology (as discussed in Chapter 3), suggests an association with the erosion of crystalline bedrocks (Brasier and Shields, 2000).

Overall, the SEM-EDS mineral maps and XRD mineralogical analysis, show a variable prevalence of siliciclastic detrital material in all lithologies, with a dominance of sheet silicates and quartz, even in carbonate-rich facies. These findings agree with past observations (Arnaud & Fairchild, 2011; Brasier & Shields, 2000; Fairchild et al., 2018; Prave et al., 2009; Sawaki et al., 2010; Thomas et al., 2004), evidenced here by fine-grained siliciclastic particles in post-Snowball sediments and the prevalence of coarser quartz grains in tillite and pre-Snowball samples. The tillites are noted for hosting abundant detrital grains likely associated with illite, muscovite, albite, and, to a lesser extent, kaolinite (Figure 4.4 and Table 3. 2). Illite and muscovite are quantitatively more abundant in the post-Snowball facies. As demonstrated earlier, although detected in the pre-Snowball rocks, illite is not always present in readily quantifiable amounts. Typically, chemical weathering of most rock-forming silicates promotes secondary formation of clay minerals and Fe(III)- and Al-oxides, with an accumulation of residual quartz, heavy minerals, and sheet silicates like muscovite and biotite (Galán, 2006). Sediments and soils originating from this process can predictably contain >50% sheet silicates and Fe oxyhydroxides by volume, depending on the nature of the source rocks and prevailing climatic conditions (Galán, 2006; Warr, 2022). The variable occurrence of illite and muscovite across all sampled lithologies could be due to varying degrees of detrital supply or distinct local diagenetic pathways, while the largely low kaolinite content may be the result of possible transformation because kaolinite reacts with K-feldspar to form illite during burial diagenesis (Warr, 2022) and with alkaline fluids during metasomatism. Although chlorite can also form as a low-grade metamorphic mineral, with further transformation to muscovite at higher temperatures, the mineralogy of the facies is consistent with their suggested low metamorphic grade and observed preservation of

primary features (Arnaud & Fairchild, 2011; Brasier & Shields, 2000; Fairchild et al., 2018; Prave et al., 2009; Sawaki et al., 2010; Thomas et al., 2004). Further, the notable prevalence of quartz and sheet silicates (mainly clay minerals), including co-occurrence with tectosilicate albite, hints at the dominant supply of clastic debris to the primary sediments, derived from physical erosion of intermediate-to-felsic continental rocks (Figure 4.4).

4.4.2 PO_4^{3-} Enrichment Dynamics in Cryogenian Seawater

To determine how P was liberated from rocks on land, transported to the ocean, and then made accessible to photosynthetic organisms, the mineralogy and the behaviour of mobile and immobile trace metals were analysed. A wide range of geochemical changes emerged along the studied lithostratigraphic section (Figures 4.9- 4.15, Tables 3.3-3.4 and Table A2), distinguished by persistently elevated bulk sediment P_2O_5, TiO_2, Al_2O_5, Fe_2O_3, V, Cr, and Ni concentrations in the tillite and immediate post-Snowball samples, with much lower and more variable concentrations recorded in the PS-16 section of the Port a t-Struthain rocks in the upper BDF (Figure 4.9a-c & e and Figure 4.15a-c). The high concentration of Al_2O_5 and TiO_2, especially in the tillite and immediate post-Snowball samples, agree with the prevalence of various mineral phases pointing to substantial detrital contribution to sediment accumulation across the sequence. To test this idea, elemental normalization to Ti — a detrital indicator of authigenic enrichment (Ruttenberg and Berner,1993; Heiri et al., 2001) — shows subtle enrichment consisting of two broad patterns across the stratigraphic profile (Figure 4.9j-p). This relationship is highlighted by two observations. First, a reasonable stratigraphic correlation exists between P/Ti and Fe/Ti and to some degree with Mn/Ti ratios (Figure 4.9n-p), although generally, MnO does not show significant lithostratigraphic variations (Figure 4.9d). Second, a broad minimal correlation is observed for V/Ti, Cr/Ti,

Ni/Ti, and Co/Ti (Figure 4.14e-h), suggesting that their accumulation was co-regulated by the same sedimentary processes.

Interestingly, Cr/Ti is anomalous in the sense that in the lower BDF, when the other elements display multiple peaks, Cr/Ti distribution remains uniform but becomes noticeable when enrichment in most elements is muted in the upper BDF Port a t-Struthain section (i.e., the PS-16 samples). To add to these observations, the near static Al_2O_3 to TiO_2 ratios (Figure 4.9f) are interpreted to either reflect stable detrital contribution and/or potential long-term sediment accumulation from a similar rock source. This point is revisited subsequently.

Comparable Fe_2O_3 to TiO_2 and P_2O_5 to TiO_2 ratios, together with Loss on Ignition (LOI) being inversely correlated with P_2O_5 and Fe_2O_3 content throughout the sampled section (Figures 4.9r - 4.10), suggest bulk sediment P_2O_5 and Fe_2O_3 are most likely preserved in inorganic instead of organic and carbonate mineral phases. Where LOI values are elevated, they presumably predict higher combustible sedimentary organic and/or carbonate content, while lower values indicate the contrary, due to the higher susceptibility of carbonates and organic matter to complete combustion to CO_2 under elevated temperatures (Heiri et al., 2001). Indeed, the lowest LOI values are recorded in the carbonate-poor PATF and lower BDF section where sustained peak P_2O_5 and Fe_2O_3 concentrations are found, compared to the minor and more variable P_2O_5 content in the carbonate-rich LLF and upper BDF PS-16 facies (Figure 4.9c, e & j). Higher LOI values that tend to relate inversely with P_2O_5 and Fe_2O_3 concentrations across the section (Figure 4.10) are unique to the carbonate-rich LLF and PS-16 upper BDF samples. Measured trace metals are generally enriched across the sequence relative to UCC values (Figure 4.15d-g). Notably, significant co-enrichment of P is also observed in the tillites and upwards relative to the UCC, compared to pre-Snowball times (Figure 4.15b). Despite their overall similar redox properties, Mn enrichment patterns relative to the UCC are dissimilar to those of Fe,

particularly in some tillite and immediate post Snowball samples (Figure4.15a & c), pointing perhaps to different enrichment pathways or the known differences in sensitivity to reduction. Chromium shows two anomalous enrichment peaks relative to UCC, one in the LLF that is also seen for V and Fe and a second corresponding to samples shown above to have high Cr/Ti ratios in the upper BDF (Figure 4.14j and Figure 4.15a, f & j).

The generally low C_{org} levels across the sampled sequence (Figure 4.1b) are considered to be of little importance to sedimentary P and Fe preservation. This is consistent with the inverse relationship these two key elements expressed with respect to LOI, discussed earlier. Moreover, positive correlations are revealed for P_2O_5 and Fe_2O_3 and poorly mobile TiO_2 and Al_2O_3 across lithostratigraphy, although they are much weaker with respect to Al_2O_3 for the pre-Snowball Earth LLF samples (Figure 4.12a-c). The strong correlations between TiO_2, P_2O_5 and Fe_2O_3 for tillites and post-Snowball facies may consequently be the result of sediment source homogenization by the indiscriminate erosional action of melting ice sheets. Regardless, these observations provide further evidence for across sequence P_2O_5 and Fe_2O_3 enrichment by detritus.

The low C_{org} and negative $\delta^{13}C_{carbonate}$ distribution in the facies (Figures 4.1-4.2 and Table 4.1) suggest microbial oxidation of C_{org} likely prevailed at the sediment-water interface, which would have promoted the release of organic-bound P into seawater and sediment porewater, influencing dissolved aqueous P content and eventual incorporation into various sedimentary minerals. However, the low C_{org} of Precambrian has also been used to argue against a significant contribution from P in the microbial oxidation of C_{org} (Johnson et al., 2020; Rasmussen et al., 2021). It is also possible that prevailing environmental conditions influenced the ongoing microbial transformation of P-rich C_{org} and Fe-ox_{HR} minerals to trigger enough diagenetic sediment porewater P supersaturation (Ruttenberg and Berner, 1993). For example, the geochemical data suggest that bulk primary sediment P was

predominantly associated with non-calcium bearing minerals such as Fe-ox_{HR} and unreactive detrital silicate phases (Figure 4.13a-b and Figure 4.17), which would have starved primary sediments of dissolved P. Except for some immediate post-Snowball samples, across-sequence CaO and P_2O_5 inverse correlations, being up to 79% for the tillites (Figure 4.13a-b), corroborate limited potential P preservation in non-calcium bearing mineral phases. As discussed above, this view is supported by low LOI, low-carbonate facies associated with bulk high P_2O_5/Fe_2O_3 ratios and high LOI, high-carbonate lithologies with bulk low-P_2O_5/Fe_2O_3 ratios (Figure 4.10). Overall decreasing P_2O_5 concentration coincides with C_{org} content that increases from post-Snowball to pre-Snowball facies (Figure 4.13c), signalling either possible diagenetic P enrichment or loss in primary sediments through microbial oxidation of organic-rich P biomass originating from the water column. Indeed, our lowest $\delta^{13}C_{org}$ and C_{org} values in the tillites and immediate post-Snowball interval (Figure 4.1a-b) coincide with P_2O_5 enrichment compared to the low P_2O_5 pre-Snowball samples (Figure 4.13c-d). Based on these observations, microbial recycling of organic-rich P at the sediment-water interface could explain the increasing prevalence of apatite in the immediate post-Snowball interval. However, the data suggest that the P supersaturation required to spontaneously precipitate large amounts of apatite precursor phases and significant substitution in carbonate minerals (Ruttenberg and Berner, 1993; Dodd et al., 2021) was limited, especially in the pre-Snowball interval. Instead, our results indicate that dominant P supply and enrichment in the primary sediments mostly reflect detrital loading with non-apatite minerals. Moreover, as we show below, the synthesis of Ca-rich P minerals was perhaps limited by abundant Fe-ox_{HR} particles acting as efficient scavengers of dissolved PO_4^{3-} at the sediment seawater interface.

Redox-sensitive Mn shows a weak negative correlation with TiO_2 and Al_2O_3 across all facies (Figure A2), suggesting that Mn enrichment pathways are to some extent decoupled

from those of P_2O_5 and Fe_2O_3, particularly given the considerable positive correlation between P_2O_5, TiO_2, and Al_2O_3 (Figure 4.9). Except for the short-lived spike in Cr enrichment in the upper BDF relative to Ti, overall, our data do not indicate that significant oxidative/chemical weathering of terrestrial rocks was a predominant mechanism for PO_4^{3-} delivery to seawater throughout the sampled section. This observation is consistent with independent findings pointing to primary sediment detrital inputs of continental provenance (Arnaud & Fairchild, 2011; Fairchild et al., 2018; Prave et al., 2009; Sawaki et al., 2010; Thomas et al., 2004), reinforced by our stronger physical rather than chemical weathering indicators. This relationship is further strengthened by the association of average UCC profiles (as mentioned in Chapter 3) with the continental margin location of the sedimentary basin.

High Cr/Ti ratios recorded during the GOE were previously ascribed to the mobilization of dissolved Cr from land to the ocean by acid rock drainage via the activity of acidophilic aerobic bacteria following oxygenation of the atmosphere (Konhauser et al., 2011). A similar but previously unreported acidification event could explain the brief spike in Cr/Ti ratios in the upper BDF. However, a close look at the data indicates that total P_2O_5 and Fe_2O_3 contents immediately before, during and after the transient increase in Cr/Ti ratios remained low, suggesting that even if this event was triggered by acidic weathering of terrestrial rocks, it cannot explain the behaviour, source, and mechanism of P_2O_5 enrichment in our samples.

Further, the highly soluble properties of ferrous and ferric Fe under extremely acidic conditions characteristic of acid rock drainage (Akcil and Koldas, 2006) should translate to relative co-enrichment of Fe and Cr in the sediments with respect to poorly mobile Ti. This relationship is not seen in the studied section. Moreover, the broad expression of similar but conservative Fe/Ti and P/Ti profiles throughout the BDF and the tillite formation are consistent with reported low to moderate chemical weathering indices in the tillites (Panahi

and Young, 1997). Thus, the combined data better reflect terrestrial detritus (clay minerals) contributing to high bulk P_2O_5 and Fe_2O_3 enrichment in the PATF and the lower BDF section, assuming continental erosion by melting ice sheets was the principal source of detrital inputs into the sediment pile. Moreover, our bulk P data are consistent with historical records showing a substantial spike in the P content of Cryogenian fine-grained marine siliciclastic rocks (Figure 4.9).

4.4.3 Phosphorus and Iron Dynamics During the Post-Snowball Transition

In light of the above discussions (phosphate was delivered to seawater by terrestrial sheet silicate detritus), the question is posed whether P was associated with Fe in the primary sediments (e.g., highly reactive iron phases) and, if so, whether such a relationship can provide insights into seawater dissolved P profiles. The distribution of leachable highly reactive Fe (Fe_{HR}) phases in the form of Fe-ox_{HR} + pyrite Fe and poorly reactive sheet silicate Fe (Figure 4.16a-b) was explored according to Poulton and Canfield (2005), Poulton and Canfield (2011) and Raiswell et al. (2018). The ratio of leachable Fe-ox_{HR} over total Fe content, suggests that Fe-ox_{HR} constitutes only a small proportion of total Fe across the sequence, with distinct fluctuations that parallel low pre-Snowball P_2O_5, immediate post-Snowball high P_2O_5 and late post-Snowball low P_2O_5 intervals (Figure 4.16c). A similar pattern is noted when Fe-ox_{HR} concentrations are compared to unreactive sheet silicate Fe content, with the data suggesting that the majority of Fe throughout the sampled stratigraphy is largely present as unreactive silicates. These data are consistent with the above observations pointing to significant detrital contribution to sediment Fe enrichment, as opposed to chemical sedimentation.

Bulk sediment P analysis, as shown by the results (Figure 4.17), provides important clues on the overall behaviour of P in marine waters (Feely et al., 1998; Bjerrum and Canfield, 2002; Planavsky et al., 2010; Reinhard et al., 2017). However, bulk sediment P content is a poor differentiator of reactive and unreactive P composition and therefore is an unreliable indicator of P bioavailability. Instead, I consider the linear correlation between Fe-ox_{HR}-bound P and dissolved P (Wheat et al., 1996; Feely et al., 1998; Bjerrum and Canfield, 2002; Planavsky et al., 2010) in modern marine systems as the best estimator of dissolved P behaviour during sediment deposition, following the recommendation of Thompson and others (Thompson et al., 2019).

The sheet silicates in the tillites and immediate post-Snowball, record the highest leachable P content. Overall, the distribution of P between the sheet silicates and the Fe-ox_{HR} reservoir indicates that high P enrichment in association with sheet silicates at the terminal Snowball immediate post-Snowball greenhouse transition is marked by redistribution of P to a putative magnetite sink (Figure 4.18a). A corresponding ~twofold reduction in the size of the leachable Fe-ox_{HR} inventory at this time would have reduced the potential removal efficiency of dissolved PO_4^{3-} from seawater by an equally similar magnitude since Fe-ox_{HR} is otherwise a strong P sink (Wheat et al., 1996; Feely et al., 1998; Bjerrum and Canfield, 2002). This process alone would have enabled the substantial build-up of dissolved PO_4^{3-} in immediate post-Snowball seawater relative to the period before and after, both distinguished by a higher Fe-ox_{HR} reservoir (Figure 4.18a). Furthermore, the peaking of putative sheet silicate P in the tillites, which is hundreds of times above baseline detection concentrations of 5.47 ppb in the pre-Snowball interval, is consistent with rock flour production expected with the mechanical grinding action of melting ice sheets on the bedrock. This supposition is supported by SEM-EDS imaging showing elevated fine-grained sheet silicate clasts in the immediate post-Snowball samples (Figure 4.4).

I assume that the coincidental rise of appreciable P enrichment in immediate post-Snowball magnetite grains, relative to the tillite interval, points to increasing immediate post-Snowball co-precipitation of magnetite and dissolved PO_4^{3-} out of seawater. A test of this hypothesis finds that peaks in leachable magnetite-associated P/Fe ratios correlate with the appearance and persistence of magnetite-bound P at the tillite post-Snowball boundary and upwards (Figure 4.18b). This up-section correlation between magnetite-bound P concentration and magnetite P/Fe ratios, suggests magnetite precipitation captures a snapshot of the potential dissolved PO_4^{3-} content of the reservoir from which it formed. The distinctly variable but higher P/Fe values in the late low-P_2O_5 post-Snowball interval are best explained by the emergent long-term moderate presence and persistence of magnetite-bound P in the facies (Figure 4.18b). The mostly non-variant magnetite-bound P trend at this time, except for a single spike, points to steady scavenging of PO_4^{3-} by an increasingly scarce magnetite reservoir, instead of a rise in dissolved PO_4^{3-} content.

The release of bound PO_4^{3-} to seawater and/or sediment pore water by diagenetic dissolution of Fe-ox_{HR} minerals could, however, account for the two times smaller Fe-ox_{HR} budget in the immediate post-Snowball P_2O_5-rich rocks, compared to the P_2O_5-depleted sediments that bracket this interval. Yet, because diagenesis results in considerable loss of Fe-ox_{HR}-bound P, this interval should be accompanied by a parallel lowering of sedimentary P_2O_5 and Fe-ox_{HR}-associated P content if this were the case. Instead, we observe a co-increase in both bulk P_2O_5 and potential magnetite-bound P at this time. Further, the comparatively lower pre/late post-Snowball P_2O_5 and magnetite P reservoirs cannot be explained by reductive dissolution of Fe-ox_{HR} since their Fe-ox_{HR} inventories are about twice the size found in the P_2O_5-rich immediate post-Snowball section. In addition, the transition of bulk Fe/Al ratios (as discussed in the next chapter) from the higher values expected with enhanced authigenic Fe enrichment during the pre-Snowball time to lower

detrital Fe/Al ratios averaging ~0.5 in the tillites and for most of the post-Snowball sediments, is consistent with negligible reductive Fe mobilisation by diagenetic microbial Fe-reduction (Lyons et al., 2003; Lyons and Severmann, 2006; Raiswell et al., 2018). Importantly, the enrichment of P in the leachable immediate post-Snowball magnetite reservoir, which comes after a rise in associated sheet silicate-bound P, is best explained by the transfer of sheet silicate-bound P to seawater, followed by chemical enrichment in the sediment pile by Fe-ox_{HR} produced in the greenhouse interval.

My estimates are conservative within reasonable error margins, considering that the designation of extractable Fe-$_{oxHR}$ phases in the defined Fe mineral pools can at times be misleading. For example, goethite was previously detected in the ammonium oxalate extract attributed to magnetite (Hepburn et al., 2020). My data are nonetheless consistent with SEM-EDS mineral imaging and bulk XRD mineralogical analysis, which failed to detect putative goethite-enriched phases as a major mineral constituent in the samples, suggesting an absence or low levels below detection (Figure 4.4). This observation is consistent with potential pre-Snowball magnetite contributing only an estimated ~5.4% P to the total extractable P pool, compared to up to 37.8% for the post-Snowball time.

4.4.4 Magnetite Precipitation and Seawater Dissolved P Behaviour

Magnetite, a common Fe mineral in Precambrian Fe-rich sedimentary rocks, often forms through a combination of biotic and abiotic processes involving ferrihydrite and green rust precursors (Konhauser et al., 2005; Halama et al., 2016; Halevy et al., 2017; Han et al., 2020; Han et al., 2021). In this light, green rust and ferrihydrite are thought to sequester and bury dissolved seawater trace nutrients in the sedimentary pile (Hansen and Poulsen, 1999; Zegeye et al., 2012). Particularly, the ability for both green rust and ferrihydrite to bind aqueous PO_4^{3-} has been demonstrated experimentally (Wheat et al., 1996; Feely et al., 1998;

Bjerrum and Canfield, 2002; Konhauser et al., 2007; Barthélémy et al., 2012; Chi Fru et al., 2016b; Hemmingsson et al., 2018), with green rust reported to possess a greater propensity to bind PO_4^{3-} than ferric Fe (Barthélémy et al., 2012). It is thus reasonable to assume that the incorporation of P into magnetite crystals scaled proportionally with the concentration of primary seawater green rust and ferrihydrite magnetite precursors. Nonetheless, although prograde metamorphism exerts a negligible effect on magnetite transformation, it can become significant in the presence of olivine (Klein, 2005; Frost et al., 2007). Mineralogical appraisal of studied samples by XRD and SEM-EDS mapping, however, failed to identify olivine as an important mineral phase throughout the sequence, while the influence of hydrothermal fluids on Fe distribution appears to be insignificant (Figures 4.4- 4.8). Moreover, a lack of covariation between carbonate Fe and magnetite Fe reservoirs across sequence stratigraphy, further suggests little or no thermal breakdown of Fe carbonates to magnetite by burial metamorphism (Rasmussen and Muhling, 2018). Importantly, spontaneous binding of PO_4^{3-} to magnetite occurs by physical adsorptive intermolecular attractive forces and by chemical transfer of electrons between magnetite and PO_4^{3-} molecules, promoting an adsorption capacity of ~57.8 mg of PO_4^{3-} per gram and resulting in a positive correlation between magnetite-bound and dissolved PO_4^{3-} (Daou et al., 2007). This binding of dissolved PO_4^{3-} by magnetite enhances magnetite's stability (Daou et al., 2007; Ajmal et al., 2018) and therefore enhancement of possible long-term preservation in sediments.

The prevalence of putative magnetite grains, particularly in the immediate post-glacial P_2O_5-rich interval, compared to the low P_2O_5 intervals (Figure 4.4), reflects nascent post-glacial seawater conditions, probably related to the balance between seawater oxygen content and local Fe sedimentary mechanisms as shown in next chapter. For instance, modern turbid Arctic glacial outflows generally display high dissolved Fe content of up to

20 μM, which decreases to nanomolar concentrations at the shelf-fjord water mixing boundary (Hopwood et al., 2020). This trend results from the rapid flocculation of dissolved Fe at this interface and the binding of particle surfaces because of increasing salinity and pH, triggering the loss of up to 98% of total dissolved Fe (Boyle et al., 1977; Hopwood et al., 2020). Similar rapid precipitation of particulate Fe with increasing oxygenation at Snowball melt water-seawater interfaces would have accelerated the scavenging of dissolved P released by clay minerals along the gradients of rising salinity and pH in the continental margin waters (Froelich, 1988; Hao et al., 2021a). This process would have favoured the preferential formation of magnetite as allowed by local thermodynamic conditions of redox, electrical conductivity, pH, and temperature (Gnanaprakash et al., 2007; Pang et al., 2007). For instance, magnetite precipitation and stability may have been favoured at the lower temperatures and pH conditions that accompanied the immediate post-glacial CO_2-rich world (Gnanaprakash et al., 2007; Pang et al., 2007). Thus, considering the linear relationship existing between magnetite-bound and aqueous PO_4^{3-} (Ajmal et al., 2018), PO_4^{3-} bioavailability in the immediate post-Snowball waters potentially increased by at least 20-fold compared to pre-Snowball conditions. Unlike the immediate post-Snowball interval, putative immediate pre-Snowball magnetite-bound P remained below the instrument detection limit of ~5 ppb, with the data indicating that unreactive silicate-bound P dominated bulk P burial before and during the Sturtian Snowball (Figure 4.18).

4.5 Conclusion

This study reveals bulk P content comparable to previously published concentrations for fine-grain siliciclastic Cryogenian facies. These data suggest that Cryogenian continental seawater P bioavailability before, during, and after the Sturtian glaciations may have been limited by persistent detrital and variable Fe-ox_{HR} loading. Further, microbial recycling of organic-rich P at the primary sediment-water interface was insufficient to generate sediment

porewater P saturation to spontaneously trigger vast precipitation of calcium-bearing P minerals across the sequence. This observation limits potential diagenetic interference with primary sediment P content. Production of dissolved sheet silicate bound PO_4^{3-} would have been facilitated by grinding the bedrock by thawing ice sheets, with the generation of sub-glacial acidity (Macdonald et al., 2018). These subglacial acidic conditions, combined with acidic water produced by the immediate post-Snowball high CO_2 atmosphere (Huang et al., 2016), would have sustained chemical leaching of P from rocks, including apatite minerals (Smith et al., 1977). The sheet silicate clay minerals that are expected to more easily bind PO_4^{3-} in more acidic conditions (Froelich, 1988; Gérard, 2016; Hao et al., 2021a) transported and liberated bound PO_4^{3-} to seawater following contact with higher marine pH (Froelich, 1988; Violante & Pigna, 2002; Hao et al., 2021a) and salinity (Némery & Garnier, 2007; Warr, 2022). The sudden decline in leachable sheet silicate P entering the immediate post-Snowball state, followed by an abrupt rise in magnetite P content by at least a factor of 200 compared to Pre-Snowball hints at a potential switch in P sink from clays to seawater. The increase in dissolved seawater P promoted primary productivity and oxygenation, with the resultant recycled biomass P captured together with dissolved inorganic P and preserved by Fe-ox_{HR} minerals generated in the oxidized water column. Taken together, the data indicate a major switch from marine waters with low dissolved PO_4^{3-} content to an enlarged inventory created by a deglaciating Cryogenian Snowball clay factory. The fertilization of the ocean with P likely promoted the rapid development of more oxygenated waters soon immediately following the end of the Sturtian Snowball glaciation, as explored in the next chapter.

Chapter 5: Redox Condition across Sturtian Glaciation

5.1 Introduction

The clay mineral composition during the Sturtian Snowball glaciation varied with climate, as shown in previous chapters. Chapter 4 connects these clay mineral variations to the supply of phosphorus (P) to seawater across the Sturtian Snowball Cryogenian interval. This chapter explores whether this climate-driven link between clay minerals and P influenced the oxygenation of Cryogenian seawater and the atmosphere. Tracking climatic and oceanic redox changes throughout the Neoproterozoic Cryogenian geological timeline is crucial for a better understanding of the coevolution of life and environment throughout Earth's history (e.g., Canfield et al., 2007; Lenton et al., 2014; Ding et al., 2019). Recent studies suggest that the Neoproterozoic climatic transitions from icehouse to greenhouse conditions may have been attributed to the delivery of nutrients by clay minerals, enhancing primary productivity in the Cryogenian interglacial ocean (Chi Fru et al., 2023) which led to biological innovation and diversification (Brocks et al., 2017; Bowyer et al., 2023).

While still highly debated, over the past decade, understanding of the Neoproterozoic Ocean's chemical evolution has evolved markedly. Some studies suggest that Neoproterozoic Ocean redox chemistry was highly variable, and did not proceed unidirectionally but instead went through a series of oxygenation pulses (Krause et al., 2022; Lyons et al., 2024), with oxic surface waters commonly underlain by ferruginous conditions (e.g., Canfield et al., 2007; Planavsky et al., 2011; Poulton and Canfield, 2011). Geochemical evidence points to the development of multiple oceanic oxygenation events, local or global, in the wake of the Sturtian and Marinoan Snowball glaciations (Sahoo et al.,

2012; Zhang et al., 2015; Lau et al., 2017; Meng et al., 2024; Meng et al., 2024), across an otherwise largely anoxic ocean.

The Neoproterozoic Oxygenation Event (NOE), was originally interpreted as an increase in atmospheric oxygen from Proterozoic to near-modern levels (generally from 1–10% PAL) (Kump, 2008; Lyons et al., 2014), with some studies highlighting that this event did not lead to full oxygenation of Earth's deep oceans (Stockey et al., 2024). The NOE is often considered to be synchronously and causally associated with the Cryogenian Snowball Earth glaciations (Planavsky et al., 2010; Shields-Zhou and Och, 2011; Sahoo et al., 2012). The Great Oxidation Event (GOE) has been associated with high weathering intensities and high kaolinite production on land that shuttled nutrient fluxes from the continents into marine environments (Hao et al., 2021a). As a corollary, this work establishes whether such a connection exists between the Sturtian Cryogenian Period and the post-glacial oxygenation events.

As introduced in Chapter 1, the trajectory of Earth’s ocean-atmosphere oxygenation is often inferred from geochemical proxies that record changing seawater redox conditions, such as iron (Fe) speciation, redox-sensitive elements concentrations (e.g., uranium (U) and molybdenum (Mo)) and their isotopic compositions and iodine/calcium (I/Ca) ratios in various sedimentary archives formed largely on continental shelf settings (Chun et al., 2010; Clarkson et al., 2014, 2016; Lu et al., 2010; Frei et al., 2011, 2013; Zhou et al., 2014, 2015; Gilleaudeau et al., 2016). These oceanic redox proxies range in sensitivity from local to global and from qualitative to quantitative. Regarding the oceanic redox state during Cryogenian interglacial, different views have emerged from the various geochemical proxies used to investigate the redox evolution of the atmosphere and oceans. The first proposition argues that extensive but short-lived stepwise ocean oxygenation immediately in the interglacial period following the Sturtian glaciation, as supported by Fe isotope data (Tahata

et al., 2015; Zhang et al., 2015; Kunzmann et al., 2017) and U isotope data (Lau et al., 2017). The other view hypothesizes that anoxia prevailed during interglacial times based on Fe speciation (Feng et al., 2010; Li et al., 2012; Scheller et al., 2018) or redox stratified (Dong et al., 2023). Thus, it appears that the extent of post-Sturtian Snowball seawater oxygenation might have varied locally, regionally and globally, but the reason for this variability remains unknown.

In this chapter, I utilize carbonate-associated U isotope ($^{238}U/^{235}U$, reported as $\delta^{238}U_{CAU}$), U concentrations, Fe/Al, and Fe speciation data to investigate the redox conditions in the near continental margin seawater setting in Scotland—characterized by the massive deposition of the Port Askaig tillites associated with the Sturtian Snowball Earth glaciations (Brasier and Shields, 2000; Thomas et al., 2004; Prave et al., 2009; Sawaki et al., 2010; Arnaud and Fairchild, 2011; Fairchild et al., 2018), described in the previous chapters.

5.2 Methods

The redox condition for the studied samples was investigated by U isotopes (details of the methodology are presented in Chapter 2, section 2.2.5.1) and iron speciation (see Chapter 2 and section 2.2.5.2 for a description of the methods).

5.3 Results

The geochemical data from leachates obtained by chemical dissolution of the carbonate fraction of bulk samples ($\delta^{238}U_{CAU}$, $\delta^{234}U_{CAU}$, and elemental concentration ratio (Mg, Ca, Mn, Sr, Th and U)) Fe speciation and Fe/Al, are presented for different stratigraphic sections below (Figures 5.1-5.2 & Table 5.1).

Table 5.1| Stable isotope ($\delta^{13}C_{carbonate}$ and $\delta^{18}O_{carbonate}$), $\delta^{238}U_{CAU}$, and the elemental concentration ratio ((Mg/Ca), Sr/Ca, Mn/Sr and Th/U) and Iron speciation for studied samples.

	$\delta^{13}C_{carbonate}$	$\delta^{18}O_{carbonate}$	$\delta^{238}U_{CAU}$	2SE	$\delta^{234}U_{CAU}$	2SE	U/(Mg+Ca)	Mg/Ca	Sr/Ca	Mn/Sr	Th/U	Fe_{HR}/Fe_T	Fe_{py}/Fe_{Hr}
	(V-PDB)	**(V-PDB)**	‰		‰		**µmol/mol**	**mol/mol**	**mol/mol**	**mol/mol**	**mol/mol**		
PS_16_01	4.63	-15.09	-	-	-	-	-	-	-	-	-	0.38	0.63
PS_16_02	5.14	-14.75	-	-	-	-	-	-	-	-	-	0.85	0.02
PS_16_03	10.10	-11.82	-0.49	0.05	897	1	0.12	0.84	0.001	1.90	1.80	-	-
PS_16_05	-6.33	-14.4	-0.33	0.06	448	1	1.52	0.70	0.001	9.80	1.80	-	
PS-16-06	-2.50	-14.98	-0.20	0.09	247	6	0.22	0.73	0.001	29.20	0.80	-	-
PS_16_09	-3.68	-12.18	0.08	0.09	607	2	1.48	0.77	0.001	6.80	0.30	-	-
PS-16-10	5.64	-14.49	-	-	-	-	-	-	-	-	-	0.10	-
PS-16-11	-5.68	-11.87	-0.03	0.04	700	2	0.82	0.31	0.001	3.80	1.70	0.90	0.73
PS-16-12	-7.00	-12.72	0.07	0.03	142	1	0.93	0.08	0.001	9.60	0.60	0.79	0.70
BH-16-02	-2.78	-9.69	-0.14	0.04	153	2	2.38	0.93	0.001	36.60	41.70	0.16	0.10
BH_16_03	-3.08	-12.28	-0.39	0.05	356	2	0.34	0.89	0.001	24.50	14.30	0.21	-
BH_16_03b	-3.17	-10.99	-	-	-	-	-	-	-	-	-	0.2	-
Ci_16_01	-5.18	-13.41	-0.40	0.05	211	2	23.89	0.93	0.004	4.40	6.10	0.15	0.28
Ci_16_02	-3.80	-11.01	-	-	-	-	-	-	-	-	-	0.06	0.81
PAT1	-4.57	-7.61	-0.24	0.04	568	1	1.17	0.13	0.003	4.60	13.10	0.78	0.04
PAT2	-5.03	-12.36	-0.09	0.04	615	1	1.01	0.05	0.003	3.70	3.90	1.14	0.45
PAT4	-0.91	-12.69	-0.14	0.05	450	2	0.14	0.82	0.001	13.30	3.10	-	-
PAT5	-0.65	-12.72	-0.02	0.03	678	1	0.16	0.88	0.001	6.10	2.20	-	-
LL_16_b1	0.21	-7.56	-	-	-	-	-	-	-	-	-	0.39	0.04
LL_16_d	0.66	-4.40	-0.28	0.04	581	0	0.08	0.97	0.001	3.50	1.20	0.47	0.19
LL-16_e	0.56	-6.26	-0.26	0.05	869	2	0.06	0.92	0.001	5.20	4.10	-	-
LL-16_g	1.11	-12.13	-0.28	0.03	280	1	0.02	0.01	0.002	0.10	2.50	0.90	0.64
LL-16_h	-	-	-	-	-	-	-	-	-	-	-	0.47	0.27
LL_16_i	-0.88	-6.35	-0.53	0.05	2923	1	0.03	0.98	0.001	21.90	29.00	-	-
LL-16_j1	3.27	-8.39	-0.32	0.03	407	1	0.24	0.02	0.001	1.30	7.80	-	-
LL_16_j2	3.47	-7.74	0.10	0.05	2744	1	0.05	0.99	0.001	5.50	6.40	-	-

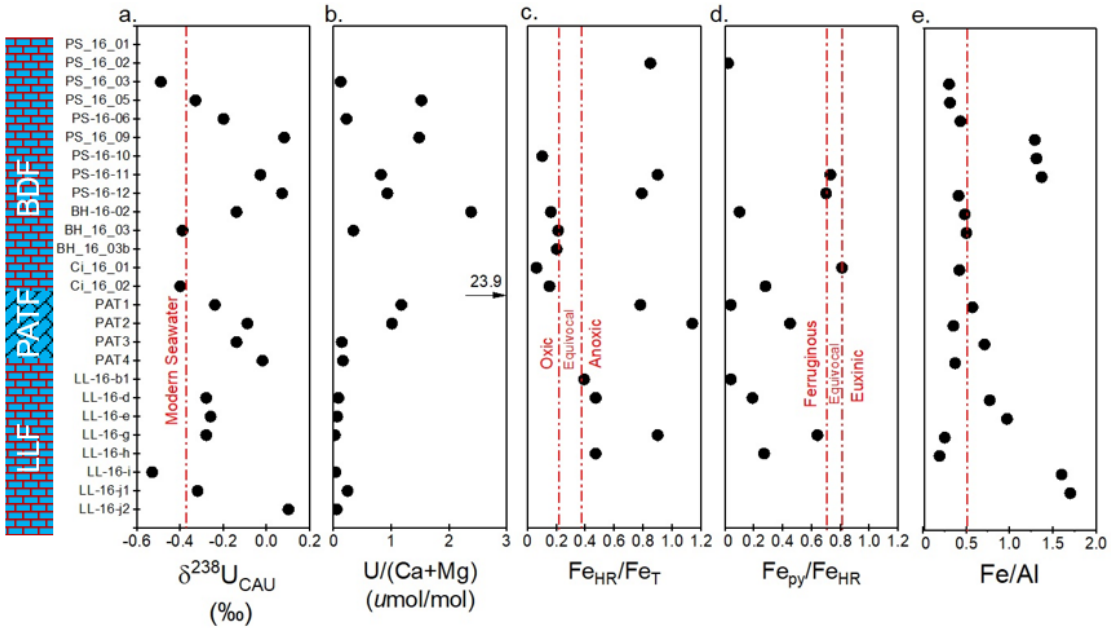

Figure 5.1| Geochemical data for $\delta^{238}U_{CAU}$, U/(Ca+Mg), iron speciation (Fe_{HR}/Fe_T, and Fe_{py}/Fe_{HR}) and Fe/Al for the studied samples.

5.3.1 Lossit Limestone Formation Samples

The Lossit limestone leachates show variable $\delta^{238}U_{CAU}$ ranging from -0.53 to 0.01‰, and low U/(Ca+Mg) concentrations from 0.02 to 0.24 µmol/mol (Figure 5.1a-b & Table 5.1). The three samples towards the upper section of the Lossit Limestone are more homogeneous in $\delta^{238}U_{CAU}$ (~ -0.28‰). Highly reactive iron over total iron (Fe_{HR}/Fe_T) values are above 0.38 while Fe_{Py}/Fe_{HR} values are below 0.6 (Figure 5.1c-d &Table 5.1). Samples of Lossit limestone formation show variability in Fe/Al ratios, containing both high and low, while most samples have Fe/Al > 0.5 (Figure 5.1e).

5.3.2 Tillite Samples

The $\delta^{238}U_{CAU}$ of the tillite leachates show a relatively narrow range from −0.24 to −0.02‰ with an overall decrease in the values upward in the section, with U/(Ca+Mg) concentration from 0.14 to 1.17 µmol/mol (Figure 5.1a-b & Table 5.1). The Fe_{HR}/Fe_T values are above

0.38, while the Fe_{Py}/Fe_{HR} values are below 0.6 (Figure 5.1c-d & Table 5.1). Tillite samples have variability in Fe/Al ratios which show high and low than 0.5.

5.3.3 Bonahaven Dolomite Formation Samples

The Bonahaven leachates from the samples deposited during the early stages of the post-Snowball glaciations (Bh-16-03 and Ci-16-01), have similar $\delta^{238}U_{CAU}$ at ~ -0.40‰, overlapping with the modern seawater value (-0.38 ± 0.01 ‰), while the third sample (Bh-16-02) has a higher $\delta^{238}U_{CAU}$ ~ - 0.14 ‰ (Figure 5.1a & Table 5.1). The U/(Ca+Mg) is low for Bh-16-03 and Bh-16-02 samples (< 2.4 μmol/mol) while sample Ci-16-01 has the highest value in the entire data set (23.9 μmol/mol) (Figure 5.1b & Table 5.1). The Fe_{HR}/Fe_T ratios have values below 0.22 in immediate post-glaciation succession. All samples have Fe_{Py}/Fe_{HR} < 0.6 except one (Ci-16-02). The late post-Snowball samples show a larger variation in $\delta^{238}U_{CAU}$ from 0.07 to -0.49 ‰, with samples going from higher to lower $\delta^{238}U_{CAU}$ upwards in the stratigraphy (Figure 5.1a & Table 5.1). The U/(Ca+Mg) ratios for these samples range between 0.12 to 1.52 μmol/mol (Figure 5.1b & Table 5.1). Their corresponding Fe_{HR}/Fe_T ratios are all above 0.38, apart from one sample (PS-16-02) with a value of 0.10 and most samples have Fe_{Py}/Fe_{HR} between 0.6 - 0.7 except PS-16-02 (0.02) (Figure 5.1c-d & Table 5.1). The immediate post-Snowball samples predominantly have Fe/Al values less than 0.5 values, while the range of late post-Snowball samples is between 0.3 – 1.4 (Figure 5.1e).

5.3.4 Geochemical Diagenetic Indices

In addition to the measured U isotopes, a range of geochemical data may attest to diagenetic influence on the data. Traditional proxies to evaluate the effects of diagenesis include Mn/Sr, $\delta^{13}C_{carbonate}$, and $\delta^{18}O_{carbonate}$ for meteoric alteration (the $\delta^{13}C_{carbonate}$ and $\delta^{18}O_{carbonate}$ values are reported relative to V-PDB (Vienna Pee Dee Belemnite), Mg/Ca (mol/mol) and Sr/Ca

(mol/mol) ratios for dolomitization/mineralogical transformations (aragonite to calcite), Th/U (mol/mol) for detrital (e.g., clay) components and $\delta^{234}U_{CAU}$,, which are shown in Figure 5.2 &Table 5.1.

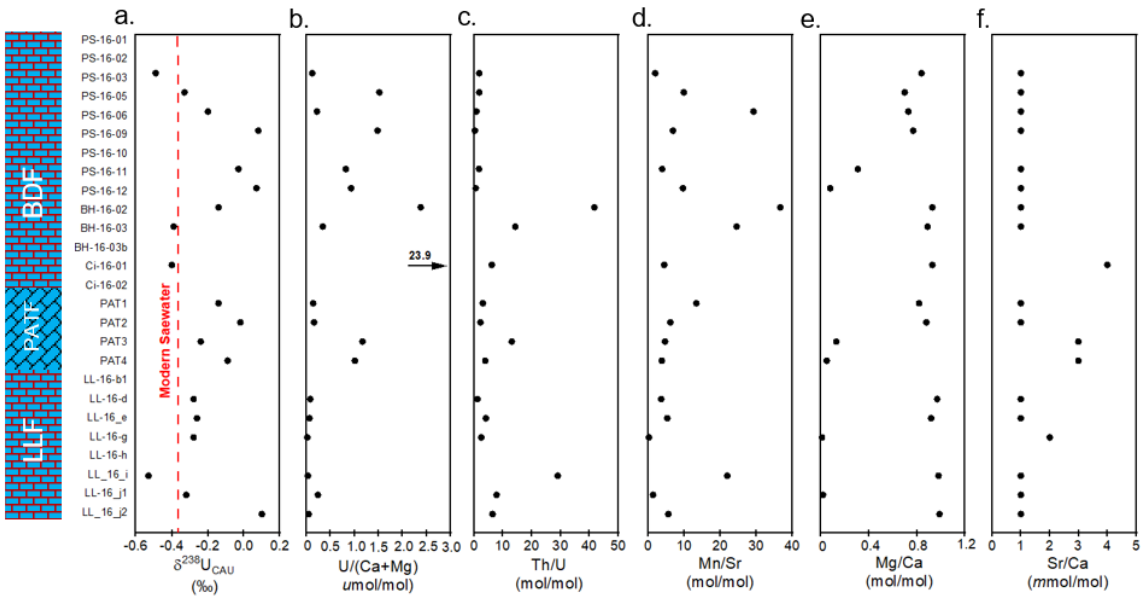

Figure 5.2| Geochemical data for a. $\delta^{238}U_{CAU}$, b. U/(Ca+Mg), and diagenetic indices c. Th/U, d. Mn/Sr, e. Mg/Ca and f. Sr/Ca for the studied samples.

The bulk $\delta^{13}C_{carbonate}$ and $\delta^{18}O_{carbonate}$ range between – 7.0 to 10.10 ‰ and -15.09 to -4.40 ‰ (Table 5.1), respectively. The pre-/late-Snowball samples are marked by higher $\delta^{13}C_{carbonate}$ excursions than tillite and immediate post-Snowball values. Cross plots between Mn/Sr and $\delta^{13}C_{carbonate}$ and $\delta^{18}O_{carbonate}$ to investigate potential meteoric diagenetic trends show no correlation (Figure 5.3).

The Th/U ratios for the studied samples vary between 0.3 and 42.1 mol/mol (Figure 5.2c & Table 5.1). Four samples show Th/U values higher than 10 mol/mol. These samples are the Lossit limestone formation sample (LL-16-I2: 9.0 mol/mol), tillite sample (PAT1: 13.1 mol/mol), and Bonahaven dolomite formation samples (BH-16-02 and BH-16-03: 41.7 mol/mol and 14.3 mol/mol, respectively).

The Mn/Sr ratios for the studied samples range between 0.1 to 37 (mol/mol) (Figure 5.2d &Table 5.1). Five samples show high Mn/Sr values > 10 (mol/mol). These samples are the

Lossit limestone formation sample (LL-16-I: 21.9 mol/mol), tillite sample (PAT3: 13.3 mol/mol) and Bonahaven dolomite formation samples (BH-16-02, BH-16-03 and PS-16-06: 36.6 mol/mol, 24.5 mol/mol and 29.2 mol/mol respectively).

The Mg/Ca values range from 0.05 to 0.99 mol/mol for the studied samples (Figure 5.2e & Table 5.1), where most Lossit limestone formation and late Bonahaven dolomite formation samples are dolomite-rich compared to tillite and early Bonahaven dolomite formation samples. All samples show a low Sr/Ca ratio below 0.004 mol/mol (Figure 5.2f & Table 5.1). Cross-plots of U/ (Ca+Mg) concentration and $\delta^{238}U_{CAU}$ with other indices of potential diagenetic alteration $_{are}$ shown in Figure 5.4. There are no clear significant trends observed (also see Table 5.2). All carbonate leachates for studied samples show $\delta^{234}U$ values higher than 142‰ (Table 5.1).

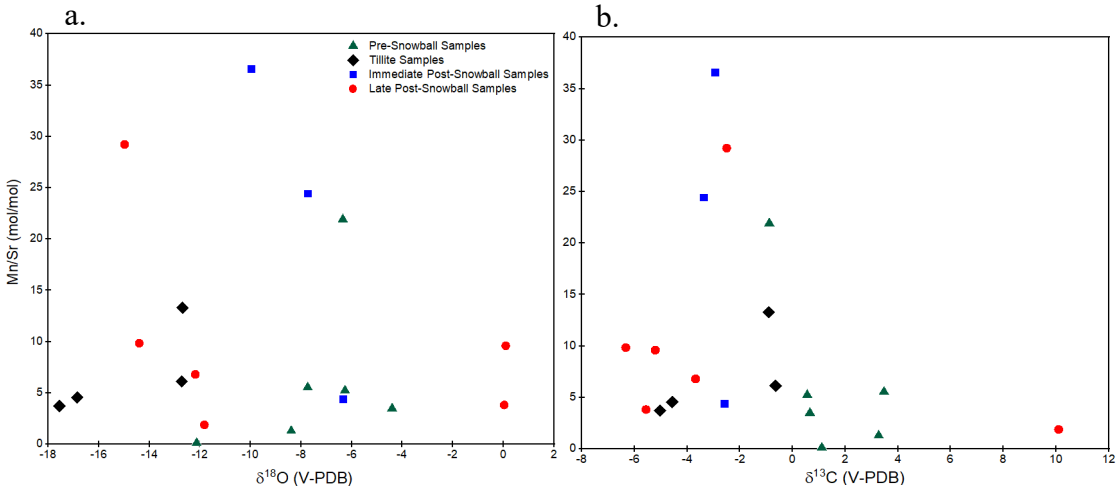

Figure 5.3| Cross-plots of Mn/Sr with a. stable isotope $\delta^{18}O_{carbonate}$ and b. stable isotope $\delta^{13}C_{carbonate}$.

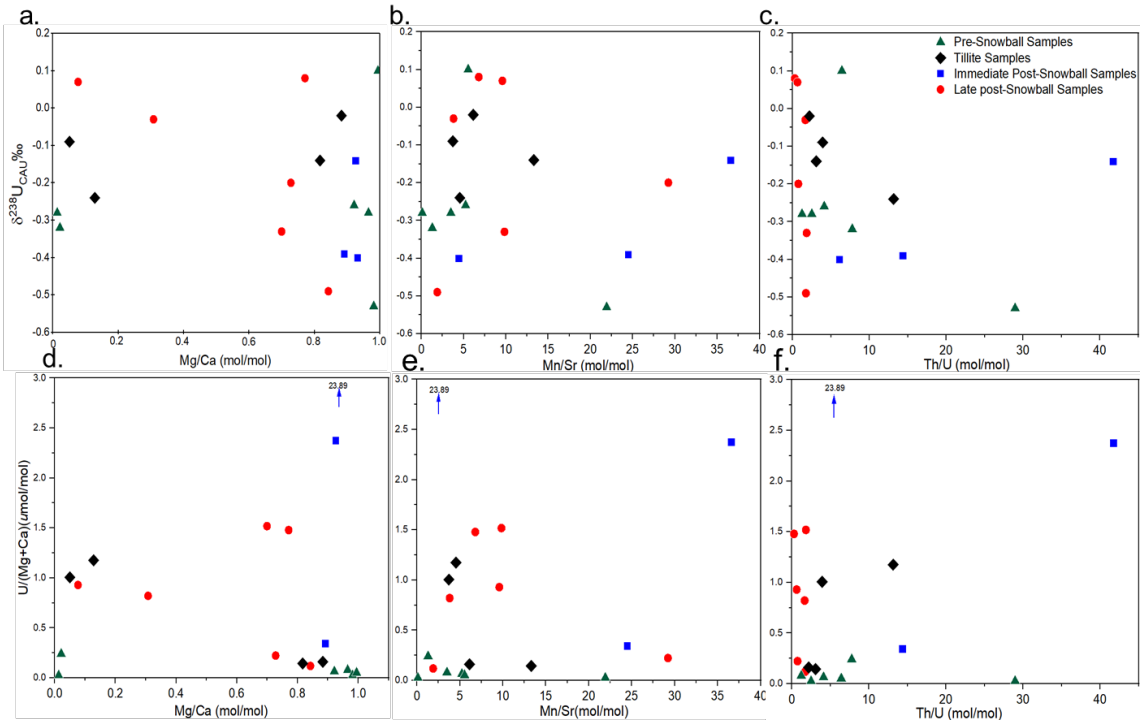

Figure 5.4| Cross-plots of geochemical data a. $\delta^{238}U_{CAU}$ vs. Mg/Ca. b. $\delta^{238}U_{CAU}$ vs. Mn/Sr. c. $\delta^{238}U_{CAU}$ vs. Th/U and d. U/(Mg+Ca) vs. Mg/Ca. e. U/(Mg+Ca) vs. Mg Mn/Sr. f. U/(Mg+Ca) vs. Th/U for studied samples across Sturtian glaciation.

5.4 Discussion

5.4.1 Evaluating Diagenetic Influences on the Carbonate $\delta^{238}U$ Signatures

Before considering the paleoenvironmental implications of the data, it is essential to evaluate the various syngenetic to diagenetic processes and contaminants that may influence the measured $\delta^{238}U_{CAU}$ signatures in the samples. The potential impact of meteoric and/or pore-water fluids on preserved U isotope signatures and detrital contamination may be examined using indicators, such as $\delta^{18}O_{carbonate}$, $\delta^{13}C_{carbonate}$, Mn/Sr, and Mg/Ca, and Sr/Ca ratios and detrital-sensitive Th/U ratios. Trace elements that are substituted into the lattice of carbonate minerals, such as Sr and Mn, can be used as diagenetic indicators. Diagenetic alteration (meteoric and burial fluids) tends to deplete carbonates in Sr relative to seawater (Banner

and Hanson, 1990). In contrast, pore-waters during burial can also be substantially enriched in Mn, particularly under reducing conditions. This commonly leads to Mn enrichment in diagenetic phases formed during burial.

These general relationships have led to the establishment of traditional criteria to assess the fidelity of primary geochemical signatures in carbonate rocks such as the Mn/Sr ratio (e.g., Jacobsen and Kaufman, 1999; Gilleaudeau et al., 2018) where higher ratios attest to diagenetic overprinting. A Mn/Sr ratio with a cutoff of 3–10 (mol/mol) with ratios below considered primarily pristine has been suggested for Precambrian carbonate sedimentary rocks (Kaufman and Knoll, 1995). Although there is no evidence to suggest that these Mn/Sr cut-offs can be reliably used to screen for alteration of $\delta^{238}U$ in carbonate rocks (Chen et al., 2018), high Mn/Sr would indicate potential issues with later diagenetic U uptake. The Mn/Sr ratios of the studied samples range between 0.1 to 36.6 (mol/mol) with five samples out of 19 showing Mn/Sr ratios >10, indicating that some samples may have experienced significant meteoritic influence, while others may not have been affected. The $\delta^{238}U_{CAU}$ of the five samples with high Mn/Sr (>10) varies from 13.3- 36.6 (mol/mol) [PS-16-06, Bh-16-02, Bh-16-03, PAT3, LL-16-i], with no clear trend between these, although it includes the samples with the lowest measured $\delta^{238}U_{CAU}$ in the dataset. As mentioned in section 5.3.4, there are no systematic correlations between Mn/Sr vs. $\delta^{238}U_{CAU}$ and Mn/Sr vs. U/(Ca+Mg) concentrations as shown in Figures 5.4b & e and Table 5.2. Furthermore, $\delta^{18}O_{carb}$ and $\delta^{13}C_{carbonate}$ have been used to test the meteoric diagenesis. The isotopic composition of oxygen in carbonates can be altered during diagenesis owing to the high concentration of oxygen in diagenetic fluids (e.g., Jacobsen and Kaufman, 1999; Gilleaudeau et al., 2018). The $\delta^{18}O_{carbonate}$ values of the samples mostly range between -15.09 and -4.40 ‰, which is within the expected range for well-preserved Precambrian carbonates (Shields and Veizer 2002). There is no relationship between $\delta^{18}O_{carbonate}$ and $\delta^{13}C_{carbonate}$ vs. Mn/Sr ratios (Figure

5.3) in the sample set that would suggest a significant diagenetic alteration. Besides that, water/rock ratio modelling has shown that $\delta^{238}U$ is more resistant to diagenesis than $\delta^{18}O_{cab}$ (Lau et al., 2017; Chen et al., 2018). Dolomitization has been proposed to promote the reduction of uranium, resulting in porewater [U] and $\delta^{238}U$ values that do not reflect seawater, which would then be incorporated into early diagenetic carbonate cement (Romaniello et al., 2013). Romaniello et al. (2013) observed $\delta^{238}U$ changes associated with dolomitization in a modern Bahamian tidal pond, as reflected in a strong correlation of $\delta^{238}U$ with Mg/Ca ($R^2 = 0.96$, $p < .001$). However, Chen et al. (2018) and Tissot et al. (2018) show that dolomitization may have little effect on $\delta^{238}U$ for some samples. Further suggestions that dolomitization may be of limited concern for paleo-$\delta^{238}U$ records come from a global compilation of $\delta^{238}U$ studies across the Permian-Triassic boundary (Zhang et al., 2018a). In the study of Chen et al. (2021) no commonly used criteria to screen Precambrian carbonate samples for diagenesis (e.g., Mn/Sr and Mg/Ca ratios) were adopted because in the Precambrian most carbonate units were dolomitized shortly after deposition and have high Mn/Sr and Mg/Ca ratios but preserve primary radiogenic Sr isotopic values. There is no significant correlation between Mg/Ca vs. $\delta^{238}U_{CAU}$ or U/ (Ca+Mg) in this sample set (Figure 5.4a &d &Table 5.2), suggesting that dolomitization does not systematically alter the U concentration and isotope systematics. Mineralogical transformations (aragonite to calcite) are not likely to have significantly affected carbonate $\delta^{238}U$ values in this study. This is evidenced by a relatively low Sr/Ca (< 0.01) ratio for most samples and no significant correlations with $\delta^{238}U_{CAU}$.

The incorporation of detrital U can cause measured carbonate $\delta^{238}U$ compositions to deviate from that of the targeted carbonate. In studies of organic-rich siliciclastic rocks the detrital-bound U component may influence bulk [U] and some studies have normalized [U] to [Th], assuming the latter only being associated with the siliciclastic rock, to take into

account detrital input (Cheng et al., 2020; Jost et al., 2017). We examined this possibility by looking at the Th/U ratio in the leachates. Thorium is present mainly in the terrigenous detrital fraction, sourced from continental weathering with little ability to move during diagenesis under most conditions of the surface Earth. Thorium has only one common oxidation state (IV); therefore, its concentration in seawater is not affected by water mass redox changes. To minimize the potential for detrital contamination in the carbonate leachates, the samples were dissolved in 1 N acetic acid, which should minimize the dissolution of silicates and organic matter (Clarkson et al., 2021). The leachates show a range of Th/U from 0.3 to 42 (mol/mol) (Figure 5.2 & Table 5.1). Compared to the average upper crustal Th/U bulk silicate Earth of ~3.8 (mol/mol) (McLennan, 2001). Some samples may have been affected by detrital U contamination as indicated by high Th/U ratios. In this study, samples with Th/U ratios >10 mol/mol are likely candidates for some detrital influence, e.g. dissolution of clays with high Th/U from previous weathering loss of U, although Th addition, e.g via adsorption, within porewaters, particularly under reducing conditions, is another possibility for elevated Th/U (e.g. Dong et al., 2022). The $\delta^{238}U_{CAU}$ and U/(Ca+Mg) data are not positively correlated with Th/U ratios (Figure 5.4c&e and Table 5.2). Taken together the Mn/Sr and Th/U ratios identify a range of samples with secondary indicators of potential significant porewater/burial diagenesis and detrital influence, suggesting a cautious approach is needed for interpreting the $\delta^{238}U_{CAU}$ and U/(Ca+Mg) for those samples (Figure 5.5).

These samples are LL-16-i (pre-Snowball sample), PAT1 and PAT3 (tillite samples), Bh-16-02 and Bh-16-03 (immediate post-Snowball samples), and PS-16-06 (post-Snowball sample). Samples Bh-16-02, Bh-16-03 and LL-16-i have both Mn/Sr and Th/U >10. For the remaining dataset, there is no systematic evidence for alteration of the $\delta^{238}U$ signature from these processes.

In addition to the diagenetic proxies discussed above, $\delta^{234}U$ data also offer insights into the potential for recent uranium (U) addition or loss in the analyzed samples (Andersen et al., 2010, 2017). The activity ratio of ^{234}U to ^{238}U ($^{234}U/^{238}U$) in natural materials is often not at secular equilibrium (i.e., an activity ratio of 1), primarily due to decay chain disequilibrium mechanisms. A key process contributing to this disequilibrium is alpha recoil redistribution, in which ^{234}U atoms are physically displaced from their original lattice sites during the alpha decay of ^{238}U (Chabaux et al.,2003). This recoil effect can eject ^{234}U into pore waters or more reactive mineral phases, enhancing its mobility relative to the parent isotope. As a result, ^{234}U can become enriched in fluids or labile solid phases, leading to elevated $^{234}U/^{238}U$ activity ratios in carbonate leachates, even without recent U addition. Additionally, a range of biogeochemical processes also influences uranium isotope fractionation (e.g., oxidative weathering, adsorption and desorption onto mineral surfaces, and dissolution reactions). All of these can contribute to the differential mobility and isotopic partitioning of ^{234}U and ^{238}U (Robinson et al., 2006; Tomiak et al., 2016).

In ancient carbonate samples, deviations of $\delta^{234}U$ values from secular equilibrium can, in principle, be used to detect recent (up to ~2 Myr) diagenetic uranium (U) mobilisation or alteration (Cheng et al., 2013). This is because any post-depositional addition or removal of uranium can disturb the natural decay-series balance, especially between ^{234}U and ^{238}U. In practice, however, all analysed samples in this study exhibit elevated $\delta^{234}U$ values (higher than 142 ‰) and ^{234}U excesses relative to ^{238}U. While such enrichments might suggest recent uranium addition or open-system behaviour, these patterns are characteristic of carbonate leachates derived from ancient samples and do not necessarily reflect diagenetic overprinting within the past ~2 Myr.

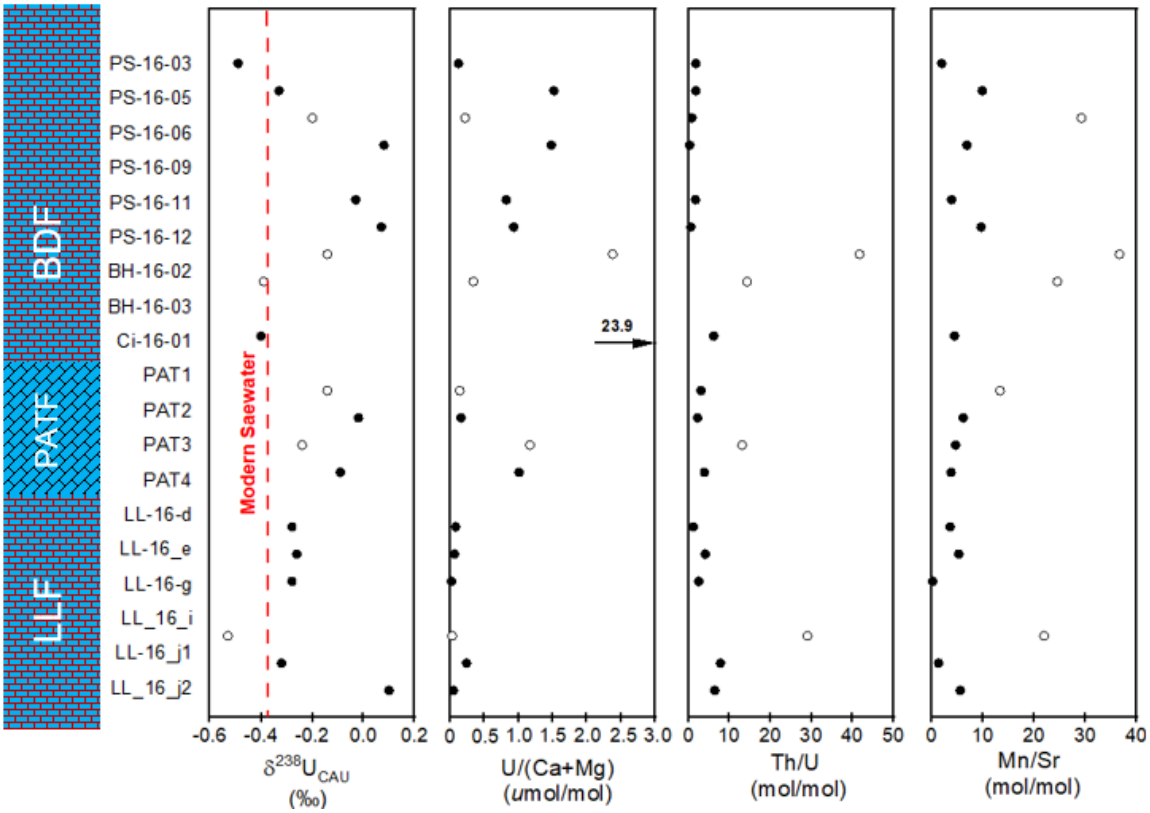

Figure 5.5| Geochemical data for $\delta^{238}U_{CAU}$ (‰), U/ (Mg+Ca), Th/U and Mn/Sr, open symbols highlight samples with high Th/U and Mn/Sr.

Table 5.2 Correlation matrix between diagenetic proxies and $\delta^{238}U_{CAU}$.

	$\delta^{13}C_{carbonate}$	$\delta^{18}O_{carbonate}$	$\delta^{238}U_{CAU}$	U/(Mg+Ca)	Mg/Ca	Sr/Ca	Mn/Sr	Th/U
$\delta^{13}C_{carbonate}$	1.00							
$\delta^{18}O_{carbonate}$	0.34	1.00						
$\delta^{238}U_{CAU}$	-0.29	-0.14	1.00					
U/(Mg+Ca)	-0.28	-0.24	-0.22	1.00				
Mg/Ca	0.25	0.18	-0.24	0.18	1.00			
Sr/Ca	-0.33	-0.14	-0.13	0.71	-0.29	1.00		
Mn/Sr	-0.25	-0.14	-0.07	-0.09	0.41	-0.31	1.00	
Th/U	-0.07	0.33	-0.22	0.02	0.26	-0.05	0.68	1.00

5.4.2 Tracking the Evolution of Water Column and Pore Water Redox Conditions

5.4.2.1 Implications for Seawater Redox by Iron Speciation

Iron speciation proxy is widely used for tracking paleo-depositional ocean redox conditions through geological time (e.g., Poulton, 2021; Meng et al., 2024; Rutledge et al., 2024; Tu et al., 2024; Yang et al., 2024). It was originally developed for fine-grained siliciclastic marine sediments; however, further research has shown the applicability of the iron speciation proxy for other rock types, including carbonates (Clarkson et al., 2014). The arbitrary cut-off is normally set at around 0.5 wt.% Fe, with carbonate-rich samples with <0.5% Fe content tending to produce anomalously high Fe_{HR}/Fe_T ratios (Clarkson et al., 2014). The reconstructed Fe-based redox trends were therefore evaluated for deviations as a function of Fe and carbonate content. The absence of significant differences regardless of total Fe and carbonate content, resulting in consistent trends along sequence stratigraphy, was taken to imply a negligible impact of carbonate content on the reliability of the Fe-based redox proxy. I further interpret the general lack of significant deviations in the Fe-based redox proxy profiles as a reflection of the significant siliciclastic and Fe-rich content of the studied lithologies (Brasier and Shields, 2000; Thomas et al., 2004; Prave et al., 2009; Sawaki et al., 2010; Arnaud and Fairchild, 2011; Fairchild et al., 2018), including those containing carbonates, as established by geochemical analyses.

The high sedimentation rate can cause dilution effects, which can diminish Fe_{HR} (Raiswell et al., 2018). Therefore, the sedimentation rate should be evaluated before implementing the Fe speciation in the studied samples. The best estimate of sedimentation rate is that the BDF succession up to the top of member 3 (as described in Table 2.1), formed within 250 Kyr following the end of the Sturtian snowball glaciation, according to the

following logic: In the original Snowball Earth hypothesis, cap carbonates were thought to have formed within 10 Kyr, based on instantaneous melting models. However, subsequent magnetic reversals within cap carbonates pointed to longer timeframes, consistent with post-glacial sediment starvation because of seawater level rise (Rooney et al., 2011).

There is a transition from coarse-grained sediments to being very fine-grained up the studied sequence, consistent with a rise in seawater level and reduction in detrital loading after the Sturtian glaciation. In addition, globally, $\delta^{13}C_{carbonate}$ values generally recover from -5‰ towards more positive excursions following the transition from the Sturtian icehouse into the greenhouse interval (Rooney et al., 2011; Fairchild et al., 2018). Similarly, published $\delta^{13}C_{carbonate}$ values for the immediate Bonahaven dolomite formation (BDF) succession upwards to member 3, as are the data here (Table 5.1), switch towards a more positive $\delta^{13}C_{carbonate}$ values immediately above the PATF. Also, the abrupt shift of $\delta^{13}C_{carbonate}$ to up to +10‰ in member 4 in the BDF is far more extreme than any reported worldwide, leading some workers to equate this to the "Keele Peak" in Canada (e.g., Halverson et al., 2005).

However, the occurrence of member 4 halfway up the Sturtian post-Snowball interval towards the Marinoan Snowball Earth poses a problem, particularly because member 4 is estimated to be older than the Keele Peak. Although no explanation for the anomalous positive $\delta^{13}C_{carbonate}$ value was given, Fairchild interpreted member 4 (Table 2.1) in a PhD thesis as a supratidal dolomitic deposit. Therefore, the top of member 3 in the BDF lies within the bounds of the timeframe when the negative $\delta^{13}C_{carbonate}$ values were yet to consistently rise towards the strong positive values recorded in member 4. In the absence of radiometric dates for the BDF, unique cyclostratigraphic constraints were used in the widely accepted classic Sturtian Snowball Earth succession in Svalbard (Brasier and Shields, 2000), to estimate sedimentation rates for the BDF. Here, the $\delta^{13}C_{carbonate}$ values > -5‰ are consistently recorded up to ~10 m in the immediate post-glacial section which

terminates in a shale facies succession. Within this succession, 0.5 m thick precessional cycles estimated to represent 18 Kyr in duration are linked to 6-8 Myr interglacial (Fairchild et al., 2016). To a first approximation, the 10 m thick succession above which $\delta^{13}C_{carbonate}$ switches to ≥ -5‰ values, formed over an estimated 200-250 Kyr interval, is related to the time of deposition of the 300 m thick BDF unit up to member 3, based on stratigraphical correlation and similar and consistent ≤-5‰ $\delta^{13}C_{carbonate}$ values. This suggests an estimated 30 times faster sedimentation rate for the BDF compared to the Svalbard succession, accounted for by syn-depositional faulting and basin subsidence associated with the Dalradian Supergroup.

This has implications for the accuracy of the iron-based redox proxy because sedimentation rates of up to 0.0077 m yr^{-1} are reported to falsify its sensitivity and accuracy (Poulton and Canfield, 2011; Hardisty et al., 2018; Raiswell et al., 2018). The above calculations suggest a maximum sedimentation rate of 0.0015 m yr^{-1} for the BDF up to member 3, which is 4× slower than the rate expected to strongly interfere with the accuracy of the iron-based redox proxy (Poulton and Canfield, 2011; Hardisty et al., 2018; Raiswell et al., 2018). Moreover, evidence suggests that depositional rates during the formation of the BDF sequence switched to a slower pace because of global seawater transgression slowing down sediment supply to the basin. Hence if anything, the iron-based proxy is expected to become more accurate in their prediction of bottom seawater oxygenation at this time, as false oxygenation trends can be produced during rapid sediment accumulation (Poulton and Canfield, 2011; Hardisty et al., 2018; Raiswell et al., 2018). The signal remains consistently anoxic during the deposition of the 1.1 km thick PATF succession, whose sedimentation rates were likely much faster than for the BDF. Moreover, throughout the sequence, the redox signal appears unaffected by carbonate concentration; staying consistently anoxic or

oxic, depending on the interval, regardless of whether carbonate concentrations varied from near 0.0 wt.% to 50 wt.%.

According to the above, the impact of sedimentation rates was determined to be negligible in the studied samples, considering that estimated values are four times lower than those expected to compromise the sensitivity of the Fe-based redox proxy (Raiswell et al., 2018). It is important to note that sedimentary Fe speciation primarily indicates the redox state of the bottom seawater above the depositional setting of the sample rather than the full surface ocean (Poulton and Canfield, 2011). Average Fe_{HR}/Fe_T ratios vary from 0.55±0.21, 0.16±0.04, and 0.68±0.30 for the pre-Snowball and tillite samples, the immediate post-Snowball, and the late post-Snowball intervals, respectively (Figure 5.1c & Table 5.1). Their corresponding average Fe_{Py}/Fe_T ratios are 0.21±0.22, 0.31±0,34, and 0.42±0.31, respectively (Figure 5.1 & Table 5.1). The Fe_{py}/Fe_{HR} ratios of <0.8 suggest deposition of the entire sediment profile in mainly ferruginous-like conditions, although the Fe_{HR}/Fe_T ratios of <0.22 in the immediate post-Snowball interval are consistent with oxygenated waters, while the >0.38 Fe_{HR}/Fe_T ratios indicate anoxic bottom water depositional conditions for the pre-Snowball, tillites, and late post-Snowball samples (Poulton and Canfield, 2005; Poulton and Canfield, 2011; Raiswell et al., 2018). These results are consistent with previous Fe speciation studies from the Guitouwan section, Shennongjia area, South China (Wang et al., 2024).

The oxygenation trends are further highlighted by enrichments of total Fe relative to aluminium (Fe/Al) profiles (Lyons et al., 2003; Lyons and Severmann, 2006; Clarkson et al., 2014; Raiswell et al., 2018) across the sequence (Figure 5.1e). A particular advantage of the Fe_T/Al proxy is that it is not affected by post-depositional transformation of unsulfidized Fe_{HR} to less reactive minerals (Poulton and Raiswell, 2002; Lyons and Severmann, 2006; Poulton et al., 2010). Thus, Fe_T/Al with Fe-speciation provides a powerful means to evaluate

water column redox conditions. The average value of Fe_T/Al in modern sediments under oxic conditions is approximately 0.55±0.11 (Raiswell et al., 2018; Vosteen et al., 2024). In this regard, the >0.5 pre-Snowball Fe_T/Al ratios are generally consistent with higher sediment pyrite enrichments, compared to tillites samples depleted in pyrite and the immediate post-Snowball facies (Figure 5.1e). Such high Fe_T/Al values have been linked to the deposition of anoxic sediments beneath modern sulfide-enriched seawater and lower values to oxic settings characterized by limited C_{org} supply to sediments (Lyons et al., 2003; Lyons and Severmann, 2006; Vosteen et al., 2024). Due to the persistent supply of continental detritus as mentioned in chapters 3 and 4, together with overall sedimentation rates that do not compromise the Fe_{HR}/Fe_T proxy as discussed above, the >0.5 Fe_T/Al ratios are best explained by syngenetic changes in anoxic pyrite precipitation. The <0.5 Fe_T/Al ratios, however, do not effectively delineate the pyrite-poor anoxic tillites from the apparently oxic immediate post-Snowball deposit (Figure 5.1c), possibly due to increased input of Al-rich detritus during deposition of the tillites and immediate post-Snowball facies (as mentioned in chapter 3 & 4). Similarly, <0.5 Fe_T/Al ratios in the anoxic pyrite-poor late post-Snowball interval, as suggested by the Fe_{HR}/Fe_T redox proxy, are followed by a small >0.5 Fe_T/Al spike corresponding to anoxic conditions (Figure 5.1c) and pyrite enrichment at the top of the section (Figures 5.1d & e). Fe speciation finding from the studied samples are consistent with the study done in Guitouwan section, Shennongjia area, South China by Fe speciation (Xubin Wang et al. 2024).

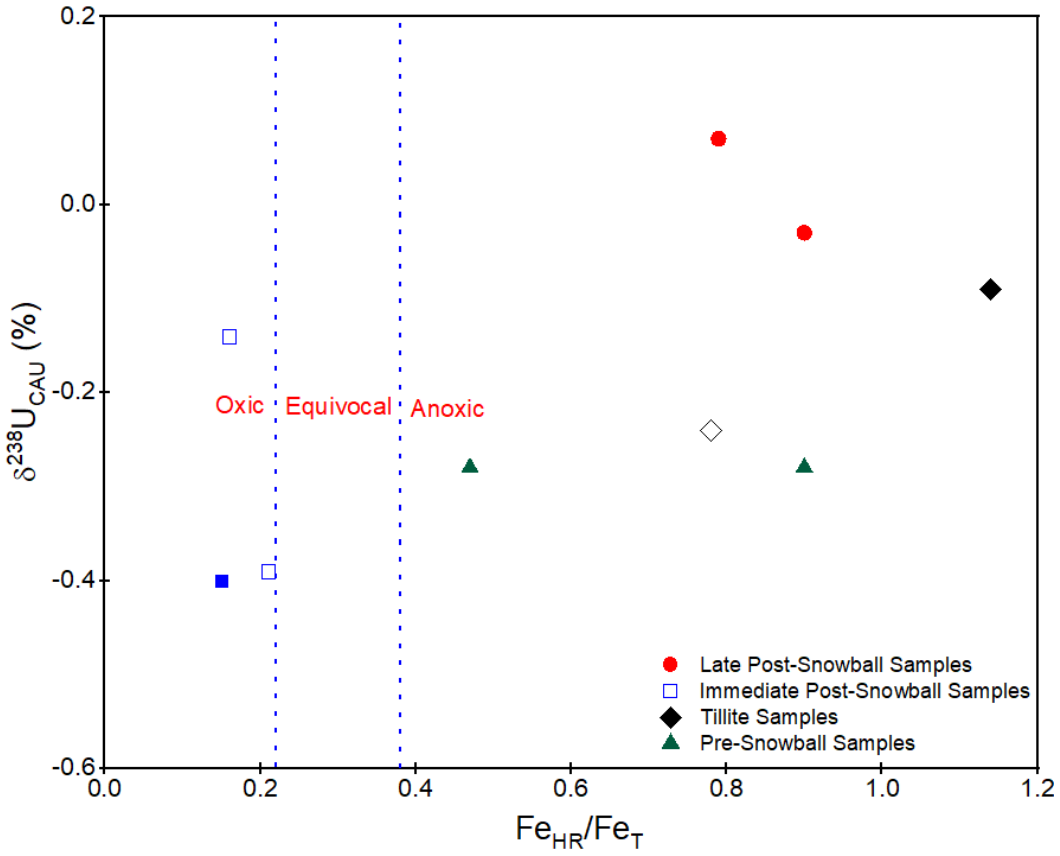

Figure 5.6| Uranium isotopes vs. iron speciation for the studied samples. Open symbols indicate potential diagenetic disturbance.

5.4.2.2 Implications for seawater redox by uranium isotopes

The dataset, refined excluding the samples with signatures of diagenetic disturbance, has $\delta^{238}U_{CAU}$ ranging from -0.49 to +0.1 ‰ (Figure 5.1a & Figure 5.5). Based on several lines of evidence this range suggests that most samples are affected by localised syn- to early diagenetic effects, rather than direct recorders of seawater $\delta^{238}U$. Previous data have shown that localised reducing conditions lead to elevated $\delta^{238}U$ in carbonates (Andersen et al., 2014; Tissot and Dauphas, 2015; Rolison et al., 2017). Most of the studied samples have $\delta^{238}U_{CAU}$ values higher than -0.2 ‰ which suggests localised reducing conditions, given this value it is difficult to reconcile with a seawater value based on knowledge of the marine $\delta^{238}U$ mass balance (e.g. Andersen et al., 2016).

Samples with both Fe_{HR}/Fe_T and $\delta^{238}U_{CAU}$ data are plotted in Figure 5.6. Here, there is an overall trend of the two immediate post-Snowball Earth samples (Bh-16-03 and Ci-16-02) with the lowest $\delta^{238}U_{CAU}$ of -0.39 and -0.40‰ respectively, and have Fe_{HR}/Fe_T values within the defined 'oxic' settings, while the two late post-Snowball Earth samples (PS-16-11 and PS-16-12) with the highest $\delta^{238}U_{CAU}$ of -0.03 and 0.07‰ respectively, have Fe_{HR}/Fe_T values indicate anoxic settings. These results fit the overall trend in modern settings where reducing pore-waters leads to higher $\delta^{238}U$ in carbonates (Bruggmann et al., 2022; Romaniello et al., 2013). While one of the immediate post-Snowball Earth samples has an elevated $\delta^{238}U_{CAU}$ (Bh-16-02 with -0.14‰) plotting in the 'oxic' setting. The samples having Fe_{HR}/Fe_T within the 'anoxic' setting have more elevated $\delta^{238}U_{CAU}$ than the two 'oxic' samples described above (Figure 5.6). Although there are many similarities in the redox behaviour of U and Fe, there are also significant differences (Belli and Taillefert, 2018).

Uranium reduction primarily occurs at or below the sediment-water interface, at a redox potential similar to that for iron reduction. Particularly, U reduction and uptake into sediments, is likely dominantly occurring from pore-waters at depth in sediments when reducing conditions are reached from oxygen-limitation (Andersen et al., 2014; Andersen et al., 2017). In contrast, the Fe-speciation proxy may attest to the reducing lower water column or sediment-water interface conditions, but it does not directly relate to the oxygenation state of the surface water column (Poulton and Canfield, 2005; Raiswell et al., 2018). With this in mind, the $\delta^{238}U_{CAU}$ may show sensitivity to redox conditions with an overall increase in carbonates within sediments going from oxic to sub-oxic (reducing conditions at depth in sediments) and fully anoxic conditions.

In summary, it is possible to build a framework for expected $\delta^{238}U_{CAU}$ based on the redox environment and the carbonate deposited in the sediments and associated U isotope fractionation. Figure 5.7 illustrates the framework of how different depositional

environments impact the observed $\delta^{238}U$ in sediments. Firstly, the carbonate in the sediments can be hypothesised to come from predominantly two sources, a pool of biogenic planktonic and benthic formed carbonates, which on deposition at the seafloor becomes part of the sediments, and an abiotic pool of carbonate cement formed in-situ from pore-waters in the sediments.

In a first scenario of an oxidised water column and upper sediment environment, with any reducing pore-water conditions below precipitation of carbonate cement from pore-waters the $\delta^{238}U_{CAU}$ is likely to be close to the seawater composition (Figure 5.7a). In modern oxic oceans, uranium occurs primarily in the highly soluble U(VI) oxidation state, dominantly in the form of the uranyl carbonate complexes. The modern analogy shows that the $\delta^{38}U_{CAU}$ is near seawater for U uptake in carbonates under these conditions. Therefore, marine carbonate formed in oxic seawater will, capture the near U isotope signature of seawater and is a useful proxy to provide insights about the global oxygenation state of the oceans at any given time.

On the other hand, in a more extreme second scenario of a fully anoxic deeper ocean and sediment environment, the carbonates in the sediment would have a different $\delta^{238}U$ (Figure 5.7c). Primary productivity in the upper oxic part of the ocean would provide a planktonic carbonate flux with U in the +6 form and $\delta^{238}U_{CAU}$ near seawater, while a benthic biogenic source of carbonate would be limited from the reducing conditions. Abiotic carbonate formation and U^{+4} uptake from the porewaters and potentially from the anoxic water column, however, would lead to large U isotope fractionation governed by the redox reaction (e.g., Andersen et al., 2017). Under anoxic conditions (Figure 5.7c), the reduction of U(VI) to U(IV) generates large isotopic fractionation of up to 1.2‰, as observed in some organic-rich reducing sediments (Andersen et al., 2020; Clarkson et al., 2023).

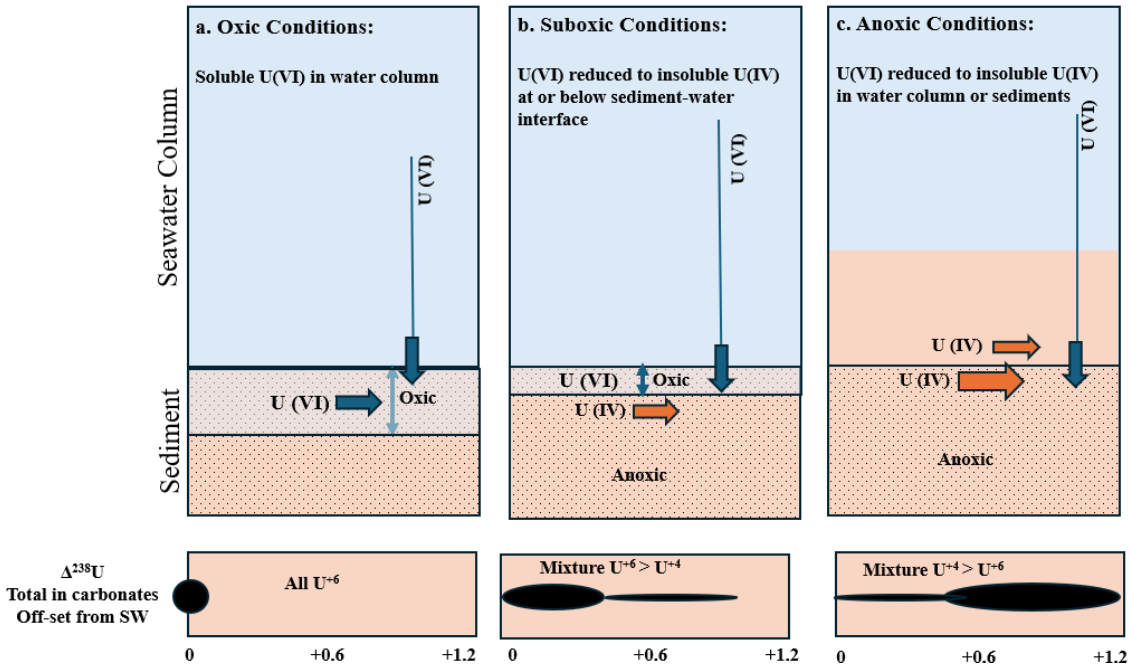

Figure 5.7| Schematic representation of U concentration and $\delta^{238}U$ in the water column under oxic, sub-oxic and anoxic conditions. The blue zone represents the seawater column, dotted brown zone represents sediment. The lower panel shows the range of $\Delta^{238}U_{anox}$ observed in modern and recent sediments (see text for further details).

Thus, the uptake of U^{+4} in the reducing carbonates will lead to a $\delta^{238}U_{CAU}$ higher than contemporary seawater. How large this expressed U isotope fractionation is, depends on several factors, including the U isotope fractionation factor and potential transport reaction limitations, which may lower the overall $\delta^{238}U$ (Andersen et al., 2014). The mean $\delta^{238}U_{CAU}$ in such environments would depend on the $\delta^{238}U$ of the reductively formed carbonates and the proportion of U between this and the planktonic contribution. Overall, however, a high $\delta^{238}U_{CAU}$ is expected, similar to the observations in organic-rich sediments from euxinic basins e.g. the Cariaco Basin (Andersen et al., 2014), Saanich Inlet (Holmden et al., 2015), and Baltic Sea (Noordmann et al., 2015).

A third scenario to consider is a setting in-between these two settings, with oxic seawater and the upper sediment, but with reducing pore-waters below, an oxic penetration depth in the sediment pile (Figure 5.7b). Here both the biotic planktic and benthic carbonate

deposition would provide carbonates with U^{+6} and $\delta^{238}U_{CAU}$ near seawater, however, carbonate cement formed from pore-waters in the lower reducing part of the sediments would incorporate U^{+4} with a U isotope fractionation towards heavier values. The isotope fractionation in this setting, however, would likely be muted from transport reaction limitations, where the soluble U(VI) is diffusing through the oxic penetration zone before being reduced from the porewaters in the same way as suggested for U uptake in modern sub-oxic siliciclastic-rich settings (Andersen et al., 2017; Andersen et al., 2020). The overall $\delta^{238}U_{CAU}$ in this setting is again a mixture of the oxic and reductive U uptake in the carbonate and U isotope fractionation. Thus, an $\delta^{238}U_{CAU}$ elevated from $\delta^{238}U$ of contemporary seawater is expected, but likely lower than the anoxic water column scenario discussed before, given the proportion of the planktonic and benthic carbonate component is relatively larger than the reductive U component and the latter has a lower expressed U isotope fractionation. This latter sub-oxic scenario is likely in any setting with an organic-carbon flux to the sediments that do not lead to full water column anoxia but leads to regionally anoxic conditions (e.g. modern upwelling and shelf-zone environments) and observed in Bahamian sediments (Romaniello et al., 2013, Chen et al., 2018; Tissot et al., 2018,).

This framework is consistent with Clarkson et al. (2023) concluding that there is large variability in Neoproterozoic $\delta^{238}U$ values in reducing settings that have a strong environmental control affecting isotope enrichment during reduction. With this framework to interpret the localised redox conditions, it is possible to interpret the temporal redox evolution in the samples screened for diagenetic effects (Figure 5.5), the range of $\delta^{238}U_{CAU}$ values for the Lossit limestone formation samples, with the highest $\delta^{238}U_{CAU}$ in the stratigraphically oldest sample (0.10‰) before the remaining samples move to lower values (-0.32 to -0.26‰). While the contemporary seawater value is unknown, the Fe-speciation data do classify these samples are being deposited in an anoxic environment. The $\delta^{238}U$

framework, suggests that the environment shifted from a stratified anoxic ocean towards a more dynamic but less overall reducing environment ('sub-oxic' in the framework). In the Tillite samples above the $\delta^{238}U_{CAU}$ increases slightly ($\delta^{238}U$ of −0.2 to -0.09‰) suggesting a setting either sub-oxic or moving towards full ocean anoxia. The decrease in $\delta^{238}U_{CAU}$ (-0.40 ‰) for the immediate post-Snowball sample shows $\delta^{238}U_{CAU}$ similar to modern oxygenated seawater (~−0.38‰) and combined with the oxic setting in the Fe_{HR}/Fe_T (Figure 5.1) and Fe/Al ratios, it suggests a deposition during oxygenated conditions. This sample also has the highest U/(Mg+Ca) of all samples (Figure 5.1b), which could attest to a large marine U reservoir, where high deglacial continental weathering U flux and lower marine U removal from ocean sinks would be in support of an oxygenated ocean at this time-interval. The data, however, indicates that this is a brief oxygenation event, which is then followed by an increase of $\delta^{238}U_{CAU}$ for late post-Snowball samples ($\delta^{238}U_{CAU}$ up to 0.08‰). I attribute the higher $\delta^{238}U_{CAU}$ values in pre-Snowball, together with Fe_{HR}/Fe_T data showing post-Snowball was deposited under anoxic conditions, as being most consistent with fully anoxic ocean conditions above the setting. Lastly, the stratigraphically youngest Bonhaven samples suggest a return to more oxic conditions with the lowest $\delta^{238}U_{CAU}$ (-0.04 ‰) measured in this unit of the screened data set. The $\delta^{238}U_{CAU}$ shows a refined redox evolution across the Sturtian Snowball from fully anoxic to suboxic and oxic periods. With this framework, the results show a short transit to the oxygenated ocean immediately after Sturtian Snowball as indicated by sample Ci-16-01 with $\delta^{238}U$ of -0.4 ‰. The $\delta^{238}U$ findings for this study agree with those reported by Lau et al. (2017) from the Taishir Formation in Mongolia.

5.5 Conclusion

This study reveals the ocean redox across Sturtian Snowball Earth glaciation via carbonate-associated uranium isotope ($\delta^{238}U_{CAU}$), Fe speciation and Fe/Al ratios. The results show marine redox fluctuations across the studied successions. Although, most $\delta^{238}U_{CAU}$ values indicate localised anoxic/suboxic pore-water, the integrated data ($\delta^{238}U_{CAU}$, Fe speciation and Fe/Al) confirm a brief shift towards more oxygenated conditions in the immediate aftermath of the Sturtian glaciation followed by a return to anoxia. The close agreement between three independent paleo-redox proxies (i.e., Fe speciation, Fe/Al ratios and $\delta^{238}U_{CAU}$) provides strong support for a robust paleo-redox reconstruction for the studied basin. The alignment of the current data with similar $\delta^{238}U$ results from the Taishir Formation in Mongolia (Lau et al., 2017), with Fe speciation finding from the Guitouwan section, Shennongjia area, South China (Xubin Wang et al. 2024) and with Fe isotope data (Tahata et al., 2015; Zhang et al., 2015; Kunzmann et al., 2017) suggest the end of the Sturtian Snowball was followed by a global but transient oxygenation event. In addition, Krause et al. (2022) suggest that O_2 recovered after the Sturtian by using quantitative reconstruction of O_2 levels during the entire Neoproterozoic. This temporary oxygenation following the Sturtian Snowball Earth was associated with increased weathering and nutrient delivery (e.g., P) by clay minerals to the seawater (Chi Fru et al., 2023; Al Bahri et al., 2024). The decline of sheet silicate-bound P from the high tillite concentrations (Chi Fru et al., 2023), cause the return to reducing conditions in the seawater.

Chapter 6: Conclusions and Future Work

This chapter provides a concise summary and reflection on the work presented throughout this thesis.

6.1 Contribution to Knowledge

A combination of mineralogical and geochemical analysis was applied to the studied samples of the ca. 350 m thick stromatolitic Pre-Snowball Lossit Limestone deposit formed in a tropical seawater setting, the deglaciating 1-km thick Port Askaig Tillites and the overlying post-Snowball deposits, beginning with the Bonahaven dolomite Formation extending upwards for over 350 m from Islay and the Garvellachs Island, Scotland. This thesis has investigated the clay mineral phases and provides a comprehensive mineralogical map of these sedimentary rock units, deposited before, during and after the Sturtian Snowball glaciation in Islay, Scotland (chapter 3), the role of clay minerals in nutrient delivery (Chapter 4) and seawater oxygenation dynamic across the Sturtian Snowball (Chapter 5).

6.1.1 Chapter 3

This chapter focuses on mineralogical investigations, weathering processes, and the paleoenvironmental conditions of the studied sedimentary rocks. These rocks were analysed by high-resolution petrographic scanning electron microscopy-energy dispersive x-ray spectroscopy, combined with bulk and <2μ clay-size fraction X-ray diffraction mineralogical analysis and trace and major element geochemistry. The studied sediments show no evidence of high-grade metamorphic alternation. However, they have undergone some degree of post-depositional diagenetic modifications such as K-metasomatism,

particularly, in the pre-/post-glacial samples. The study reveals a dominant presence of illite in all three distinct lithologies. The glacial till is enriched with chlorite, while authigenic kaolinite is more prevalent in the pre-glacial and post-glacial greenhouse facies, but scarce in the glaciogenic tillites. The Al_2O_3/TiO_2 ratios showed that the studied samples were derived from intermediate igneous and felsic rocks with compositional variation of granite and granodiorite as indicated by the La-Th-Sc ternary diagram. Discriminant binary plots of Th/Sc vs Zr/Sc ratios, indicative of insignificant modification of primary sediment composition by hydraulic sorting and recycling processes, together with chemical weathering indices, point to moderate to intense chemical weathering of the pre-glacial and post-glacial source rocks. Much lower chemical weathering indices, coupled with distinct chlorite composition in the glacial till, are consistent with mechanical tillage of continental landmass by the terminal Snowball melting ice sheets. The moderate to intense chemical weathering indices in the pre-and post-glacial deposits correspond with greenhouse conditions of elevated atmospheric CO_2 content and temperature. In contrast, mechanical erosion by glaciers dominated the deglacial period, reflected in the low weathering indices and the composition of glacial till.

6.1.2 Chapter 4

In this chapter, I employed Fe and P sequential extraction, alongside stable isotopes ($\delta^{13}C_{carbonate}$, $\delta^{13}C_{org}$ and $\delta^{18}O_{carbonate}$), organic carbon (C_{org}) and carbonate concentrations, bulk and trace elemental and mineralogical analysis to unravel the link between clay mineral formation and the supply of nutrients to seawater across the Sturtian Snowball Earth interval. Major elements (Al, P, Fe and Mn) and trace elements (Cr, V, Ni and Co) were normalized with Ti, a detrital indicator of authigenic enrichment, to interpret detrital source and assess

elemental enrichment patterns. The correlation analysis within the bulk geochemistry analyses indicates strong relationships between P, Fe, and trace elements, with Al and Ti. The separation of different mineral phases through a sequential extraction approach provides a powerful tool for studying the distribution of P among different reservoirs. The results indicate that P variations are strongly associated with sheet silicate and iron oxides throughout the studied sequence. The increasing bioavailability of P in the immediate post-Snowball phases is associated with the supply of sheet silicate-bound P (clay minerals) to seawater during deglaciation. The evidence points to a sink switch of sheet silicate-bound P to seawater-derived iron oxides under post-glaciation seawater conditions. The volume of P bound to iron oxides was therefore considered to reflect seawater P content before, during, and after the glaciation.

6.1.3 Chapter 5

Seawater redox evolution across the sampled interval was reconstructed through the application of multiple paleo-redox proxies—$\delta^{238}U_{CAU}$, iron speciation and Fe_T/Al. The evaluation of the diagenetic control on the geochemical signatures of $^{238}U_{CAU}$ was tested by the traditional proxies; meteoric alteration by Mn/Sr, $\delta^{13}C_{carbonate}$ and $\delta^{18}O_{carbonate}$, dolomitization/mineralogical transformations (aragonite to calcite) by Mg/Ca and Sr/Ca, and detrital influence by Th/U. After screening the data for post-deposition alternation and localised porewater diagenesis, the immediate post-Snowball sample was found to have a $\delta^{238}U_{CAU}$ value of −0.40 ± 0.05% (2SD) similar to the modern ocean, with coeval Fe speciation values of $Fe_{HR}/Fe_T < 0.22$ and Fe_T/Al ratios of ~0.5, consistent with deposition beneath localised oxic waters. In contrast, the overlying late post-Snowball and the underlying tillite and pre-Snowball successions bracketing this oxic event have $Fe_{HR}/Fe_T > 0.38$ consistent with formation beneath anoxic-ferruginous waters. The data suggests a short-

lived change from localised anoxic to oxic waters across the transition from icehouse to greenhouse conditions, followed by a reversal to anoxic waters.

6.1.4 Concluding Remark

This thesis unravels the interplay between Earth's climate state, weathering linked to clay mineral production and the supply of nutrients to seawater, with phosphorus shown to have played a critical role in post-glacial Snowball Earth seawater oxygenation. It provides a mechanistic explanation of how Snowball Earth climates effectively supply nutrients to seawater and the consequence on planetary oxidation state. Furthermore, this research contributes to a broader understanding of the interactions between geological processes, biogeochemical processes and biological evolution in the context of global climate change.

6.2 Future Work

To better understand global geochemical changes during the Cryogenian period, further studies of Sturtian sediments are crucial. This will help determine whether Scotland's Islay and Garvellach formations represent unique biogeochemical conditions or if they archive a broader record of Cryogenian glaciations. Comparing these findings to younger Marinoan glaciations could reveal global patterns and quantify the role these events played in expanding marine nutrient reservoirs—particularly seawater phosphate, which sustains the modern biosphere. The work described here could pave the way for further developing biogeochemical models to track seawater oxygenation trends before, during, and after Snowball Earth events, based on clay mineral formation dynamics across Earth's history. Their associated nutrient content could offer insights into primary production and oxygenation dynamics on a global scale, particularly with respect to the Neoproterozoic Snowball Earth climate interval.

References

Abbot, D.S., Voigt, A. and Koll, D. (2011). The Jormungand global climate state and implications for Neoproterozoic glaciations. *Journal of Geophysical Research: Atmospheres,* 116(D18).

Abbot, D.S., Voigt, A., Branson, M., Pierrehumbert, R.T., Pollard, D., Le Hir, G. and Koll, D.D. (2012). Clouds and snowball Earth deglaciation. *Geophysical Research Letters,* 39(20).

Abbot, D.S., Voigt, A., Li, D., Hir, G.L., Pierrehumbert, R.T., Branson, M., Pollard, D. and B. Koll, D.D. (2013). Robust elements of Snowball Earth atmospheric circulation and oases for life. *Journal of Geophysical Research: Atmospheres,* 118(12), pp. 6017–6027.

Abbott, A.N., Löhr, S. and Trethewy, M. (2019). Are clay minerals the primary control on the oceanic rare earth element budget? *Frontiers in Marine Science,* 6, p. 504.

Ajmal, Z., Muhmood, A., Usman, M., Kizito, S., Lu, J., Dong, R. and Wu, S. (2018). Phosphate removal from aqueous solution using iron oxides: adsorption, desorption and regeneration characteristics. *Journal of colloid and interface science,* 528, pp. 145–155.

Akcil, A. and Koldas, S. (2006). Acid Mine Drainage (AMD): causes, treatment and case studies. *Journal of cleaner production,* 14(12–13), pp. 1139–1145.

Al Bahri, J., Bankole, O., Muir, D., El Albani, A., Oldroyd, A., Contreras, D., Andersen, M. and Fru, E.C. (2024). Clay mineral geochemistry and paleoenvironmental reconstruction across the Cryogenian Sturtian Snowball glaciation. *Precambrian Research,* 410, p. 107498.

Al-Jaroudi, S.S., Ul-Hamid, A., Mohammed, A.-R.I. and Saner, S. (2007). Use of X-ray powder diffraction for quantitative analysis of carbonate rock reservoir samples. *Powder Technology,* 175(3), pp. 115–121.

Albani, A.E., Bengtson, S., Canfield, D.E., Bekker, A., Macchiarelli, R., Mazurier, A., Hammarlund, E.U., Boulvais, P., Dupuy, J.J., Fontaine, C. and Fursich, F.T. (2010). Large colonial organisms with coordinated growth in oxygenated environments 2.1 Gyr ago. *Nature* 466(7302), pp. 100–104.

Alcott, L.J., Mills, B.J.W., Bekker, A. and Poulton, S.W. (2022). Earth's Great Oxidation Event facilitated by the rise of sedimentary phosphorus recycling. *Nature Geoscience,* 15(3), pp. 210–215.

Algeo, T.J. and Ingall, E. (2007). Sedimentary Corg:P ratios, paleocean ventilation, and Phanerozoic atmospheric pO2. *Palaeogeography, Palaeoclimatology, Palaeoecology,* 256(3–4), pp. 130–155.

Algeo, T.J. and Liu, J. (2020). A re-assessment of elemental proxies for paleoredox analysis. *Chemical Geology,* 540.

Allen, P.A. and Etienne, J.L. (2008). *Sedimentary challenge to Snowball Earth*. *Nature Geoscience, 1*(12), pp.817-825.

Analytical, P. (2001). New analytical software for XRD simplifies identification of complex phase mixtures. *Journal of Applied Crystallography*, *34*(6), pp.788-788.

Anders, E. and Grevesse, N. (1989). Abundances of the elements: Meteoritic and solar. *Geochimica et Cosmochimica acta*,*53*(1), pp.197-214.

Andersen, M.B., Elliott, T., Freymuth, H., Sims, K.W.W., Niu, Y. and Kelley, K.A. (2015). The terrestrial uranium isotope cycle. *Nature,* 517(7534), pp. 356–359.

Andersen, M.B., Matthews, A., Bar-Matthews, M. and Vance, D. (2020). Rapid onset of ocean anoxia shown by high U and low Mo isotope compositions of sapropel S1. *Geochemical Perspectives Letters,* 15, p. 10-14.

Andersen, M.B., Romaniello, S., Vance, D., Little, S.H., Herdman, R. and Lyons, T.W. (2014). A modern framework for the interpretation of 238U/235U in studies of ancient ocean redox. *Earth and Planetary Science Letters,* 400, pp. 184–194.

Andersen, M.B., Stirling, C.H. and Weyer, S. (2017). Uranium isotope fractionation. In: *Non-Traditional Stable Isotopes*. *Reviews in Mineralogy and Geochemistry*, pp. 799–850.

Andersen, M.B., Stirling, C.H., Zimmermann, B. and Halliday, A.N. (2010). Precise determination of the open ocean 234U/238U composition. Geochemistry, Geophysics, Geosystems, 11(12).

Andersen, M.B., Vance, D., Keech, A.R., Rickli, J. and Hudson, G. (2013). Estimating U fluxes in a high-latitude, boreal post-glacial setting using U-series isotopes in soils and rivers. *Chemical Geology,* 354, pp. 22–32.

Andersen, M.B., Vance, D., Morford, J.L., Bura-Nakić, E., Breitenbach, S.F.M. and Och, L. (2016). Closing in on the marine 238U/235U budget. *Chemical Geology,* 420, pp. 11–22.

Anderson, R.P., Tarhan, L.G., Cummings, K.E., Planavsky, N.J. and Bjørnerud, M. (2016). Macroscopic structures in the 1.1 Ga continental Copper Harbor Formation: Concretions or fossils? *Palaios,* 31(7), pp. 327–338.

Árkai, P. and Ghabrial, D.S. (1997). Chlorite crystallinity as an indicator of metamorphic grade of low-temperature meta-igneous rocks; a case study from the Bukk Mountains, Northeast Hungary. Clay minerals, 32(2), pp.205-222.

Arnaud, E. and Fairchild, I.J. (2011). The Port Askaig Formation, Dalradian Supergroup, Scotland. *Geological Society, London, Memoirs* 36(1), pp. 635–642.

Asael, D., Rouxel, O., Poulton, S.W., Lyons, T.W. and Bekker, A. (2018). Molybdenum record from black shales indicates oscillating atmospheric oxygen levels in the early Paleoproterozoic. *American Journal of Science*, *318*(3), pp.275-299.

Aubineau, J., Bankole, O.M., Baron, F., Grégoire, B. and El Albani, A. (2021). Authigenic kaolinite and sudoite in sandstones from the Paleoproterozoic Franceville sub-basin (Gabon). *Comptes Rendus. Géoscience,* 353(1), pp. 209–226.

Aubineau, J., ElAlbani, A., Bekker, A., Somogyi, A., Bankole, O.M., Macchiarelli, R., Meunier, A., Riboulleau, A., Reynaud, J.Y. and Konhausesr, K.O. (2019). Microbially induced potassium enrichment in Paleoproterozoic shales and implications for reverse weathering on early Earth. *Nature Communications,* 10(1), pp. 1–9.

Bahlburg, H. and Dobrzinski, N. (2011). A review of the Chemical Index of Alteration (CIA) and its application to the study of Neoproterozoic glacial deposits and climate transitions. *Geological Society, London, Memoirs,* 36(1), pp. 81–92.

Baldermann, A., Abdullayev, E., Taghiyeva, Y., Alasgarov, A. and Javad-Zada, Z. (2020). Sediment petrography, mineralogy and geochemistry of the Miocene Islam Dağ Section (Eastern Azerbaijan): Implications for the evolution of sediment provenance, palaeo-environment and (post-) depositional alteration patterns. *Sedimentology,* 67(1), pp. 152–172.

Baldermann, A., Banerjee, S., Czuppon, G., Dietzal, M., Farkas, J., Lohr, S., Moser, U., Scheiblhofer, E., Wright, N.M. and Zack, T. (2022). Impact of green clay authigenesis on element sequestration in marine settings. *Nature Communications,* 13(1), pp. 1–11.

Baldermann, A., Warr, L.N., Letofsky-Papst, I. and Mavromatis, V. (2015). Substantial iron sequestration during green-clay authigenesis in modern deep-sea sediments. *Nature Geoscience,* 8(11), pp. 885–889.

Banerjee, A. (2016). Estimation of dolomite formation: Dolomite precipitation and dolomitization. *Journal of the Geological Society of India*, *87*, pp.561-572.

Banner', J.L. and Hanson, G.N. (1990). *Calculation of simultaneous isotopic and trace element variations during water-rock interaction with applications to carbonate diagenesis*. *Geochimica et Cosmochimica Acta, 54*(11), pp.3123-3137.

Bao, H., Lyons, J.R. and Zhou, C. (2008). Triple oxygen isotope evidence for elevated CO2 levels after a Neoproterozoic glaciation. *Nature,* 453(7194), pp. 504–506.
Barthélémy, K., Naille, S., Despas, C., Ruby, C. and Mallet, M. (2012). Carbonated ferric green rust as a new material for efficient phosphate removal. *Journal of colloid and interface science,* 384(1), pp. 121–127.
Beghin, J., Storme, J.Y., Blanpied, C., Gueneli, N., Brocks, J.J., Poulton, S.W. and Javaux, E.J. (2017). Microfossils from the late Mesoproterozoic – early Neoproterozoic Atar/El Mreïti Group, Taoudeni Basin, Mauritania, northwestern Africa. *Precambrian Research,* 291, pp. 63–82.
Bekker, A., Holland, H.D., Wang, P.L., Rumble Iii, D., Stein, H.J., Hannah, J.L., Coetzee, L.L. and Beukes, N.J. (2004). *Dating the rise of atmospheric oxygen*. *Nature, 427*(6970), pp.117-120.
Belli, K.M. and Taillefert, M. (2018). Geochemical controls of the microbially mediated redox cycling of uranium and iron. *Geochimica et Cosmochimica Acta,* 235, pp. 431–449.
Benitez-Nelson, C.R. (2000). The biogeochemical cycling of phosphorus in marine systems. *Earth-Science Reviews,* 51(1–4), pp. 109–135.
Bennett, W.W. and Canfield, D.E. (2020). Redox-sensitive trace metals as paleoredox proxies: A review and analysis of data from modern sediments. *Earth-Science Reviews,* 204, p.103175.
Berner, R.A. (2006). GEOCARBSULF: A combined model for Phanerozoic atmospheric O2 and CO2. *Geochimica et Cosmochimica Acta,* 70(23 SPEC. ISS.), pp. 5653–5664.
Berner, R.A. and Berner, R.A. (2004). *The Phanerozoic carbon cycle: CO2 and O2*. Oxford University Press.
Berner, R.A., Beerling, D.J., Dudley, R., Robinson, J.M. and Wildman, R.A. (2003). Phanerozoic atmospheric oxygen. *Annual Review of Earth and Planetary Sciences,* 31, pp. 105–134.
Bethke, C.M. and Altaner, S.P. (1986). Layer-by-layer mechanism of smectite illitization and application to a new rate law. *Clays and Clay Minerals,* 34(2), pp. 136–145.
Betts, H.C., Puttick, M.N., Clark, J.W., Williams, T.A., Donoghue, P.C.J. and Pisani, D. (2018). Integrated genomic and fossil evidence illuminates life's early evolution and eukaryote origin. *Nature ecology & evolution, 2*(10), pp. 1556–1562.
Bhatia, M.P., Das, S.B., Xu, L., Charette, M.A., Wadham, J.L. and Kujawinski, E.B. (2013). Organic carbon export from the Greenland ice sheet. *Geochimica et Cosmochimica Acta,* 109, pp. 329–344.
Bhattacharyya, K.G. and Sen Gupta, S. (2006). Adsorption of chromium (VI) from water by clays. *Industrial & engineering chemistry research, 45*(21), pp. 7232–7240.
Bigeleisen, J. (1996). Nuclear Size and Shape Effects in Chemical Reactions. Isotope Chemistry of the Heavy Elements. *Journal of the American Chemical Society*, 118(15), pp.3676-3680.
Bindeman, I.N., Schmitt, A.K. and Evans, D.A.D. (2010). Limits of hydrosphere-lithosphere interaction: Origin of the lowest-known $\delta^{18}O$ silicate rock on Earth in the Paleoproterozoic Karelian rift. *Geology, 38*(7), pp. 631–634.
Bish, D.L. and Howard, S.A. (1988). Quantitative phase analysis using the Rietveld method. *Journal of Applied Crystallography* 21(2), pp. 86–91.
Bjerrum, C.J. and Canfield, D.E. (2002). Ocean productivity before about 1.9 Gyr ago limited by phosphorus adsorption onto iron oxides. *Nature,* 417(6885), pp. 159–162.
Bland, W.J. and Rolls, D. (2016). *Weathering: an introduction to the scientific principles*. Routledge.

Bontognali T. R. R., Vasconcelos C., Warthmann R. J., Lundberg R. and McKenzie J. A. (2012) Dolomite-mediating bacterium isolated from the sabkha of Abu Dhabi (UAE). Terra Nova 24, 248–254.
Boström, K. (1970). Submarine volcanism as a source for iron. *Earth and planetary science letters, 9(*4), pp. 348–354.
Boström, K., Joensuu, O., Valdes, S. and Riera, M. (1972). Geochemical history of South Atlantic Ocean sediments since late Cretaceous. *Marine Geology, 12*(2), pp. 85–121.
Boström, K., Kraemer, T. and Gartner, S. (1973). Provenance and accumulation rates of opaline silica, Al, Ti, Fe, Mn, Cu, Ni and Co in Pacific pelagic sediments. *Chemical Geology, 11*(2), pp. 123–148.
Boström, K., Peterson, M.N.A., Joensuu, O. and Fisher, D.E. (1969). Aluminum-poor ferromanganoan sediments on active oceanic ridges. *Journal of Geophysical Research, 74*(12), pp. 3261–3270.
Bowyer, F.T. Zhuravlev, A.Y., Wood, R., Shields, G.A., Zhou, Y., Curtis, A., Poulton, S.W., Condon, D.J., Yang, C. and Zhu, M. (2022). Calibrating the temporal and spatial dynamics of the Ediacaran - Cambrian radiation of animals. *Earth-Science Reviews,* 225, p.103913
Bowyer, F.T., Krause, A.J., Song, Y., Huang, K.J., Fu, Y., Shen, B., Li, J., Zhu, X.K., Kipp, M.A., van Maldegem, L.M. and Brocks, J.J. (2023). Biological diversification linked to environmental stabilization following the Sturtian Snowball glaciation. *Science Advances*, *9*(34), p. eadf9999.
Bowyer, F.T., Shore, A.J., Wood, R.A., Alcott, L.J., Thomas, A.L., Butler, IB., Curtis A., Hainanan, S., Curtis-Walcott, S., Penny,A.M. and Poulton, S.W. (2020). Regional nutrient decrease drove redox stabilisation and metazoan diversification in the late Ediacaran Nama Group, Namibia. *Scientific Reports, 10*(1), p. 2240.
Boyle, E.A., Edmond, J.M. and Sholkovitz, E.R. (1977). The mechanism of iron removal in estuaries. *Geochimica et Cosmochimica Acta, 4*1(9), pp. 1313–1324.
Bozdag, G.O., Libby, E., Pineau, R., Reinhard, C.T. and Ratcliff, W.C. (2021). Oxygen suppression of macroscopic multicellularity. *Nature communications, 12*(1), p. 2838.
Please make sure you liaise with your supervisors to discuss these.
Bozkaya, Ö., Yalcin, H. and Schroeder, P.A. (2017). Two-step mode of clay formation in the extensional basins: Cambrian–Ordovician clastic rocks of the Antalya unit, SW Turkey. *Clay Minerals*, *52*(3), pp. 365–389.
Bradbury, M.H. and Baeyens, B. (2009). Sorption modelling on illite Part I: Titration measurements and the sorption of Ni, Co, Eu and Sn. *Geochimica et Cosmochimica Acta, 73*(4), pp. 990–1003.
Brady, M.P., Tostevin, R. and Tosca, N.J. (2022). Marine phosphate availability and the chemical origins of life on Earth. *Nature Communications, 13*(1), p.5162.
Brasier, M.D. and Shields, G. (2000). Neoproterozoic chemostratigraphy and correlation of the Port Askaig glaciation, Dalradian Supergroup of Scotland. *Journal of the Geological Society,* 157(5), pp. 909–914.
Brennecka, G.A., Herrmann, A.D., Algeo, T.J. and Anbar, A.D. (2011). Rapid expansion of oceanic anoxia immediately before the end-Permian mass extinction. *Proceedings of the National Academy of Sciences, 108*(43), pp. 17631-17634.
Brigatti, M.F., Galan, E. and Theng, B.K.G. (2006). Chapter 2 Structures and Mineralogy of Clay Minerals. *Developments in Clay Science, 1*(C), pp. 19–86.
Brindley, G.W. (1980). Quantitative X-ray mineral analysis of clays.
Brocks, J.J., Jarrett, A.J.M., Sirantoine, E., Hallmann, C., Hoshino, Y. and Liyanage, T. (2017). The rise of algae in Cryogenian oceans and the emergence of animals. *Nature* 548(7669), pp. 578–581.

Broecker, W.S. and Peng, T.-H. (1982). *Tracers in the Sea*. Lamont-Doherty Geological Observatory. *Tracers in the sea, 690.*

Brown, G. (1984). Crystal structures of clay minerals and related phyllosilicates. *Philosophical Transactions of the Royal Society of London, 240*(A311), pp. 221–240.

Bruggmann, S., Gilleaudeau, G.J., Romaniello, S.J., Severmann, S., Canfield, D.E., Anbar, A.D., Scholz, F. and Frei, R. (2022). Uranium isotope cycling on the highly productive Peruvian margin. *Chemical Geology,* 590, p. 120705.

Brüske, A., Weyer, S., Zhao, M.Y., Planavsky, N.J., Wegwerth, A., Neubert, N., Dellwig, O., Lau, K.V. and Lyons, T.W. (2020). Correlated molybdenum and uranium isotope signatures in modern anoxic sediments: Implications for their use as paleo-redox proxy. *Geochimica et Cosmochimica Acta,* 270, pp. 449–474.

Buatois, L.A., Narbonne, G.M., Mángano, M.G., Carmona, N.B. and Myrow, P. (2014). Ediacaran matground ecology persisted into the earliest Cambrian. *Nature Communications,* 5(1), p.3544.

Budyko, M.I. (1969). The effect of solar radiation variations on the climate of the Earth. *Tellus A: Dynamic Meteorology and Oceanography, 21*(5), p. 611.

Buick, R., Des Marais, D.J., Knoll, A.H. (1995). Stable isotopic compositions of carbonates from the Mesoproterozoic Bangemall Group, northwestern Australia. Chemical Geology 123, 153–171.

Buick, R. (2008). When did oxygenic photosynthesis evolve? In: *Philosophical Transactions of the Royal Society B: Biological Sciences*. Royal Society, pp. 2731–2743.

Bura-Nakić, E., Andersen, M.B., Archer, C., de Souza, G.F., Marguš, M. and Vance, D. (2018). Coupled Mo-U abundances and isotopes in a small marine euxinic basin: Constraints on processes in euxinic basins. *Geochimica et Cosmochimica Acta,* 222, pp. 212–229.

Burley, S. and Worden, R. (2009). *Sandstone diagenesis: recent and ancient*. John Wiley & Sons.

Canfield, D.E. (2005). The early history of atmospheric oxygen: Homage to Robert M. Garrels. *Annual Review of Earth and Planetary Sciences,* 33, pp. 1–36.

Canfield, D.E., Ngombi-Pemba, L., Hammarlund, E.U., Bengtson, S., Chaussidon, M., Gauthier-Lafaya, F., Meunier, A., Riboulleau, A., Rollion-Bard, C., Rouxel, O. and Asael, D. (2013). Oxygen dynamics in the aftermath of the Great Oxidation of Earth's atmosphere. *Proceedings of the National Academy of Sciences of the United States of America,* 110(42), pp. 16736–16741.

Canfield, D.E., Poulton, S.W. and Narbonne, G.M. (2007). Late-Neoproterozoic deep-ocean oxygenation and the rise of animal life. *Science,* 315(5808), pp. 92–95.

Cárdenas, A.L. and Harries, P.J. (2010). Effect of nutrient availability on marine origination rates throughout the Phanerozoic eon. *Nature Geoscience, 3*(6), pp. 430–434.

Catling, D.C. and Claire, M.W. (2005). How earth's atmosphere evolved to an oxic state: A status report. *Earth and Planetary Science Letters,* 237(1–2), pp. 1–20.

Chamley, H. and Chamley, H. (1989). Clay formation through weathering. In: *Clay sedimentology*. Springer, pp. 21–50.

Chabaux, F., J. Riotte, and O. Dequincey (2003), U-Th-Ra frac-tionation during weathering and river transport, in Uranium-Series Geochemistry, Rev. in Mineral. and Geochem.,vol. 52, pp. 533–576, doi:10.2113/0520533, Mineral. Soc.of Am., Washington, D. C.

Chang, B., Li, C., Liu, D., Foster, I., Tripati, A., Lloyd, M.K., Maradiaga, I., Luo, G., An, Z., She, Z. and Xie, S. (2020). Massive formation of early diagenetic dolomite in the Ediacaran Ocean: Constraints on the "dolomite problem". *Proceedings of the national academy of sciences*, *117*(25), pp.14005-14014.

Chen, B., Hu, C., Mills, B.J., He, T., Andersen, M.B., Chen, X., Liu, P., Lu, M., Newton, R.J., Poulton, S.W and Shields, G.A. (2022). A short-lived oxidation event during the early

Ediacaran and delayed oxygenation of the Proterozoic ocean. *Earth and Planetary Science Letters,* 577, p. 117274.
Chen, X., Romaniello, S.J., Herrmann, A.D., Hardisty, D., Gill, B.C. and Anbar, A.D. (2018). Diagenetic effects on uranium isotope fractionation in carbonate sediments from the Bahamas. *Geochimica et Cosmochimica Acta,* 237, pp. 294–311.
Chen, X., Romaniello, S.J., Herrmann, A.D., Wasylenki, L.E. and Anbar, A.D. (2016). Uranium isotope fractionation during coprecipitation with aragonite and calcite. *Geochimica et Cosmochimica Acta,* 188, pp. 189–207.
Cheng, H., Edwards, R.L., Shen, C.C., Polyak, V.J., Asmerom, Y., Woodhead, J., Hellstrom, J., Wang, Y., Kong, X., Spötl, C. and Wang, X. (2013). Improvements in 230Th dating, 230Th and 234U half-life values, and U–Th isotopic measurements by multi-collector inductively coupled plasma mass spectrometry. Earth and Planetary Science Letters, 371, pp.82-91.
Chen, X., Tissot, F.L.H., Jansen, M.F., Bekker, A., Liu, C.X., Nie, N.X., Halverson, G.P., Veizer, J. and Dauphas, N. (2021). The uranium isotopic record of shales and carbonates through geologic time. *Geochimica et Cosmochimica Acta,* 300, pp. 164–191.
Cheng, C., Busigny, V., Ader, M., Thomazo, C., Chaduteau, C. and Philippot, P. (2019). Nitrogen isotope evidence for stepwise oxygenation of the ocean during the Great Oxidation Event. *Geochimica et Cosmochimica Acta*, *261*, pp.224-247.
Chi Fru, E., Aubineau, J., Bankole, O., Ghnahalla, M., Tamehe, L.S. and El Albani, A. (2024). Hydrothermal seawater eutrophication triggered local macrobiological experimentation in the 2100 Ma Paleoproterozoic Francevillian sub-basin. *Precambrian Research,* 409, p. 107453.
Chi Fru, E., Bahri, J.A., Brosson, C., Bankole, O., Aubineau, J., ElAlbani, A., Nederbragt, A., Oldroyd, A., Skelton, A., Lowhagen, L. and Webster, D. (2023). Transient fertilization of a post-Sturtian Snowball ocean margin with dissolved phosphate by clay minerals. *Nature Communications,* 14(1), p.8418.
Chi Fru, E., Hemmingsson, C., Holm, M., Chiu, B. and Iñiguez, E. (2016b). Arsenic-induced phosphate limitation under experimental Early Proterozoic oceanic conditions. *Earth and Planetary Science Letters*, *434*, pp.52-63.
Chi Fru, E., Rodríguez, N.P., Partin, C.A., Lalonde, S.V., Andersson, P., Weiss, D.J., El Albani, A., Rodushkin, I. and Konhauser, K.O. (2016a). Cu isotopes in marine black shales record the Great Oxidation Event. *Proceedings of the National Academy of Sciences*, *113*(18), pp.4941-4946.
Chi Fru, E., Somogyi, A., El Abani, A., Medjoubi, K., Aubineau, J., Robbins, L.J., Lalonde, S.V. and Konhauser, K.O. (2019). The rise of oxygen-driven arsenic cycling at ca. 2.48 Ga. *Geology,* 47(3), pp. 243–246.
Chipera, S.J. and Bish, D.L. (2013). Fitting full X-ray diffraction patterns for quantitative analysis: a method for readily quantifying crystalline and disordered phases.
Chun, C.O.J., Delaney, M.L. and Zachos, J.C. (2010). Paleoredox changes across the Paleocene-Eocene thermal maximum, Walvis Ridge (ODP Sites 1262, 1263, and 1266): Evidence from Mn and U enrichment factors. *Paleoceanography,* 25(4).
Clarkson, M.O., Hennekam, R., Sweere, T.C., Andersen, M.B., Reichart, G.J. and Vance, D. (2021). Carbonate associated uranium isotopes as a novel local redox indicator in oxidatively disturbed reducing sediments. *Geochimica et Cosmochimica Acta,* 311, pp. 12–28.
Clarkson, M.O., Müsing, K., Andersen, M.B. and Vance, D. (2020). Examining pelagic carbonate-rich sediments as an archive for authigenic uranium and molybdenum isotopes using reductive cleaning and leaching experiments. *Chemical Geology,* 539, p. 119412.

Clarkson, M.O., Poulton, S.W., Guilbaud, R. and Wood, R.A. (2014). Assessing the utility of Fe/Al and Fe-speciation to record water column redox conditions in carbonate-rich sediments. *Chemical Geology,* 382, pp. 111–122.

Clarkson, M.O., Sweere, T.C., Chiu, C.F., Hennekam, R., Bowyer, F. and Wood, R.A. (2023). Environmental controls on very high δ238U values in reducing sediments: Implications for Neoproterozoic seawater records. *Earth-Science Reviews,* 237, p.104306.

Cohen, P.A. and Kodner, R.B. (2022). The earliest history of eukaryotic life: Uncovering an evolutionary story through the integration of biological and geological data. *Trends in Ecology & Evolution,* 37(3), pp. 246–256.

Cole, D.B., Planavsky, N.J., Longley, M., Böning, P., Wilkes, D., Wang, X., Swanner, E.D., Wittkop, C., Loydell, D.K., Busigny, V. and Knudsen, A.C. (2020). Uranium isotope fractionation in non-sulfidic anoxic settings and the global uranium isotope mass balance. *Global Biogeochemical Cycles*, *34*(8), p.e2020GB006649.

Combaudon, V., Sissmann, O., Bernard, S., Viennet, J.C., Megevand, V., Le Guillou, C., Guélard, J., Martinez, I., Guyot, F., Derluyn, H. and Deville, E. (2024). Are the Fe-rich-clay veins in the igneous rock of the Kansas (USA) Precambrian crust of magmatic origin?. *Lithos*,*474*, p.107583.

Condie, K.C. (1993). Chemical composition and evolution of the upper continental crust: Contrasting results from surface samples and shales. *Chemical geology*, *104*(1-4), pp.1-37.

Corsetti, F.A., Olcott, A.N. and Bakermans, C. (2006). The biotic response to Neoproterozoic snowball earth. *Palaeogeography, Palaeoclimatology, Palaeoecology,* 232(2–4), pp. 114–130.

Cotten, J., Le Dez, A., Bau, M., Caroff, M., Maury, R.C., Dulski, P., Fourcade, S., Bohn, M. and Brousse, R. (1995). Origin of anomalous rare-earth element and yttrium enrichments in subaerially exposed basalts: evidence from French Polynesia. *Chemical Geology*, *119*(1-4), pp.115-138.

Crowe, S.A., Døssing, L.N., Beukes, N.J., Bau, M., Kruger, S.J., Frei, R. and Canfield, D.E. (2013). Atmospheric oxygenation three billion years ago. *Nature,* 501(7468), pp. 535–538.

Crowe, S.A., Paris, G., Katsev, S., Jones, C., Kim, S.T., Zerkle, A.L., Nomosatryo, S., Fowle, D.A., Adkins, J.F., Sessions, A.L. and Farquhar, J. (2014). Sulfate was a trace constituent of Archean seawater. *Science*, *346*(6210), pp.735-739.

Cui, H., Kaufman, A.J., Peng, Y., Liu, X.M., Plummer, R.E. and Lee, E.I. (2018). The Neoproterozoic Hüttenberg δ13C anomaly: Genesis and global implications. *Precambrian Research,* 313, pp. 242–262.

Cullers, R.L. (2000). The geochemistry of shales, siltstones and sandstones of Pennsylvanian-Permian age, Colorado, USA: Implications for provenance and metamorphic studies. *Lithos,* 51(3), pp. 181–203.

Dahl, T.W., Boyle, R.A., Canfield, D.E., Connelly, J.N., Gill, B.C., Lenton, T.M. and Bizzarro, M. (2014). Uranium isotopes distinguish two geochemically distinct stages during the later Cambrian SPICE event. *Earth and Planetary Science Letters,* 401, pp. 313–326.

Dahl, T.W., Canfield, D.E., Rosing, M.T., Frei, R.E., Gordon, G.W., Knoll, A.H. and Anbar, A.D. (2011). Molybdenum evidence for expansive sulfidic water masses in ~750Ma oceans. *Earth and Planetary Science Letters,* 311(3–4), pp. 264–274.

Danovaro, R., Dell'Anno, A., Pusceddu, A., Gambi, C., Heiner, I. and Møbjerg Kristensen, R. (2010). The first metazoa living in permanently anoxic conditions. *BMC biology*,*8*, pp.1-10.

Daou, T.J., Begin-Colin, S., Greneche, J.M., Thomas, F., Derory, A., Bernhardt, P., Legaré, P. and Pourroy, G. (2007). Phosphate adsorption properties of magnetite-based nanoparticles. *Chemistry of Materials*, *19*(18), pp.4494-4505.

Darroch, S.A.F., Smith, E.F., Laflamme, M. and Erwin, D.H. (2018). Ediacaran Extinction and Cambrian Explosion. *Trends in Ecology and Evolution,* 33(9), pp. 653–663.

Defforey, D. and Paytan, A. (2018). Phosphorus cycling in marine sediments: Advances and challenges. *Chemical Geology*, *477*, pp.1-11.

Delaney, M.L. (1998). Phosphorus accumulation in marine sediments and the oceanic phosphorus cycle. *Global Biogeochemical Cycles,* 12(4), pp. 563–572.

Dias, I.A., Cury, L.F., Titon, B.G., Athayde, G.B., Fedalto, G., da Rocha Santos, L., Soares, A.P., de Vasconcelos Müller Athayde, C. and Manuela Bahniuk Rumbeslperger, A. (2020). The occurrence of authigenic clay minerals in alkaline-saline lakes, Pantanal Wetland (Nhecolândia Region, Brazil). *Minerals*, *10*(8), p.718.

Ding, H., Ma, D., Yao, C., Lin, Q. and Jing, L. (2016). Implication of the chemical index of alteration as a paleoclimatic perturbation indicator: an example from the lower Neoproterozoic strata of Aksu, Xinjiang, NW China. *Geosciences Journal,* 20(1), pp. 13–26.

Ding, W., Dong, L., Sun, Y., Ma, H., Xu, Y., Yang, R., Peng, Y., Zhou, C. and Shen, B. (2019). Early animal evolution and highly oxygenated seafloor niches hosted by microbial mats. *Scientific Reports*,*9*(1), p.13628.

Dodd, M.S., Shi, W., Li, C., Zhang, Z., Cheng, M., Gu, H., Hardisty, D.S., Loyd, S.J., Wallace, M.W., vS. Hood, A. and Lamothe, K. (2023). Uncovering the Ediacaran phosphorus cycle. *Nature*, *618*(7967), pp.974-980.

Dodd, M.S., Zhang, Z., Li, C., Algeo, T.J., Lyons, T.W., Hardisty, D.S., Loyd, S.J., Meyer, D.L., Gill, B.C., Shi, W. and Wang, W. (2021). Development of carbonate-associated phosphate (CAP) as a proxy for reconstructing ancient ocean phosphate levels. *Geochimica et Cosmochimica Acta*, *301*, pp.48-69.

Dos Santos, F.H., da Silva Amaral, W., Chi-Fru, E., de Souza, A.C.B. and Bosco-Santos, A. (2022). Paleoproterozoic manganese oxide precipitation in oxic seawater surface and reductive enrichment in anoxic seafloor. *Chemical Geology*, *588*, p.120655.

Du, Q., Qin, Z., Wang, J., Wang, Z., Deng, Q. and Yang, F. (2021). The Cryogenian Nanhuan System (South China) during the interglacial-glacial transition: geochemistry, sedimentary provenance, and tectonic setting. *International Geology Review,* 63(12), pp. 1540–1558.

Dunk, R.M., Mills, R.A. and Jenkins, W.J. (2002). A reevaluation of the oceanic uranium budget for the Holocene. *Chemical Geology*, *190*(1-4), pp.45-67.

Edmonsond, S., Nadeau, M.D., Turner, A.C., Wu, Z., Geyman, E.C., Ahm, A.S.C., Dyer, B., Oleynik, S., McGee, D., Stolper, D.A. and Higgins, J.A. (2024). Shallow carbonate geochemistry in the Bahamas since the last interglacial period. *Earth and Planetary Science Letters*, *627*, p.118566.

Egger, M., Jilbert, T., Behrends, T., Rivard, C. and Slomp, C.P. (2015). Vivianite is a major sink for phosphorus in methanogenic coastal surface sediments. *Geochimica et Cosmochimica Acta,* 169, pp. 217–235.

El Albani, A., Bengtson, S., Canfield, D.E., Riboulleau, A., Rollion Bard, C., Macchiarelli, R., Ngombi Pemba, L., Hammarlund, E., Munirer, A., Moubiya Mouele, I. and Benzerara, K. (2014). The 2.1 Ga old Francevillian biota: Biogenicity, taphonomy and biodiversity. *PLoS ONE,* 9(6), p.e99438.

El Albani, A., Konhauser, K.O., Somogyi, A., Ikouanga, J.N., Lamboux, A., Blichert-Toft, J., Chi-Fru, E., Fontaine, C., Mazurier, A., Riboulleau, A. and Pierson-Wickmann, A.C. (2023). A search for life in Palaeoproterozoic marine sediments using Zn isotopes and geochemistry. *Earth and Planetary Science Letters,* 612, p.118169.

Elert, K. and Rodriguez-Navarro, C. (2022). Degradation and conservation of clay-containing stone: A review. *Construction and Building Materials,* 330, p.127226.

Elrick, M., Polyak, V., Algeo, T.J., Romaniello, S., Asmerom, Y., Herrmann, A.D., Anbar, A.D., Zhao, L. and Chen, Z.Q. (2017). Global-ocean redox variation during the middle-late

Permian through Early Triassic based on uranium isotope and Th/U trends of marine carbonates. *Geology,* 45(2), pp. 163–166.
Ernst, R.E., Wingate, M.T.D., Buchan, K.L. and Li, Z.X. (2008). Global record of 1600-700 Ma Large Igneous Provinces (LIPs): Implications for the reconstruction of the proposed Nuna (Columbia) and Rodinia supercontinents. *Precambrian Research,* 160(1–2), pp. 159–178.
Erwin, D.H. (2015). Early metazoan life: Divergence, environment and ecology. *Philosophical Transactions of the Royal Society B: Biological Sciences,* 370(1684).
Erwin, D.H., Laflamme, M., Tweedt, S.M., Sperling, E.A., Pisani, D. and Peterson, K.J. (2011). The Cambrian conundrum: early divergence and later ecological success in the early history of animals. *Science,* 334(6059), pp. 1091–1097.
Essington, M.E. (2015). *Soil and water chemistry: an integrative approach*. CRC press.
Evans, D.A.D. and Raub, T.D. (2011). Chapter 7: Neoproterozoic glacial palaeolatitudes: A global update. *Geological Society Memoir,* 36(1), pp. 93–112. doi: 10.1144/M36.7.
Fabre, S. and Berger, G. (2012). How tillite weathering during the snowball Earth aftermath induced cap carbonate deposition. *Geology,* 40(11), pp. 1027–1030.
Fairchild, I.J., 1980. Sedimentation and origin of a late Precambrian" dolomite" from Scotland. Journal of Sedimentary Research, 50(2), pp.423-446.
Fairchild, I.J. and Spiro, B. (1990). Carbonate minerals in glacial sediments: geochemical clues to palaeoenvironment. *Geological Society, London, Special Publications,* 53(1), pp. 201–216.
Fairchild, I.J., Bonnand, P., Davies, T., Fleming, E.J., Grassineau, N., Halverson, G.P., Hambrey, M.J., McMillan, E.M., McKay, E., Parkinson, I.J. and Stevenson, C.T. (2016). The Late Cryogenian warm interval, NE Svalbard: chemostratigraphy and genesis. *Precambrian Research,* 281, pp. 128–154.
Fairchild, I.J., Spencer, A.M., Ali, D.O., Anderson, R.P., Anderton, R., Boomer, I., Dove, D., Evans, J.D., Hambrey, M.J., Howe, J. and Sawaki, Y. (2018). Tonian-Cryogenian boundary sections of Argyll, Scotland. *Precambrian Research,* 319, pp. 37–64.
Fakhraee, M., Tarhan, L.G., Reinhard, C.T., Crowe, S.A., Lyons, T.W. and Planavsky, N.J. (2023). Earth's surface oxygenation and the rise of eukaryotic life: Relationships to the Lomagundi positive carbon isotope excursion revisited. *Earth-Science Reviews,* 240, p.104398.
Farquhar, J., Bao, H. and Thiemens, M. (2000). Atmospheric influence of Earth's earliest sulfur cycle. *Science,* 289(5480), pp. 756–758.
Fdlmi, K.B. (1996). *The phosphorus cycle, phosphogenesis and marine phosphate-rich deposits*. *Earth-Science Reviews*, *40*(1-2), pp.55-124.
Fedo, C.M., Wayne Nesbitt, H. and Young, G.M. (1995). Unraveling the effects of potassium metasomatism in sedimentary rocks and paleosols, with implications for paleoweathering conditions and provenance. *Geology,* 23(10), pp. 921–924.
Feely, R.A., Trefry, J.H., Lebon, G.T. and German, C.R. (1998). The relationship between P/Fe and V/Fe ratios in hydrothermal precipitates and dissolved phosphate in seawater. *Geophysical Research Letters,* 25(13), pp. 2253–2256.
Feng, L.J., Chu, X.L., Huang, J., Zhang, Q.R. and Chang, H.J. (2010). Reconstruction of paleo-redox conditions and early sulfur cycling during deposition of the Cryogenian Datangpo Formation in South China. *Gondwana Research,* 18(4), pp. 632–637.
Föllmi, K.B., Arn, K., Hosein, R., Adatte, T. and Steinmann, P. (2009). Biogeochemical weathering in sedimentary chronosequences of the Rhône and Oberaar Glaciers (Swiss Alps): rates and mechanisms of biotite weathering. *Geoderma,* 151(3–4), pp. 270–281.

Frei, R., Gaucher, C., Døssing, L.N. and Sial, A.N. (2011). Chromium isotopes in carbonates - A tracer for climate change and for reconstructing the redox state of ancient seawater. *Earth and Planetary Science Letters,* 312(1–2), pp. 114–125.

Frei, R., Gaucher, C., Poulton, S.W. and Canfield, D.E. (2009). Fluctuations in Precambrian atmospheric oxygenation recorded by chromium isotopes. *Nature,* 461(7261), pp. 250–253.

Frei, R., Gaucher, C., Stolper, D. and Canfield, D.E. (2013). Fluctuations in late Neoproterozoic atmospheric oxidation - Cr isotope chemostratigraphy and iron speciation of the late Ediacaran lower Arroyo del Soldado Group (Uruguay). *Gondwana Research,* 23(2), pp. 797–811.

Froelich, P.N. (1988). Kinetic control of dissolved phosphate in natural rivers and estuaries: a primer on the phosphate buffer mechanism 1. *Limnology and oceanography*, 33(4part2), pp. 649–668.

Froelich, P.N., Arthur, M.A., Burnett, W.C., Deakin, M., Hensley, V., Jahnke, R., Kaul, L., Kim, K.H., Roe, K., Soutar, A. and Vathakanon, C. (1988). Early diagenesis of organic matter in Peru continental margin sediments: phosphorite precipitation. *Marine Geology*, *80*(3-4), pp.309-343.

Frost, C.D., von Blanckenburg, F., Schoenberg, R., Frost, B.R. and Swapp, S.M. (2007). Preservation of Fe isotope heterogeneities during diagenesis and metamorphism of banded iron formation. *Contributions to Mineralogy and Petrology,* 153, pp. 211–235.

Furquim, S.A.C., Graham, R.C., Barbiero, L., de Queiroz Neto, J.P. and Vallès, V. (2008). Mineralogy and genesis of smectites in an alkaline-saline environment of Pantanal wetland, Brazil. *Clays and Clay Minerals,* 56(5), pp. 579–595.

Galán, E. (2006). Genesis of clay minerals. *Developments in clay science,* 1, pp. 1129–1162.

Gao, Y., Long, X., Luo, J., Dong, Y., Lan, C., Huang, Z. and Zhao, J. (2021). Provenance and Hf isotopic variation of Precambrian detrital zircons from the Qilian Orogenic Belt, NW China: Evidence to the transition from breakup of Columbia to the assembly of Rodinia. *Precambrian Research,* 357, p.106153.

Garrels, R.M. and Mackenzie, F.T. (1971). Evolution of sedimentary rocks (p. 397). New York: Norton.

Gérard, F. (2016). Clay minerals, iron/aluminum oxides, and their contribution to phosphate sorption in soils - A myth revisited. *Geoderma,* 262, pp. 213–226.

Gibbs, C.R. (1976). Characterization and application of ferrozine iron reagent as a ferrous iron indicator. *Analytical Chemistry,* 48(8), pp. 1197–1201.

Gilleaudeau, G.J., Frei, R., Kaufman, A.J., Kah, L.C., Azmy, K., Bartley, J.K., Chernyavskiy, P. and Knoll, A.H. (2016). Oxygenation of the mid-Proterozoic atmosphere: Clues from chromium isotopes in carbonates. *Geochemical Perspectives Letter,s* 2(2), pp. 178–187.

Gilleaudeau, G.J., Romaniello, S.J., Luo, G., Kaufman, A.J., Zhang, F., Klaebe, R.M., Kah, L.C., Azmy, K., Bartley, J.K., Zheng, W. and Knoll, A.H. (2019). Uranium isotope evidence for limited euxinia in mid-Proterozoic oceans. *Earth and Planetary Science Letters,* 521, pp. 150–157.

Gilleaudeau, G.J., Sahoo, S.K., Kah, L.C., Henderson, M.A. and Kaufman, A.J. (2018). Proterozoic carbonates of the Vindhyan Basin, India: Chemostratigraphy and diagenesis. *Gondwana Research,* 57, pp. 10–25.

Gnanaprakash, G., Mahadevan, S., Jayakumar, T., Kalyanasundaram, P., Philip, J. and Raj, B. (2007). Effect of initial pH and temperature of iron salt solutions on formation of magnetite nanoparticles. *Materials chemistry and Physics,* 103(1), pp. 168–175.

Godfrey, C., Fan, M., Jesmok, G., Upadhyay, D. and Tripati, A. (2018). Petrography and stable isotope geochemistry of Oligocene-Miocene continental carbonates in south Texas: Implications for paleoclimate and paleoenvironment near sea-level. *Sedimentary Geology*, 367, pp. 69–83.

Goto, K.T., Anbar, A.D., Gordon, G.W., Romaniello, S.J., Shimoda, G., Takaya, Y., Tokumaru, A., Nozaki, T., Suzuki, K., Machida, S. and Hanyu, T. (2014). Uranium isotope systematics of ferromanganese crusts in the Pacific Ocean: Implications for the marine 238U/235U isotope system. *Geochimica et Cosmochimica Acta,* 146, pp. 43–58.

Gu, X. and Evans, L.J. (2007). Modelling the adsorption of Cd(II), Cu(II), Ni(II), Pb(II), and Zn(II) onto Fithian illite. *Journal of Colloid and Interface Science,* 307(2), pp. 317–325.

Guilbaud, R., Poulton, S.W., Butterfield, N.J., Zhu, M. and Shields-Zhou, G.A. (2015). A global transition to ferruginous conditions in the early Neoproterozoic oceans. *Nature Geoscience,* 8(6), pp. 466–470.

Guilbaud, R., Poulton, S.W., Thompson, J., Husband, K.F., Zhu, M., Zhou, Y., Shields, G.A. and Lenton, T.M. (2020). Phosphorus-limited conditions in the early Neoproterozoic ocean maintained low levels of atmospheric oxygen. *Nature Geoscience, 13*(4), pp. 296–301.

Halama, M., Swanner, E.D., Konhauser, K.O. and Kappler, A. (2016). Evaluation of siderite and magnetite formation in BIFs by pressure–temperature experiments of Fe (III) minerals and microbial biomass. *Earth and Planetary Science Letters,* 450, pp. 243–253.

Halevy, I., Alesker, M., Schuster, E.M., Popovitz-Biro, R. and Feldman, Y. (2017). A key role for green rust in the Precambrian oceans and the genesis of iron formations. *Nature Geoscience, 10*(2), pp. 135–139.

Hallam, A., Grose, J.A. and Ruffell, A.H. (1991). Palaeoclimatic significance of changes in clay mineralogy across the Jurassic-Cretaceous boundary in England and France. *Palaeogeography, Palaeoclimatology, Palaeoecology, 81*(3–4), pp. 173–187.

Halverson, G.P., Hoffman, P.F., Schrag, D.P., Maloof, A.C. and Rice, A.H.N. (2005). Toward a Neoproterozoic composite carbon-isotope record. *Geological Society of America Bulletin, 117*(9–10), pp. 1181–1207.

Han, S., Löhr, S.C., Abbott, A.N., Baldermann, A., Shields, G.A., Cui, H., Kaufman, A.J., Chen, B. and Yu, B. (2024). Authigenic clay mineral constraints on spatiotemporal evolution of restricted, evaporitic conditions during deposition of the Ediacaran Doushantuo Formation. *Earth and Planetary Science Letters, 626*, p. 118524.

Han, X., Tomaszewski, E.J., Schoenberg, R., Konhauser, K.O., Amor, M., Pan, Y., Warter, V., Kappler, A. and Byrne, J.M. (2021).Using Zn and Ni behavior during magnetite precipitation in banded iron formations to determine its biological or abiotic origin. *Earth and Planetary Science Letters,* 568, p. 117052.

Han, X., Tomaszewski, E.J., Sorwat, J., Pan, Y., Kappler, A. and Byrne, J.M. (2020). Effect of microbial biomass and humic acids on abiotic and biotic magnetite formation. *Environmental Science & Technology, 54*(7), pp. 4121–4130.

Hansen, H.C.B. and Poulsen, I.F. (1999). Interaction of synthetic sulphate "green rust" with phosphate and the crystallization of vivianite. *Clays and Clay Minerals, 47*(3), pp. 312–318.

Hao, W., Kashiwabara, T., Jin, R., Takahashi, Y., Gingras, M., Alessi, D.S. and Konhauser, K.O. (2020). Clay minerals as a source of cadmium to estuaries. *Scientific Reports,* 10(1), pp. 1–12.

Hao, W., Mänd, K., Li, Y., Alessi, D.S., Somelar, P., Moussavou, M., Romashkin, A.E., Lepland, A., Kirsimäe, K., Planavsky, N.J. and Konhauser, K.O. (2021a). The kaolinite shuttle links the Great Oxidation and Lomagundi events. *Nature Communications, 12*(1), p.2944.

Hao, W., Mänd, K., Swaren, L., Myers, K.D., Lalonde, S., Wilmeth, D.T., Van Zuilen, M., Wilson, S., Alessi, D.S. and Konhauser, K.O. (2021b).Trace Elemental Partitioning on Clays Derived From Hydrothermal Muds of the El Tatio Geyser Field, Chile. *Journal of Geophysical Research: Solid Earth, 126*(5), p.e2020JB021422.

Hao, W., Pudasainee, D., Gupta, R., Kashiwabara, T., Alessi, D.S. and Konhauser, K.O. (2019). Effect of Acidic Conditions on Surface Properties and Metal Binding Capacity of Clay Minerals. *ACS Earth and Space Chemistry,* 3(11), pp. 2421–2429.

Hardisty, D.S., Lyons, T.W., Riedinger, N., Isson, T.T., Owens, J.D., Aller, R.C., Rye, D.M., Planavsky, N.J., Reinhard, C.T., Gill, B.C. and Masterson, A.L. (2018). An evaluation of sedimentary molybdenum and iron as proxies for pore fluid paleoredox conditions. *American Journal of Science, 318*(5), pp. 527–556.

Hawkings, J., Wadham, J., Tranter, M., Telling, J., Bagshaw, E., Beaton, A., Simmons, S.L., Chandler, D., Tedstone, A. and Nienow, P. (2016). The Greenland Ice Sheet as a hot spot of phosphorus weathering and export in the Arctic. *Global Biogeochemical Cycles,* 30(2), pp. 191–210.

Hawkings, J.R., Skidmore, M.L., Wadham, J.L., Priscu, J.C., Morton, P.L., Hatton, J.E., Gardner, C.B., Kohler, T.J., Stibal, M., Bagshaw, E.A. and Steigmeyer, A. (2020). Enhanced trace element mobilization by Earth's ice sheets. *Proceedings of the National Academy of Sciences*, *117*(50), pp.31648-31659.

Hawkings, J.R., Wadham, J.L., Tranter, M., Raiswell, R., Benning, L.G., Statham, P.J., Tedstone, A., Nienow, P., Lee, K. and Telling, J. (2014). Ice sheets as a significant source of highly reactive nanoparticulate iron to the oceans. *Nature Communications,* 5(1), pp.1-8.

Hayashi, K.I., Fujisawa, H., Holland, H.D. and Ohmoto, H. (1997). Geochemistry of~ 1.9 Ga sedimentary rocks from northeastern Labrador, Canada.*Geochimica et cosmochimica acta*,*61*(19), pp.4115-4137.

He, Z., Clarkson, M.O., Andersen, M.B., Archer, C., Sweere, T.C., Kraal, P., Guthauser, A., Huang, F. and Vance, D. (2021). Temporally and spatially dynamic redox conditions on an upwelling margin: The impact on coupled sedimentary Mo and U isotope systematics, and implications for the Mo-U paleoredox proxy. *Geochimica et Cosmochimica Acta*, *309*, pp.251-271.

Heiri, O., Lotter, A.F. and Lemcke, G. (2001). Loss on ignition as a method for estimating organic and carbonate content in sediments: reproducibility and comparability of results. *Journal of paleolimnology,* 25, pp. 101–110.

Hemmingsson, C., Pitcairn, I.K. and Fru, E.C. (2018). Evaluation of phosphate-uptake mechanisms by Fe (III)(oxyhydr) oxides in Early Proterozoic oceanic conditions. *Environmental Chemistry,* 15(2), pp. 18–28.

Henderson, G.M., Slowey, N.C. and Haddad, G.A. (1999). Fluid flow through carbonate platforms: constraints from 234U/238U and Cl− in Bahamas pore-waters. *Earth and Planetary Science Letters*, *169*(1-2), pp.99-111.

Hepburn, L.E., Butler, I.B., Boyce, A. and Schröder, C. (2020). The use of operationally-defined sequential Fe extraction methods for mineralogical applications: A cautionary tale from Mössbauer spectroscopy. *Chemical Geology,* 543, p. 119584.

Herrmann, A.D., Gordon, G.W. and Anbar, A.D. (2018). Uranium isotope variations in a dolomitized Jurassic carbonate platform (Tithonian; Franconian Alb, Southern Germany). *Chemical Geology,* 497, pp. 41–53.

Hiess, J., Condon, D.J., McLean, N. and Noble, S.R. (2012). 238U/235U systematics in terrestrial uranium-bearing minerals. *Science,* 335(6076), pp. 1610–1614.

Higgins, J.A., Blättler, C.L., Lundstrom, E.A., Santiago-Ramos, D.P., Akhtar, A.A., Ahm, A.C., Bialik, O., Holmden, C., Bradbury, H., Murray, S.T. and Swart, P.K. (2018). Mineralogy, early marine diagenesis, and the chemistry of shallow-water carbonate sediments. *Geochimica et Cosmochimica Acta*, *220*, pp.512-534.

Hillier, S. (1999). Quantitative analysis of clay and other minerals in sandstones by X-ray powder diffraction (XRPD). *Clay mineral cements in sandstones*, pp. 213–251.

Hodgskiss, M.S., Lalonde, S.V., Crockford, P.W. and Hutchings, A.M. (2021). A carbonate molybdenum isotope and cerium anomaly record across the end-GOE: Local records of global oxygenation. *Geochimica et Cosmochimica Acta*, *313*, pp.313-339.

Hodson, A., Nowak, A., Sabacka, M., Jungblut, A., Navarro, F., Pearce, D., Ávila-Jiménez, M.L., Convey, P. and Vieira, G. (2017). Climatically sensitive transfer of iron to maritime Antarctic ecosystems by surface runoff. *Nature Communications*, *8*(1), p.14499.

Hoffman, P.F. (2013). The Great Oxidation and a Siderian snowball Earth: MIF-S based correlation of Paleoproterozoic glacial epochs. *Chemical Geology,* 362, pp. 143–156.

Hoffman, P.F. and Li, Z.X. (2009). A palaeogeographic context for Neoproterozoic glaciation. *Palaeogeography, Palaeoclimatology, Palaeoecology,* 277(3–4), pp. 158–172.

Hoffman, P.F. and Schrag, D.P. (2002). The snowball Earth hypothesis: Testing the limits of global change. *Terra Nova,* 14(3), pp. 129–155.

Hoffman, P.F., Abbot, D.S., Ashkenazy, Y., Benn, D.I., Brocks, J.J., Cohen, P.A., Cox, G.M., Creveling, J.R., Donnadieu, Y., Erwin, D.H. and Fairchild, I.J. (2017). Snowball Earth climate dynamics and Cryogenian geology-geobiology. *Science Advances*, *3*(11), p.e1600983.

Hoffman, P.F., Kaufman, A.J., Halverson, G.P. and Schrag, D.P. (1998). A Neoproterozoic snowball earth. *science*, *281*(5381), pp.1342-1346.

Holland, H.D. (2006). The oxygenation of the atmosphere and oceans. *Philosophical Transactions of the Royal Society B: Biological Sciences,* 361(1470), pp. 903–915.

Holmden, C., Amini, M. and Francois, R. (2015). Uranium isotope fractionation in Saanich Inlet: A modern analog study of a paleoredox tracer. *Geochimica et Cosmochimica Acta,* 153, pp. 202–215.

Hood, A. v S., Penman, D.E., Lechte, M.A., Wallace, M.W., Giddings, J.A. and Planavsky, N.J. (2021). Neoproterozoic syn-glacial carbonate precipitation and implications for a snowball Earth. *Geobiology, 20(2), pp.175-193*.

Hood, A.V.S. and Wallace, M.W. (2014). Marine cements reveal the structure of an anoxic, ferruginous Neoproterozoic Ocean. *Journal of the Geological Society,* 171(6), pp. 741–744.

Hood, A.V.S., Planavsky, N.J., Wallace, M.W., Wang, X., Bellefroid, E.J., Gueguen, B. and Cole, D.B. (2016). Integrated geochemical-petrographic insights from componentselective δ238U of Cryogenian marine carbonates. *Geology,* 44(11), pp. 935–938.

Hood, A.V.S., Wallace, M.W. and Drysdale, R.N. (2011). Neoproterozoic aragonite-dolomite seas? Widespread marine dolomite precipitation in Cryogenian reef complexes. *Geology,* 39(9), pp. 871–874.

Hopwood, M.J., Carroll, D., Dunse, T., Hodson, A., Holding, J.M., Iriarte, J.L., Ribeiro, S., Achterberg, E.P., Cantoni, C., Carlson, D.F. and Chierici, M. 2020). How does glacier discharge affect marine biogeochemistry and primary production in the Arctic? *The Cryosphere, 14*(4), pp. 1347–1383.

Hopwood, M.J., Statham, P.J., Tranter, M. and Wadham, J.L. (2014). Glacial flours as a potential source of Fe(II) and Fe(III) to polar waters. *Biogeochemistry,* 118(1–3), pp. 443–452.

Huang, K.J., Teng, F.Z., Shen, B., Xiao, S., Lang, X., Ma, H.R., Fu, Y. and Peng, Y. (2016). Episode of intense chemical weathering during the termination of the 635 Ma Marinoan glaciation. *Proceedings of the National Academy of Sciences,*113(52), pp. 14904–14909.

Husler, J., Ferriss, E.D.A., Helean, K.B., Bryan, C.R. and Brady, P. V. (2011). Optimised ferrozine micro-method for the determination of ferrous and ferric iron in rocks and minerals. *Geostandards and Geoanalytical Research,* 35(1), pp. 39–44.

Ikouanga, J.N.G., Fontaine, C., Bourdelle, F., Abd Elmola, A., Aubineau, J., Bankole, O.M., Reisberg, L., Pierson-Wickmann, A.C., Riboulleau, A., Trentesaux, A. and Laforest, C.

(2023). Taphonomy of early life (2.1 Ga) in the francevillian basin (Gabon): Role of organic mineral interactions. *Precambrian Research,* 395, p. 107155.
Ingall, E. and Jahnke, R. (1994). Evidence for enhanced phosphorus regeneration from marine sediments overlain by oxygen depleted waters. *Geochimica et Cosmochimica Acta*, *58*(11), pp.2571-2575.
Ingall, E. and Jahnke, R. (1997). Influence of water-column anoxia on the elemental fractionation of carbon and phosphorus during sediment diagenesis. *Marine Geology*, 139(1–4), pp. 219–229.
Isson, T.T. and Planavsky, N.J. (2018). Reverse weathering as a long-term stabilizer of marine pH and planetary climate. *Nature,* 560(7719), pp. 471–475.
Jacobsen, S.B. and Kaufman, A.J. (1999). The Sr, C and O isotopic evolution of Neoproterozoic seawater. *Chemical Geology,* 161(1–3), pp. 37–57.
Jaisi, D.P. and Blake, R.E. (2010). Tracing sources and cycling of phosphorus in Peru Margin sediments using oxygen isotopes in authigenic and detrital phosphates. *Geochimica et Cosmochimica Acta,* 74(11), pp. 3199–3212.
Javaux, E.J. and Lepot, K. (2018). The Paleoproterozoic fossil record: implications for the evolution of the biosphere during Earth's middle-age. *Earth-Science Reviews,* 176, pp. 68–86.
Jeandel, C. and Oelkers, E.H. (2015). The influence of terrigenous particulate material dissolution on ocean chemistry and global element cycles. *Chemical Geology,* 395, pp. 50–66.
JIANG, W. and Peacor, D.R. (1994). Formation of corrensite, chlorite and chlorite-mica stacks by replacement of detrital biotite in low-grade pelitic rocks. *Journal of Metamorphic Geology,* 12(6), pp. 867–884.
Johnson, B.R., Tostevin, R., Gopon, P., Wells, J., Robinson, S.A. and Tosca, N.J. (2020). Phosphorus burial in ferruginous SiO2-rich Mesoproterozoic sediments. *Geology,* 48(1), pp. 92–96.
Johnson, B.W., Poulton, S.W. and Goldblatt, C. (2017). Marine oxygen production and open water supported an active nitrogen cycle during the Marinoan Snowball Earth. *Nature Communications,* 8(1) , p.1316.
Johnson, J.E., Gerpheide, A., Lamb, M.P. and Fischer, W.W. (2014). O2 constraints from Paleoproterozoic detrital pyrite and uraninite. *Bulletin, 126*(5–6), pp. 813–830.
Johnston, D.T., Macdonald, F.A., Gill, B.C., Hoffman, P.F. and Schrag, D.P. (2012). Uncovering the Neoproterozoic carbon cycle. *Nature,* 483(7389), pp. 320–323.
Jones, C., Nomosatryo, S., Crowe, S.A., Bjerrum, C.J. and Canfield, D.E. (2015). Iron oxides, divalent cations, silica, and the early earth phosphorus crisis. *Geology*, *43*(2), pp. 135–138.
Jost, A.B., Bachan, A., van de Schootbrugge, B., Lau, K. V., Weaver, K.L., Maher, K. and Payne, J.L. (2017). Uranium isotope evidence for an expansion of marine anoxia during the end-Triassic extinction. *Geochemistry, Geophysics, Geosystems*, *18*(8), pp. 3093–3108.
Kah, L.C., Lyons, T.W. and Frank, T.D. (2004). Low marine sulphate and protracted oxygenation of the Proterozoic biosphere. *Nature*, *431*(7010), pp.834-838.
Kasemann, S.A., Hawkesworth, C.J., Prave, A.R., Fallick, A.E. and Pearson, P.N. (2005). Boron and calcium isotope composition in Neoproterozoic carbonate rocks from Namibia: evidence for extreme environmental change. *Earth and Planetary Science Letters,* 231(1–2), pp. 73–86.
Kaufman, A.J. and Knoll, A.H. (1995). Neoproterozoic variations in the C-isotopic composition of seawater: stratigraphic and biogeochemical implications. *Precambrian research*, *73*(1-4), pp.27-49.
Kaufman, A.J., Hayes, J.M., Knoll, A.H. and Germs, G.J. (1991). Isotopic compositions of carbonates and organic carbon from upper Proterozoic successions in Namibia: stratigraphic

variation and the effects of diagenesis and metamorphism. *Precambrian Research*,*49*(3-4), pp.301-327.
Kaufman, A.J., Sial, A.N., Frimmel, H.E. and Misi, A. (2009). Neoproterozoic to Cambrian palaeoclimatic events in southwestern Gondwana. *Developments in Precambrian Geology*, *16*, pp.369-388.
Keeling, R.F., Körtzinger, A. and Gruber, N. (2010). Ocean deoxygenation in a warming world. *Annual Review of Marine Science, 2*(1), pp. 199–229.
Keil, R.G. and Mayer, L.M. (2014). Mineral matrices and organic matter. *Treatise on geochemistry*, pp.337-359.
Kennedy, M., Droser, M., Mayer, L.M., Pevear, D. and Mrofka, D. (2006). Late Precambrian oxygenation; inception of the clay mineral factory. *Science, 311*(5766), pp. 1446–1449.
Kim, J., Kimura, Y., Puchala, B., Yamazaki, T., Becker, U. and Sun, W. (2023). Dissolution enables dolomite crystal growth near ambient conditions. *Science*, *382*(6673), pp.915-920.
Kim, J., Li, W., Philips, B.L. and Grey, C.P. (2011). Phosphate adsorption on the iron oxyhydroxides goethite (α-FeOOH), akaganeite (β-FeOOH), and lepidocrocite (γ-FeOOH): a 31 P NMR study. *Energy & Environmental Science, 4(*10), pp. 4298–4305.
Kipp, M.A. and Stüeken, E.E. (2017). Biomass recycling and Earth's early phosphorus cycle. *Science advances*,*3*(11), p.eaao4795.
Kipp, M.A., Li, H., Ellwood, M.J., John, S.G., Middag, R., Adkins, J.F. and Tissot, F.L.H. (2022). 238U, 235U and 234U in seawater and deep-sea corals: A high-precision reappraisal. *Geochimica et Cosmochimica Acta,* 336, pp. 231–248.
Kirschvink, J.L. (1992). Late Proterozoic low-latitude global glaciation: the snowball Earth. *The proterozoic biosphere,* 52, pp. 51–52.
Kirschvink, J.L., Gaidos, E.J., Bertani, L.E., Beukes, N.J., Gutzmer, J., Maepa, L.N. and Steinberger, R.E. (2000). Paleoproterozoic snowball Earth: Extreme climatic and geochemical global change and its biological consequences. *Proceedings of the National Academy of Sciences*, *97*(4), pp.1400-1405.
Klein, C. (2005). Some Precambrian banded iron-formations (BIFs) from around the world: Their age, geologic setting, mineralogy, metamorphism, geochemistry, and origins. *American Mineralogist*, *90*(10), pp. 1473–1499.
Klinkhammer, G.P. and Palmer, M.R. (1991). Uranium in the oceans: where it goes and why. *Geochimica et Cosmochimica Acta*, *55*(7), pp.1799-1806
Knoll, A.H., Bergmann, K.D. and Strauss, J. V. (2016). Life: The first two billion years. *Philosophical Transactions of the Royal Society B: Biological Sciences,* 371(1707).
Knoll, A.H., Javaux, E.J., Hewitt, D. and Cohen, P. (2006). Eukaryotic organisms in Proterozoic oceans. *Philosophical Transactions of the Royal Society B: Biological Sciences*, *361*(1470), pp.1023-1038.
Kolodiazhnyi, O.I. (2021). Phosphorus compounds of natural origin: Prebiotic, stereochemistry, application. *Symmetry, 13*(5), p. 889.
Konhauser, K.O., Lalonde, S. V., Amskold, L. and Holland, H.D. (2007). Was there really an archean phosphate crisis? *Science, 315*(5816), p. 1234.
Konhauser, K.O., Lalonde, S.V., Planavsky, N.J., Pecoits, E., Lyons, T.W., Mojzsis, S.J., Rouxel, O.J., Barley, M.E., Rosìere, C., Fralick, P.W. and Kump, L.R. (2011). Aerobic bacterial pyrite oxidation and acid rock drainage during the Great Oxidation Event. *Nature*, *478*(7369), pp.369-373.
Konhauser, K.O., Newman, D.K. and Kappler, A. (2005). The potential significance of microbial Fe (III) reduction during deposition of Precambrian banded iron formations. *Geobiology*, *3*(3), pp. 167–177.

Kopp, R.E., Kirschvink, J.L., Hilburn, I.A. and Nash, C.Z. (2005). The Paleoproterozoic snowball Earth: a climate disaster triggered by the evolution of oxygenic photosynthesis. *Proceedings of the National Academy of Sciences*, *102*(32), pp.11131-11136

Krause, A.J., Mills, B.J.W., Merdith, A.S., Lenton, T.M. and Poulton, S.W. (2022). Extreme variability in atmospheric oxygen levels in the late Precambrian. *Science advances, 8*(41), p. eabm8191.

Krause, A.J., Mills, B.J.W., Zhang, S., Planavsky, N.J., Lenton, T.M. and Poulton, S.W. (2018). Stepwise oxygenation of the Paleozoic atmosphere. *Nature Communications, 9*(1), p. 4081.

Krause, A.J., Sluijs, A., van der Ploeg, R., Lenton, T.M. and Pogge von Strandmann, P.A.E. (2023). Enhanced clay formation key in sustaining the Middle Eocene Climatic Optimum. *Nature Geoscience, 16(8), pp.730-738*.

Krause S., Liebetrau V., Gorb S., Sa ´nchez-Roma ´n M., McKenzie J. A. and Treude T. (2012) Microbial nucleation of Mg-rich dolomite in exopolymeric substances under anoxic modern seawater salinity: new insight into an old enigma. Geology 40, 587–590.

Krauskopf, K. and Bird, D. (1995). Surface chemistry: the solution-mineral interface. Introduction to geochemistry (Ed MG-HI Editions) Mc Graw-Hill International Editions edn. *Earth sciences and geology series*, pp. 135–163.

Ku, T.L., Knauss, K.G. and Mathieu, G.G. (1977). Uranium in open ocean: concentration and isotopic composition. *Deep-Sea Research, 24*(11), pp. 1005–1017.

Kump, L.R. (2008). The rise of atmospheric oxygen. *Nature, 451*(7176), pp. 277–278.

Kump, L.R. and Arthur, M.A. (1999). Interpreting carbon-isotope excursions: carbonates and organic matter. *Chemical Geology,* 161(1–3), pp. 181–198.

Kunzmann, M., Gibson, T.M., Halverson, G.P., Hodgskiss, M.S., Bui, T.H., Carozza, D.A., Sperling, E.A., Poirier, A., Cox, G.M. and Wing, B.A. (2017). Iron isotope biogeochemistry of Neoproterozoic marine shales. *Geochimica et Cosmochimica Acta*, *209*, pp.85-105.

Kyrpides N, Overbeek R, Ouzounis C (1999) Universal protein families and the functional content of the last universal common ancestor. J Mol Evol 49:413–423

Laakso, T.A. and Schrag, D.P. (2014). Regulation of atmospheric oxygen during the Proterozoic. *Earth and Planetary Science Letters,* 388, pp. 81–91.

Laakso, T.A. and Schrag, D.P. (2017). A theory of atmospheric oxygen. *Geobiology, 15*(3), pp. 366–384.

Laakso, T.A., Sperling, E.A., Johnston, D.T. and Knoll, A.H. (2020). Ediacaran reorganization of the marine phosphorus cycle. *Proceedings of the national academy of sciences*, *117*(22), pp.11961-11967.

Landry, C.J., Koretsky, C.M., Lund, T.J., Schaller, M. and Das, S. (2009). Surface complexation modeling of Co(II) adsorption on mixtures of hydrous ferric oxide, quartz and kaolinite. *Geochimica et Cosmochimica Acta*, *73*(13), pp. 3723–3737.

Langmuir, D. (1978). Uranium solution-mineral equilibria at low temperatures with applications to sedimentary ore deposits. *Geochimica et Cosmochimica Acta*, *42*(6), pp.547-569.

Lanson, B., Beaufort, D., Berger, G., Bauer, A., Cassagnabere, A. and Meunier, A. (2002). Authigenic kaolin and illitic minerals during burial diagenesis of sandstones: a review. *Clay minerals, 37*(1), pp. 1–22.

Lanson, B., Sakharov, B.A., Claret, F. and Drits, V.A. (2009). Diagenetic smectite-to-illite transition in clay-rich sediments: A reappraisal of x-ray diffraction results using the multi-specimen method. *American Journal of Science,* 309(6), pp. 476–516.

Large, R.R., Halpin, J.A., Lounejeva, E., Danyushevsky, L.V., Maslennikov, V.V., Gregory, D., Sack, P.J., Haines, P.W., Long, J.A., Makoundi, C. and Stepanov, A.S. (2015). Cycles of nutrient trace elements in the Phanerozoic Ocean. *Gondwana Research*, *28*(4), pp.1282-1293.

Lau, K. V., Macdonald, F.A., Maher, K. and Payne, J.L. (2017). Uranium isotope evidence for temporary ocean oxygenation in the aftermath of the Sturtian Snowball Earth. *Earth and Planetary Science Letters,* 458, pp. 282–292.

Lau, K.V., Maher, K., Altiner, D., Kelley, B.M., Kump, L.R., Lehrmann, D.J., Silva-Tamayo, J.C., Weaver, K.L., Yu, M. and Payne, J.L. (2016). Marine anoxia and delayed Earth system recovery after the end-Permian extinction. *Proceedings of the National Academy of Sciences*, *113*(9), pp.2360-2365.

Lee, C.T.A., Yeung, L.Y., McKenzie, N.R., Yokoyama, Y., Ozaki, K. and Lenardic, A. (2016). Two-step rise of atmospheric oxygen linked to the growth of continents. *Nature Geoscience,* 9(6), pp. 417–424.

Lenton, T.M., Boyle, R.A., Poulton, S.W., Shields-Zhou, G.A. and Butterfield, N.J. (2014). Co-evolution of eukaryotes and ocean oxygenation in the Neoproterozoic era. *Nature Geoscience, 7*(4), pp. 257–265.

Lewis, J.P., Weaver, A.J. and Eby, M. (2007). Snowball versus slushball Earth: Dynamic versus nondynamic sea ice? *Journal of Geophysical Research: Oceans, 112*(11).

Lewis, J.P., Weaver, A.J., Johnston, S.T. and Eby, M. (2003). Neoproterozoic 'snowball Earth': Dynamic sea ice over a quiescent ocean. *Paleoceanography, 18*(4), pp. 16.1-16.8.

Li, C., Love, G.D., Lyons, T.W., Scott, C.T., Feng, L., Huang, J., Chang, H., Zhang, Q. and Chu, X. (2012). Evidence for a redox stratified Cryogenian marine basin, Datangpo Formation, South China. *Earth and Planetary Science Letters*, 331, pp.246-256.

Li, F., Penman, D., Planavsky, N., Knudsen, A., Zhao, M., Wang, X., Isso, T., Huang, K.,

Wei, G., Zhang, S., Shen, J., Zhu, X., Shen, B. (2021a). Reverse weathering may amplify post-Snowball atmospheric carbon dioxide levels. *Precambrian Research*, 364, p.106279.

Li, M., Wignall, P.B., Dai, X., Hu, M. and Song, H. (2021b). Phanerozoic variation in dolomite abundance linked to oceanic anoxia. *Geology*, *49*(6), pp. 698–702.

Liang, X., Lin, X., Wei, G., Ma, L., He, H., Santos-Carballal, D., Zhu, J., Zhu, R. and De Leeuw, N.H. (2021). Competitive adsorption geometries for the arsenate As (V) and phosphate P (V) oxyanions on magnetite surfaces: Experiments and theory. *American Mineralogist*, *106*(3), pp.374-388.

Liivamägi, S., Środoń, J., Bojanowski, M.J., Stanek, J.J. and Roberts, N.M.W. (2021). Precambrian paleosols on the Great Unconformity of the East European Craton: an 800-million-year record of Baltica's climatic conditions. *Precambrian Research,* 363, p. 106327.

Liu, D., Xu, Y., Papineau, D., Yu, N., Fan, Q., Qiu, X. and Wang, H. (2019. Experimental evidence for abiotic formation of low-temperature proto-dolomite facilitated by clay minerals. *Geochimica et Cosmochimica Acta*, *247*, pp.83-95

Liu, J., Zhu, R., Ma, L., Fu, H., Lin, X., Parker, S.C. and Molinari, M. (2021). Adsorption of phosphate and cadmium on iron (oxyhydr) oxides: A comparative study on ferrihydrite, goethite, and hematite. *Geoderma,* 383, p. 114799.

Liu, N., Liu, L., Qu, X., Yang, H., Wang, L. and Zhao, S. (2011). Genesis of authigene carbonate minerals in the Upper Cretaceous reservoir, Honggang Anticline, Songliao Basin: A natural analog for mineral trapping of natural CO2 storage. *Sedimentary Geology,* 237(3–4), pp. 166–178.

Loron, C.C., Rainbird, R.H., Turner, E.C., Greenman, J.W. and Javaux, E.J. (2019). Organic-walled microfossils from the late Mesoproterozoic to early Neoproterozoic lower Shaler Supergroup (Arctic Canada): Diversity and biostratigraphic significance. *Precambrian Research,* 321, pp. 349–374.

Love, G.D., Grosjean, E., Stalvies, C., Fike, D.A., Grotzinger, J.P., Bradley, A.S., Kelly, A.E., Bhatia, M., Meredith, W., Snape, C.E. and Bowring, S.A. (2009). Fossil steroids record the appearance of Demospongiae during the Cryogenian period. *Nature*,*457*(7230), pp.718-721.

Lu, Z., Jenkyns, H.C. and Rickaby, R.E.M. (2010). Iodine to calcium ratios in marine carbonate as a paleo-redox proxy during oceanic anoxic events. *Geology, 38*(12), pp. 1107–1110.
Lyons, T.W. and Severmann, S. (2006). A critical look at iron paleoredox proxies: New insights from modern euxinic marine basins. *Geochimica et Cosmochimica Acta, 70*(23), pp. 5698–5722.
Lyons, T.W., Droser, M.L., Lau, K. V. and Porter, S.M. (2018). Early Earth and the rise of complex life. *Emerging Topics in Life Sciences, 2*(2),
Lyons, T.W., Reinhard, C.T. and Planavsky, N.J. (2014). The rise of oxygen in Earth's early ocean and atmosphere. *Nature, 506*(7488), pp. 307–315.
Lyons, T.W., Tino, C.J., Fournier, G.P., Anderson, R.E., Leavitt, W.D., Konhauser, K.O. and Stüeken, E.E. (2024). Co-evolution of early Earth environments and microbial life. *Nature Reviews Microbiology*, pp. 1-15.
Lyons, T.W., Werne, J.P., Hollander, D.J. and Murray, R.W. (2003). Contrasting sulfur geochemistry and Fe/Al and Mo/Al ratios across the last oxic-to-anoxic transition in the Cariaco Basin, Venezuela. *Chemical Geology*, *195*(1–4), pp. 131–157.
Ma, H., Shen, B., Lang, X., Peng, Y., Huang, K., Huang, T., Fu, Y. and Tang, W. (2022). Active biogeochemical cycles during the Marinoan global glaciation. *Geochimica et Cosmochimica Acta*, *321*, pp.155-169.
Macdonald, F.A., Schmitz, M.D., Crowley, J.L., Roots, C.F., Jones, D.S., Maloof, A.C., Strauss, J.V., Cohen, P.A., Johnston, D.T. and Schrag, D.P. (2010). Calibrating the cryogenian. *Science*,*327*(5970), pp.1241-1243.
Macdonald, M.L., Wadham, J.L., Telling, J. and Skidmore, M.L. (2018). Glacial erosion liberates lithologic energy sources for microbes and acidity for chemical weathering beneath glaciers and ice sheets. *Frontiers in Earth Science,* 6, p. 416476.
Maloney, K.M., Halverson, G.P., Lechte, M., Gibson, T.M., Bui, T.H., Schiffbauer, J.D. and Laflamme, M. (2024). The paleoredox context of early eukaryotic evolution: insights from the Tonian Mackenzie Mountains Supergroup, Canada. *Geobiology, 22*(3), p. e12598.
Manning, B.A. and Goldberg, S. (1997). Adsorption and stability of arsenic (III) at the clay mineral− water interface. *Environmental science & technology*, *31*(7), pp. 2005–2011.
Mantovani, M. and Becerro, A.I. (2010). Illitization of kaolinite: The effect of pressure on the reaction rate. *Clays and Clay Minerals, 58*(6), pp. 766–771.
Marotzke, J. and Botzet, M. (2007). Present-day and ice-covered equilibrium states in a comprehensive climate model. *Geophysical Research Letters, 34*(16).
Marshall, C.R. (2006). Explaining the Cambrian 'explosion' of animals. *Annual Review of Earth and Planetary Sciences, 34* (1), pp. 355–384.
Mather, C.C., Lampinen, H.M., Tucker, M., Leopold, M., Dogramaci, S., Raven, M. and Gilkes, R.J. (2023). Microbial influence on dolomite and authigenic clay mineralisation in dolocrete profiles of NW Australia. Geobiology, 21(5), pp.644-670.
Mavris, C., Plötze, M., Mirabella, A., Giaccai, D., Valboa, G. and Egli, M. (2011). Clay mineral evolution along a soil chronosequence in an Alpine proglacial area. *Geoderma, 165*(1), pp. 106–117.
McLennan, S.M. (2001). Relationships between the trace element composition of sedimentary rocks and upper continental crust. *Geochemistry, Geophysics, Geosystems,* 2(4).
McLennan, S.M. and Taylor, S.R. (1991). Sedimentary rocks and crustal evolution: tectonic setting and secular trends. *The Journal of geology, 99*(1), pp. 1–21.
McLennan, S.M., Hemming, S., McDaniel, D.K. and Hanson, G.N. (1993). Geochemical approaches to sedimentation, provenance, and tectonics.
Meng, Z., Wang, Z., Ju, P., Zhou, X., Li, C., Zhang, Z., Zhang, X. and Huang, K.J. (2024). Marine redox fluctuations during the Marinoan glaciation. *Global and Planetary Change*, *235*, p.104396.

Meunier, A., Velde, B. and Velde, B. (2004). *Illite: Origins, evolution and metamorphism*. Springer Science & Business Media.
Migaszewski, Z.M., Gałuszka, A., Pasławski, P. and Starnawska, E. (2007). An Influence of Pyrite Oxidation on Generation of Unique Acidic Pit Water: A Case Study, Podwiśniówka Quarry, Holy Cross Mountains (South-Central Poland). *Polish Journal of Environmental Studies* 16(3).
Mills, D.B., Francis, W.R., Vargas, S., Larsen, M., Elemans, C.P., Canfield, D.E. and Wörheide, G. (2018). The last common ancestor of animals lacked the HIF pathway and respired in low-oxygen environments. *Elife*, *7*, p.e31176.
Mills, D.B., Ward, L.M., Jones, C., Sweeten, B., Forth, M., Treusch, A.H. and Canfield, D.E. (2014). Oxygen requirements of the earliest animals. *Proceedings of the National Academy of Sciences, 111*(11), pp. 4168–4172.
Mitchell, R. and Evans, D.A. (2023). The balanced billion. GSA Today 34 (2), 10-11.
Moore, D.M. and Reynolds Jr, R.C. (1989). X-Ray Diffraction and the Identification and Analysis of Clay Minerals-Oxford University Press.
Moreno-Maroto, J.M. and Alonso-Azcárate, J. (2018). What is clay? A new definition of "clay" based on plasticity and its impact on the most widespread soil classification systems. *Applied Clay Science*, *161*, pp.57-63.
Müller, M., Mentel, M., van Hellemond, J.J., Henze, K., Woehle, C., Gould, S.B., Yu, R.Y., van der Giezen, M., Tielens, A.G. and Martin, W.F. (2012). Biochemistry and evolution of anaerobic energy metabolism in eukaryotes. *Microbiology and Molecular Biology Reviews*, *76*(2), pp.444-495.
Némery, J. and Garnier, J. (2007). Typical features of particulate phosphorus in the Seine estuary (France). *Hydrobiologia*, 588(1), pp. 271–290.
Nesbitt, H.W. and Young, G.M. (1982). *Early Proterozoic climates and plate motions inferred from major element chemistry of Intites*. *Nature*, 299, pp. 715–717.
Nesbitt, H.W. and Young, G.M. (1984). Prediction of some weathering trends of plutonic and volcanic rocks based on thermodynamic and kinetic considerations. *Geochimica et cosmochimica acta, 48*(7), pp. 1523–1534.
Newman, D.K., Neubauer, C., Ricci, J.N., Wu, C.-H. and Pearson, A. (2016). Cellular and molecular biological approaches to interpreting ancient biomarkers. *Annual Review of Earth and Planetary Sciences* 44(1), pp. 493–522.
Nieto, F., Velilla, N., Peacor, D.R. and Huertas, M.O. (1994). Regional retrograde alteration of sub-greenschist facies chlorite to smectite. Contributions to Mineralogy and Petrology, 115, pp.243-252.
Ngombi-Pemba, L., Albani, A. El, Meunier, A., Grauby, O. and Gauthier-Lafaye, F. (2014). From detrital heritage to diagenetic transformations, the message of clay minerals contained within shales of the Palaeoproterozoic Francevillian basin (Gabon). *Precambrian Research, 255*(P1), pp. 63–76.
Noordmann, J., Weyer, S., Montoya-Pino, C., Dellwig, O., Neubert, N., Eckert, S., Paetzel, M. and Böttcher, M.E. (2015). Uranium and molybdenum isotope systematics in modern euxinic basins: Case studies from the central Baltic Sea and the Kyllaren fjord (Norway). *Chemical Geology*, *396*, pp.182-195.
Nutman, A.P., Bennett, V.C., Friend, C.R.L., Van Kranendonk, M.J. and Chivas, A.R. (2016). Rapid emergence of life shown by discovery of 3,700-million-year-old microbial structures. *Nature, 537*(7621), pp. 535–538.
Och, L.M. and Shields-Zhou, G.A. (2012). The Neoproterozoic oxygenation event: Environmental perturbations and biogeochemical cycling. *Earth-Science Reviews, 110*(1–4), pp. 26–57.

Ohmoto, H., Watanabe, Y., Ikemi, H., Poulson, S.R. and Taylor, B.E. (2006). Sulphur isotope evidence for an oxic Archaean atmosphere. *Nature, 442*(7105), pp. 908–911.

Ossa, F.O., Hofmann, A., Wille, M., Spangenberg, J.E., Bekker, A., Poulton, S.W., Eickmann, B. and Schoenberg, R. (2018). Aerobic iron and manganese cycling in a redox-stratified Mesoarchean epicontinental sea. *Earth and planetary science letters*,*500*, pp.28-40.

Ossa, F.O., Pons, M.L., Bekker, A., Hofmann, A., Poulton, S.W., Andersen, M.B., Agangi, A., Gregory, D., Reinke, C., Steinhilber, B. and Marin-Carbonne, J. (2023). Zinc enrichment and isotopic fractionation in a marine habitat of the c. 2.1 Ga Francevillian Group: A signature of zinc utilization by eukaryotes?. *Earth and Planetary Science Letters*, *611*, p.118147.

Ossa, F.O., Spangenberg, J.E., Bekker, A., König, S., Stüeken, E.E., Hofmann, A., Poulton, S.W., Yierpan, A., Varas-Reus, M.I., Eickmann, B. and Andersen, M.B. (2022). Moderate levels of oxygenation during the late stage of Earth's Great Oxidation Event. *Earth and Planetary Science Letters*, *594*, p.117716.

Ozdes, D., Duran, C. and Senturk, H.B. (2011). Adsorptive removal of Cd (II) and Pb (II) ions from aqueous solutions by using Turkish illitic clay. *Journal of Environmental Management, 92*(12), pp. 3082–3090.

Pace, N.R. (2009). Problems with "procaryote". *Journal of bacteriology*, *191*(7), pp.2008-2010.

Paige-Green, P. (1980). The clay mineralogy of Dwyka tillite in Southern Africa and its effect on the geotechnical properties. *South African Journal of Geology*, *83*(2), pp.291-296.

Panahi, A. and Young, G.M. (1997). A geochemical investigation into the provenance of the Neoproterozoic Port Askaig Tillite, Dalradian Supergroup, western Scotland. *Precambrian Research, 85*(1–2), pp. 81–96.

Pang, S.C., Chin, S.F. and Anderson, M.A. (2007). Redox equilibria of iron oxides in aqueous-based magnetite dispersions: Effect of pH and redox potential. *Journal of colloid and interface science, 311*(1), pp. 94–101.

Papineau, D. (2010). Global biogeochemical changes at both ends of the Proterozoic: insights from phosphorites. *Astrobiology, 10*(2), pp. 165–181.

Papineau, D., Purohit, R., Fogel, M.L. and Shields-Zhou, G.A. (2013). High phosphate availability as a possible cause for massive cyanobacterial production of oxygen in the Paleoproterozoic atmosphere. *Earth and Planetary Science Letters,* 362, pp. 225–236.

Parfrey, L.W., Lahr, D.J., Knoll, A.H. and Katz, L.A. (2011). Estimating the timing of early eukaryotic diversification with multigene molecular clocks. *Proceedings of the National Academy of Sciences*, *108*(33), pp.13624-13629.

Parnell, J. and Boyce, A.J. (2017). Microbial sulphate reduction during Neoproterozoic glaciation, Port Askaig Formation, UK. *Journal of the Geological Society*, *174*(5), pp. 850–854.

Partin, C.A., Bekker, A., Planavsky, N.J., Scott, C.T., Gill, B.C., Li, C., Podkovyrov, V., Maslov, A., Konhauser, K.O., Lalonde, S.V. and Love, G.D. (2013a). Large-scale fluctuations in Precambrian atmospheric and oceanic oxygen levels from the record of U in shales. *Earth and Planetary Science Letters*, *369*, pp.284-293.

Partin, C.A., Lalonde, S. V., Planavsky, N.J., Bekker, A., Rouxel, O.J., Lyons, T.W. and Konhauser, K.O. (2013b). Uranium in iron formations and the rise of atmospheric oxygen. *Chemical Geology* 362, pp. 82–90. doi: 10.1016/j.chemgeo.2013.09.005.

Pasquier, V., Fike, D.A., Révillon, S. and Halevy, I. (2022). A global reassessment of the controls on iron speciation in modern sediments and sedimentary rocks: A dominant role for diagenesis. *Geochimica et Cosmochimica Acta,* 335, pp. 211–230.

Paytan, A. and McLaughlin, K. (2007). The oceanic phosphorus cycle. *Chemical reviews, 107*(2), pp. 563–576.

Pecoits, E., Gingras, M.K., Barley, M.E., Kappler, A., Posth, N.R. and Konhauser, K.O. (2009). Petrography and geochemistry of the Dales Gorge banded iron formation: Paragenetic sequence, source and implications for palaeo-ocean chemistry. *Precambrian Research, 172*(1–2), pp. 163–187.

Petrash, D.A., Bialik, O.M., Bontognali, T.R., Vasconcelos, C., Roberts, J.A., McKenzie, J.A. and Konhauser, K.O. (2017). Microbially catalyzed dolomite formation: from near-surface to burial. Earth-Science Reviews, 171, pp.558-582.

Philippot, P., Ávila, J.N., Killingsworth, B.A., Tessalina, S., Baton, F., Caquineau, T., Muller, E., Pecoits, E., Cartigny, P., Lalonde, S.V. and Ireland, T.R. (2018). Globally asynchronous sulphur isotope signals require re-definition of the Great Oxidation Event. *Nature Communications*, *9*(1), p.2245.

Planavsky, N.J., Asael, D., Hofmann, A., Reinhard, C.T., Lalonde, S.V., Knudsen, A., Wang, X., Ossa Ossa, F., Pecoits, E., Smith, A.J. and Beukes, N.J. (2014a). Evidence for oxygenic photosynthesis half a billion years before the Great Oxidation Event. *Nature Geoscience*, *7*(4), pp.283-286.

Planavsky, N.J., McGoldrick, P., Scott, C.T., Li, C., Reinhard, C.T., Kelly, A.E., Chu, X., Bekker, A., Love, G.D. and Lyons, T.W. (2011). Widespread iron-rich conditions in the mid-Proterozoic Ocean. *Nature*, *477*(7365), pp.448-451.

Planavsky, N.J., Reinhard, C.T., Wang, X., Thomson, D., McGoldrick, P., Rainbird, R.H., Johnson, T., Fischer, W.W. and Lyons, T.W. (2014b). Low Mid-Proterozoic atmospheric oxygen levels and the delayed rise of animals. *science*, *346*(6209), pp.635-638.

Planavsky, N.J., Rouxel, O.J., Bekker, A., Lalonde, S. V., Konhauser, K.O., Reinhard, C.T. and Lyons, T.W. (2010). The evolution of the marine phosphate reservoir. *Nature,* 467(7319), pp. 1088–1090.

Pogge Von Strandmann, P.A.E., Stüeken, E.E., Elliott, T., Poulton, S.W., Dehler, C.M., Canfield, D.E. and Catling, D.C. (2015). Selenium isotope evidence for progressive oxidation of the Neoproterozoic biosphere. *Nature Communications, 6*(1), p. 10157.

Poulton, S.W. (2017). Early phosphorus redigested. *Nature Geoscience, 10*(2), pp. 75–76.

Poulton, S.W. (2021). *The iron speciation paleoredox proxy*. Cambridge University Press.

Poulton, S.W. and Canfield, D.E. (2005). Development of a sequential extraction procedure for iron: Implications for iron partitioning in continentally derived particulates. *Chemical Geology 214*(3–4), pp. 209–221.

Poulton, S.W. and Canfield, D.E. (2011). Ferruginous conditions: a dominant feature of the ocean through Earth's history. *Elements, 7*(2), pp. 107–112.

Poulton, S.W. and Raiswell, R. (2002). The low-temperature geochemical cycle of iron: from continental fluxes to marine sediment deposition. *American journal of science, 302*(9), pp. 774–805.

Poulton, S.W., Bekker, A., Cumming, V.M., Zerkle, A.L., Canfield, D.E. and Johnston, D.T. (2021). A 200-million-year delay in permanent atmospheric oxygenation. *Nature 592*(7853), pp. 232–236.

Poulton, S.W., Fralick, P.W. and Canfield, D.E. (2010). Spatial variability in oceanic redox structure 1.8 billion years ago. *Nature Geoscience*, *3*(7), pp. 486–490.

Poulton, S.W., Krom, M.D. and Raiswell, R. (2004). A revised scheme for the reactivity of iron (oxyhydr)oxide minerals towards dissolved sulfide. *Geochimica et Cosmochimica Acta, 68*(18), pp. 3703–3715.

Prave, A.R., Fallick, A.E., Thomas, C.W. and Graham, C.M. (2009). A composite C-isotope profile for the Neoproterozoic Dalradian Supergroup of Scotland and Ireland. *Journal of the Geological Society, 166*(5), pp. 845–857.

Pufahl, P.K. and Hiatt, E.E. (2012). Oxygenation of the Earth's atmosphere–ocean system: a review of physical and chemical sedimentologic responses. *Marine and Petroleum Geology, 32*(1), pp. 1–20.
Rafiei, M. and Kennedy, M. (2019). Weathering in a world without terrestrial life recorded in the Mesoproterozoic Velkerri Formation. *Nature Communications, 10*(1), p.3448.
Rafiei, M., Löhr, S., Baldermann, A., Webster, R. and Kong, C. (2020). Quantitative petrographic differentiation of detrital vs diagenetic clay minerals in marine sedimentary sequences: Implications for the rise of biotic soils. *Precambrian Research, 350*, p.105948. .
Raiswell, R., Hardisty, D.S., Lyons, T.W., Canfield, D.E., Owens, J.D., Planavsky, N.J., Poulton, S.W. and Reinhard, C.T. (2018). The iron paleoredox proxies: A guide to the pitfalls, problems and proper practice. *American Journal of Science, 318*(5), pp. 491–526.
Raiswell, R., Newton, R. and Wignall, P.B. (2001). An indicator of water-column anoxia: resolution of biofacies variations in the Kimmeridge Clay (Upper Jurassic, UK). *Journal of Sedimentary Research, 71*(2), pp. 286–294.
Ramos, D.P.S., Morgan, L.E., Lloyd, N.S. and Higgins, J.A. (2018). Reverse weathering in marine sediments and the geochemical cycle of potassium in seawater: Insights from the K isotopic composition (41K/39K) of deep-sea pore-fluids. *Geochimica et Cosmochimica Acta,* 236, pp. 99–120.
Rasmussen, B. and Muhling, J.R. (2018). Making magnetite late again: Evidence for widespread magnetite growth by thermal decomposition of siderite in Hamersley banded iron formations. *Precambrian Research*, 306, pp. 64–93.
Rasmussen, B., Muhling, J.R., Suvorova, A. and Fischer, W.W. (2021). Apatite nanoparticles in 3.46–2.46 Ga iron formations: Evidence for phosphorus-rich hydrothermal plumes on early Earth. *Geology, 49*(6), pp. 647–651.
Rasmussen, B., Muhling, J.R., Tosca, N.J. and Fischer, W.W. (2023). Did nutrient-rich oceans fuel Earth's oxygenation? *Geology* 51(5), pp. 444–448. doi: 10.1130/G50835.1.
Reed, S.J.B. (2005). *Electron microprobe analysis and scanning electron microscopy in geology*. Cambridge university press.
Reeder, R.J., Nugent, M., Lamble, G.M., Tait, C.D. and Morris, D.E. (2000). Uranyl incorporation into calcite and aragonite: XAFS and luminescence studies. *Environmental Science and Technology, 34*(4), pp. 638–644.
Reinhard, C.T. and Planavsky, N.J. (2020). Biogeochemical controls on the Redox evolution of earth's oceans and atmosphere. *Elements, 16*(3), pp. 191–196.
Reinhard, C.T. and Planavsky, N.J. (2022). The history of ocean oxygenation. *Annual Review of Marine Science*, *14*(1), pp.331-353.
Reinhard, C.T., Planavsky, N.J., Gill, B.C., Ozaki, K., Robbins, L.J., Lyons, T.W., Fischer, W.W., Wang, C., Cole, D.B. and Konhauser, K.O. (2017). Evolution of the global phosphorus cycle. *Nature, 541*(7637), pp. 386–389.
Reinhold, C. (1998). Multiple episodes of dolomitization and dolomite recrystallization during shallow burial in Upper Jurassic shelf carbonates: eastern Swabian Alb, southern Germany. *Sedimentary Geology*, *121*(1-2), pp.71-95.
Renforth, P., Washbourne, C.-L., Taylder, J. and Manning, D.A.C. (2011). Silicate production and availability for mineral carbonation.
Rickard, D. (1997). Kinetics of pyrite formation by the H2S oxidation of iron (II) monosulfide in aqueous solutions between 25 and 125 C: The rate equation. *Geochimica et Cosmochimica Acta, 6*1(1), pp. 115–134.
Rieu, R., Allen, P.A., Plötze, M. and Pettke, T. (2007). Climatic cycles during a Neoproterozoic 'snowball' glacial epoch. *Geology,* 35(4), pp. 299–302.
Robbins, L.J., Fakhraee, M., Smith, A.J., Bishop, B.A., Swanner, E.D., Peacock, C.L., Wang, C.L., Planavsky, N.J., Reinhard, C.T., Crowe, S.A. and Lyons, T.W. (2023). Manganese

oxides, Earth surface oxygenation, and the rise of oxygenic photosynthesis. *Earth-Science Reviews*, *239*, p.104368.
Robinson, L.F., Adkins, J.F., Fernandez, D.P., Burnett, D.S., Wang, S.L., Gagnon, A.C. and Krakauer, N. (2006). Primary U distribution in scleractinian corals and its implications for U series dating. Geochemistry, Geophysics, Geosystems, 7(5).
Roberts, A.P. and Turner, G.M. (1993). Diagenetic formation of ferrimagnetic iron sulphide minerals in rapidly deposited marine sediments, South Island, New Zealand. *Earth and Planetary Science Letters, 115*(1–4), pp. 257–273.
Rolison, J.M., Stirling, C.H., Middag, R. and Rijkenberg, M.J.A. (2017). Uranium stable isotope fractionation in the Black Sea: Modern calibration of the 238U/235U paleo-redox proxy. *Geochimica et Cosmochimica Acta,* 203, pp. 69–88.
Romaniello, S.J., Herrmann, A.D. and Anbar, A.D. (2013). Uranium concentrations and 238U/235U isotope ratios in modern carbonates from the Bahamas: Assessing a novel paleoredox proxy. *Chemical Geology,* 362, pp. 305–316.
Rooney, A.D., Chew, D.M. and Selby, D. (2011). Re–Os geochronology of the Neoproterozoic–Cambrian Dalradian Supergroup of Scotland and Ireland: implications for Neoproterozoic stratigraphy, glaciations and Re–Os systematics. *Precambrian Research, 185*(3–4), pp. 202–214.
Rose, B.E. (2015). Stable "Waterbelt" climates controlled by tropical ocean heat transport: A nonlinear coupled climate mechanism of relevance to Snowball Earth. *Journal of Geophysical Research: Atmospheres*, *120*(4), pp.1404-1423.
Rosing, M.T. and Frei, R. (2004). U-rich Archaean sea-floor sediments from Greenland - indications of > 3700 Ma oxygenic photosynthesis. *Earth and Planetary Science Letters, 217*(3–4), pp. 237–244.
Rudnick, R.L. and Gao, S. (2003). Composition of the Continental Crust. In: *Treatise on Geochemistry*, pp. 1–64.
Runnegar, B. (2000). Loophole for snowball Earth. *Nature, 405*(6785), pp. 403–404.
Rutledge, R.L., Gilleaudeau, G.J., Remírez, M.N., Kaufman, A.J., Lyons, T.W., Bates, S. and Algeo, T.J. (2024). Productivity and organic carbon loading control uranium isotope behavior in ancient reducing settings: Implications for the paleoredox proxy. *Geochimica et Cosmochimica Acta,* 368, pp. 197–213.
Ruttenberg, K.C. (2003). The global phosphorus cycle. *Treatise on geochemistry,* 8, p. 682.
Ruttenberg, K.C. and Berner, R.A. (1993). Authigenic apatite formation and burial in sediments from non-upwelling, continental margin environments. *Geochimica et cosmochimica acta*, *57*(5), pp.991-1007.
Sahoo, S.K., Planavsky, N.J., Jiang, G., Kendall, B., Owens, J.D., Wang, X., Shi, X., Anbar, A.D. and Lyons, T.W. (2016). Oceanic oxygenation events in the anoxic Ediacaran ocean. *Geobiology*, *14*(5), pp. 457–468.
Sahoo, S.K., Planavsky, N.J., Kendall, B., Wang, X., Shi, X., Scott, C., Anbar, A.D., Lyons, T.W. and Jiang, G. (2012). Ocean oxygenation in the wake of the Marinoan glaciation. *Nature, 489*(7417), pp. 546–549.
Saldi, G.D., Daval, D., Guo, H., Guyot, F., Bernard, S., Le Guillou, C., Davis, J.A. and Knauss, K.G. (2015). Mineralogical evolution of Fe–Si-rich layers at the olivine-water interface during carbonation reactions. *American mineralogist,* 100(11–12), pp. 2655–2669.
Sandaruwan, C., Adikaram, M., Madugalla, N., Pitawala, A., Ishiga, H. and Udagedara, T. (2022). Mineralogy and geochemistry of beach sediments associated with the Precambrian crystalline rocks (Vijayan Complex) of Sri Lanka; perspective for heavy minerals. *Regional Studies in Marine Science,* 55, p. 102579.

Sánchez-Román, M., Vasconcelos, C., Schmid, T., Dittrich, M., McKenzie, J.A., Zenobi, R. and Rivadeneyra, M.A. (2008). Aerobic microbial dolomite at the nanometer scale: Implications for the geologic record. Geology, 36(11), pp.879-882.

Satkoski, A.M., Beukes, N.J., Li, W., Beard, B.L. and Johnson, C.M. (2015). A redox-stratified ocean 3.2 billion years ago. *Earth and Planetary Science Letters,* 430, pp. 43–53.

Sawaki, Y., Kawai, T., Shibuya, T., Tahata, M., Omori, S., Komiya, T., Yoshida, N., Hirata, T., Ohno, T., Windley, B.F. and Maruyama, S. (2010). 87Sr/86Sr chemostratigraphy of Neoproterozoic Dalradian carbonates below the Port Askaig glaciogenic Formation, Scotland. *Precambrian Research, 179*(1–4), pp. 150–164.

Scheffler, K., Buehmann, D. and Schwark, L. (2006). Analysis of late Palaeozoic glacial to postglacial sedimentary successions in South Africa by geochemical proxies–Response to climate evolution and sedimentary environment. *Palaeogeography, Palaeoclimatology, Palaeoecology, 240*(1–2), pp. 184–203.

Scheffler, K., Hoernes, S. and Schwark, L. (2003). Global changes during Carboniferous–Permian glaciation of Gondwana: Linking polar and equatorial climate evolution by geochemical proxies. *Geology, 31*(7), pp. 605–608.

Scheller, E.L., Dickson, A.J., Canfield, D.E., Korte, C., Kristiansen, K.K. and Dahl, T.W. (2018). Ocean redox conditions between the snowballs – Geochemical constraints from Arena Formation, East Greenland. *Precambrian Research,* 319, pp. 173–186.

Schlesinger, W.H. (1997). Biogeochemistry: an analysis of global change.

Schopf, J.W. (2006). Fossil evidence of Archaean life. *Philosophical Transactions of the Royal Society B: Biological Sciences, 361*(1470), pp. 869–885.

Schrag, D.P., Berner, R.A., Hoffman, P.F. and Halverson, G.P. (2002). On the initiation of a snowball Earth. *Geochemistry, Geophysics, Geosystems, 3*(6), pp. 1–21.

Scott, C., Lyons, T.W., Bekker, A., Shen, Y., Poulton, S.W., Chu, X. and Anbar, A.D. (2008). Tracing the stepwise oxygenation of the Proterozoic ocean. *Nature, 452*(7186), pp. 456–459.

Shen, W., Zhu, X., Yan, B., Li, J., Liu, P. and Poulton, S.W. (2022). Secular variation in seawater redox state during the Marinoan Snowball Earth event and implications for eukaryotic evolution. *Geology, 50*(11), pp. 1239–1244.

Shen, Y., Canfield, D.E. and Knoll, A.H. (2002). Middle Proterozoic Ocean chemistry: evidence from the McArthur Basin, northern Australia. *American Journal of Science*, *302*(2), pp.81-109.

Shi, F., Shi, X., Su, X., Fang, X., Wu, Y., Cheng, Z. and Yao, Z. (2018). Clay minerals in Arctic Kongsfjorden surface sediments and their implications on provenance and paleoenvironmental change. *Acta Oceanologica Sinica, 37*(5), pp. 29–38.

Shields-Zhou, G. and Och, L. (2011). The case for a neoproterozoic oxygenation event: Geochemical evidence and biological consequences. *GSA Today, 21*(3), pp. 4–11.

Shields, G. and Veizer, J. (2002). Precambrian marine carbonate isotope database: Version 1.1. *Geochemistry, Geophysics, Geosystems* 3(6), pp.1-of.

Shields, G.A. (2017). Earth system transition during the Tonian–Cambrian interval of biological innovation: nutrients, climate, oxygen and the marine organic carbon capacitor.

Shields, G.A., Mills, B.J., Zhu, M., Raub, T.D., Daines, S.J. and Lenton, T.M. (2019). Unique Neoproterozoic carbon isotope excursions sustained by coupled evaporite dissolution and pyrite burial. *Nature Geoscience*, *12*(10), pp.823-827.

Shifa, Z., Xiaomin, Z., Xin, L., Dong, W. and Dongna, Z. (2016). Authigenic minerals and diagenetic evolution in altered volcanic materials and their impacts on hydrocarbon reservoirs: evidence from the lower Permian in the northwestern margin of Junggar Basin, China. *Arabian Journal of Geosciences, 9*(2), pp. 1–19.

Shuster, A.M., Wallace, M.W., van Smeerdijk Hood, A. and Jiang, G. (2018). The Tonian Beck Spring Dolomite: Marine dolomitization in a shallow, anoxic sea. *Sedimentary Geology,* 368, pp. 83–104.

Simoneit, B.R.T. (2004). Biomarkers (molecular fossils) as geochemical indicators of life. *Advances in Space Research* 33(8), pp. 1255–1261.

Singer, A. (1980). The paleoclimatic interpretation of clay minerals in soils and weathering profiles. *Earth-Science Reviews,* 15(4), pp. 303–326.

Skelton, A., Lewerentz, A., Kleine, B., Webster, D. and Pitcairn, I. (2015). Structural channelling of metamorphic fluids on Islay, Scotland: implications for paleoclimatic reconstruction. *Journal of Petrology,* 56(11), pp. 2145–2172.

Skelton, A.D.L., Valley, J.W., Graham, C.M., Bickle, M.J. and Fallick, A.E. (2000). The correlation of reaction and isotope fronts and the mechanism of metamorphic fluid flow. *Contributions to Mineralogy and Petrology,* 138, pp. 364–375.

Slomp, C.P. and Van Cappellen, P. (2007). The global marine phosphorus cycle: sensitivity to oceanic circulation. *Biogeosciences*,*4*(2), pp.155-171.

Slomp, C.P., Thomson, J. and de Lange, G.J. (2004). Controls on phosphorus regeneration and burial during formation of eastern Mediterranean sapropels. *Marine Geology,* 203(1–2), pp. 141–159.

Smith, E.A., Mayfield, C.I. and Wong, P.T.S. (1977). Physical and chemical characterization of selected natural apatites in synthetic and natural aqueous solutions. *Water, Air, and Soil Pollution,* 8, pp. 401–415.

Song, H., An, Z., Ye, Q., Stüeken, E.E., Li, J., Hu, J., Algeo, T.J., Tian, L., Chu, D., Song, H. and Xiao, S. (2023). Mid-latitudinal habitable environment for marine eukaryotes during the waning stage of the Marinoan snowball glaciation. *Nature Communications,* 14(1), p. 1564.

Spence, G.H., Le Heron, D.P. and Fairchild, I.J. (2016). Sedimentological perspectives on climatic, atmospheric and environmental change in the Neoproterozoic Era. *Sedimentology,* 63(2), pp. 253–306.

Sperling, E.A., Knoll, A.H. and Girguis, P.R. (2015). The Ecological Physiology of Earth's Second Oxygen Revolution. *Annual Review of Ecology, Evolution, and Systematics,* 46, pp. 215–235.

Środoń, J. (2002). Quantitative mineralogy of sedimentary rocks with emphasis on clays and with applications to K-Ar dating. *Mineralogical Magazine, 66*(5), pp. 677–687.

Środoń, J., Eberl, D.D. and Bailey, S.W. (1984). Illite. *Micas,* 13, pp. 495–544.

Stern, R.J. and Miller, N.R. (2021). Neoproterozoic Glaciation—Snowball Earth Hypothesis. *Encyclopedia Geol.(Second Edition), D. Alderton & SA Elias, Eds.(Oxford: Academic Press, Elsevier)*, pp. 546–556.

Stirling, C.H., Andersen, M.B., Potter, E.K. and Halliday, A.N. (2007). Low-temperature isotopic fractionation of uranium. *Earth and Planetary Science Letters,* 264(1–2), pp. 208–225.

Stockey, R.G., Cole, D.B., Farrell, U.C., Agić, H., Boag, T.H., Brocks, J.J., Canfield, D.E., Cheng, M., Crockford, P.W., Cui, H. and Dahl, T.W. (2024). Sustained increases in atmospheric oxygen and marine productivity in the Neoproterozoic and Palaeozoic eras. *Nature Geoscience,* 17(7), pp. 667–674.

Stüeken, E.E., Kipp, M.A., Koehler, M.C. and Buick, R. (2016). The evolution of Earth's biogeochemical nitrogen cycle. *Earth-Science Reviews*, *160*, pp.220-239.

Sugitani, K., Mimura, K., Nagaoka, T., Lepot, K. and Takeuchi, M. (2013). Microfossil assemblage from the 3400Ma Strelley Pool Formation in the Pilbara Craton, Western Australia: Results form a new locality. *Precambrian Research,* 226, pp. 59–74.

Summons, R.E., Welander, P. V and Gold, D.A. (2022). Lipid biomarkers: molecular tools for illuminating the history of microbial life. *Nature Reviews Microbiology, 20*(3), pp. 174–185.

Sverjensky, D.A. and Lee, N. (2010). The great oxidation event and mineral diversification. *Elements, 6*(1), pp. 31–36.
Swanson-Hysell, N.L., Rose, C.V., Calmet, C.C., Halverson, G.P., Hurtgen, M.T. and Maloof, A.C. (2010). Cryogenian glaciation and the onset of carbon-isotope decoupling. *Science*, *328*(5978), pp.608-611.
Swart, P.K. (2015). The geochemistry of carbonate diagenesis: The past, present and future. *Sedimentology*, *62*(5), pp. 1233–1304.
Swart, P.K. and Oehlert, A.M. (2018). Revised interpretations of stable C and O patterns in carbonate rocks resulting from meteoric diagenesis. *Sedimentary Geology*, *364*, pp.14-23.
Swart, P.K. (1988). The elucidation of dolomitization events using nuclear track mapping.
Tahata, M., Sawaki, Y., Yoshiya, K., Nishizawa, M., Komiya, T., Hirata, T., Yoshida, N., Maruyama, S. and Windley, B.F. (2015). The marine environments encompassing the Neoproterozoic glaciations: Evidence from C, Sr and Fe isotope ratios in the Hecla Hoek Supergroup in Svalbard. *Precambrian Research,* 263, pp. 19–42.
Tanner, P.W.G., Bendall, C.A., Pickett, E.A., Roberts, J.L., Treagus, J.E. and Stephenson, D. (2013). The Dalradian rocks of the south-west Grampian Highlands of Scotland. *Proceedings of the Geologists' Association, 124*(1–2), pp. 83–147.
Taylor, S. and McLennan, S. (1985). The continental crust: its composition and evolution. *Geoscience Texts*, *312*.
Thiry, M. (2000). Palaeoclimatic interpretation of clay minerals in marine deposits: an outlook from the continental origin. *Earth-Science Reviews,* 49(1–4), pp. 201–221.
Thomas, C., Graham, C., Ellam, R. and Fallick, A. (2004). 87Sr/86Sr chemostratigraphy of Neoproterozoic Dalradian limestones of Scotland and Ireland: constraints on depositional ages and time scales. *Journal of the Geological Society,* 161(2), pp. 229–242.
Thompson, J., Poulton, S.W., Guilbaud, R., Doyle, K.A., Reid, S. and Krom, M.D. (2019). Development of a modified SEDEX phosphorus speciation method for ancient rocks and modern iron-rich sediments. *Chemical Geology,* 524, pp. 383–393.
Tissot, F.L., Chen, C., Go, B.M., Naziemiec, M., Healy, G., Bekker, A., Swart, P.K. and Dauphas, N. (2018). Controls of eustasy and diagenesis on the 238U/235U of carbonates and evolution of the seawater (234U/238U) during the last 1.4 Myr. *Geochimica et Cosmochimica Acta,* 242, pp. 233–265.
Tissot, F.L.H. and Dauphas, N. (2015). Uranium isotopic compositions of the crust and ocean: Age corrections, U budget and global extent of modern anoxia. *Geochimica et Cosmochimica Acta,* 167, pp. 113–143.
Tiwari, M., Singh, A.K. and Sinha, D.K. (2015). Stable isotopes: Tools for understanding past climatic conditions and their applications in chemostratigraphy. In: *chemostratigraphy*. Elsevier, pp. 65–92.
Tomiak, P.J., Andersen, M.B., Hendy, E.J., Potter, E.K., Johnson, K.G. and Penkman, K.E. (2016). The role of skeletal micro-architecture in diagenesis and dating of Acropora palmata. Geochimica et Cosmochimica Acta, 183, pp.153-175.
Tosca, N.J., Johnston, D.T., Mushegian, A., Rothman, D.H., Summons, R.E. and Knoll, A.H. (2010). Clay mineralogy, organic carbon burial, and redox evolution in Proterozoic oceans. *Geochimica et Cosmochimica Acta,* 74(5), pp. 1579–1592.
Tostevin, R. and Ahmed, I.A.M. (2023). Micronutrient availability in Precambrian oceans controlled by greenalite formation. *Nature Geoscience, 16*(12), pp. 1188–1193.
Tostevin, R., Shields, G.A., Tarbuck, G.M., He, T., Clarkson, M.O. and Wood, R.A. (2016). Effective use of cerium anomalies as a redox proxy in carbonate-dominated marine settings. *Chemical Geology,* 438, pp. 146–162.
Tribovillard, N., Algeo, T.J., Lyons, T. and Riboulleau, A. (2006). Trace metals as paleoredox and paleoproductivity proxies: an update. *Chemical geology, 232*(1–2), pp. 12–32.

Tu, C., Diamond, C.W., Stüeken, E.E., Cao, M., Pan, W. and Lyons, T.W. (2024). Dynamic evolution of marine productivity, redox, and biogeochemical cycling track local and global controls on Cryogenian sea-level change. *Geochimica et Cosmochimica Acta,* 365, pp. 114–135.

Tucker, M.E. (1982). Precambrian dolomites: petrographic and isotopic evidence that they differ from Phanerozoic dolomites. *Geology, 10*(1), pp. 7–12.

Turner, E.C. (2021). Possible poriferan body fossils in early Neoproterozoic microbial reefs. *Nature, 596*(7870), pp. 87–91.

Tyrrell, T. (1999). The relative influences of nitrogen and phosphorus on oceanic primary production. *Nature*, *400*(6744), pp.525-531.

Uncles, R.J., Stephens, J.A. and Harris, C. (2006). Properties of suspended sediment in the estuarine turbidity maximum of the highly turbid Humber Estuary system, UK. *Ocean Dynamics,* 56(3–4), pp. 235–247.

Van Cappellen, P. and Ingall, E.D. (1994). Benthic phosphorus regeneration, net primary production, and ocean anoxia: A model of the coupled marine biogeochemical cycles of carbon and phosphorus. *Paleoceanography,* 9(5), pp. 677–692.

Velde, B., Suzuki, T. and Nicot, E. (1986). Pressure-temperature-composition of illite/smectite mixed-layer minerals: Niger delta mudstones and other examples. *Clays & Clay Minerals, 34*(4), pp. 435–441.

Velde, B.B. and Meunier, A. (2008). *The origin of clay minerals in soils and weathered rocks*. Springer Science & Business Media.

Verdel, C. and Campbell, M. (2017). Neoproterozoic carbon isotope stratigraphy of the Amadeus Basin, central Australia. *Bulletin*, *129*(9-10), pp.1280-1299.

Violante, A. and Pigna, M. (2002). Competitive Sorption of Arsenate and Phosphate on Different Clay Minerals and Soils. *Soil Science Society of America Journal, 66*(6), pp. 1788–1796.

Viollier, E., Inglett, P.W., Hunter, K., Roychoudhury, A.N. and Van Cappellen, P. (2000). The ferrozine method revisited: Fe (II)/Fe (III) determination in natural waters. *Applied geochemistry, 15*(6), pp. 785–790.

Voigt, A. and Abbot, D.S. (2012). Sea-ice dynamics strongly promote Snowball Earth initiation and destabilize tropical sea-ice margins. *Climate of the Past* 8(6), pp. 2079–2092. doi: 10.5194/cp-8-2079-2012.

Vosteen, P., Kossack, M., Vogt, C., Andersen, C.H., Geilert, S., Zabel, M. and Scholz, F. (2024). Iron redox shuttling and uptake by silicate minerals on the Namibian mud belt. *Geochimica et Cosmochimica Acta, 386,* pp.1-17.

Wallace, M.W., Hood, A., Shuster, A., Greig, A., Planavsky, N.J. and Reed, C.P. (2017). Oxygenation history of the Neoproterozoic to early Phanerozoic and the rise of land plants. *Earth and Planetary Science Letters,* 466, pp. 12–19.

Walsh, A., Ball, T. and Schultz, D.M. (2019). Extreme sensitivity in Snowball Earth formation to mountains on PaleoProterozoic supercontinents. *Scientific Reports,* 9(1).

Walters, C.C., Peters, K.E. and Moldowan, J.M. (2020). History of Life from the Hydrocarbon Fossil Record. *Hydrocarbons, Oils and Lipids: Diversity, Origin, Chemistry and Fate*, pp. 409–443.

Walton, C.R., Ewens, S., Coates, J.D., Blake, R.E., Planavsky, N.J., Reinhard, C., Ju, P., Hao, J. and Pasek, M.A. (2023). Phosphorus availability on the early Earth and the impacts of life. *Nature Geoscience, 16*(5), pp. 399–409.

Wang, P., Du, Y., Yu, W., Algeo, T.J., Zhou, Q., Xu, Y., Qi, L., Yuan, L. and Pan, W. (2020). The chemical index of alteration (CIA) as a proxy for climate change during glacial-interglacial transitions in Earth history. *Earth-Science Reviews,* 201, p.103032.

Wang, W., Li, C., Dodd, M.S., Algeo, T.J., Zhang, Z., Cheng, M. and Hou, M. (2023). A DOM regulation model for dolomite versus calcite precipitation in the Ediacaran Ocean: Implications for the "dolomite problem". *Precambrian Research*, *385*, p.106947.

Wang, X., Dong, L., Ma, H., Lang, X. and Wang, R. (2024). Primary productivity recovery and shallow-water oxygenation during the Sturtian deglaciation in South China. *Global and Planetary Change,* 241, p. 104546.

Wang, X., Planavsky, N.J., Reinhard, C.T., Hein, J.R. and Johnson, T.M. (2016). A cenozoic seawater redox record derived from 238U/235U in ferromanganese crusts. *American Journal of Science,* 315(11), pp. 64–83.

Ward, B.A., Dutkiewicz, S., Jahn, O. and Follows, M.J. (2012). A size-structured food-web model for the global ocean. *Limnology and Oceanography,* 57(6), pp. 1877–1891.

Warr, L.N. (2022). Earth's clay mineral inventory and its climate interaction: A quantitative assessment. *Earth-Science Reviews,* 234, p.104198.

Warren, S.G., Brandt, R.E., Grenfell, T.C. and McKay, C.P. (2002). Snowball Earth: Ice thickness on the tropical ocean. *Journal of Geophysical Research: Oceans* 107(10), pp.31-1.

Weaver, C.E. (1967). Potassium, illite and the ocean. *Geochimica et cosmochimica acta*, *31*(11), pp. 2181–2196.

Weaver, C.E. (1989). *Clays, muds, and shales*. Elsevier.

Wei, G.Y., Wei, W., Wang, D., Li, T., Yang, X., Shields, G.A., Zhang, F., Li, G., Chen, T., Yang, T. and Ling, H.F. (2020). Enhanced chemical weathering triggered an expansion of euxinic seawater in the aftermath of the Sturtian glaciation. *Earth and Planetary Science Letters,* 539, p. 116244.

Weyer, S., Anbar, A.D., Gerdes, A., Gordon, G.W., Algeo, T.J. and Boyle, E.A. (2008). Natural fractionation of 238U/235U. *Geochimica et Cosmochimica Acta,* 72(2), pp. 345–359.

Wheat, C.G., Feely, R.A. and Mottl, M.J. (1996). Phosphate removal by oceanic hydrothermal processes: An update of the phosphorus budget in the oceans. *Geochimica et Cosmochimica Acta, 60*(19), pp. 3593–3608.

White, A.F. and Brantley, S.L. (1995). Chemical weathering rates of silicate minerals: an overview. *Chemical weathering rates of silicate minerals*, *31*, pp.1-22.

Wilson, M.J. (1999). The origin and formation of clay minerals in soils: past, present and future perspectives. *Clay Minerals, 34*(1), pp. 7–25. doi: 10.1180/000985599545957.

Won, C.D., Hong, H. and Pak, K.R. (2020). Origin of clay minerals on section of Luochuan loesspalaeosol in Shaanxi Province, northwest China. *Frontiers of Earth Science,* 14(4), pp. 684–694.

Wood, R., Liu, A.G., Bowyer, F., Wilby, P.R., Dunn, F.S., Kenchington, C.G., Cuthill, J.F.H., Mitchell, E.G. and Penny, A. (2019). Integrated records of environmental change and evolution challenge the Cambrian Explosion. *Nature Ecology and Evolution, 3*(4), pp. 528–538.

Worden, R. and Morad, S. (2009). *Clay mineral cements in sandstones*. John Wiley & Sons.

Worden, R.H., Griffiths, J., Wooldridge, L.J., Utley, J.E.P., Lawan, A.Y., Muhammed, D.D., Simon, N. and Armitage, P.J. (2020). Chlorite in sandstones. *Earth-Science Reviews* 204, p.103105.

Xiaofeng, L., Zenglin, H., Jiwei, L., Xiaodan, G., Xuping, X. and Shifeng, L. (2023). Carbon and oxygen isotope characteristics of carbonate rocks in the Mesoproterozoic Jixian System of the Ordos Basin and their implications. *Scientific Reports, 13*(1), p. 14082.

Xiong, Y., Guilbaud, R., Peacock, C.L., Cox, R.P., Canfield, D.E., Krom, M.D. and Poulton, S.W. (2019). Phosphorus cycling in Lake Cadagno, Switzerland: A low sulfate euxinic ocean analogue. *Geochimica et Cosmochimica Acta,* 251, pp. 116–135.

Xu, D., Wang, X., Zhu, J.M., Jiang, G., Shi, X., Wang, X. and Sahoo, S.K. (2022). Chromium isotope evidence for oxygenation events in the Ediacaran Ocean. *Geochimica et Cosmochimica Acta,* 323, pp. 258–275.

Xu, L., Lehmann, B., Weyer, S., Wen, H., Mao, J., Neubert, N. and Jian, W. (2024). Inverse Mo versus U isotope correlation of Early Cambrian highly metalliferous black shales in South China indicates synsedimentary metal enrichment from a near-modern ocean. *Mineralium Deposita*, *59*(1), pp.155-167.

Yang, X., Mao, J., Li, R., Huang, F., He, C., Zhao, C., Wei, W., Yang, G., Xiong, Y. and Poulton, S.W. (2024). Fluctuating oxygenation and dynamic iron cycling in the late Paleoproterozoic Ocean. *Earth and Planetary Science Letters, 626*, p. 118554.

Yang, Z., Wu, P., Fu, Y., Qiao, W., Qin, Y., Li, C., Xia, P., Guo, C., Long, X. and Wu, L. (2022). Coupling of the redox history and enrichment of Ni-Mo in black shale during the early Cambrian: Constraints from S-Fe isotopes and trace elements of pyrite, South China. *Ore Geology Reviews*, *143*, p.104749.

Ye, Y., Zhang, S., Wang, H., Wang, X., Tan, C., Li, M., Wu, C. and Canfield, D.E. (2021). Black shale Mo isotope record reveals dynamic ocean redox during the Mesoproterozoic Era. *Geochemical Perspectives Letters*, *18*, pp.16-21.

Yu, H., Zheng, W., Cui, X. and Zhou, J. (2024). Influence of Mineralogical Characteristics on Mechanical Properties of Montney Tight Formations Using Instrumented Indentation Test and SEM–EDS Analysis. *Rock Mechanics and Rock Engineering*, pp. 1–18.

Yuan, K., Rukai, Z., Kouqi, L., Jingya, Z. and Surong, Z. (2024). Detrital and authigenic clay minerals in shales: A review on their identification and applications. Heliyon.

Zach A. Diloreto, Sanchit Garg, Tomaso R. R. Bontognali & Maria Dittrich , M. (2021). Modern dolomite formation caused by seasonal cycling of oxygenic phototrophs and anoxygenic phototrophs in a hypersaline sabkha. Scientific Reports 11, 4170.

Zane, A., Sassi, R. and Guidotti, C.V. (1998). New data on metamorphic chlorite as a petrogenetic indicator mineral, with special regard to greenschist-facies rocks. The Canadian Mineralogist, 36(3), pp.713-726.

Zegeye, A., Bonneville, S., Benning, L.G., Sturm, A., Fowle, D.A., Jones, C., Canfield, D.E., Ruby, C., MacLean, L.C., Nomosatryo, S. and Crowe, S.A. (2012). Green rust formation controls nutrient availability in a ferruginous water column. *Geology, 40*(7), pp. 599–602.

Zerkle, A.L., Poulton, S.W., Newton, R.J., Mettam, C., Claire, M.W., Bekker, A. and Junium, C.K. (2017). Onset of the aerobic nitrogen cycle during the Great Oxidation Event. *Nature*, *542*(7642), pp.465-467.

Zhai, L., Wu, C., Ye, Y., Zhang, S. and Wang, Y. (2018). Fluctuations in chemical weathering on the Yangtze Block during the Ediacaran–Cambrian transition: Implications for paleoclimatic conditions and the marine carbon cycle. *Palaeogeography, Palaeoclimatology, Palaeoecology,* 490, pp. 280–292.

Zhang, F., Algeo, T.J., Romaniello, S.J., Cui, Y., Zhao, L., Chen, Z.Q. and Anbar, A.D. (2018c). Congruent Permian-Triassic δ238U records at Panthalassic and Tethyan sites: Confirmation of global-oceanic anoxia and validation of the U-isotope paleoredox proxy. *Geology,* 46(4), pp. 327–330. doi: 10.1130/G39695.1.

Zhang, F., Romaniello, S.J., Algeo, T.J., Lau, K.V., Clapham, M.E., Richoz, S., Herrmann, A.D., Smith, H., Horacek, M. and Anbar, A.D. (2018b). Multiple episodes of extensive marine anoxia linked to global warming and continental weathering following the latest Permian mass extinction. S*cience advances*, *4*(4), p.e1602921.

Zhang, F., Xiao, S., Kendall, B., Romaniello, S.J., Cui, H., Meyer, M., Gilleaudeau, G.J., Kaufman, A.J. and Anbar, A.D. (2018a). Extensive marine anoxia during the terminal Ediacaran Period. *Science advances*,*4*(6), p.eaan8983.

Zhang F., Xu H., Shelobolina E. S., Konishi H., Converse B., Shen Z. and Roden E. E. (2015) The catalytic effect of boundextracellular polymeric substances excreted by anaerobic microorganisms on Ca-Mg carbonate precipitation: implications for the ‘‘dolomite problem”. Am. Mineral. 100, 483–494.

Zhang, F., Zhu, X., Yan, B., Kendall, B., Peng, X., Li, J., Algeo, T.J. and Romaniello, S. (2015). Oxygenation of a Cryogenian Ocean (Nanhua Basin, South China) revealed by pyrite Fe isotope compositions. *Earth and Planetary Science Letters,* 429, pp. 11–19.

Zhang, G., Chen, D., Huang, K.-J., Liu, M., Huang, T., Yeasmin, R. and Fu, Y. (2021). Dramatic attenuation of continental weathering during the Ediacaran-Cambrian transition: Implications for the climatic-oceanic-biological co-evolution. *Global and Planetary Change,* 203, p. 103518.

Zhang, Y.L., Bao, Z.D., Zhao, Y., Jiang, L., Zhou, Y.Q. and Gong, F.H. (2017). Origins of authigenic minerals and their impacts on reservoir quality of tight sandstones: Upper Triassic Chang-7 Member, Yanchang Formation, Ordos Basin, China. *Australian Journal of Earth Sciences*, *64*(4), pp. 519–536.

Zhao, Y., Zou, X., Gao, J., Wang, C., Li, Y., Yao, Y., Zhao, W. and Xu, M. (2018). Clay mineralogy and source-to-sink transport processes of Changjiang River sediments in the estuarine and inner shelf areas of the East China Sea. *Journal of Asian Earth Sciences,* 152, pp. 91–102.

Zhou, L., McKenna, C.A., Long, D.G.F. and Kamber, B.S. (2017). LA-ICP-MS elemental mapping of pyrite: An application to the Palaeoproterozoic atmosphere. *Precambrian Research,* 297, pp. 33–55.

Zhou, X., Jenkyns, H.C., Owens, J.D., Junium, C.K., Zheng, X.Y., Sageman, B.B., Hardisty, D.S., Lyons, T.W., Ridgwell, A. and Lu, Z. (2015). Upper ocean oxygenation dynamics from I/Ca ratios during the Cenomanian-Turonian OAE 2. *Paleoceanography, 30*(5), pp. 510–526.

Zhou, X., Thomas, E., Rickaby, R.E.M., Winguth, A.M.E. and Lu, Z. (2014). I/Ca evidence for upper ocean deoxygenation during the PETM. *Paleoceanography,* 29(10), pp. 964–975.

Zhu, G., Yan, H., Chen, W., Yan, L., Zhang, K., Li, T., Chen, Z., Wu, G. and Santosh, M. (2020). Discovery of Cryogenian interglacial source rocks in the northern Tarim, NW China: Implications for Neoproterozoic paleoclimatic reconstructions and hydrocarbon exploration. *Gondwana Research,* 80, pp. 370–384.

Zhu, S., Zhu, M., Knoll, A.H., Yin, Z., Zhao, F., Sun, S., Qu, Y., Shi, M. and Liu, H., 2016. Decimetre-scale multicellular eukaryotes from the 1.56-billion-year-old Gaoyuzhuang Formation in North China. *Nature Communications,* 7(1), p. 11500.

Appendix

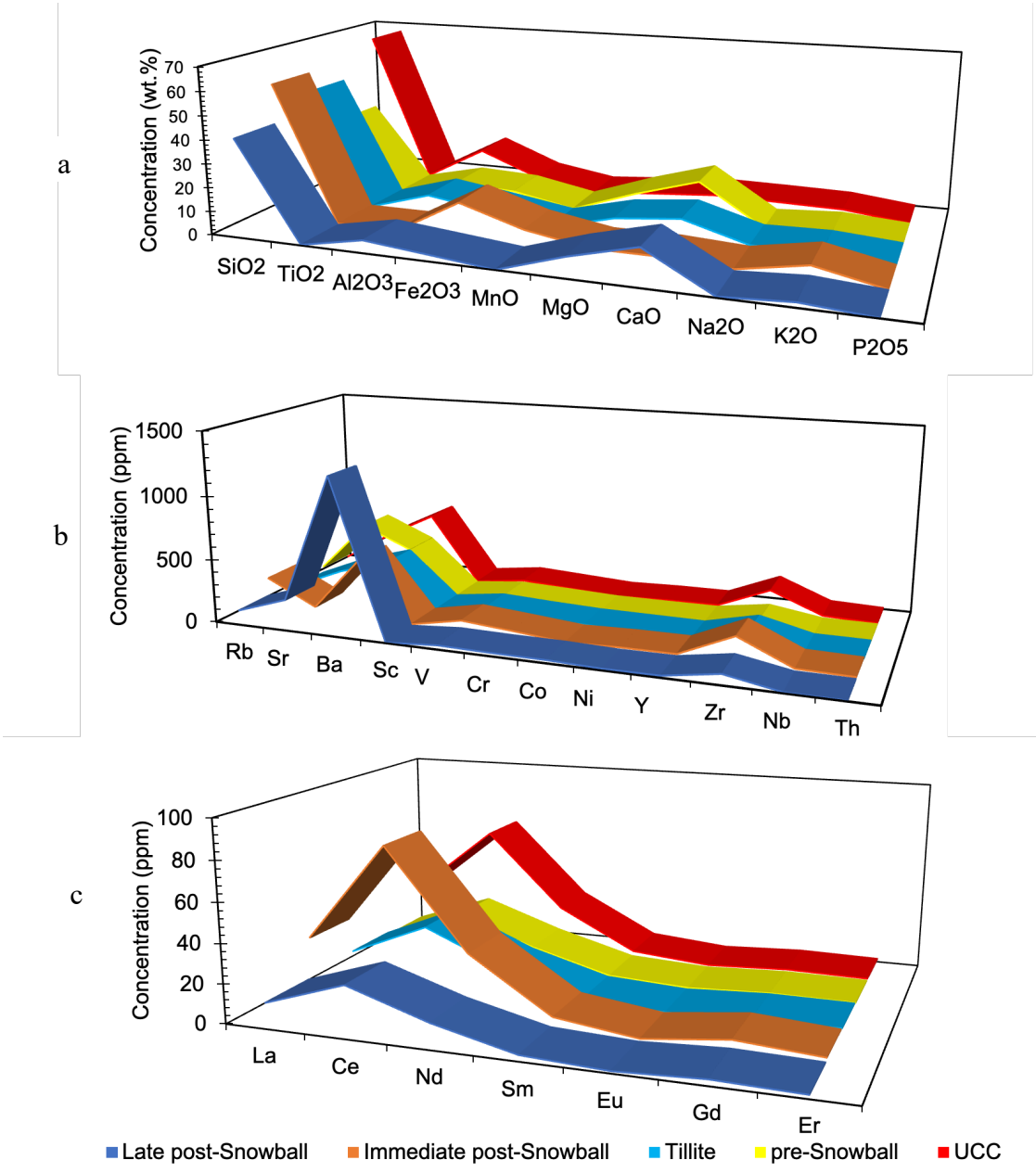

Figure A1| Average major and trace element composition compared with average Upper Continental Crust (UCC) composition. UCC are adapted from Rudnick RL and Gao S. 2003. Composition of the upper continental crust. *Treatise on Geochemistry* 3, 1-64

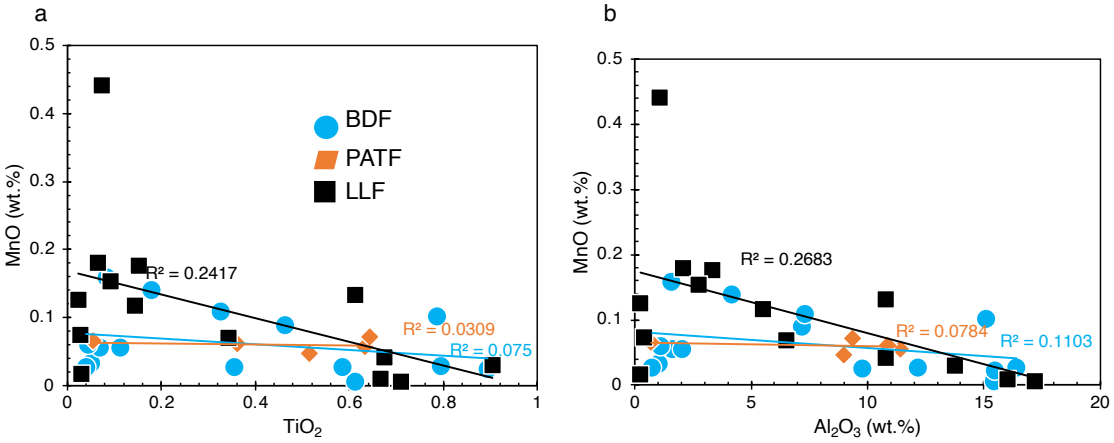

Figure A2| MnO versus TiO_2 (a) and Al_2O_3 (b) cross plots. LLF, Lossit Limestone formation. PATF, Port Askaig Tillite Formation. BDF, Bonahaven Dolomite Formation.

Table A. 1| Pearson's correlation matrix for bulk major element oxides and trace elements for the studied samples.

		SiO_2	TiO_2	Al_2O_3	Fe_2O_3	MnO	MgO	CaO	Na_2O	K_2O	P_2O_5
Pre- Snowball samples	SiO_2	1									
	TiO_2	0.91	1								
	Al_2O_3	0.94	0.95	1							
	Fe_2O_3	0.63	0.71	0.53	1						
	MnO	-0.58	-0.54	-0.56	-0.24	1					
	MgO	-0.70	-0.71	-0.71	-0.43	0.78242	1				
	CaO	-0.92	-0.85	-0.86	-0.68	0.30	0.38	1			
	Na_2O	0.57	0.42	0.66	-0.13	-0.26	-0.42	-0.46	1		
	K_2O	0.92	0.97	0.99	0.56	-0.5708	-0.72	-0.84	0.58	1	
	P_2O5	0.58	0.71	0.50	0.94	-0.27	-0.45	-0.60	-0.20	0.56	1
Tillite samples		SiO_2	TiO_2	Al_2O_3	Fe_2O_3	MnO	MgO	CaO	Na_2O	K_2O	P_2O_5
	SiO_2	1									
	TiO_2	0.66	1								
	Al_2O_3	0.99	0.73	1							
	Fe_2O_3	0.58	0.86	0.64	1						
	MnO	-0.82	-0.76	-0.84	-0.41	1					
	MgO	-0.99	-0.63	-0.97	-0.58	0.77	1				
	CaO	-0.98	-0.79	-0.99	-0.70	0.85	0.97	1			
	Na_2O	0.66	-0.12	0.59	-0.13	-0.37	-0.67	-0.51	1		
	K_2O	0.48	0.98	0.56	0.90	-0.63	-0.45	-0.63	-0.33	1	
	P_2O_5	0.73	0.99	0.78	0.90	-0.75	-0.72	-0.84	-0.02	0.94	1
Immediate Post-Snowball samples		SiO_2	TiO_2	Al_2O_3	Fe_2O_3	MnO	MgO	CaO	Na_2O	K_2O	P_2O_5
	SiO_2	1									
	TiO_2	0.56	1								
	Al_2O_3	0.71	-0.17	1							
	Fe_2O_3	-0.69	0.20	-0.99	1						
	MnO	-0.99	-0.59	-0.68	0.66	1					
	MgO	-0.99	-0.58	-0.70	0.70	0.99	1				
	CaO	-0.99	-0.44	-0.80	0.79	0.98	0.99	1			
	Na_2O	0.60	-0.31	0.99	-0.99	-0.57	-0.59	-0.71	1		
	K_2O	-0.78	0.06	-0.99	0.99	0.76	0.77	0.86	-0.97	1	
	P_2O_5	-0.95	-0.28	-0.90	0.88	0.94	0.95	0.98	-0.82	0.94	1
Late post-Snowball samples		SiO_2	TiO_2	Al_2O_3	Fe_2O_3	MnO	MgO	CaO	Na_2O	K_2O	P_2O_5
	SiO_2	1									
	TiO_2	0.16	1								
	Al_2O_3	0.25	0.96	1							
	Fe_2O_3	-0.03	0.80	0.61	1						
	MnO	-0.47	-0.17	-0.29	0.15	1					
	MgO	-0.88	-0.27	-0.31	-0.11	0.42	1				
	CaO	-0.86	-0.52	-0.60	-0.29	0.40	0.67	1			
	Na_2O	-0.68	-0.06	-0.25	0.40	0.49	0.61	0.52	1		
	K_2O	0.29	0.95	0.99	0.58	-0.31	-0.34	-0.61	-0.30	1	
	P_2O_5	0.090	0.85	0.81	0.70	0.03	-0.16	-0.43	-0.18	0.81	1

Samples		SiO_2	TiO_2	Al_2O_3	Fe_2O_3	MnO	MgO	CaO	Na_2O	K_2O	P_2O_5
Pre-Snowball samples	Sr	-0.49	-0.49	-0.49	-0.28	-0.18	-0.28	0.80	-0.33	-0.49	-0.19
	Ba	0.94	0.95	0.95	0.49	-0.39	-0.65	-0.84	0.56	0.96	0.40
	Sc	0.96	0.98	0.94	0.69	-0.35	-0.67	-0.88	0.59	0.93	0.65
	V	0.87	0.94	0.87	0.80	-0.32	-0.61	-0.83	0.36	0.88	0.77
	Cr	0.98	0.99	1.00	0.43	-0.44	-0.70	-0.85	0.70	0.99	0.40
	Co	0.88	0.87	0.90	0.37	-0.30	-0.48	-0.86	0.76	0.86	0.37
	Ni	0.69	0.77	0.71	0.71	-0.26	-0.50	-0.67	0.36	0.68	0.77
	Y	0.66	0.62	0.57	0.69	0.05	-0.24	-0.75	0.50	0.51	0.62
	Nb	0.98	0.98	0.99	0.44	-0.42	-0.68	-0.86	0.67	0.99	0.38
	Th	0.95	0.93	0.97	0.27	-0.38	-0.63	-0.83	0.75	0.97	0.21
Tillite samples	Sr	0.17	-0.97	-0.05	-0.94	-0.38	-0.17	0.22	0.70	-0.93	-0.99
	Ba	-0.50	0.98	-0.25	0.69	0.02	0.55	0.15	-0.89	0.98	0.87
	Sc	-0.36	1.00	-0.11	0.82	0.19	0.38	-0.02	-0.82	0.99	0.95
	V	-0.65	0.94	-0.42	0.59	0.01	0.68	0.32	-0.95	0.97	0.82
	Cr	-0.34	0.98	-0.07	0.76	0.05	0.40	-0.02	-0.79	0.96	0.90
	Co	-0.62	-0.49	-0.77	-0.82	-0.41	0.60	0.87	-0.06	-0.36	-0.64
	Ni	-0.30	0.46	-0.07	0.01	-0.77	0.50	0.19	-0.41	0.46	0.21
	Y	0.91	-0.72	0.77	-0.29	0.04	-0.90	-0.69	0.98	-0.82	-0.57
	Nb	0.41	0.69	0.60	0.92	0.43	-0.40	-0.73	-0.18	0.58	0.81
	Th	0.72	-0.89	0.50	-0.50	0.07	-0.76	-0.42	0.96	-0.94	-0.74
Immediate post-Snowball samples	Sr	-0.65	0.27	-1.00	1.00	0.61	0.63	0.74	-1.00	0.98	0.85
	Ba	0.67	-0.23	1.00	-1.00	-0.64	-0.66	-0.77	1.00	-0.99	-0.87
	Sc	-0.99	-0.67	-0.62	0.60	1.00	0.99	0.97	-0.50	0.70	0.91
	V	0.04	0.85	-0.67	0.69	-0.08	-0.06	0.09	-0.77	0.58	0.26
	Cr	1.00	0.58	0.70	-0.68	-1.00	-1.00	-0.99	0.59	-0.78	-0.95
	Co	0.38	-0.55	0.92	-0.93	-0.34	-0.36	-0.50	0.97	-0.87	-0.64
	Ni	-0.66	-0.99	0.05	-0.08	0.69	0.68	0.55	0.20	0.06	0.40
	Y	-0.38	0.55	-0.92	0.93	0.34	0.35	0.49	-0.96	0.87	0.64
	Nb	0.00	0.83	-0.70	0.72	-0.05	-0.03	0.13	-0.79	0.61	0.30
	Th	0.85	0.05	0.97	-0.97	-0.83	-0.84	-0.91	0.93	-0.99	-0.97
Late post-Snowball samples	Sr	-0.92	-0.61	-0.65	-0.44	0.64	0.95	0.97	0.90	-0.67	-0.40
	Ba	0.96	0.36	0.41	0.30	-0.34	-0.97	-0.93	-0.64	0.42	0.17
	Sc	0.32	0.99	0.98	0.93	-0.47	-0.49	-0.59	-0.64	0.98	0.76
	V	0.25	0.98	0.95	0.95	-0.33	-0.43	-0.52	-0.66	0.95	0.84
	Cr	0.77	0.82	0.83	0.72	-0.49	-0.87	-0.91	-0.86	0.84	0.58
	Co	0.77	-0.30	-0.27	-0.40	-0.10	-0.64	-0.55	-0.36	-0.25	-0.37
	Ni	0.12	0.68	0.65	0.71	-0.02	-0.27	-0.32	-0.74	0.67	0.95
	Y	0.09	0.89	0.86	0.94	-0.08	-0.28	-0.36	-0.62	0.86	0.96
	Nb	0.33	0.97	0.96	0.91	-0.47	-0.49	-0.58	-0.56	0.96	0.68
	Th	0.32	1.00	0.99	0.95	-0.46	-0.49	-0.59	-0.65	0.99	0.81

Table A. 2| Trace and rare earth elements (ppm) and major elements (wt%) data for the sampled sequence. LD, lower than detection limit.

Samples	SiO_2	TiO_2	$A_{l2}O_3$	Fe_2O_3	MnO	MgO	CaO	Na_2O	K2O	P_2O_5	LOI
PS-16-00	64.3	0.61	15.4	4.7	0.006	3.00	0.14	0.09	7.34	0.147	3.12
PS-16-03	6.2	0.05	1.0	0.4	0.033	20.07	29.33	0.43	0.23	0.045	43.10
PS-16-04	7.7	0.07	1.6	0.7	0.056	18.70	28.73	0.39	0.47	0.061	41.75
PS-16-05	68.6	0.35	9.8	3.0	0.027	3.37	2.78	0.08	4.58	0.151	6.04
PS-16-06	90.6	0.04	1.1	0.5	0.060	1.24	2.06	0.17	0.46	0.026	3.12
PS-16-01	22.9	0.18	4.2	3.0	0.140	13.20	21.37	0.75	1.56	0.086	32.07
PS-16-08	35.5	0.11	2.0	1.0	0.056	1.67	31.83	0.19	0.83	0.054	25.03
PS-16-09	9.7	0.08	1.6	2.0	0.160	17.16	27.43	0.54	0.46	0.073	40.39
PS-16-10	28.3	0.46	7.2	9.5	0.090	8.90	15.15	0.70	2.95	0.146	19.38
PS-16-11	77.4	0.04	0.8	1.0	0.027	1.58	9.19	0.01	0.30	0.080	8.52
PS-16-12	33.6	0.33	7.3	3.0	0.109	10.98	15.22	0.04	3.50	0.176	24.32
PS-16-13	58.2	0.58	12.2	4.2	0.027	3.80	4.03	1.36	4.81	0.191	9.38
Ci-16-01	61.6	0.79	16.4	6.9	0.028	2.20	0.25	1.90	5.81	0.218	2.84
BH-16-02	61.7	0.89	15.5	7.5	0.024	2.14	0.66	0.87	6.18	0.238	3.60
BH-16-03	53.5	0.79	15.1	7.6	0.102	3.80	3.21	0.70	6.42	0.285	7.37
PAT1	67.7	0.63	11.4	6.6	0.057	2.34	2.23	2.19	3.20	0.217	3.53
PAT2	69.3	0.36	10.9	3.9	0.062	1.23	3.35	4.03	1.70	0.146	3.87
PAT3	58.7	0.64	9.4	6.7	0.072	4.23	5.20	0.82	3.45	0.228	9.35
PAT4	56.3	0.51	9.0	3.4	0.047	5.80	7.20	1.52	2.76	0.166	12.50
PAT5	1.7	0.05	0.7	1.0	0.066	20.76	30.19	0.01	0.13	0.041	45.71
LL-16-d	37.8	0.14	5.5	2.6	0.117	10.49	15.59	1.12	1.25	0.054	24.76
LL-16-d	6.8	0.03	0.4	1.3	0.074	19.69	28.43	0.01	0.14	0.032	43.33
LL-16-d	21.8	0.09	2.7	2.1	0.154	15.10	22.33	0.02	0.70	0.035	34.71
LL-16-e	44.8	0.61	10.8	16.7	0.133	5.68	5.25	0.05	3.63	0.265	10.85
LL-16-e	16.6	0.07	2.1	2.0	0.181	16.62	24.66	0.08	0.03	0.061	37.91
LL-16-f	26.2	0.15	3.3	4.9	0.177	12.19	20.54	1.02	0.17	0.092	31.29
LL-16-f	57.7	0.90	13.8	12.9	0.030	2.45	1.37	0.09	5.01	0.234	5.12
LL-16-f	54.4	0.34	6.5	10.2	0.070	5.03	7.92	0.45	1.78	0.145	13.47
LL-16-g	58.0	0.67	16.0	4.1	0.010	1.34	5.36	1.25	5.00	0.101	7.23
LL-16-h	67.2	0.71	17.2	3.4	0.006	1.48	<LD	1.14	5.83	0.042	2.87
LL-16-f	53.7	0.67	10.8	10.7	0.042	4.83	5.14	0.08	4.36	0.273	9.74
LL-16-i	6.1	0.07	1.1	1.8	0.441	19.35	28.29	0.36	0.20	0.047	42.68
LL-16-j1	2.3	0.03	0.2	0.3	0.018	0.80	54.01	0.00	0.06	0.041	42.53
LL-16-j2	4.6	0.02	0.2	0.9	0.126	20.14	29.79	0.00	0.02	0.026	44.59

Samples	Rb	Sr	Ba	Sc	V	Cr	Co	Ni	Y	Zr	Nb	La	Ce	Nd	Sm	Eu	Gd	Dy	Er	Yb	Th
PS-16-00	287	6.2	424	12.5	84.3	52.6	9.1	9.2	21.4	173	21.9	39.2	79.7	36.6	6.4	1.19	5.1	3.8	1.9	2.46	10.0
PS-16-03	<LD	255	54.3	0.8	6.6	5.2	4.5	2.6	4.9	12.0	0.3	3.6	7.4	3.7	1.0	0.20	0.5	0.8	0.7	0.39	1.1
PS-16-04	<LD	414	1492	1.2	9.3	6.4	5.6	3.3	9.1	18.5	1.5	4.4	9.1	5.6	1.1	0.32	1.2	1.3	0.5	0.76	1.7
PS-16-05	131	31.3	505	5.6	38.4	33.4	26.8	10.9	15.5	163	7.9	17.7	38.1	17.7	3.4	0.62	3.0	2.4	1.6	1.56	5.7
PS-16-06	<LD	27.4	539	0.7	7.1	33.2	85.4	2.5	3.6	18.8	1.0	5.2	10.5	4.8	0.8	0.28	0.7	0.6	0.1	0.27	0.8
PS-16-01	26	301	185	3.2	22.7	19.3	5.2	7.8	18.2	57.7	3.2	6.7	14.8	8.6	2.2	0.74	2.9	3.2	1.8	1.54	2.5
PS-16-08	44	1172	10120	1.6	15.0	12.1	19.3	3.0	23.3	76.9	2.8	7.6	16.4	8.6	2.7	1.60	3.2	3.6	2.0	2.27	3.0
PS-16-09	<LD	315	220	1.2	15.5	8.7	3.8	3.6	10.2	34.7	2.4	5.3	12.6	5.1	1.3	0.37	1.5	1.7	1.3	0.77	1.6
PS-16-10	85	177	304	7.1	61.4	39.0	25.7	54.5	27.9	178	13.4	18.0	34.8	17.5	3.7	0.70	4.5	4.8	2.8	2.97	8.8
PS-16-11	<LD	48.1	49.4	0.6	6.4	7.2	54.1	7.1	6.3	14.7	1.2	4.9	8.6	5.1	1.0	0.25	1.2	1.0	0.4	0.59	1.4
PS-16-12	85	116	249	5.8	54.7	33.0	22.0	16.1	21.3	94.1	7.3	12.2	25.1	13.2	3.1	0.63	3.3	3.4	2.1	1.85	5.1
PS-16-13	139	60.2	644	10.4	70.7	60.3	30.9	29.3	19.7	147	13.2	25.6	53.7	24.0	4.6	0.75	4.0	3.1	2.1	2.17	9.1
Ci-16-01	238	39	670	14.7	80.8	61.1	27.0	30.3	19.0	181	22.6	18.5	76.8	19.4	4.3	0.70	4.2	3.8	1.6	2.23	21.9
BH-16-02	259	72	449	14.4	103	61.5	14.0	25.5	36.9	256	28.8	54.5	115	54.8	10.7	1.66	7.7	6.4	3.5	3.90	17.8
BH-16-03	283	80	383	16.3	91.2	48.1	15.8	31.5	34.4	205	25.7	27.1	57.3	26.7	5.3	1.01	5.7	5.6	3.1	3.54	14.0
PAT1	93	113.8	512	11.1	82.3	57.8	20.9	27.5	19.4	154	15.2	21.2	44.3	18.8	3.7	0.69	2.8	2.3	1.1	1.35	7.0

PAT2	43	176	293	6.7	39.6	30.0	28.2	16.9	24.2	133	10.6	21.4	45.2	20.3	4.4	0.81	4.2	3.9	2.2	2.80	24.2
PAT3	101	113	511	11.0	89.5	53.8	26.4	19.3	14.9	121	13.0	13.0	28.3	14.3	2.6	0.70	2.8	2.6	1.7	1.65	3.5
PAT4	81	157	459	9.1	80.0	46.4	33.5	27.7	15.5	130	9.1	17.6	37.1	16.5	3.6	0.65	3.1	2.4	1.7	1.75	5.4
PAT5	<LD	662	12.3	0.6	6.0	6.2	3.8	5.0	2.8	11.0	0.9	1.9	5.0	2.5	0.3	0.05	0.0	0.5	0.3	0.23	0.8
LL-16-d	27	436	193	3.5	21.8	17.3	7.2	8.8	9.8	37.2	1.8	6.1	11.5	7.2	1.5	0.33	1.5	1.4	1.2	0.99	1.9
LL-16-d	<LD	308	14.7	0.3	6.5	3.0	6.4	3.4	2.5	7.8	0.4	2.1	4.1	2.7	1.0	0.07	0.4	0.3	0.4	0.17	0.2
LL-16-d	<LD	348	101	1.7	11.5	8.0	9.5	5.2	7.1	45	2.0	4.2	10.7	5.1	0.8	0.23	1.0	0.9	0.3	0.63	1.8
LL-16-e	<LD	249	479	13.5	95.4	49.9	11.3	24.1	17.5	110	11.0	19.4	38.9	20.2	3.9	0.83	3.6	3.1	2.0	1.96	5.3
LL-16-f	177	512	1559	18.8	158	52.6	8.0	15.2	15.3	162	12.1	36.5	72.7	32.6	6.1	1.21	4.0	2.6	1.5	1.84	7.7
LL-16-f	44	587	578	8.7	67.0	28.6	22.6	9.7	13.1	70.6	2.4	14.3	29.4	16.5	3.9	0.65	2.5	2.5	1.4	1.27	4.2
LL-16-g	178	66.9	405	11.4	64.5	73.5	19.8	26.7	10.5	171	13.4	17.3	33.4	16.2	2.8	0.29	2.2	1.9	1.2	1.54	9.8
LL-16-h	229	37.2	768	13.1	64.9	76.8	13.2	6.6	14.9	195	18.6	48.7	99.0	49.0	9.1	1.65	6.5	3.1	1.4	1.77	12.7
LL-16-f	132	235	794	12.3	98.4	50.3	15.2	17.5	16.6	115	17.9	20.7	40.7	20.1	3.7	0.73	3.0	2.8	1.6	1.76	5.5
LL-16-i	<LD	277	50.2	1.0	5.9	6.4	6.7	3.0	7.9	33.7	1.1	5.9	13.2	6.2	1.4	0.11	1.1	1.2	0.3	0.64	2.2
LL-16-j1	<LD	2387	7.3	0.4	2.7	3.6	2.4	2.0	2.6	2.4	0.1	2.1	6.3	1.5	0.2	0.02	0.4	0.3	0.3	0.15	0.3
LL-16-j2	<LD	330	0	0.1	3.0	3.4	5.8	2.9	9.8	2.4	0.3	3.6	9.1	4.7	0.9	0.10	1.3	1.5	0.6	0.84	1.4